Stem Cells International

Mesenchymal Stem Cells as Promoters, Enhancers, and Playmakers of the Translational Regenerative Medicine 2018

Special Issue Editor in Chief: Andrea Ballini
Guest Editors: Marco Tatullo, Salvatore Scacco, and Dario Coletti

Mesenchymal Stem Cells as Promoters, Enhancers, and Playmakers of the Translational Regenerative Medicine 2018

Stem Cells International

Mesenchymal Stem Cells as Promoters, Enhancers, and Playmakers of the Translational Regenerative Medicine 2018

Special Issue Editor in Chief: Andrea Ballini
Guest Editors: Stefania Cantore, Salvatore Scacco, Dario Coletti, and Marco Tatullo

Copyright © 2018 Hindawi. All rights reserved.

This is a special issue published in "Stem Cells International." All articles are open access articles distributed under the Creative Commons Attribution License, which permits unrestricted use, distribution, and reproduction in any medium, provided the original work is properly cited.

Editorial Board

James Adjaye, Germany
Cinzia Allegrucci, UK
Eckhard U. Alt, USA
Francesco Angelini, Italy
James A. Ankrum, USA
Stefan Arnhold, Germany
Marta Baiocchi, Italy
Andrea Ballini, Italy
Dominique Bonnet, UK
Philippe Bourin, France
Daniel Bouvard, France
Anna T. Brini, Italy
Annelies Bronckaers, Belgium
Silvia Brunelli, Italy
Stefania Bruno, Italy
Bruce A. Bunnell, USA
Kevin D. Bunting, USA
Benedetta Bussolati, Italy
Leonora Buzanska, Poland
A. C. Campos de Carvalho, Brazil
Stefania Cantore, Italy
Yilin Cao, China
Marco Cassano, Switzerland
Alain Chapel, France
Isotta Chimenti, Italy
Mahmood S. Choudhery, Pakistan
Pier Paolo Claudio, USA
Gerald A. Colvin, USA
Mihaela Crisan, UK
Radbod Darabi, USA
Joery De Kock, Belgium
Frederic Deschaseaux, France
Marcus-André Deutsch, Germany
Varda Deutsch, Israel
Valdo Jose Dias Da Silva, Brazil
Massimo Dominici, Italy
Leonard M. Eisenberg, USA
Georgina Ellison, UK
Alessandro Faroni, UK
F. J. Fernández-Avilés, Spain
Jess Frith, Australia
Ji-Dong Fu, USA
Alessandro Giacomello, Italy
Maria M. Estima Gomes, Portugal
Cristina Grange, Italy
Stan Gronthos, Australia
Hugo Guerrero-Cazares, USA
Jacob H. Hanna, Israel
David A. Hart, Canada
Alexandra Harvey, Australia
Yohei Hayashi, Japan
Tong-Chuan He, USA
Boon C. Heng, Hong Kong
Xiao J. Huang, China
Thomas Ichim, USA
Joseph Itskovitz-Eldor, Israel
Elena Jones, UK
Christian Jorgensen, France
Oswaldo Keith Okamoto, Brazil
Alexander Kleger, Germany
Diana Klein, Germany
Valerie Kouskoff, UK
Andrzej Lange, Poland
Laura Lasagni, Italy
Renke Li, Canada
Tao-Sheng Li, Japan
Shinn-Zong Lin, Taiwan
Risheng Ma, USA
Yupo Ma, USA
Marcin Majka, Poland
Giuseppe Mandraffino, Italy
Athanasios Mantalaris, UK
Cinzia Marchese, Italy
Katia Mareschi, Italy
Hector Mayani, Mexico
Jason S. Meyer, USA
Eva Mezey, USA
Susanna Miettinen, Finland
Toshio Miki, USA
Claudia Montero-Menei, France
Christian Morsczeck, Germany
Patricia Murray, UK
Federico Mussano, Italy
Mustapha Najimi, Belgium
Norimasa Nakamura, Japan
Bryony A. Nayagam, Australia
Karim Nayernia, UK
Krisztian Nemeth, USA
Francesco Onida, Italy
Sue O'Shea, USA
Gianpaolo Papaccio, Italy
Kishore B. S. Pasumarthi, Canada
Yuriy A. Petrenko, Czech Republic
Alessandra Pisciotta, Italy
Diego Ponzin, Italy
Stefan Przyborski, UK
Bruno Pèault, USA
Peter J. Quesenberry, USA
Pranela Rameshwar, USA
F. J. Rodríguez-Lozano, Spain
Bernard A. J. Roelen, Netherlands
Alessandro Rosa, Italy
Peter Rubin, USA
Hannele T. Ruohola-Baker, USA
Benedetto Sacchetti, Italy
Ghasem Hosseini Salekdeh, Iran
Antonio Salgado, Portugal
Fermin Sanchez-Guijo, Spain
Anna Sarnowska, Poland
Heinrich Sauer, Germany
Coralie Sengenes, France
Dario Siniscalco, Italy
Shimon Slavin, Israel
Sieghart Sopper, Austria
Valeria Sorrenti, Italy
Giorgio Stassi, Italy
Ann Steele, USA
Alexander Storch, Germany
Bodo Eckehard Strauer, Germany
Hirotaka Suga, Japan
Gareth Sullivan, Norway
Masatoshi Suzuki, USA
Kenichi Tamama, USA
Corrado Tarella, Italy
N. J.E.E. Tirnitz-Parker, Australia
Daniele Torella, Italy
Hung-Fat Tse, Hong Kong
Marc L. Turner, UK
Aijun Wang, USA
Darius Widera, UK
Bettina Wilm, UK
Dominik Wolf, Austria

Wasco Wruck, Germany
Qingzhong Xiao, UK
Takao Yasuhara, Japan
Zhaohui Ye, USA
Holm Zaehres, Germany
Elias T. Zambidis, USA
Ludovic Zimmerlin, USA
Ewa K. Zuba-Surma, Poland
Eder Zucconi, Brazil
Maurizio Zuccotti, Italy
Nicole Isolde zur Nieden, USA

Contents

Hindawi
Stem Cells International
Volume 2018, Article ID 6927401, 2 pages
https://doi.org/10.1155/2018/6927401

Editorial

Mesenchymal Stem Cells as Promoters, Enhancers, and Playmakers of the Translational Regenerative Medicine 2018

Andrea Ballini,[1] **Stefania Cantore**,[2] **Salvatore Scacco**,[1] **Dario Coletti**,[3] **and Marco Tatullo**[4]

[1]*Department of Basic Medical Sciences, Neurosciences and Sense Organs, University of Bari "Aldo Moro", Bari, Italy*
[2]*City Unity College, Athens, Greece*
[3]*Institut de Biologie-Biology of Adaptation and Aging (B2A), Université Pierre et Marie Curie, Paris, France*
[4]*Biomedical Section, Tecnologica Research Institute, Crotone, Italy*

Correspondence should be addressed to Andrea Ballini; andrea.ballini@me.com

Received 18 September 2018; Accepted 18 September 2018; Published 30 October 2018

Copyright © 2018 Andrea Ballini et al. This is an open access article distributed under the Creative Commons Attribution License, which permits unrestricted use, distribution, and reproduction in any medium, provided the original work is properly cited.

Mesenchymal stem cells (MSCs) are currently being tested in preclinical and clinical trials for their ability to foster wound healing and tissue regeneration [1].

They are well known to show a therapeutic potential largely depending on their ability to secrete proregenerative cytokines, making these cells an attractive option for improving the treatment of chronic wounds. The wound microenvironment is a miscellaneous key factor in the local management of the healing process: players such as the extracellular matrix or the resident and recruited cells with paracrine activity are able to determine the way and the appropriateness of the regenerative processes [2].

Dental-derived mesenchymal stem cells (D-dMSCs) are an intriguing milestone of the regenerative medicine, with regard to their potential of differentiating into osteogenic, adipogenic, and chondrogenic lineages [3–5], possessing in this way the potential to significantly influence the bone and periodontal treatment strategies in the future [6–9].

Despite the multiple barriers to their clinical use, MSCs or D-dMSCs have shown sufficient promise to garner a primary place in the field of translational medicine. In fact, MSC and D-dMSC therapies have significant implications for human health: clinical studies are greatly needed to confirm or stimulate the basic and translational researches aimed at reaching cutting-edge results [10–13].

The special issue has reported articles on MSCs used as a therapeutic aid in clinical and surgical applications. The topics in translational medicine reported were the MSC therapy for intravertebral disc regeneration (J. Jia et al.) and the cell therapy as a promising aid for cerebral vasculature (B. Y. Choi et al.), as well as for the proper management of thin endometrium (J. Zhao et al.).

The most reported translational use of MSC/D-dMSC therapy is related to bone tissue regeneration: in fact, many authors have investigated on the osteogenic ability of different stem cell types and genes, such as TGFβ1 that enhances MSC commitment to either the osteogenic or adipogenic lineages by reorganizing the actin cytoskeleton (M. Elsafadi et al.), as well as on the use of a PRP blood clot stabilizer to treat infrabony periodontal defects (M. Saleem et al.) and the use of vitamin D in dental-derived MSCs that promote osteogenic differentiation through the modulation of $\alpha V\beta 3$ (F. Posa et al.), the role played by the ganglioside GM1 in the osteogenic differentiation of human tendon stem cells (S. Bergante et al.), or via low-frequency pulsed electromagnetic fields (P. S. P. Poh et al.)

Some authors have focused their researches on umbilical cord stem cells, due to their large application on translational medicine (D. R. Kwon et al.), as well on miRNA-132 MSC-derived exosomes in the treatment of myocardial infarction (T. Ma et al.).

Finally, experimental findings from in silico studies, on the one hand, highlighted the promotive role of hypoxia in MSC proliferation (S. Gao et al.); on the other hand, it was reported that an *in vitro* loading model (2D and 3D in combination with different scaffolds) represents a simple and

very efficient way to investigate molecular events during orthodontic tooth movement (M. Janjic et al.).

In this special issue, the editors together with the involved authors have well described the MSCs and D-dMSCs in their different but fundamental roles as promoters, enhancers, and playmakers of the translational regenerative medicine. Starting from the contents of our issue, the scientific community will be stimulated to experiment new ideas, to improve the knowledge of the MSCs/D-dMSCs, and to speed up their clinical application, so as to improve the future therapies.

Conflicts of Interest

The authors declare that there is no conflict of interest regarding the publication of this editorial.

Andrea Ballini
Stefania Cantore
Salvatore Scacco
Dario Coletti
Marco Tatullo

References

[1] J. Galipeau, M. Krampera, J. Barrett et al., "International Society for Cellular Therapy perspective on immune functional assays for mesenchymal stromal cells as potency release criterion for advanced phase clinical trials," *Cytotherapy*, vol. 18, no. 2, pp. 151–159, 2016.

[2] A. Ballini, S. Scacco, D. Coletti, S. Pluchino, and M. Tatullo, "Mesenchymal stem cells as promoters, enhancers, and playmakers of the translational regenerative medicine," *Stem Cells International*, vol. 2017, Article ID 3292810, 2 pages, 2017.

[3] A. Ballini, A. Boccaccio, R. Saini, P. Van Pham, and M. Tatullo, "Dental-derived stem cells and their secretome and interactions with bioscaffolds/biomaterials in regenerative medicine: from the in vitro research to translational applications," *Stem Cells International*, vol. 2017, Article ID 6975251, 3 pages, 2017.

[4] F. Paduano, M. Marrelli, F. Palmieri, and M. Tatullo, "CD146 expression influences periapical cyst mesenchymal stem cell properties," *Stem Cell Reviews*, vol. 12, no. 5, pp. 592–603, 2016.

[5] A. di Benedetto, F. Posa, C. Carbone et al., "NURR1 downregulation favors osteoblastic differentiation of MSCs," *Stem Cells International*, vol. 2017, Article ID 7617048, 10 pages, 2017.

[6] S. Cantore, V. Crincoli, A. Boccaccio et al., "Recent advances in endocrine, metabolic and immune disorders: mesenchymal stem cells (MSCs) and engineered scaffolds," *Endocrine, Metabolic & Immune Disorders Drug Targets*, vol. 18, no. 5, pp. 466–469, 2018.

[7] A. Boccaccio, A. E. Uva, M. Fiorentino, G. Monno, A. Ballini, and A. Desiate, "Optimal load for bone tissue scaffolds with an assigned geometry," *International Journal of Medical Sciences*, vol. 15, no. 1, pp. 16–22, 2018.

[8] A. Ballini, A. Scattarella, V. Crincoli et al., "Surgical treatment of gingival overgrowth with 10 years of follow-up," *Head & Face Medicine*, vol. 6, no. 1, p. 19, 2010.

[9] A. Ballini, S. Tetè, A. Scattarella et al., "The role of anticyclic citrullinated peptide antibody in periodontal disease," *International Journal of Immunopathology and Pharmacology*, vol. 23, no. 2, pp. 677–681, 2010.

[10] C. Lechanteur, A. Briquet, O. Giet, O. Delloye, E. Baudoux, and Y. Beguin, "Clinical-scale expansion of mesenchymal stromal cells: a large banking experience," *Journal of Translational Medicine*, vol. 14, no. 1, p. 145, 2016.

[11] M. Tatullo, G. M. Simone, F. Tarullo et al., "Antioxidant and antitumor activity of a bioactive polyphenolic fraction isolated from the brewing process," *Scientific Reports*, vol. 6, no. 1, article 36042, 2016.

[12] M. Marrelli, S. Gentile, F. Palmieri, F. Paduano, and M. Tatullo, "Correlation between surgeon's experience, surgery complexity and the alteration of stress related physiological parameters," *PLoS One*, vol. 9, no. 11, article e112444, 2014.

[13] A. Uccelli and D. J. Prockop, "Why should mesenchymal stem cells (MSCs) cure autoimmune diseases?," *Current Opinion in Immunology*, vol. 22, no. 6, pp. 768–774, 2010.

Hindawi
Stem Cells International
Volume 2018, Article ID 3069741, 10 pages
https://doi.org/10.1155/2018/3069741

Research Article

Therapeutic Effects of VEGF Gene-Transfected BMSCs Transplantation on Thin Endometrium in the Rat Model

Zhao Jing,[1] Yan Yi,[1] Huang Xi,[1] Lun-Quan Sun,[2] and Li Yanping[1]

[1]*Reproductive Medicine Center, Xiangya Hospital, Central South University, Changsha, Hunan, China*
[2]*Center for Molecular Medicine, Xiangya Hospital, Central South University, Hunan, China*

Correspondence should be addressed to Li Yanping; lyp7798@126.com

Received 21 June 2018; Accepted 2 September 2018; Published 30 October 2018

Academic Editor: Andrea Ballini

Copyright © 2018 Zhao Jing et al. This is an open access article distributed under the Creative Commons Attribution License, which permits unrestricted use, distribution, and reproduction in any medium, provided the original work is properly cited.

Objective. Bone mesenchymal stem cells (BMSCs) transplantation has a therapeutic effect on the thin endometrium in animal researches and clinical trials. The present study aims at assessing whether transplantation of VEGF-transfected BMSCs (VEGF-BMSCs) have a better therapeutic effect on endometrial regeneration and endometrial receptivity compared with BMSCs therapy alone. *Methods*. Sprague-Dawley (SD) rats were used in the study. Thin endometrium model was established with 95% ethanol injection into uterine. VEGF-BMSCs or BMSCs was transplanted via tail vein IV injection. Endometrial thickness, morphology, and pinopodes were assessed by hematoxylin and eosin (HE) staining and scanning electron microscope (SEM). The proteins and mRNAs expressions of markers for endometrial cells and endometrial receptivity were measured after treatment. The fertility testing was done to assess the embryo implantation efficiency. *Results*. VEGF-BMSCs transplantation significantly increased endometrial thickness compared with the BMSCs group and the control group. There was no significant difference in endometrial thickness between VEGF-BMSCs group and sham operation group. Importantly, in protein level, expressions of cytokeratin, vitamin, VEGF, LIF, and integrin $\alpha_v\beta_3$ in VEGF-BMSC group were increased dramatically compared with those of the control group and BMSC group both 4 days and 8 days after stem cells transplantation. Accordingly, mRNA expression of LIF and integrin $\alpha_v\beta_3$ was significantly upregulated compared with those of the control group and BMSC group both 4 and 8 days after treatment. The pinopodes were developed better in the VEGF-BMSCs group and the sham operation group compared with BMSCs group and the control group. The number of embryo implantation is largest in the sham operation group, followed by VEGF-BMSCs group, BMSCs group, and the control group. *Conclusions*. Transplantation of VEGF gene-transfected BMSCs may be a better therapeutic treatment for thin endometrium than stem cell therapy alone.

1. Introduction

A thin endometrium often means impaired endometrial receptivity, which has been well recognized as a critical factor in implantation failure [1–4]. At present, there was no uniform definition for "thin endometrium". A number of studies suggested that a minimal endometrial thickness of 6 mm is required for embryo implantation [5]. Several treatments, such as estrogen, aspirin, pentoxifylline, and endometrial injury, have been tried to improve the regeneration of the endometrium. However, improvement was not very obvious with the available treatments [6–8]. It is still a big challenge to find a useful treatment for thin endometrium [9].

Until now, the most promising treatment for thin endometrium or Asherman syndrome (AS) seems to be the stem-cell therapy. There have been many animal and human reports about the treatment effect of stem cells transplantation on the thin endometrium. A number of animal experiments showed that the thin endometrium was significantly improved after stem cells transplantation [10–13]. Clinical reports showed that infertile women with thin endometrium or AS had a significant increase in endometrial thickness after stem cells treatment and enhanced pregnancy rates [14–17].

It was reported that thin endometrium pathophysiologic features were as follows: increased flow impedance of radial arteries has a detrimental effect on the glandular epithelium,

leading to a decreased level of vascular endothelial growth factor (VEGF). At last, poor vascular development and impaired blood flow of the endometrium were caused [18]. VEGF was an angiogenesis factor and play a critical role in angiogenesis via branching of old blood vessels or sprouting of new blood vessels. Recently, stem cells transplantation has been discussed as a treatment for thin endometrium. So, the present study aimed at investigating whether the VEGF gene-transfected BMSCs (VEGF-BMSCs) have a better effect on the thin endometrium.

2. Materials and Methods

2.1. Animals. Seven–nine weeks Sprague-Dawley (SD) rats weighing 150–250 g were used in the experiments. All animal experiments were performed in strict line with the "National Institutes of Health Guide for the Care and Use of Laboratory Animals". The present study was reviewed and approved by the Institutional Review Board and the Ethics Committee of Xiangya Hospital, Central South University.

2.2. BMSCs' Collection and Culture. Bone marrow was aspirated and prepared from the femurs and tibia of an adult, male/female, SD rats. The bone marrow was digested, cultured, and filtered according to a previous study [19]. When reaching at least 80% confluence, the stem cells were collected with 0.05% trypsin-EDTA (Gibco). BMSCs were cultured at a density of 3000 to 6000/cm^2, and the fourth to sixth passages BMSCs were used for transfection and transplantation.

2.3. Plasmid Preparation and Transfection of Rat BMSC. Human $VEGF_{165}$ was integrated into the pCR3.1 plasmid, which was published previously. 1 μg of plasmid DNA of $hVEGF_{165}$ was used for transfection per 100,000 cells, and the empty pCR3.1 combined with 3 μL of metafectene was used as control group per 100,000 cells. These cells were transferred to BMSCs culture medium 6 hours later and were kept overnight. Before transplantation, 5^*10^6 of the stem cells was suspended in saline at a concentration of 50,000 cells/μL.

2.4. Groups. Standardized laboratory conditions, including air-condition rooms and plenty of water and food, were applied to keep the rats. According to our preliminary study, a thin endometrium rat model was built by injecting anhydrous ethanol into the uterus cavity of rats [20]. One hundred rats were divided into four groups randomly, which included the control group (iv-injected saline into tail vein 6–8 hours after modeling, $n = 25$), BMSC group (iv-injected BMSCs into tail vein 6–8 hours after modeling, $n = 25$), VEGF-BMSC group (in-injected VEGF-BMSCs into tail vein 6–8 hours after modeling, $n = 25$), and sham operation group (operation without modeling, $n = 25$).

For scanning electron microscopy (SEM) and fertility testing, rats were anesthetized and killed with overdose 10% chloral hydrate (1.125 g/kg) at 4 days ($n = 10$) and 9 days ($n = 10$) after the appearance of vaginal plugs. The rats were anesthetized and killed with overdose 10% chloral hydrate (1.125 g/kg) at three estrus cycles after BMSCs treatment. The vaginal smear was observed to determine the estrous cycles. The uteri were excised after the rats were sacrificed. For further research, uteri of rats were sectioned and stored in liquid nitrogen and/or formalin.

2.5. Hematoxylin and Eosin (HE) Staining. HE staining was performed according to a previous study [21]. The slides with 5 μm thickness were completely covered in xylene twice and rehydrated in a series of ethanol with gradually decreased concentration. The slides were rinsed with deionized demineralized water, dyed in hematoxylin for about 50 seconds, rinsed with deionized demineralized water once again, and at last dyed in eosin for 3 seconds. The slides of the endometrium were dehydrated with a series of ethanol in xylene and mounted with Permount mounting medium after the color reaction. The endometrial morphology and the endometrial thickness were examined and compared between groups.

2.6. Immunohistochemistry. For immunohistochemistry, the uterine were stored in 4% paraformaldehyde and embedded in paraffin. Serial slides with about 6 μm were prepared, deparaffinized in xylene, rehydrated with different concentrations ethanol, and rinsed with water. Endogenous peroxidase was blocked with 3% hydrogen peroxidase. Slides were treated with chondroitin ABC lyase (0.15 U/mL) and blocked with 10% normal goat serum for 1 hour. Expressions of cytokeratin, vimentin, integrin $\alpha_v\beta_3$, and leukemia inhibitory factor (LIF) proteins were performed by incubating slides of rat uteri with rabbit polyclonal antibodies against cytokeratin, vimentin, integrin $\alpha_v\beta_3$, and LIF overnight at 4°C. Slides were incubated with secondary antibodies at 1 : 3000 dilution followed by DAB solution for 1 hour. Then, slides were briefly stained with hematoxylin solution (15 seconds) (Gill no. 3; Sigma) and evaluated by a microscope (Nikon).

2.7. Western Blotting. Total protein was extracted from uterine tissues according to the protocol, and the concentration of protein was confirmed with a Precision Red Assay (Cytoskeleton Inc.). Equal amounts of protein were stained with loading dye and separated with 12% SDS-PAGE. Protein was then transferred to polyvinylidene difluoride (PVDF) membrane and was incubated with 5% bovine serum albumin (BSA). The membrane was exposed to anti-VEGF antibody (1 : 500), anti-cytokeratin antibody (1 : 500), anti-vimentin antibody (1 : 500), anti-integrinα_v antibody (1 : 300), anti-integrinβ_3 antibody (1 : 300), and anti-LIF antibody (1:300) overnight. The blots were washed with tris-buffer saline and incubated with secondary anti-rabbit IgG (1 : 3000; Cell Signaling Technology) for 1 hour at room temperature. The protein content was detected using SuperSignal West Pico (Pierce Biotechnology). Anti-β-actin antiserum (Sigma) was used as an internal standard between groups.

2.8. Real-Time PCR. Total RNA was collected from the harvested uteri by the use of an extraction reagent (Trizol; Gibco) and was dissolved in water treated with diethylpyrocarbonate, and the concentration was measured by a spectrophotometer (UV-1601). In order to determine a constant expression of a housekeeping gene in the RNA extractions, the real-time PCR of GAPDH was also performed. Any possible DNA contamination was removed with DNase I (0.2 U/μL; Ambion). Quantitative PCR reaction was performed with Biosystems 7500 Fast Real-Time PCR system and Taqman

probes. Quantitative expression level was analyzed using the 2ΔΔCt method. The PCR probe sets used are as follows:

VEGF: sense 5′- CGA CAG AAG GGG AGC AGA AAG-3′, and antisense 5′-GCA AGT ACG TTC GTT TAA CTC-3′;

LIF: sense 5′- GTC AAC TGG CTC AAC TCA ACG-3′, and antisense 5′- CTG GCA GCC CAA CTT CTT C-3′;

Integrin α_v: sense 5′- GTC AGC CCA GTC GTG TCT TAC A-3′, and antisense 5′- GGG CTT GAA ACT CCT CTT ATC TCA-3′;

Integrin β_3: sense 5′- GTG GAC CGC AAC AAC GCA-3′, and antisense 5′- ACC AAG GTA ACG CCA GGA AT-3′.

2.9. Scanning Electron Microscopy (SEM). The rats were euthanized, and the uteri were dissected and cut open longitudinally. Uteri were submerged in 2.5% glutaraldehyde and kept in this solution for 24 hours. Then the specimens were rinsed several times in phosphate buffer, fixed in 4% osmium phosphate-buffered solution, dehydrated in an acetone solution in distilled water at increasing concentrations, and kept in 100% acetone. Then the samples were dried in a critical point drier with carbon dioxide, mounted and coated with gold, and examined by SEM.

2.10. Fertility Testing. Endometrial receptivity was assessed by testing their capacity to receive fertilized ova and retain embryos for pregnancy. The rats were mating at 1 : 1 ratio with mature male rats, euthanized 9 days after the appearance of vaginal plugs, and each uterus was examined for the number of fetuses.

2.11. Statistical Analyses. The statistical software SPSS 16.0 (IBM) was applied in the present study. Measurement data were present as mean ± SD. A one-sided *t*-test was used to compare the difference between groups. For Western blot, the density of protein bands was analyzed with Image-J software, and the relative protein level was presented as a ratio of the target protein to β-actin. For real-time PCR, the relative mRNA level was obtained by comparing the target mRNA to the GAPDH from the same gel. A P level of less than 0.05 ($P < 005$) was considered to be significant.

3. Results

3.1. BMSC Phenotype. The BMSCs, obtained from rat bone marrow aspirates, were grown in the cultural medium as previously published. FACS analysis showed that CD90 and CD73 were expressed in BMSCs, whereas hematopoietic markers CD45 and CD34 were negative. The BMSCs had the capability to differentiate toward adipocytes and osteoblasts.

3.2. Histopathological Observations. Rat in BMSCs and VEGF-BMSCs group had a significantly larger number of endometrial glands, and a significant thicker endometrium compared with that of the control group. The endometrial layer of the VEGF-BMSC group showed a relatively intact structure, with more endometrial glands, capillaries and increased endometrial thickness. The endometrium of the control group was totally damaged, showing extensive coagulation necrosis, cell apoptosis in the nearly whole layer of endometrium and parts of the myometrium layer.

The endometrial thickness of the control group, BMSC group, VEGF-BMSC group, and sham operation group were as follows: 218.7 ± 20.6 μm, 598.7 ± 37.7 μm, 658.0 ± 40.0 μm, and 682.3 ± 38.2 μm, respectively. The VEGF-BMSC group had an obvious thicker endometrial lining compared with that of the control group and the BMSC group, and there was no significant difference between the VEGF-BMSC group and the sham operation group (Figure 1).

3.3. Protein Expression of VEGF, Cytokeratin, Vimentin, Integrin $\alpha_v\beta_3$, and LIF. Immunohistochemical results demonstrated that cytokeratin, integrin $\alpha_v\beta_3$, and LIF were mainly expressed in the cytoplasm of the endometrial epithelial cells, and vimentin was mainly localized in the cytoplasm of endometrial stromal cells. The expression of cytokeratin, vimentin, integrin$\alpha_v\beta_3$, and LIF in the VEGF-BMSC group and BMSC group were significantly stronger than those of the control group and were slightly weaker than those of the sham operation group without significance. (Figure 2, Supplemental Figure 1).

Western Blotting was applied to exam the expression of these proteins in the endometrium 4 days and 8 days after stem cells transplantation. Vimentin, integrin $\alpha_v\beta_3$, and LIF protein expressions were gradually increased in the control, BMSC, VEGF-BMSC, and sham operation groups, respectively. VEGF-BMSC group showed a significantly higher expression of these four proteins compared with those of control group ($P < 0.05$). VEGF expression level was the highest in the VEGF-BMSC group, followed by BMSC group, sham operation group, and control group. The cytokeratin expression level in the VEGF-BMSC group was slightly higher than that of the BMSC group and sham operation group without a significant difference and was significantly higher compared with the control group. When compared day 4 with day 8 after stem cells transplantation, there was no significant difference in the expressions of those proteins. (Figure 3, Supplemental Figure 2).

3.4. mRNA Expression of VEGF, Integrin $\alpha_v\beta_3$, and LIF. mRNA expressions of endometrial receptivity's markers 4 and 8 days after treatment are shown in Figure 4 and Supplemental Figure 3. The VEGF-BMSC group exhibited a significantly higher expression of VEGF mRNA than the BMSC group and control group and a similar level with the sham operation group. The LIF mRNA expression in the VEGF-BMSC group was significantly higher than that of the BMSC group and control group and was similar with that of the sham operation group. The integrin α_v β_3 mRNA expressions in the VEGF-BMSC group and BMSC group were similar, which were significantly higher when compared with the control group.

3.5. Pinopodes of the Endometrium. In the control group, the endometrium is thin. The microvilli were abundant, and no developed pinopodes in luminal cells were observed. In the BMSCs group and VEGF-BMSCs group, the microvilli gradually decreased in number and length. Smooth and slender

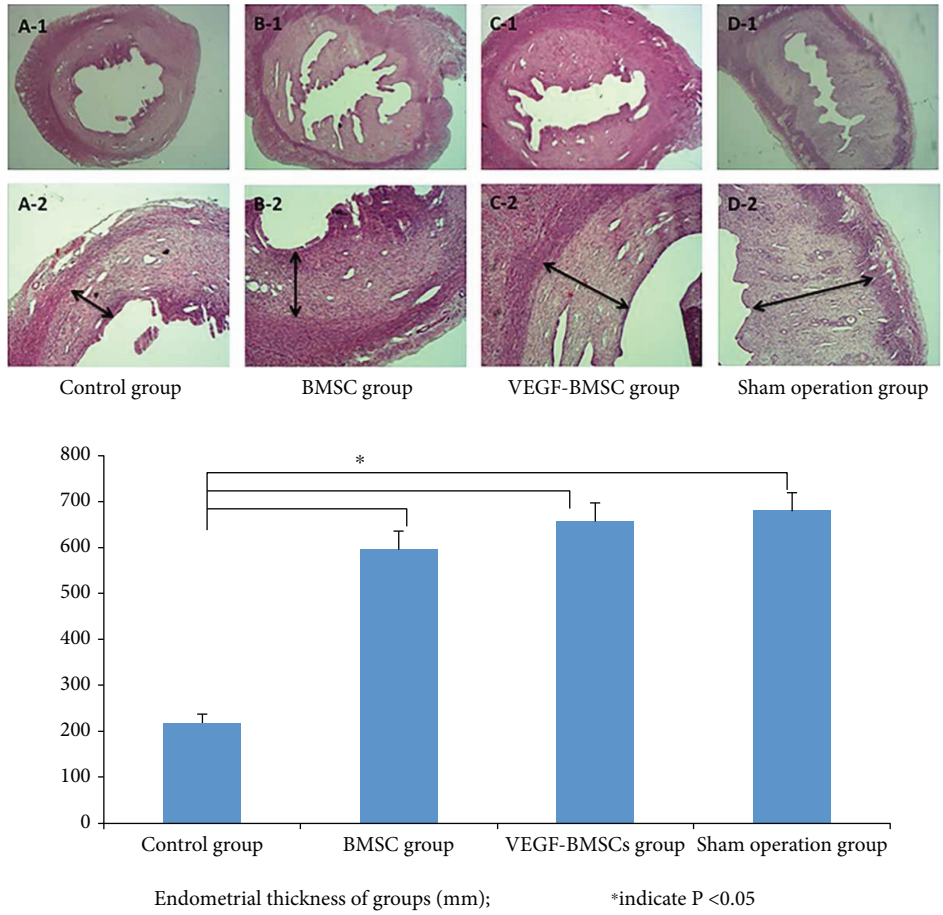

Figure 1: The morphology observation of the endometrium with HE staining (the first line were ×40; the second line were ×200). (A-1,2): control group, (B-1,2): BMSC group, (C-1,2): VEGF-BMSC group, (D-1,2): sham operation group. The bar chart represented the endometrial thickness of groups. The endometrial layer of the VEGF-BMSC group showed a relatively intact structure, with more endometrial glands, capillaries and increased endometrial thickness. The endometrium of the control group was totally damaged, showing extensive coagulation necrosis, cell apoptosis. The VEGF-BMSC group had an obvious thicker endometrial lining compared with that of the control group and the BMSC group, and there was no significant difference between the VEGF-BMSC group and the sham operation group.

membrane projections were formed from the cell apex and were transformed to pinopodes. We can observe that the pinopodes were developing and some of them had short microvilli in their surface in VEGF-BMSCs group and sham operation group. There were no significant differences between VEGF-BMSCs group and sham operation group in the number of pinopodes (Figure 5).

3.6. Embryo Implantation after VEGF-BMSCs/BMSCs Transplantation. Embryo implantation efficiency is the best index to assess the therapeutic effect of VEGF-BMSCs/BMSCs transplantation. In order to detect the effect of BMSCs/VEGF-BMSCs on the thin endometrium and endometrial receptivity, we looked at the embryo implantation efficiency in the different groups of rats. The sham operation group showed the greatest embryo implantation efficiency, followed by VEGF-BMSCs group, BMSC group, and control group. Sham operation group showed a significantly increased embryo implantation efficiency compared with BMSCs group and control group, and there was no significant difference between the sham operation group and VEGF-BMSCs group. (Figure 6, Supplemental Figure 4).

4. Discussion

There are many experimental studies showing the beneficial effects of VEGF gene-transfected stem cells transplantation on many disorders, such as bone defects, stroke, myocardial infarction, acute kidney injury, and bronchopulmonary dysplasia. [22–25].

At present, there are no reports about the VEGF gene-transfected stem cells transplantation as the treatment for thin endometrium or AS. As we all know, angiogenesis is necessary for the regeneration of endometrium after menstruation and plays a crucial role in the development of endometrial receptivity for successful embryo implantation [26, 27]. A lot of studies have explored the regulation of endometrial angiogenesis and showed that the vascularization of the endometrium was regulated by VEGF, which was expressed in the human endometrium [28–32]. Therefore,

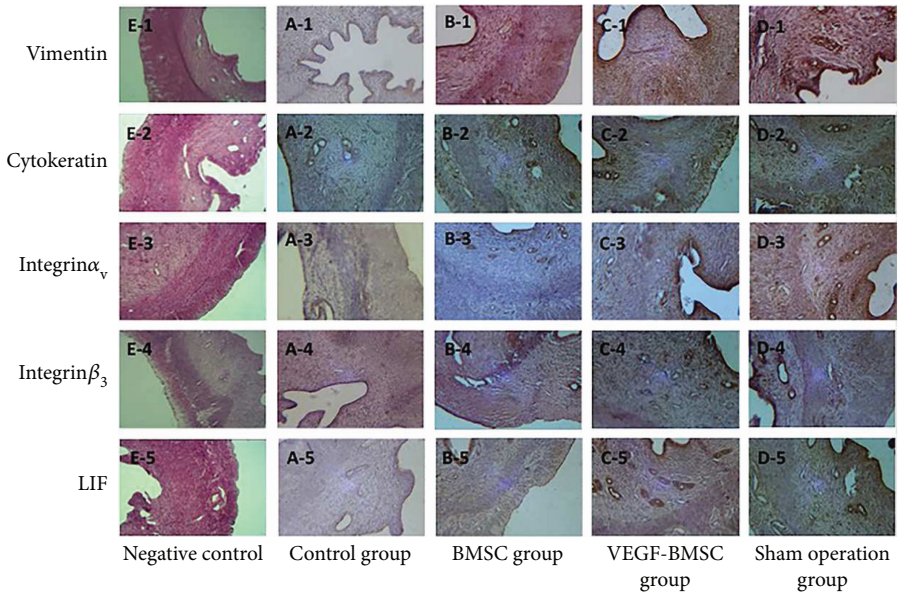

Figure 2: Protein expression of markers for endometrial cells and endometrial receptivity with immunohistochemistry. The expression of cytokeratin, vimentin, integrin$\alpha_v\beta_3$, and LIF in the VEGF-BMSC group and BMSC group was significantly stronger than those of the control group and were slightly weaker than those of the sham operation group without significance.

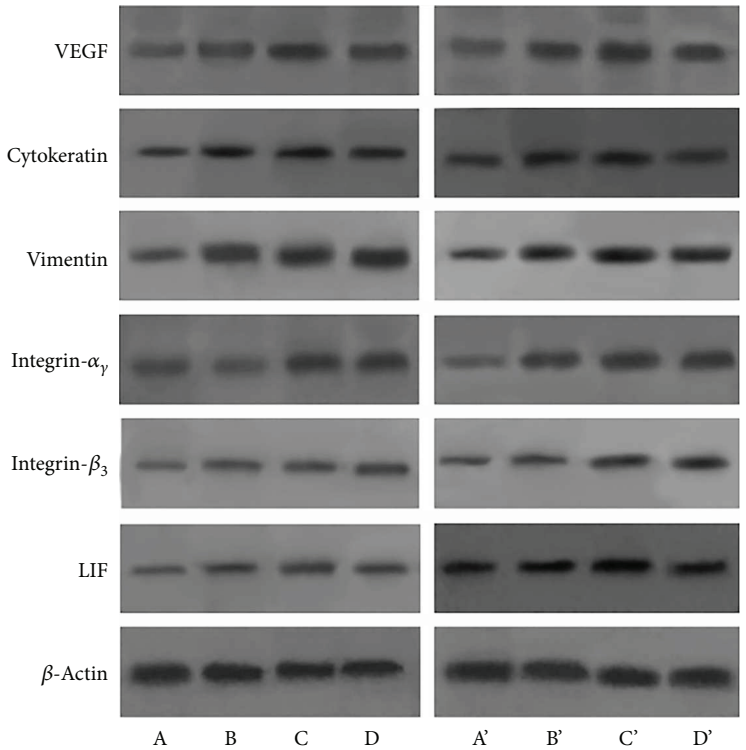

Figure 3: Protein expression of markers for endometrial cells and endometrial receptivity with Western blotting. (A, B, C, D) represent the control group, BMSC group, VEGF-BMSC group, and sham operation group 4 days after treatment, respectively. (A′, B′, C′, D′) mean these four groups 8 days after treatment. Vimentin, integrin $\alpha_v\beta_3$, and LIF protein expressions were gradually increased in the control, BMSC, VEGF-BMSC, and sham operation groups, respectively. VEGF-BMSC group showed a significantly higher expression of these four proteins compared with those of control group ($P < 0.05$). VEGF expression level was the highest in the VEGF-BMSC group, followed by BMSC group, sham operation group, and control group. The cytokeratin expression level in the VEGF-BMSC group was significantly higher compared with the control group. When compared day 4 with day 8 after stem cells transplantation, there was no significant difference in the expressions of those proteins.

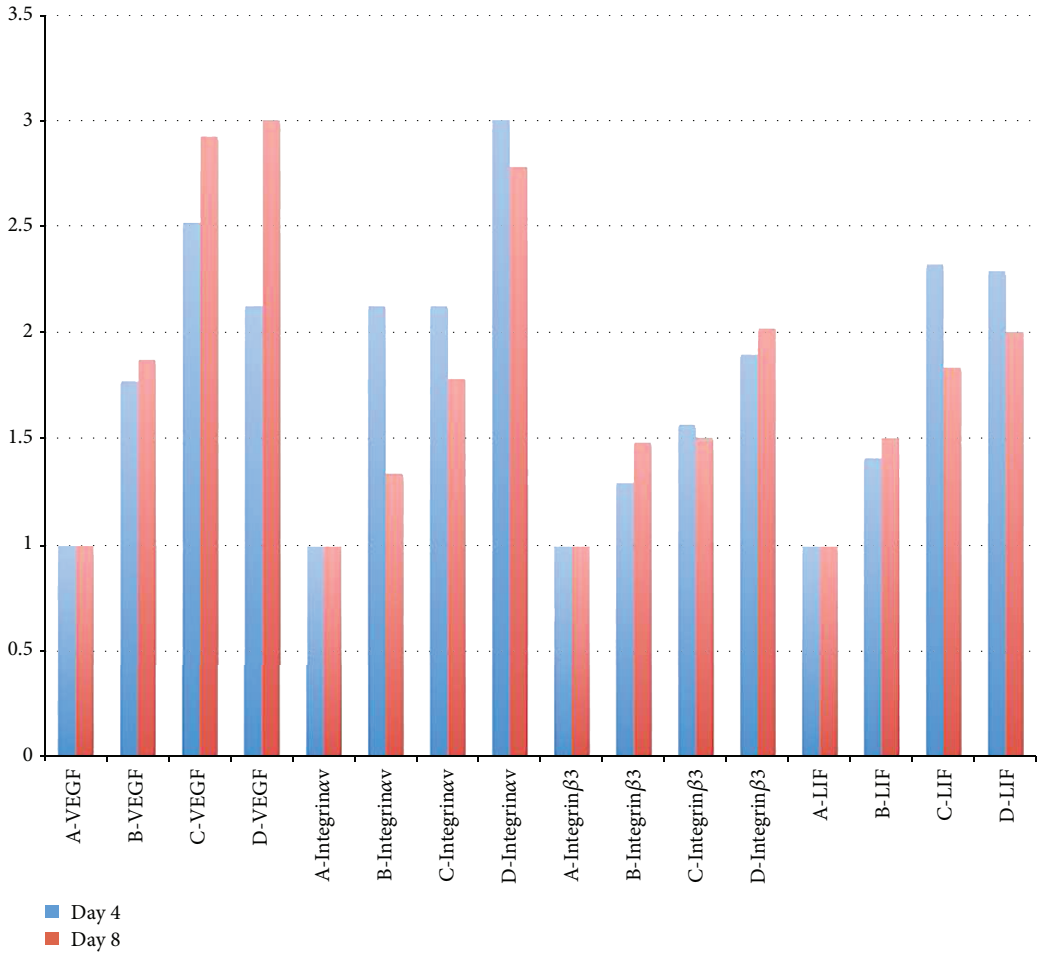

Figure 4: mRNA expressions of endometrial receptivity's markers 4 and 8 days after treatment. (A, B, C, D) represent control group, BMSC group, VEGF-BMSC group, and sham operation group, respectively. The VEGF-BMSC group exhibited a significantly higher expression of VEGF mRNA than the BMSC group and control group. The LIF mRNA expression in the VEGF-BMSC group was significantly higher than that of the BMSC group and control group and was similar with that of the sham operation group. The integrin $\alpha_v\beta_3$ mRNA expressions in the VEGF-BMSC group and BMSC group were similar, which were significantly higher when compared with the control group.

the pathophysiology of thin endometrium is damaged angiogenesis and decreased uterine blood flow.

Our previous studies have proved that BMSC transplantation could promote the growth of thin endometrium and improve the endometrial receptivity [12, 13]. It was supposed that VEGF gene-transfected BMSC would be a better therapy for thin endometrium. The present study is the first experiment, which assessed the effect of VEGF-BMSCs transplantation on thin endometrium in a rat model.

In our study, we showed that the rats in the VEGF-BMSC group had a thicker endometrium than those in the control group and BMSC group, and the expression of cytokeratin and vimentin in the VEGF-BMSC group was stronger than that in the control group and BMSC group. What we found indicated that IV infusion of VEGF-BMSCs promotes the regeneration of the endometrial cells and have a stronger therapeutic effect for thin endometrium.

We not only examined the endometrial regeneration but also assessed the endometrial receptivity. The present study found that the mRNA and protein expressions of integrin $\alpha_v\beta_3$ and LIF have significantly decreased in the thin endometrium rats without BMSC or VEGF-BMSC transplantation, and the BMSC/VEGF-BMSC treatment almost normalized the expression of integrin$\alpha_v\beta_3$ and LIF. As important regulators of endometrial function, integrin and LIF are considered to be the markers for endometrial receptivity and play a critical role in embryo implantation [33, 34]. Integrins belong to transmembrane glycoproteins family, and integrin $\alpha_1\beta_1$, $\alpha_4\beta_1$, and $\alpha_v\beta_3$ were found to be coexpressed in endometrium on days 20–24 of the human menstrual cycle [35, 36]. These three integrins have been considered as endometrial receptivity markers, and $\alpha_v\beta_3$ was found to be important in the course of embryo attachment. LIF receptors are expressed by the blastocyst as well as the endometrium, with maximum expression of LIF mRNA and protein occurring in endometrial epithelium during the implantation window, so it was considered to play an important role in implantation [37].

In addition to the protein marker of endometrial receptivity, we also observed the pinopodes, which are smooth mushroom-like projections that arise from the apical surface of the endometrium and are considered as endometrial

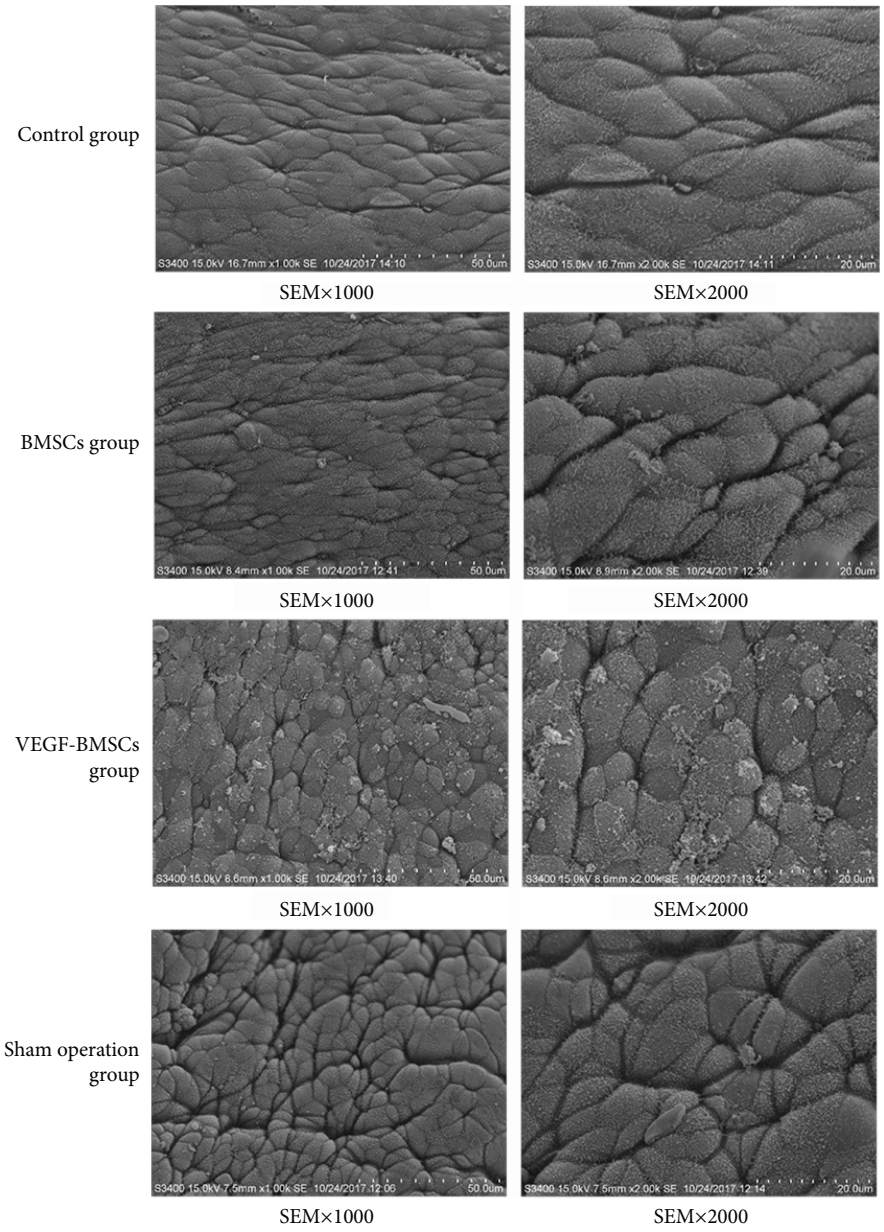

Figure 5: Scanning electron microscopy (×1000, ×2000) of the endometrial surface.

receptivity marker [38]. The pinopodes are observed for a short time period, 24 to 48 hours, during implantation in mammals [39], depending on the ovarian hormones, especially progesterone. In the rat endometrium, the appearance of pinopodes clearly demarcates the window of receptivity with a rise in numbers on day 4 of pregnancy, abundance on day 5 [40], and rapid decline on day 6 [38, 41]. The results showed that there were well-developed pinopodes in the sham operation group, BMSCs group, and VEGF-BMSCs group, and there was no pinopode in the control group. The function of pinopodes is not clear. The surfaces of pinopodes may have some receptors for adhesion molecules, which are essential for embryo implantation [42]. A vitro study observed the embryo attachment to endometrial epithelial cell and proposed that pinopode improve the attachment of blastocysts to endometrium during the processes of implantation [43].

Accordingly, the fertility testing demonstrated that embryo implantation efficiency is significantly higher in BMSCs group and VEGF-BMSCs group compared with the control group. The study has confirmed that UC-MSCs can promote endometrial proliferation and recover the endometrial embryo implantation ability [44]. This is consistent with our findings. We found that the VEGF-BMSC transplantation not only promote the endometrial regeneration but also improve the endometrial receptivity, showing a better therapeutic effect compared with BMSCs treatment alone.

Our data, which show a stronger mRNA and protein expressions of cytokeratin, vimentin, integrin $\alpha_v\beta_3$, and LIF, indicated that stem cells transplantation might not only bring

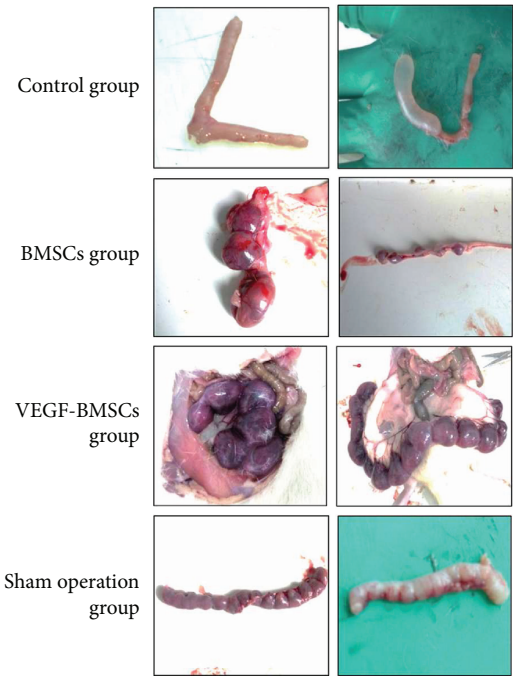

Figure 6: Embryo implantation efficiency of the control group, BMSCs group, VEGF-BMSCs group, and sham operation group.

beneficial effect on the endometrial regeneration but also bring good for endometrial receptivity improvement.

For Asherman's syndrome or thin endometrium, stem cells transplantation seems to be the most promising treatment. Several animal studies showed a significant enhancement of endometrial thickness and receptivity after MSCs transplantation into a rat model of thin endometrium [10–13]. All experimental groups showed an improvement in the fibrosis level and elucidated regenerative capabilities of BMSCs when thin endometrium rats were infused with BMSCs [12, 13]. It was found that transplanted cells could migrate to the injured uterus after intrauterine or tail vein injection. So migration to the injured sites and/or immune-regulation effect was the possible mechanisms of stem cells' effect [10, 11]. Stem cells not only promoted endometrial cell differentiation/proliferation and vascularization [10] but also decreased fibrosis, which ensured tissue repair. At last, stem cell transplantation restored the endometrial function and improved the fertility rate eventually [11].

Stem cells treatment for thin endometrium or AS was also applied in human. The first report of stem cell treatment for human was published in 2011 [14]. Autologous stromal stem cells were transplanted into the endometrial cavity with refractory thin endometrium (3.6 mm) [14]. At last, the endometrium was appropriate for embryo implantation. Another study [16] investigated six women with AS and found that transplantation of autologous BMSCs significantly improved the embryo implantation. Subsequently, Santamaria et al. [15] transplanted autologous CD133+ BMSCs into 11 AS and 5 endometrial atrophies (ET < 5 mm) women and showed endometrial functional restoration two months after cell therapy. Inspiringly, a recent study [17] found that transplantation of autologous menstrual blood-derived stromal cells (menSCs) could increase the endometrial thickness of severe AS; suggested autologous menSCs transplantation might be the most possible choice for severe AS. All of the above studies indicated that stem cells treatment was effective in endometrial regeneration.

The present study firstly explored the effect of VEGF gene-transfected BMSC transplantation on the thin endometrium and showed inspiring results. However, there were also some limitations. Firstly, the present study did not investigate the effect mechanism of VEGF-BMSCs treatment for thin endometrium. Secondly, the safety of VEGF gene-transfected BMSCs transplantation is not clear, so there is a long way to go before clinical application. Thirdly, the present only evaluated the endometrial regeneration and endometrial receptivity and did not observe the embryo implantation and pregnancy after treatment.

5. Conclusions

In conclusion, VEGF gene-transfected BMSCs transplantation would be a better therapy for thin endometrium than BMSCs transplantation alone. Further studies, which assess the safety of VEGF-BMSC treatment, the mechanisms of its effect, are needed in the future.

Data Availability

The data used to support the findings of this study are available from the corresponding author upon request.

Ethical Approval

Rat protocols were approved by the Animal Experimental and Welfare Ethics Committee of Central South University (2015007).

Conflicts of Interest

No conflict of interest with the submission of this manuscript.

Authors' Contributions

Zhao J. and Li Y. P. contributed to designing the experiment. Zhao J. and Yan Y. contributed to the conducting the animal experiment, acquiring and analysis the data. Huang X. participated in the revision of the article. All the authors contributed to the final approval of the article.

Acknowledgments

The authors thank Dr. Yi Ke, who works in the State Laboratory of Medical Genetics, Central South University of the People's Republic of China, for his great help on the experiments, and also thank everyone in the Reproductive Medicine Center of Xiangya Hospital, Central South University, for their scientific advice and encouragement. This work was supported by the National Natural Science Foundation of China (Grant No. 81401269).

Supplementary Materials

Figure S1: AOD of markers for endometrial cells and endometrial receptivity with immunohistochemistry. A, B, C, D represent the control group, BMSC group, VEGF-BMSC group, and sham operation group. Figure S2: relative level of markers for endometrial cells and endometrial receptivity with Western blotting. A, B, C, D represent the control group, BMSC group, VEGF-BMSC group, and sham operation group 4 days and 8 days after treatment. Figure S3: amplification curves, melting curves, and standard curves of PCR. Figure S4: embryo implantation efficiency of the control group, BMSC group, VEGF-BMSC group, and sham operation. *(Supplementary Materials)*

References

[1] H. I. Abdalla, A. A. Brooks, M. R. Johnson, A. Kirkland, A. Thomas, and J. W. Studd, "Endometrial thickness: a predictor of implantation in ovum recipients?," *Human Reproduction*, vol. 9, no. 2, pp. 363–365, 1994.

[2] V. Alam, L. Bernardini, J. Gonzales, R. H. Asch, and J. P. Balmaceda, "A prospective study of echographic endometrial characteristics and pregnancy rates during hormonal replacement cycles," *Journal of Assisted Reproduction and Genetics*, vol. 10, no. 3, pp. 215–219, 1993.

[3] Y. Gonen, R. F. Casper, W. Jacobson, and J. Blankier, "Endometrial thickness and growth during ovarian stimulation: a possible predictor of implantation in in vitro fertilization," *Fertility and Sterility*, vol. 52, no. 3, pp. 446–450, 1989.

[4] K. S. Richter, K. R. Bugge, J. G. Bromer, and M. J. Levy, "Relationship between endometrial thickness and embryo implantation, based on 1,294 cycles of in vitro fertilization with transfer of two blastocyst-stage embryos," *Fertility and Sterility*, vol. 87, no. 1, pp. 53–59, 2007.

[5] H. Shapiro, C. Cowell, and R. Casper, "The use of vaginal ultrasound for monitoring endometrial preparation in a donor oocyte program," *Fertility and Sterility*, vol. 59, no. 5, pp. 1055–1058, 1993.

[6] B. S. Hurst, J. T. Bhojwani, P. B. Marshburn, M. A. Papadakis, T. A. Loeb, and M. L. Matthews, "Low-dose aspirin does not improve ovarian stimulation, endometrial response, or pregnancy rates for in vitro fertilization," *Journal of Experimental & Clinical Assisted Reproduction*, vol. 2, no. 1, p. 8, 2005.

[7] G. Sher and J. D. Fisch, "Effect of vaginal sildenafil on the outcome of in vitro fertilization (IVF) after multiple IVF failures attributed to poor endometrial development," *Fertility and Sterility*, vol. 78, no. 5, pp. 1073–1076, 2002.

[8] A. A. Okusami, M. E. Moore, J. M. Hurwitz, and S. S. Richlin, "A case series of patients with endometrial insufficiency treated with pentoxifylline and alpha-tocopherol," *Fertility and Sterility*, vol. 88, article S200, 2007.

[9] O. Lebovitz and R. Orvieto, "Treating patients with "thin" endometrium – an going challenge," *Gynecological Endocrinology*, vol. 30, no. 6, pp. 409–414, 2014.

[10] I. Cervello, C. Gil-Sanchis, X. Santamaria et al., "Human $CD133^+$ bone marrow-derived stem cells promote endometrial proliferation in a murine model of Asherman syndrome," *Fertility and Sterility*, vol. 104, no. 6, pp. 1552–1560.e3, 2015.

[11] F. Alawadhi, H. Du, H. Cakmak, and H. S. Taylor, "Bone marrow-derived stem cell (BMDSC) transplantation improves fertility in a murine model of Asherman's syndrome," *PLoS One*, vol. 9, no. 5, article e96662, 2014.

[12] J. Zhao, Q. Zhang, Y. G. Wang, and Y. P. Li, "Rat bone marrow mesenchymal stem cells improve regeneration of thin endometrium in rat," *Fertility and Sterility*, vol. 101, no. 2, pp. 587–594.e3, 2014.

[13] J. Zhao, Q. Zhang, Y. G. Wang, and Y. P. Li, "Uterine infusion with bone marrow mesenchymal stem cells improves endometrium thickness in a rat model of thin endometrium," *Reproductive Sciences*, vol. 22, no. 2, pp. 181–188, 2015.

[14] C. B. Nagori, S. Y. Panchal, and H. Patel, "Endometrial regeneration using autologous adult stem cells followed by conception by in vitro fertilization in a patient of severe Asherman's syndrome," *Journal of Human Reproductive Sciences*, vol. 4, no. 1, pp. 43–48, 2011.

[15] X. Santamaria, S. Cabanillas, I. Cervello et al., "Autologous cell therapy with CD133+ bone marrow-derived stem cells for refractory Asherman's syndrome and endometrial atrophy: a pilot cohort study," *Human Reproduction*, vol. 31, no. 5, pp. 1087–1096, 2016.

[16] N. Singh, S. Mohanty, T. Seth, M. Shankar, S. Bhaskaran, and S. Dharmendra, "Autologous stem cell transplantation in refractory Asherman's syndrome: a novel cell based therapy," *Journal of Human Reproductive Sciences*, vol. 7, no. 2, pp. 93–98, 2014.

[17] J. Tan, P. Li, Q. Wang et al., "Autologous menstrual blood-derived stromal cells transplantation for severe Asherman's syndrome," *Human Reproduction*, vol. 31, no. 12, pp. 2723–2729, 2016.

[18] I. Miwa, H. Tamura, A. Takasaki, Y. Yamagata, K. Shimamura, and N. Sugino, "Pathophysiologic features of "thin" endometrium," *Fertility and Sterility*, vol. 91, no. 4, pp. 998–1004, 2009.

[19] G. Munoz-Elias, D. Woodbury, and I. B. Black, "Marrow stromal cells, mitosis, and neuronal differentiation: stem cell and precursor functions," *Stem Cells*, vol. 21, no. 4, pp. 437–448, 2003.

[20] J. Zhao, H. Gao, and Y. P. Li, "Development of an animal model for thin endometrium using 95% ethanol," *Journal of Fertilization: In vitro*, vol. 2, no. 4, 2012.

[21] W. Guo, H. Wang, S. Zou et al., "Bone marrow stromal cells produce long-term pain relief in rat models of persistent pain," *Stem Cells*, vol. 29, no. 8, pp. 1294–1303, 2011.

[22] F. Geiger, M. Beverungen, H. Lorenz, J. Wieland, M. Feher, and P. Kasten, "Bone substitute effect on vascularization and bone remodeling after application of $phVEGF_{165}$ transfected BMSC," *Journal of Functional Biomaterials*, vol. 3, no. 2, pp. 313–326, 2012.

[23] M. H. Maurer, C. Thomas, H. F. Burgers, and W. Kuschinsky, "Transplantation of adult neural progenitor cells transfected with vascular endothelial growth factor rescues grafted cells in the rat brain," *International Journal of Biological Sciences*, vol. 4, pp. 1–7, 2008.

[24] B. Chen, Q. Zeng, M. Lang, and S. Guan, "Transplantation of exogamous mesenchymal stem cells with transferred vascular endothelial growth factor gene applied for treatment of acute myocardial infarction in rat," *Basic and Clinical Medicine*, vol. 25, pp. 529–533, 2005.

[25] F. Togel, P. Zhang, Z. Hu, and C. Westenfelder, "VEGF is a mediator of the renoprotective effects of multipotent marrow

stromal cells in acute kidney injury," *Journal of Cellular and Molecular Medicine*, vol. 13, no. 8b, pp. 2109–2114, 2009.

[26] S. K. Smith, "Angiogenesis and implantation," *Human Reproduction*, vol. 15, pp. 59–66, 2000.

[27] S. K. Smith, "Angiogenesis, vascular endothelial growth factor and the endometrium," *Human Reproduction Update*, vol. 4, no. 5, pp. 509–519, 1998.

[28] S. Kashida, N. Sugino, S. Takiguchi et al., "Regulation and role of vascular endothelial growth factor in the corpus luteum during mid-pregnancy in rats," *Biology of Reproduction*, vol. 64, no. 1, pp. 317–323, 2001.

[29] A. M. Sharkey, K. Day, A. McPherson et al., "Vascular endothelial growth factor expression in human endometrium is regulated by hypoxia," *The Journal of Clinical Endocrinology and Metabolism*, vol. 85, no. 1, pp. 402–409, 2000.

[30] J. L. Shifren, J. F. Tseng, C. J. Zaloudek et al., "Ovarian steroid regulation of vascular endothelial growth factor in the human endometrium: implications for angiogenesis during the menstrual cycle and in the pathogenesis of endometriosis," *The Journal of Clinical Endocrinology and Metabolism*, vol. 81, no. 8, pp. 3112–3118, 1996.

[31] N. Sugino, S. Kashida, A. Karube- Harada, S. Takiguchi, and H. Kato, "Expression of vascular endothelial growth factor (VEGF) and its receptors in human endometrium throughout the menstrual cycle and in early pregnancy," *Reproduction*, vol. 123, no. 3, pp. 379–387, 2002.

[32] D. S. Torry, V. J. Holt, J. A. Keenan, G. Harris, M. R. Caudle, and R. J. Torry, "Vascular endothelial growth factor expression in cycling human endometrium," *Fertility and Sterility*, vol. 66, no. 1, pp. 72–80, 1996.

[33] D. S. Perrier, R. C. Charlet, F. Goffin, M. Foidart, and V. Geenen, "The implantation window," *Journal de Gynécologie, Obstétrique et Biologie de la Reproduction*, vol. 31, pp. 440–455, 2002.

[34] A. A. Acosta, L. Elberger, M. Borghi et al., "Endometrial dating and determination of the window of implantation in healthy fertile women," *Fertility and Sterility*, vol. 73, no. 4, pp. 788–798, 2000.

[35] B. A. Lessey, A. J. Castelbaum, L. Wolf et al., "Use of integrins to date the endometrium," *Fertility and Sterility*, vol. 73, no. 4, pp. 779–787, 2000.

[36] J. Wang and D. R. Armant, "Integrin-mediated adhesion and signaling during blastocyst implantation," *Cells, Tissues, Organs*, vol. 172, no. 3, pp. 190–201, 2002.

[37] A. Makker, I. Tandon, M. M. Goel, M. Singh, and M. M. Singh, "Effect of ormeloxifene, a selective estrogen receptor modulator, on biomarkers of endometrial receptivity and pinopode development and its relation to fertility and infertility in Indian subjects," *Fertility and Sterility*, vol. 91, no. 6, pp. 2298–2307, 2009.

[38] M. M. Singh, S. C. Chauhan, R. N. Trivedi, S. C. Maitra, and V. P. Kamboj, "Correlation of pinopod development on uterine luminal epithelial surface with hormonal events and endometrial sensitivity in rat," *European Journal of Endocrinology*, vol. 135, no. 1, pp. 107–117, 1996.

[39] G. Nikas, P. Drakakis, D. Loutradus et al., "Implantation: uterine pinopodes as markers of the 'nidation window' in cycling women receiving exogenous oestradiol and progesterone," *Human Reproduction*, vol. 10, no. 5, pp. 1208–1213, 1995.

[40] A. Psychoyos and P. Mandon, "Study of the surface of the uterine epithelium by scanning electron microscope. Observations in the rat at the 4th and 5th day of pregnancy," *Comptes rendus hebdomadaires des seances de I'Academie des sciences. Series D: Sciences naturelles*, vol. 272, pp. 2723–2725, 1971.

[41] C. E. Quinn, J. Detmar, and R. F. Casper, "Pinopodes are present in Lif null and Hoxa10 null mice," *Fertility and Sterility*, vol. 88, no. 4, pp. 1021–1028, 2007.

[42] D. Martel, R. Frydman, M. Glissant, C. Maggioni, D. Roche, and A. Psychoyos, "Scanning electron microscopy of postovulatory human endometrium in spontaneous cycles and cycles stimulated by hormone treatment," *The Journal of Endocrinology*, vol. 114, no. 2, pp. 319–3NP, 1987.

[43] U. Bentin-Ley, A. Sjogren, L. Nilsson, L. Hamberger, J. F. Larsen, and T. Horn, "Presence of uterine pinopodes at the embryo-endometrial interface during human implantation in vitro," *Human Reproduction*, vol. 14, no. 2, pp. 515–520, 1999.

[44] L. Zhang, Y. Li, C. Y. Guan et al., "Therapeutic effect of human umbilical cord-derived mesenchymal stem cells on injured rat endometrium during its chronic phase," *Stem Cell Research & Therapy*, vol. 9, no. 1, p. 36, 2018.

Hindawi
Stem Cells International
Volume 2018, Article ID 7162084, 12 pages
https://doi.org/10.1155/2018/7162084

Research Article

The Differential Effects of Leukocyte-Containing and Pure Platelet-Rich Plasma on Nucleus Pulposus-Derived Mesenchymal Stem Cells: Implications for the Clinical Treatment of Intervertebral Disc Degeneration

Jun Jia,[1] Shan-zheng Wang,[2,3] Liang-yu Ma,[1] Jia-bin Yu,[1] Yu-dong Guo,[2] and Chen Wang [1]

[1]*School of Medicine, Southeast University, 87 Ding Jia Qiao Road, Nanjing, Jiangsu 210009, China*
[2]*Department of Orthopaedics, Zhongda Hospital, School of Medicine, Southeast University, 87 Ding Jia Qiao Road, Nanjing, Jiangsu 210009, China*
[3]*The First Clinical Medical School, Nanjing Medical University, 300 Guangzhou Road, Nanjing, Jiangsu 210029, China*

Correspondence should be addressed to Chen Wang; wangchen_seu_edu@163.com

Received 4 June 2018; Revised 30 July 2018; Accepted 9 August 2018; Published 23 October 2018

Academic Editor: Stefania Cantore

Copyright © 2018 Jun Jia et al. This is an open access article distributed under the Creative Commons Attribution License, which permits unrestricted use, distribution, and reproduction in any medium, provided the original work is properly cited.

Background. Platelet-rich plasma (PRP) is a promising strategy for intervertebral disc degeneration. However, the potential harmful effects of leukocytes in PRP on nucleus pulposus-derived mesenchymal stem cells (NPMSCs) have seldom been studied. This study aimed at comparatively evaluating effects of pure platelet-rich plasma (P-PRP) and leukocyte-containing platelet-rich plasma (L-PRP) on rabbit NPMSCs in vitro. *Methods.* NPMSCs isolated from rabbit NP tissues were treated with L-PRP or P-PRP in vitro, and then cell proliferation and expression of stem cell markers, proinflammatory cytokines (TNF-α, IL-1β), production of ECM (extracellular matrix-related protein), and NF-κB p65 protein were validated by CCK-8 assay, real-time polymerase chain reaction, enzyme-linked immunosorbent assay, immunofluorescence, and western blot respectively. *Results.* NPMSCs differentiate into nucleus pulposus-like cells after treatment of PRPs (P-PRP and L-PRP), and NPMSCs exhibited maximum proliferation at a 10% PRP dose. L-PRP had observably higher concentration of leukocytes, TNF-α, and IL-1β than P-PRP. Furthermore, compared to P-PRP, L-PRP induced the differentiated NPMSCs to upregulate the expression of TNF-α and IL-1β, enhanced activation of the NF-κB pathway, increased the expression of MMP-1 and MMP-13, and produced less ECM in differentiated NPMSCs. *Conclusions.* Both P-PRP and L-PRP can induce the proliferation and NP-differentiation of NPMSCs. Compared to L-PRP, P-PRP can avoid the activation of the NF-κB pathway, thus reducing the inflammatory and catabolic responses.

1. Introduction

As a major cause of low back pain, intervertebral disc degeneration (IDD) is drawing increasing attention for substantial financial and health care burdens worldwide [1]. Although the etiology of IDD is currently unknown, mounting evidence has shown that the mechanical and biological degradation of the discs is considered as one of the common major causes of IDD [2]. Intervertebral disc consists of three distinct structural compositions, the outer annulus fibrosis, the inner NP (nucleus pulposus), and the upper and lower layers of endplates [3]. As the core portion of the intervertebral disc, NP plays a critical role in transmitting the load [4]. The failure of the load transmission is often considered the initiation of the disc degeneration [2]. Thus, the preservation and regeneration of the NP are often the concerns for the therapeutic strategies [5]. Currently, conservative treatments, including oral analgesics and NSAIDs, are clinically applied to alleviate the symptoms [6]. Spinal surgeries, especially those with minimal invasive techniques, can efficiently relieve the symptoms of neural compression. However, the degradation of the intervened or the adjacent discs may undergo an increasing degeneration course [7].

Currently, stem cell transplantation therapy is becoming a promising strategy when transplanted into the degenerated discs [8]. The convincing outcomes were well illustrated in many clinical and basic studies [9–11]. The microenvironment of IVD has the characteristics of low nutrition, acidity, hypertonicity, hypoxia, and high mechanical load [12]. This microenvironment not only has negative influence on original cells of the disc but also promotes apoptosis of transplanted cells [13]. It should be noted that the mesenchymal stem cells (MSCs) reside in the degenerated nucleus pulposus tissues for their regenerative potential. A recent study confirmed that the endogenic MSCs in the nucleus pulposus tissues (NPMSCs) were more resistant to hyperosmotic, acidic, and anoxic environment than the MSCs of fat sources [14]. Thus, in the degenerative disc microenvironment, the activation or transplantation of NPMSCs may have more advantages over MSCs from other tissues. As a useful MSC activator, PRP is widely investigated in tissue engineering strategy for its potential in cell proliferation and extracellular matrix [15–17]. When activated, a variety of growth factors, including PDGF, TGF, EGF, and VEGF, are secreted from the platelets, contributing to a joint regenerative effect on the damaged tissues [18]. Direct injection of PRP has been proven effective in IDD treatment by comprehensive researches [19, 20].

Although PRP is widely used for its regenerative potential, the efficacy was often in debate for its indeterminate therapeutic effect. Some studies revealed that PRP was effective in the repair of tendon injury [21–23], while others did not confirm the functional recovery of the repaired tendon and pain relief of the patients [24–26]. The inconsistency might be caused by the individual difference in patients and different preparations of PRP in each study [27]. Different preparations for PPR bring out various components, and leukocyte is one of the critical elements. Exclusion of leukocytes in PRP has been proven more beneficial for osteoarthritis [28] and bone defects [29]. In addition, PRP rich in leukocytes (L-PRP) can release high concentrations of inflammatory cytokines, which result in the activation of NF-κB pathway [28, 29]. However, the potential harmful effects of leukocytes in PRP on nucleus pulposus-derived mesenchymal stem cells (NPMSCs) have seldom been studied.

The objective of this study is to comparatively evaluate effects of P-PRP and L-PRP on rabbit NPMSCs in vitro, and a new insight is provided to improve the efficiency of PRP treatment in disc regeneration.

2. Methods

2.1. Preparation of L-PRP, P-PRP, NPMSCs, Spleen Cells, and NPCs. The use of rabbits was approved and supervised by the Animal Care and Use Committee of Southeast University. Autologous whole blood and NPMSCs were harvested from 24 New Zealand white rabbits (8 months old, 3.0–4.0 kg, female) respectively. About 27 ml of autologous whole blood was collected from each New Zealand white rabbit through the carotid artery and mixed with 3 ml acid-citrate dextrose solution A (Santa Cruz, catalog no. SC-214744) to make 30 ml of anticoagulated whole blood. 2 ml whole blood was used in quantifying the platelet and leukocyte concentrations in whole blood, and the rest 28 ml blood was left for preparation of PRP (P-PRP, L-PRP). The method of two-step centrifugation process [30] was applied to prepare the P-PRP and L-PRP. Briefly, 14 ml whole blood was centrifuged at 250g for 10 minutes at room temperature to separate the blood into three layers, platelet-containing plasma at the top, buffy coat (rich in leukocytes and platelets) in the middle, and erythrocytes at the bottom. The top two layers were transferred into a new tube and spun again at 250g for 10 minutes; most of the leukocytes, platelets, and fibrinogen precipitated. Then, most of the supernatant (poor in platelet) was discarded. The left plasma and precipitate, which were almost 2 ml, were resuspended to form the L-PRP. The other 14 ml whole blood was centrifuged at 160g for 10 minutes to separate platelet-containing plasma from buffy coat (rich in leukocytes) and erythrocytes. Then plasma layer was aspirated carefully to avoid the buffy coat and erythrocyte pollution. The plasma layer was centrifuged again at 250g for 15 minutes. Then, most of the supernatant (poor in platelet) was discarded. The left plasma and precipitate, which were almost 1.5 ml, were resuspended to form the P-PRP.

Nucleus pulposus tissue was isolated from IVDs of the New Zealand white rabbits above, minced into 1mm^3 tissue block, and digested using 0.2 mg/ml type II collagenase (Thermo Fisher, catalog no. DS56580) in DMEM-LG (GIBCO, catalog no. AB10104399) medium for 4–6 h. After centrifugation at 1500 r/min for 10 minutes (DragonLab, D3024R), the cell pellet from the discs (lumbar 3-5) of the same rabbit was cultured in 25 cm^2 cell culture dish at a density of 10^4 cells/cm^2. The cells were cultured in DMEM-LG medium supplemented with 10% fetal bovine serum (FBS) (Sigma, catalog no. BK20170120), 100 U/ml penicillin G (Hyclone, lot: J150019) and 0.1 mg/mL streptomycin (Hyclone, catalog no. K270109) under a humidified atmosphere of 95% air and 5% CO_2 at 37 °C. The medium was changed every 3 days until the cells reached 80%–90% subconfluence, then cells were harvested using 0.25% trypsin and 0.02% EDTA (Hyclone, lot: J160004) and re-suspended in the same medium. Then the cell suspension was inoculated into tissue culture dishes at a density of 50 cells/cm^2 for further culture. The images of cell morphology were performed using microscope attaching camera (OLYMPU, IX51). The NPMSCs of passage 2 were selected for further experiments.

NPCs were isolated and harvested as previously reported [31]. Nucleus pulposus tissue were obtained from the rabbits above and immediately minced into 1 mm3 tissue block and digested using 0.25% trypsin (Thermo Fisher, catalog no. 25200056) for 5 to10 minutes and 0.25% type I collagenase (Thermo Fisher, catalog no. 17100017) for 20 to 25 minutes. After centrifugation (1500 r/min, 10 min), the cell pellets were re-suspended in monolayer culture supplemented with DMEM medium containing 10% fetal bovine serum (Sigma, catalog no. BK20170120), 100 U/ml penicillin G (Hyclone, lot: J150019), and 0.1 mg/ml streptomycin (Hyclone, catalog no. K270109) under standard conditions (37 °C, 21% O_2, and 5% CO_2). The medium was changed every 3 days after the primary started to grow by static adherence. The NPCs were collected and subcultured at a ratio of 1:3 until the cells

Table 1: Sequences of primers used for RT-PCR.

Gene	Forward primers (5′-3′)	Reverse primers (5′-3′)
GAPDH	ACTTTGTGAAGCTCATTTCCTGGTA	GTGGTTTGAGGGCTCTTACTCCTT
CD29	GTCACCAACCGTAGCAA	CTCCTCATCTCATTCATCAG
CD44	CGATTTGAATATAACCTGCCGC	CGTGCCCTTCTATGAACCCA
CD166	GGACAGCCCGAAGGAATACGAA	GACACAGGCAGGGAATCACCAA
CD4	GATGGAGGTGGAACTGC	GGAAAGCCCAACACTATG
CD8	GGGTGGAAAAGGAGAAGC	AGGTGAGTGCGGGAGAC
CD14	CAGGTGCCTAAGGGACT	AATAAAGTGGGAAGCGG
IL-1β	CGGTCAAGGAGAGGAGCTTAC	GGACTAGCCCTCGCTTATCTTT
TNF-α	GGAGAAGCCGGTAGTGGAGAT	GGTCTGGTCACGGTTTGGAA
MMP-1	CGACTCGCTATCTCCAAGTGA	GTTGAACCAGTCTCCGACCA
MMP-13	GGAGGCGAGAACATCAAGCC	CGGCCTTCCCTCGTAGTGA
Oct-4	ACCTTCATCGGAAACTCCAAAG	ACTGTTAGGCTCAGGTGAACT
Nanog	CTGTGGGTTTCTGTGCTGG	CCGGCTTCAAGGCTTTCAG
Collagen II	CAGGATGTCCAGGAGGCT	GCAGTGGCGAGGTCAGTAG
Aggrecan	GGAGCCCGAGCCTATACTATTT	CCCAAGGACCAATCA

reached 80%–90% subconfluence. The P2 NPCs were used for total RNA extraction.

Spleen cells were isolated according to the method described previously [32]. Briefly, the harvested spleen tissue from the rabbits above was minced and filtrated with 70 μm cell strainer (Corning, catalog no. 431751) to obtain single-cell solution. The cell solution was subsequently centrifuged at 1000 r/min for 10 minutes. The cell pellet was subsequently treated with blood cell lysis buffer (Solarbio, catalog no. R1010-500 ml) to remove red blood cells. The precipitate of mixture of cells was used for total RNA extraction.

2.2. Component Analysis of P-PRP, L-PRP, and Whole Blood. The concentrations of leukocyte and platelet in PRP and whole blood were measured by an automatic hematology analyzer (XP-300, Sysmex, Houston, America). The P-PRP and L-PRP were activated with 10% calcium chloride solution and then incubated at 37°C for 7 d. Moreover, the supernatants were extracted from PRP which had been centrifugated at 2800g for 15 minutes. The concentrations of TNF-α and IL-1β were explored using ELISA kit (Xitang, Shanghai, China) according to the manufacturer's instructions.

2.3. Identification of Nucleus Pulposus Mesenchymal Stem Cells. The NPMSCs of passage 2 were subjected to induced differentiation by culturing them in chondrogenic, adipogenic, and osteogenic media, respectively. The cells were evaluated using Alcian blue (Sigma, catalog no. B8438), Oil Red O (Sigma, catalog no. O8010), and alizarin red (Solabio, catalog no. G8550-25), staining respectively. The outcomes were examined by an inverted microscope. RT-PCR was used to determine the expression of MSC (mesenchymal stem cell) mark genes (CD166, CD44, CD29, CD14, CD8, and CD4) from the NPMSCs, NPCs (nucleus pulposus cells), and spleen cells. Briefly, total RNA was extracted from NPMSCs, NPCs, and spleen tissue using TRIzol reagent (Thermo Fisher, catalog no. 10296010) according to the manufacturer's instructions. Reverse transcription was gained by a reverse transcription kit (Thermo Fisher, catalog no.AM334) according to the instruction sequences of the manufacturer. The sequences of primers which were used in the reactions are listed in Table 1.

2.4. Proliferation of NPMSCs in Different Concentrations of PRPs (P-PRP, L-PRP). To determine the cell viability and cell proliferation capacity, cells were examined with CCK-8 assay. The P2 NPMSCs obtained as described above were seeded in a 24-well plate (Yu can Corning/Costar, catalog no. 3415) at 10000 cells per well and maintained in a culture medium containing 2% FBS and P-PRP or L-PRP at various volume percent fractions: 0%, 5%, 10%, 15%, and 20% for 7 days. 100 μl of fresh medium containing 0.5% FBS and 10 μl CCK-8 were added to each plate and incubated for 4 h at 37°C. The optical density was detected at 450 nm, and the experiment was independently performed for three times.

2.5. Coculture of NPMSCs In Vitro. The transwell system (Costar, catalog no.JM-3450) was used for coculture of NPMSCs in this study. This transwell consists microporous membrane (0.4um) between upper and lower compartments so that there is free flow of culture medium in the two compartments. The P2 NPMSCs in the basal medium (DMEM + 2% FBS) were seeded into the bottom of the transwell system allocated to three groups (P-PRP, L-PRP, and control). The experimental groups (P-PRP or L-PRP group) were put into 10%P-PRP or 10%L-PRP, respectively, in the top compartment of the transwell system, and the top compartment containing basal medium only was set as the control group. The NPMSCs from all groups were cocultured for 14 days, and the culture medium was changed every 3 days. Concentration of PRPs in this study was adjusted to 10% (vol/vol) using basal medium (DMEM + 2% FBS) according to the proliferation of NPMSC assay above.

2.6. Measuring Expression of MMP-1, MMP-13, IL-1β, and TNF-α in Coculture NPMSCs. Cells from all groups mentioned above were harvested on day 14 by trypsinization and centrifugation. The cell pellet was used to measure cell count by an auto cellometer (Cellometer Auto 2000, Nexcelom, America), and the supernatant was used to estimate the concentrations of MMP-1, MMP-13, TNF-α, and IL-1β by respective ELISA kits according to the manufacturer's instructions (Xitang, Shanghai, China). Each experiment was repeated in triplicate.

2.7. qRT-PCR Analysis. The NPMSCs which were cultured in the transwell described above were harvested on day 14 by 2.5% trypsin and 0.02% EDTA. The gene nucleus pulposus cell-related genes (collagen II and aggrecan), mesenchymal stem cell-related genes (Oct-4, Nanog), inflammatory marker genes (TNF-α, IL-1β), and catabolic genes (MMP-1, MMP-13) were determined by qRT-PCR. In brief, TRIzol reagent (Invitrogen, CA, USA) was used to extract the total RNA from cells according to the manufacturer's instructions. Real-time PCR was performed using SYBR Premix Ex Taq II (TaKaRa, Dalian, China) and measured on an iQ5 Real-Time PCR Detection System (Bio-Rad, Hercules, CA). The PCR conditions were performed by denaturing the cDNA at 94°C for 4 min, followed by 40 cycles of amplification: 94°C for 40 s, 52°C for 40 s, and 72°C for 40 s for data collection. All samples were normalized to control and calculated using the $2^{-\Delta\Delta CT}$ analysis method. We used GAPDH expression as the endogenous control, and the sequences of primers which are used in the reactions are listed in Table 1.

2.8. Immunofluorescence. The NPMSCs were collected from the experimental groups and control groups as described above. And then, the cells were fixed with PBS containing 4% paraformaldehyde (Sigma, catalog no. D56988) for 20 minutes and washed with PBS including 1% Triton for 5 minutes. Immunostaining for nucleus pulposus cell-related proteins (collagen II and aggrecan) was implemented by blocking the cells in 2% mouse serum (Novus Biologicals, catalog no. NB600-504) and then incubated with mouse anti-rabbit collagen II antibody (Aridobio, catalog no. ARG62450) or anti-rabbit aggrecan (Novus Biologicals, catalog no. NB600-504) at 4°C overnight. The cells were washed 3 times with PBS for 5 minutes each and incubated with Alexa Fluor 594-conjugated goat anti-mouse lgG secondary antibody (Bastet, catalog no. BK0027) for 90 minutes at room temperature. The cell nucleus was counterstained by Hoechst 33342 (Thermo Fisher, catalog no. 62249). The inverted fluorescence microscope (BX53, Olympus, Japan) was used to observe the stained cells.

2.9. Western Blot Analysis. The cells from all groups mentioned above were harvested after culturing for two weeks. Extraction of total proteins in the cells was performed by using M-PER (mammalian protein extraction reagent) (Fermenta, catalog no. 26616) supplementing 1.5% (vol/vol) protease inhibitors (Bio-Rad catalog no. 161-0156). Concentration of proteins in the supernatant was measured by using the BCA Protein Assay Kit (Thermo Fisher catalog no. EC60980) according to manufacturer's instruction after centrifugation at 10000 r/min for 10 minutes. 20 μg of total cell protein extracts from each group was separated by 25% SDS polyacrylamide gel electrophoresis (Thermo Fisher, catalog no. DF65896) at 100 V for 60 minutes, then transferred onto PVDF membranes (Millipore catalog no. IPVH00010) at 100 V for 30 minutes which was blocked with 3% fat-free milk in Tris-buffered saline at room temperature for 30 minutes. The blots were incubated with anti-P65 antibody (Abcam, catalog no. ab154036), anti-aggrecan antibody (Novus Biologicals, catalog no. NB600-504), anti-collagen II antibody (Aridobio, catalog no. ARG62450), and anti-GAPDH antibody at a dilution of 1 : 1000 at 4°C overnight, followed by incubation with IgG-HRP (goat anti-mouse peroxidase-conjugated secondary antibody) (Bastet, catalog no. BK0027) at a dilution of 1 : 5000 for 1 h at room temperature. The expression of protein was detected by ECL kit (Biyuntian, catalog no. ce7827) according to the manufacturer's suggested protocols. GAPDH was used as an internal control.

2.10. Statistical Analysis. The difference between different two groups of three independent experiments was analyzed by Student's t-test. One-way analysis of variance (ANOVA) was used to analyze the difference among more than two groups. The data are presented as means ± S.D. $P < 0.05$ was considered to be statistically significant.

3. Results

3.1. NPMSCs Possessed the Typical Characteristics of MSCs for Self-Renewing, Clonogenicity, Stem Cell Markers, and Multidifferentiation Potential. After inoculation, the cells isolated from the nucleus pulposus of the disc started to grow by static adherence after 10–14 days, and the primary cells showed various shapes. They mainly comprise round macrophage-like cells and spindle-shaped fibroblast-like cells (Figure 1(a)). After low-density (50/cm^2) cell passage, the cells formed typical sunflower-like cell colonies (Figure 1(b)). In addition, the cells displayed a uniform cobblestone-like morphology at passage 2 (Figure 1(c)); RT-PCR was performed to determine the gene expression of typical MSC surface marks. As shown in Figure 1(d), the results indicated that the expression of markers in passage 2 including CD166, CD44, and CD29 which frequently exist in MSCs was significantly higher than that in NPCs. In addition, the markers containing CD14, CD8, and CD4 were seldom expressed which are negative in MSCs. Meanwhile, the cells were induced to differentiation of chondrogenesis, osteogenesis, and adipogenesis respectively (Figures 1(e)–1(g)). When the cells were cultivated in the osteogenic medium, the morphology of the cells changed on the fifth day. The calcium deposits in the cells were highly visible after 3 weeks, and then they were fixed and stained by "alizarin red." In contrast, the cells in the control group did not produce any calcium deposits which were cultivated in basic medium (Figure 1(e)). After culturing in adipogenic induction medium for 1 week, the cells gradually developed lipid droplets. The cells were stained with "Oil Red O" on day 21.

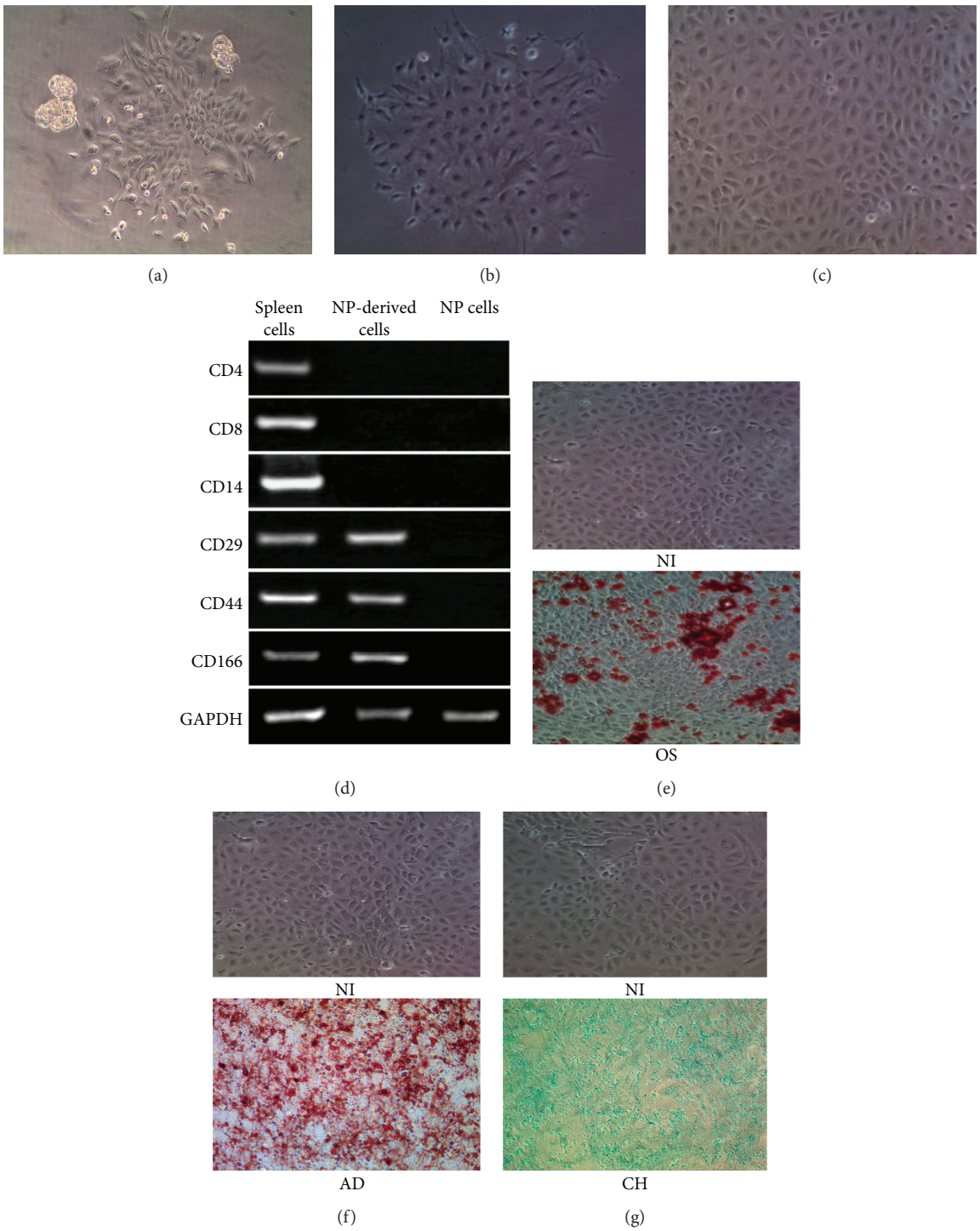

Figure 1: NPMSCs possessed the typical characteristics of MSCs for self-renewing, clonogenicity, stem cell markers, and multidifferentiation potential. (a) The morphology of primary cells (100x). (b) A typical sunflower-like cell colony at passage 1 (100x). (c) Cells displayed a uniform cobblestone-like morphology (100x). (d) The genes of CD29, CD44, and CD166 expressed strongly in cells of passage 2 but not in NP cells and seldom expressed CD14, CD8, and CD4; The spleen cells expressed all genes above as positive controls; the NP cells did not express these genes as a negative control. (e) Micrographs showing accumulation of mineralized calcium deposition in noninduced cells (NI) and osteoinduced cells (OS), as determined by alizarin red staining (100x). (f) Micrographs showing degree of lipid droplets in noninduced cells (NI) and adipoinduced cells (AD) as assessed by Oil red O staining (NI100x, AD400x). (g) Micrographs showing the levels of chondrogenesis in noninduced cells (NI) and chondrogenic induction cell (CH), as measured by Alcian blue staining.

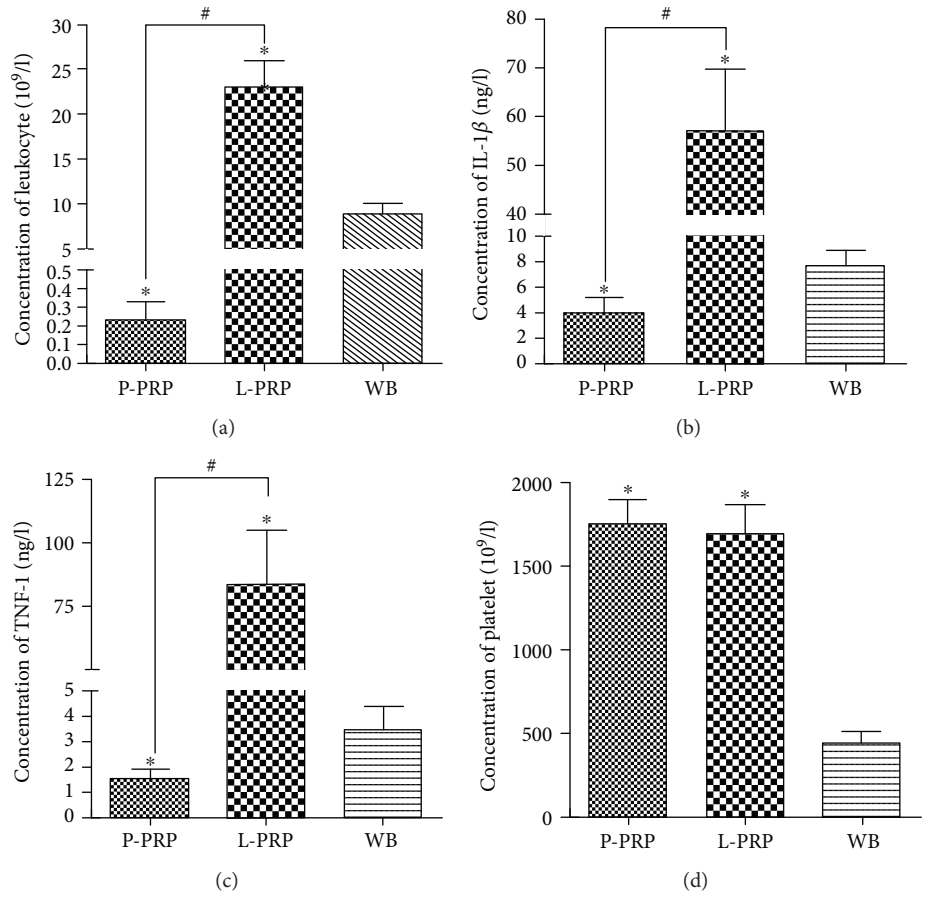

Figure 2: The concentrations of leukocytes, inflammatory cytokines (IL-1β and TNF-α), and platelet in whole blood, L-PRP and P-PRP. (a–c) The leukocytes, inflammatory cytokines, IL-1β, and TNF-α in P-PRP, L-PRP, and whole blood. (d) Platelet concentrations of P-PRP, L-PRP, and whole blood. "$*$" indicates that the difference between P-PRP or L-PRP and whole blood was statistically significant ($P < 0.05$). "#" indicates that the difference between L-PRP and P-PRP was statistically significant ($P < 0.05$). Statistical analysis using ANOVA, $n = 8$.

The cells of the control group did not have any change (Figure 1(f)). The cells differentiated into chondrocyte-like cells and emerged a much higher level of "Alcian blue" staining after culturing in a chondrogenic differentiation medium compared with control cells (Figure 1(g)).

3.2. The Concentrations of Leukocytes, Inflammatory Cytokines (IL-1β and TNF-α), and Platelet in Whole Blood, L-PRP, and P-PRP. We found that the leukocyte concentration in L-PRP was markedly higher than that in whole blood while the concentration of leukocyte in P-PRP was significantly lower than that in whole blood (Figure 2(a), $P < 0.05$). The levels of IL-1β and TNF-α in L-PRP were elevated. As shown in Figures 2(b) and 2(c), the levels of IL-1β and TNF-α in L-PRP were significantly higher than those in whole blood and P-PRP, while the levels of IL-1β and TNF-α in P-PRP were evidently lower than those in whole blood ($P < 0.05$). The concentration of platelet was similar between P-PRP and L-PRP. In addition, concentrations of platelet in P-PRP and L-PRP were 3.8-fold higher than those in whole blood (Figure 2(d)).

3.3. The Proliferation of Cells Is Dose-Dependent to PRPs. To ascertain whether PRP could functionally regulate proliferation, we performed CCK-8 assays to evaluate the role of PRPs in the progression of cells. When the cells cultured in the medium comprising different concentrations of PRPs as described above, the results displayed that cell proliferation rate showed dose-dependent response on P-PRP and L-PRP (Figure 3). The cell proliferation rate had no significant difference at the presence of 5%, 15%, and 20% P-PRP or L-PRP and increased by 60% compared with the control groups (0% PRPs). The presence of 10% P-PRP or 10% L-PRP obtained the maximum proliferation rate. There was no significant difference between L-PRP and P-PRP in each concentration ($P > 0.05$).

3.4. PRPs Promote the Differentiation of NPMSCS into Nucleus Pulposus-like Cells. To observe the effects of P-PRP and L-PRP on differentiation of NPMSCS, we first investigate the cell morphology. The results showed that controls were mainly cobblestone-like without any change (Figure 4(a)), while cell morphology of experimental groups gradually

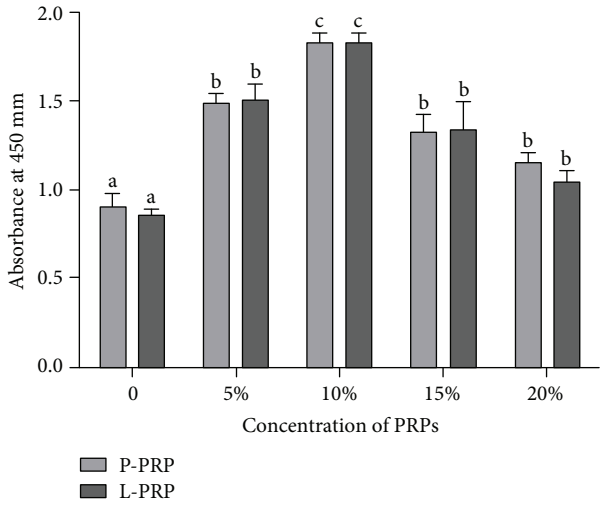

Figure 3: The proliferation of cells derived from nucleus pulposus in different concentrations of P-PRP or L-PRP. Cell proliferation was evaluated on day 7 by CCK-8 assay. The cell proliferation showed a maximum effect on 10% P-PRP and 10% L-PRP. Differences for the date from each group (P-PRP or L-PRP) performed by using one-way analysis of variance. A t test was used for determining the statistical significant difference between P-PRP and L-PRP in each concentration of PRPs. Different letters above bars indicate that the difference is statistically significant ($P < 0.05$).

changed from cobblestone-like cells to elongated spindle-shaped nucleus pulposus-like cells (Figure 4(b)). Furthermore, the results of qRT-PCR suggested that the expression of stem cell marker gene including "Oct-4 and Nanog" in the experimental groups decreased 30% compared with that in the control (Figures 4(c)). In contrast, the expression of nucleus pulposus cell-related genes (collagen II and aggrecan) in the experimental groups was 3- to 4-folds higher than that in the control group (Figure 4(d)) Moreover, there was no significant difference between P-PRP groups and L-PRP groups (Figures 4(b)–4(d)). These results indicate that both L-PRP and P-PRP induced the differentiation of NPMSCs towards the mature NP-like cells.

3.5. L-PRP Activates NF-κB Pathway in Differentiated Nucleus Pulposus-like Cells. To explore the effects of L-PRP and P-PRP on the activation of NF-κB pathway in the newly nucleus pulposus-like cells, the expression of proinflammatory genes (IL-1β, TNF-α) and catabolic genes (MMP-1, MMP-13) was determined by qRT-PCR. We observed that the expression of these genes in the L-PRP group was significantly higher than that in the P-PRP and control group (Figures 5(a) and 5(b)). In addition, we used ELISA assay to further investigate these cytokine productions in all groups. The results indicated that the L-PRP group was also significantly higher than P-PRP and control groups (Figures 5(c) and 5(d)). As shown in Figure 5(e), western blot analysis revealed that production of NF-κB/p65 in the L-PRP group was highest in all groups. Moreover, there were no significant differences about all results in the P-PRP and control group.

3.6. P-PRP Induces Differentiated Nucleus Pulposus-like Cells to Produce More Extracellular Matrix-Related Proteins. In order to evaluate the effect of P-PRP and L-PRP on productions of extracellular matrix-related proteins in nucleus pulposus-like cells, we measured the levels of collagen II and aggrecan by immunofluorescence staining and western blot analysis, respectively. Immunofluorescence staining showed that PRP treatment upregulated the productions of collagen II and aggrecan when compared with control and the cells obtained the highest staining after P-PRP treatment (Figure 6(a)). We further performed western blot analysis to determine the levels of these factors; the results also identified the result, indicating that P-PRP induced the maximum production of collagen II and aggrecan in cells (Figure 6(b)).

4. Discussion

This study determined the significance of leukocyte exclusion in PRP for the culture of NPMSCs in vitro. The isolated NPMSCs possessed the typical characteristics of MSCs for self-renewing, clonogenicity, and multidifferentiation potential. The platelet concentration was over 3 times higher in either P-PRP or L-PRP compared to the whole blood. Concentrations of leukocytes, TNF-α, and IL-1β were significantly lower in P-PRP compared with those in L-PRP. Both L-PRP and P-PRP induced the differentiation of NPMSCs towards the mature NP cells. P-PRP which induced lower concentrations of MMP-1, MMP-13, TNF-α, and IL-1β had superior efficacy on the production of ECM (collagen II and aggrecan). In addition, western blot results confirmed the high expression of NF-κB/P65 protein in the L-PRP group.

In the characterization of NPMSCs, we did not test the classic surface markers of MSCs for the lack of specific rabbit antigens by flow cytometry. To solve this problem, we conducted RT-PCT to determine the expression of these markers from the gene level. The colony-forming cells isolated from the NP highly expressed MSC-specific markers (CD29, CD44, and CD166) while minimally expressed the hematopoietic markers (CD8, CD8, and CD14). Spleen cells were used as the positive control for this study, because spleen cells, mainly including lymphocytes and monocytes, are positive for the expression of both MSC-specific and hematopoietic markers [33, 34].

Given the value of endogenic MSCs to the metabolic homeostasis of the disc, an ideal therapy is to activate and proliferate the resident MSC population. PRP, prepared by autologous blood, has been proven effective in the restoration of the degenerated discs [19, 20]. When activated, a variety of growth factors (PDGF, TGF, EGF, and VEGF) released from platelet α-granules in PRP are able to increase cell proliferation and cartilaginous matrix secretion in vitro [18]. In this study, both P-PRP and L-PRP had over 3 times higher platelet concentration compared to the whole blood. After 7 days of coculture with PRPs, NPMSCs proliferated faster than the control group. Moreover, NPMSCs exhibited active NPC shape with increased expression of nucleus pulposus cell-related genes (collagen II and aggrecan) and their protein production after treatment of PRPs for 14 days. Therefore, PRPs not only improved cell proliferation but also induced

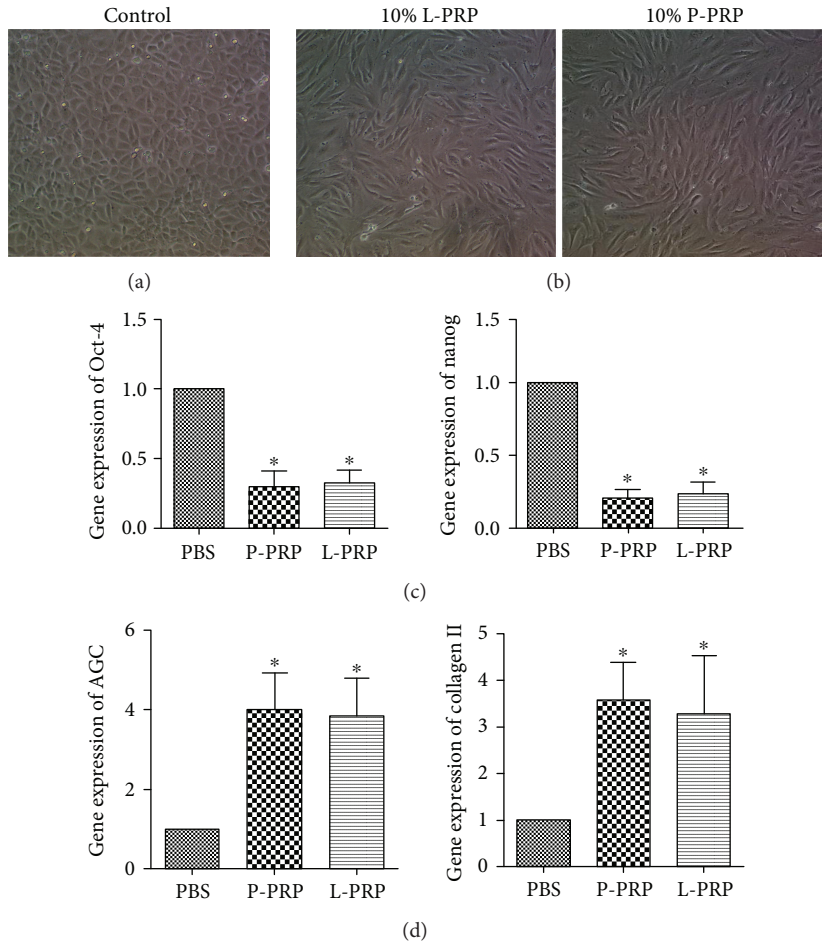

Figure 4: Effects of P-PRP and L-PRP on differentiation in the NPMSCS. (a) Cells morphology in the control. (b) Morphology of the cells treated with 10% L-PRP and 10% P-PRP. (c) mRNA expression of stem cell markers Oct-4 and Nanog, as determined by qRT-PCR. (d) mRNA expression of NP cell-related genes, aggrecan (AGC) and collagen II. "∗" indicates that the difference between P-PRP or L-PRP and control is statistically significant ($P < 0.05$). Note that cell morphology was observed under an inverted microscope (×100).

the active differentiation of NPMSCs for upregulating the extracellular matrix-related protein production.

Variations in the composition of the PRP may contribute to distinct results [21]. The exclusion of leukocytes has been proven more effective when applied in the treatment of bone defect [29], osteoarthritis [35], and acute tendon injury [36]. In this study, similar platelet concentrations of P-PRP and L-PRP resulted in significantly different ECM production in each individual group. P-PRP presents better ECM production function, which could be attributed to the exclusion of leukocytes compared to L-PRP. As typical proinflammatory cytokines, IL-1β and TNF-α are efficient activators of NF-κB signaling pathway [37–39]. In the present study, the proinflammatory genes (TNF-α and IL-1β) as well as their respective protein expression of differentiated NPMSCs in the L-PRP group were significantly higher than those in the P-PRP group. Western blot results showed the higher expression of NF-κB/P65 protein in the L-PRP group compared with P-PRP. These results are consistent with previous 132#studies showing that the NF-κB pathway is activated by the high concentration of leukocytes in L-PRP [28, 29, 40].

NF-κB signaling pathway is intimately involved in the impaired anabolism and enhanced catabolism by upregulating catabolic cytokines, MMP-1 and MMP-13 in intervertebral disc cells [41]. The anti-inflammatory effect of PRP is well confirmed by previous studies [42, 43]. In addition, PRP cleavage products were reported to be able to terminate the NF-κB pathway and downregulate the production of COX-2 [44]. However, the high concentration of leukocytes in L-PRP may counteract the anti-inflammatory potential of growth factors released from platelets [45]. In our study, L-PRP highly induced the inflammation compared to PRP with negligible leukocytes (P-PRP). In addition, NPMSCs treated with L-PRP upregulated catabolism-related genes (MMP-1, MMP-13) and their proteins compared with P-PRP. Thus, the activation of NF-κB pathway can be largely attributed to the inclusion of leukocytes in PRP. The exclusion of leukocytes from PRP resulted in less production of IL-1β and TNF-α, thus prohibiting the activation of NF-κB signaling pathway.

Our study has several limitations. First, we preliminarily confirmed the superiority of P-PRP over L-PRP

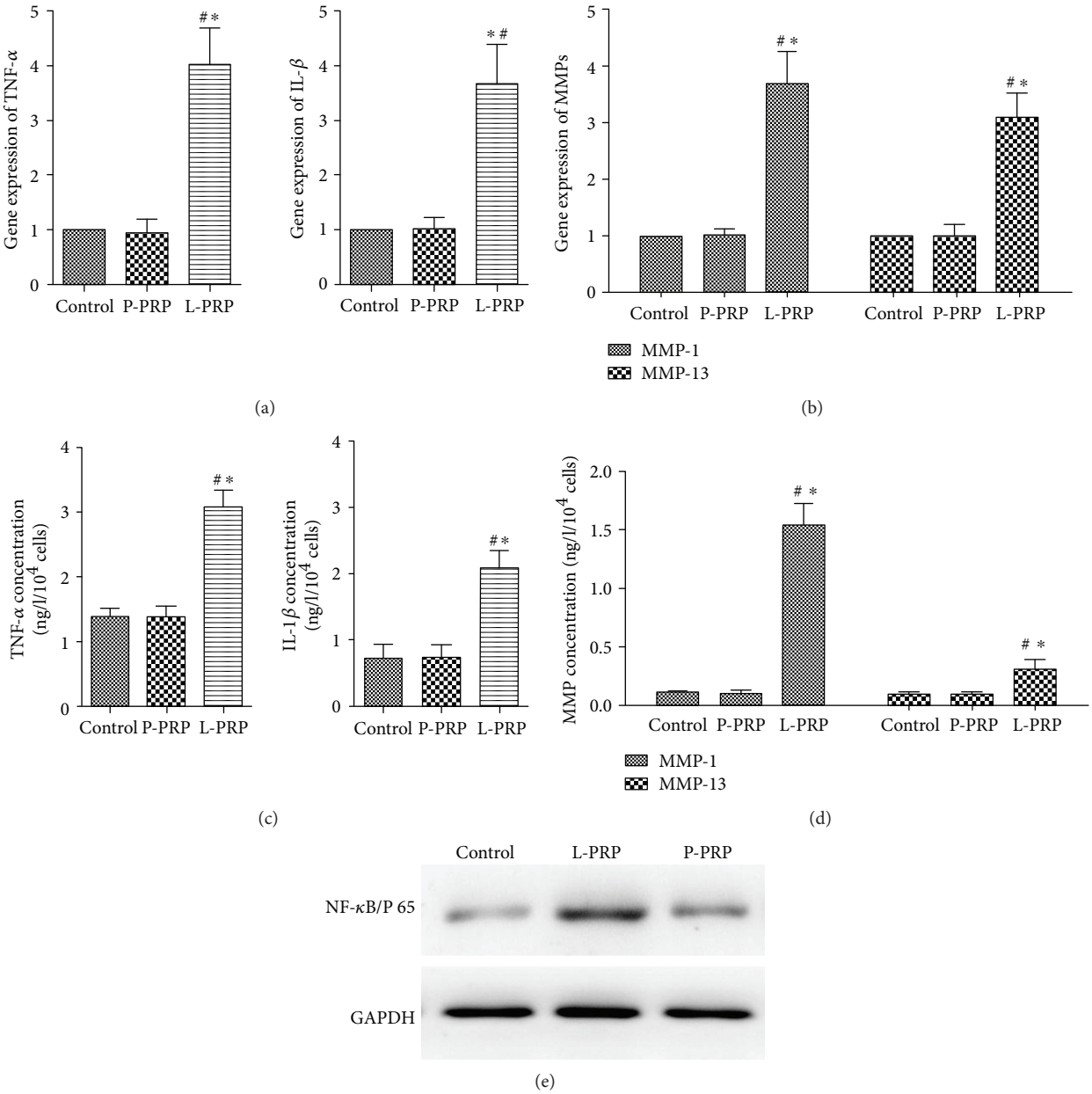

Figure 5: Effects of P-PRP and L-PRP on activation of NF-κB pathway. (a, b) mRNA expression of proinflammatory genes (IL-1β, TNF-α) and catabolic marker genes (MMP-1, MMP-13), as measured by qRT-PCR. (c, d) Production of proinflammatory cytokines (IL-1β, TNF-α) and catabolic cytokines (MMP-1, MMP-13), as determined by ELISA assay. (e) Production of NF-κB/p65 in the nucleus, as assessed by western blot. "$*$" indicates that the difference between the P-PRP or L-PRP and control was statistically significant ($P < 0.05$). "#" indicates that the difference between L-PRP and P-PRP was statistically significant ($P < 0.05$).

in the extracellular matrix-related protein accumulation of NPMSCs. However, the precise mechanism, especially the activation of NF-κB pathway, should be investigated in depth for further studies. Second, in this study, we only tested the in vitro effects of PRPs on NPMSCs. Cell culture system cannot necessarily guarantee the effect of P-PRP on NPMSCs when injected into animal models. Third, we did not investigate the effect of PRPs on the NPMSCs from the degenerated discs. When applied in a clinic, how PRPs can influence the already degenerated NPMSCs should be determined in further studies.

5. Conclusion

We demonstrated that both L-PRP and P-PRP induced the differentiation of NPMSCs towards the mature NP-like cells and exhibited similar proliferation effects on NPMSCs. However, different leukocyte levels contributed to distinct effects on the activation of NF-κB signaling pathway. Concentrated leukocytes in the L-PRP released high levels of proinflammatory cytokines, resulting in the strong activation of NF-κB signaling pathway. Although P-PRP and L-PRP exerted similar proliferation effects on NPMSCs, P-PRP showed superior

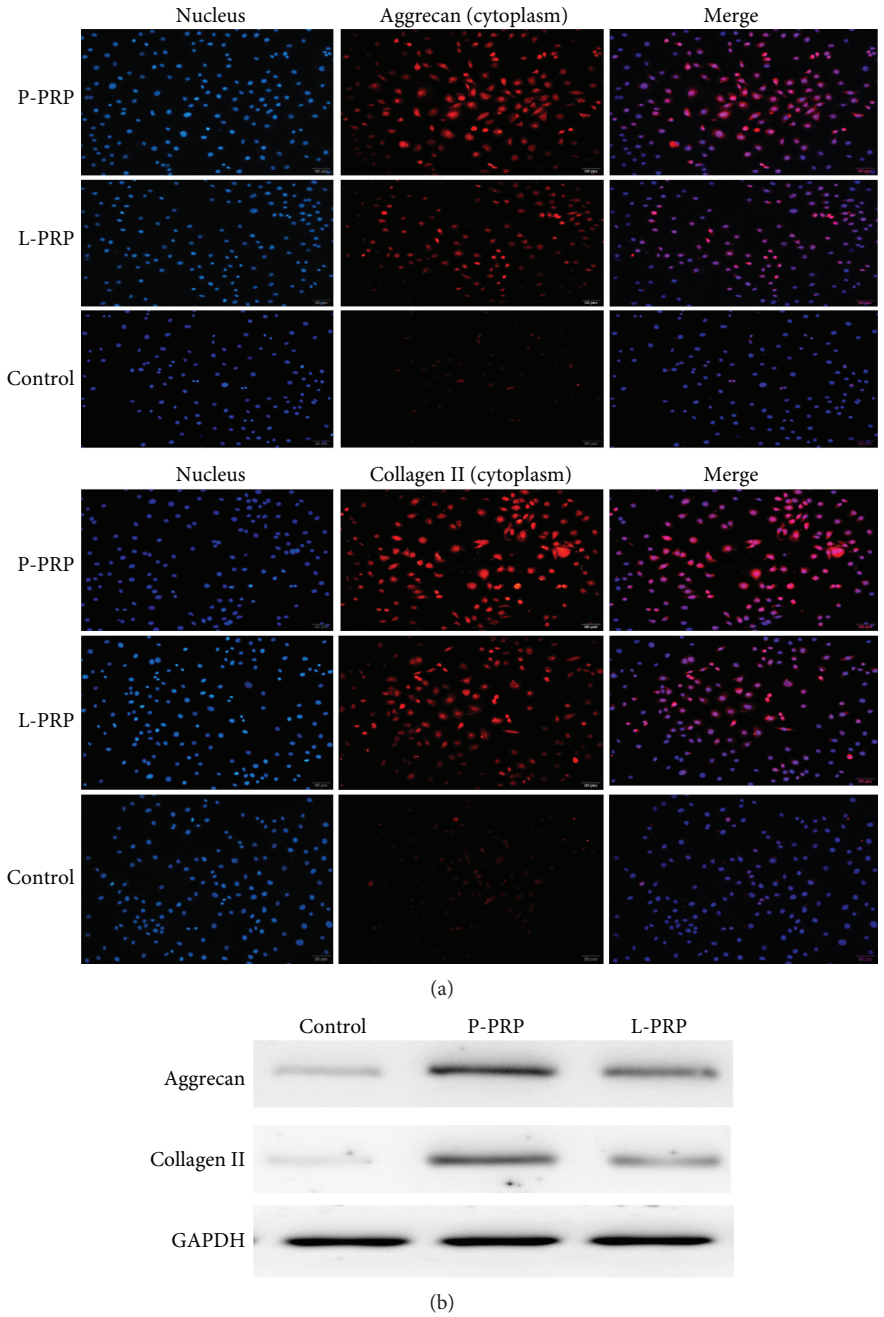

Figure 6: P-PRP induces more extracellular matrix-related proteins. (a) Collagen II and aggrecan in the cytoplasm of the coculture cells imaged by fluorescence microscopy. (b) Production of collagen II and aggrecan, as measured by western blot.

efficacy on the production of extracellular matrix-related protein. Therefore, when applied in IDD therapy, P-PRP exhibited a superior agent, which could better restore the degenerated ECM accumulation and function by activation of NPMSCs.

Data Availability

Data used to support the findings of this study are available from the corresponding author upon request.

Conflicts of Interest

The authors declare that they have no competing interests.

Acknowledgments

The funding support from the National Natural Science Foundation of China (Grant no. 81572188) for this work is gratefully acknowledged (CW).

References

[1] A. C. Schwarzer, C. N. Aprill, R. Derby, J. Fortin, G. Kine, and N. Bogduk, "The prevalence and clinical features of internal disc disruption in patients with chronic low back pain," *Spine*, vol. 20, no. 17, pp. 1878–1883, 1995.

[2] M. A. Adams and P. J. Roughley, "What is intervertebral disc degeneration, and what causes it?," *Spine*, vol. 31, no. 18, pp. 2151–2161, 2006.

[3] S. Roberts, H. Evans, J. Trivedi, and J. Menage, "Histology and pathology of the human intervertebral disc," *The Journal of Bone and Joint Surgery*, vol. 88, Supplement 2, pp. 10–14, 2006.

[4] H. A. Horner, S. Roberts, R. C. Bielby, J. Menage, H. Evans, and J. P. G. Urban, "Cells from different regions of the intervertebral disc: effect of culture system on matrix expression and cell phenotype," *Spine*, vol. 27, no. 10, pp. 1018–1028, 2002.

[5] D. Sakai, "Future perspectives of cell-based therapy for intervertebral disc disease," *European Spine Journal*, vol. 17, Supplement 4, pp. 452–458, 2008.

[6] S. K. Mirza and R. A. Deyo, "Systematic review of randomized trials comparing lumbar fusion surgery to nonoperative care for treatment of chronic back pain," *Spine*, vol. 32, no. 7, pp. 816–823, 2007.

[7] J. Karppinen, F. H. Shen, K. D. K. Luk, G. B. J. Andersson, K. M. C. Cheung, and D. Samartzis, "Management of degenerative disk disease and chronic low back pain," *The Orthopedic Clinics of North America*, vol. 42, no. 4, pp. 513–528, 2011.

[8] D. Sakai and G. B. J. Andersson, "Stem cell therapy for intervertebral disc regeneration: obstacles and solutions," *Nature Reviews Rheumatology*, vol. 11, no. 4, pp. 243–256, 2015.

[9] Y. C. Huang, V. Y. L. Leung, W. W. Lu, and K. D. K. Luk, "The effects of microenvironment in mesenchymal stem cell-based regeneration of intervertebral disc," *The Spine Journal*, vol. 13, no. 3, pp. 352–362, 2013.

[10] L. M. Benneker, G. Andersson, J. C. Iatridis et al., "Cell therapy for intervertebral disc repair: advancing cell therapy from bench to clinics," *European Cells & Materials*, vol. 27, pp. 5–11, 2014.

[11] S. Ikehara and M. Li, "Stem cell transplantation improves aging-related diseases," *Frontiers in Cell and Development Biology*, vol. 2, p. 16, 2014.

[12] J. P. G. Urban, "The role of the physicochemical environment in determining disc cell behaviour," *Biochemical Society Transactions*, vol. 30, no. 6, pp. 858–863, 2002.

[13] K. Wuertz, K. Godburn, C. Neidlinger-Wilke, J. Urban, and J. C. Iatridis, "Behavior of mesenchymal stem cells in the chemical microenvironment of the intervertebral disc," *Spine*, vol. 33, no. 17, pp. 1843–1849, 2008.

[14] B. Han, H. C. Wang, H. Li et al., "Nucleus pulposus mesenchymal stem cells in acidic conditions mimicking degenerative intervertebral discs give better performance than adipose tissue-derived mesenchymal stem cells," *Cells, Tissues, Organs*, vol. 199, no. 5-6, pp. 342–352, 2015.

[15] W. H. Chen, H. Y. Liu, W. C. Lo et al., "Intervertebral disc regeneration in an *ex vivo* culture system using mesenchymal stem cells and platelet-rich plasma," *Biomaterials*, vol. 30, no. 29, pp. 5523–5533, 2009.

[16] M. Nagae, T. Ikeda, Y. Mikami et al., "Intervertebral disc regeneration using platelet-rich plasma and biodegradable gelatin hydrogel microspheres," *Tissue Engineering*, vol. 13, no. 1, pp. 147–158, 2007.

[17] S. Z. Wang, J. Y. Jin, Y. D. Guo et al., "Intervertebral disc regeneration using platelet-rich plasma-containing bone marrow-derived mesenchymal stem cells: a preliminary investigation," *Molecular Medicine Reports*, vol. 13, no. 4, pp. 3475–3481, 2016.

[18] M. Leslie, "Cell biology. Beyond clotting: the powers of platelets," *Science*, vol. 328, no. 5978, pp. 562–564, 2010.

[19] S. Obata, K. Akeda, T. Imanishi et al., "Effect of autologous platelet-rich plasma-releasate on intervertebral disc degeneration in the rabbit anular puncture model: a preclinical study," *Arthritis Research & Therapy*, vol. 14, no. 6, p. R241, 2012.

[20] G. B. Gullung, J. W. Woodall, M. A. Tucci, J. James, D. A. Black, and R. McGuire, "Platelet-rich plasma effects on degenerative disc disease: analysis of histology and imaging in an animal model," *Evidence-Based Spine-Care Journal*, vol. 2, no. 4, pp. 13–18, 2011.

[21] M. Sanchez, E. Anitua, and I. Andia, "Poor standardization in platelet-rich therapies hampers advancement," *Arthroscopy*, vol. 26, no. 6, pp. 725-726, 2010.

[22] J. C. Peerbooms, J. Sluimer, D. J. Bruijn, and T. Gosens, "Positive effect of an autologous platelet concentrate in lateral epicondylitis in a double-blind randomized controlled trial," *American Journal of Sports Medicine*, vol. 38, no. 2, pp. 255–262, 2010.

[23] R. R. Monto, "Platelet rich plasma treatment for chronic Achilles tendinosis," *Foot & Ankle International*, vol. 33, no. 5, pp. 379–385, 2012.

[24] S. de Jonge, R. J. de Vos, A. Weir et al., "One-year follow-up of platelet-rich plasma treatment in chronic Achilles tendinopathy: a double-blind randomized placebo-controlled trial," *The American Journal of Sports Medicine*, vol. 39, no. 8, pp. 1623–1630, 2011.

[25] R. J. de Vos, A. Weir, H. T. M. van Schie et al., "Platelet-rich plasma injection for chronic Achilles tendinopathy: a randomized controlled trial," *JAMA*, vol. 303, no. 2, pp. 144–149, 2010.

[26] T. Schepull, J. Kvist, H. Norrman, M. Trinks, G. Berlin, and P. Aspenberg, "Autologous platelets have no effect on the healing of human Achilles tendon ruptures: a randomized single-blind study," *The American Journal of Sports Medicine*, vol. 39, no. 1, pp. 38–47, 2011.

[27] J. H. Wang, "Can PRP effectively treat injured tendons?," *Muscles, Ligaments and Tendons Journal*, vol. 4, no. 1, pp. 35–37, 2014.

[28] W. J. Yin, H. T. Xu, J. G. Sheng et al., "Advantages of pure platelet-rich plasma compared with leukocyte- and platelet-rich plasma in treating rabbit knee osteoarthritis," *Medical Science Monitor*, vol. 22, pp. 1280–1290, 2016.

[29] W. Yin, X. Qi, Y. Zhang et al., "Advantages of pure platelet-rich plasma compared with leukocyte- and platelet-rich plasma in promoting repair of bone defects," *Journal of Translational Medicine*, vol. 14, no. 1, p. 73, 2016.

[30] W. Yin, H. Xu, J. Sheng et al., "Optimization of pure platelet-rich plasma preparation: a comparative study of pure platelet-rich plasma obtained using different centrifugal conditions in a single-donor model," *Experimental and Therapeutic Medicine*, vol. 14, no. 3, pp. 2060–2070, 2017.

[31] P. Li, Y. Gan, Y. Xu et al., "17beta-estradiol attenuates TNF-α-induced premature senescence of nucleus pulposus cells

through regulating the ROS/NF-κB pathway," *International Journal of Biological Sciences*, vol. 13, no. 2, pp. 145–156, 2017.

[32] C. Liu, Q. Guo, J. Li et al., "Identification of rabbit annulus fibrosus-derived stem cells," *PLoS One*, vol. 9, no. 9, article e108239, 2014.

[33] D. Gibbings and A. D. Befus, "CD4 and CD8: an inside-out coreceptor model for innate immune cells," *Journal of Leukocyte Biology*, vol. 86, no. 2, pp. 251–259, 2009.

[34] M. C. Levesque, C. S. Heinly, L. P. Whichard, and D. D. Patel, "Cytokine-regulated expression of activated leukocyte cell adhesion molecule (CD166) on monocyte-lineage cells and in rheumatoid arthritis synovium," *Arthritis and Rheumatism*, vol. 41, no. 12, pp. 2221–2229, 1998.

[35] E. Assirelli, G. Filardo, E. Mariani et al., "Effect of two different preparations of platelet-rich plasma on synoviocytes," *Knee Surgery, Sports Traumatology, Arthroscopy*, vol. 23, no. 9, pp. 2690–2703, 2015.

[36] Y. Zhou, J. Zhang, H. Wu, M. V. Hogan, and J. H-C. Wang, "The differential effects of leukocyte-containing and pure platelet-rich plasma (PRP) on tendon stem/progenitor cells - implications of PRP application for the clinical treatment of tendon injuries," *Stem Cell Research & Therapy*, vol. 6, 173 pages, 2015.

[37] K. Wuertz, N. Vo, D. Kletsas, and N. Boos, "Inflammatory and catabolic signalling in intervertebral discs: the roles of NF-κB and MAP kinases," *European Cells & Materials*, vol. 23, pp. 102–120, 2012.

[38] M. Klawitter, L. Quero, J. Klasen et al., "Triptolide exhibits anti-inflammatory, anti-catabolic as well as anabolic effects and suppresses TLR expression and MAPK activity in IL-1β treated human intervertebral disc cells," *European Spine Journal*, vol. 21, no. S6, Supplement 6, pp. 850–859, 2012.

[39] L. Quero, M. Klawitter, A. Schmaus et al., "Hyaluronic acid fragments enhance the inflammatory and catabolic response in human intervertebral disc cells through modulation of toll-like receptor 2 signalling pathways," *Arthritis Research & Therapy*, vol. 15, no. 4, p. R94, 2013.

[40] Z. Xu, W. Yin, Y. Zhang et al., "Comparative evaluation of leukocyte- and platelet-rich plasma and pure platelet-rich plasma for cartilage regeneration," *Scientific Reports*, vol. 7, article 43301, 2017.

[41] K. Wuertz, N. Vo, D. Kletsas, and N. Boos, "Inflammatory and catabolic signalling in intervertebral discs: the roles of NF-κB and MAP kinases," *European Cells & Materials*, vol. 23, pp. 103–119, 2012.

[42] M. Moussa, D. Lajeunesse, G. Hilal et al., "Platelet rich plasma (PRP) induces chondroprotection via increasing autophagy, anti-inflammatory markers, and decreasing apoptosis in human osteoarthritic cartilage," *Experimental Cell Research*, vol. 352, no. 1, pp. 146–156, 2017.

[43] J. Zhang, K. K. Middleton, F. H. Fu, H. J. Im, and J. H. C. Wang, "HGF mediates the anti-inflammatory effects of PRP on injured tendons," *PLoS One*, vol. 8, no. 6, article e67303, 2013.

[44] R. C. Pereira, M. Scaranari, R. Benelli et al., "Dual effect of platelet lysate on human articular cartilage: a maintenance of chondrogenic potential and a transient proinflammatory activity followed by an inflammation resolution," *Tissue Engineering. Part A*, vol. 19, no. 11-12, pp. 1476–1488, 2013.

[45] F. Réadini, A. Mauviel, S. Pronost, G. Loyau, and J. P. Pujol, "Transforming growth factor β exerts opposite effects from interleukin-1β on cultured rabbit articular chondrocytes through reduction of interleukin-1 receptor expression," *Arthritis and Rheumatism*, vol. 36, no. 1, pp. 44–50, 1993.

Hindawi
Stem Cells International
Volume 2018, Article ID 3290372, 11 pages
https://doi.org/10.1155/2018/3290372

Research Article

MicroRNA-132, Delivered by Mesenchymal Stem Cell-Derived Exosomes, Promote Angiogenesis in Myocardial Infarction

Teng Ma, Yueqiu Chen, Yihuan Chen, Qingyou Meng, Jiacheng Sun, Lianbo Shao, Yunsheng Yu, Haoyue Huang, Yanqiu Hu, Ziying Yang, Junjie Yang, and Zhenya Shen

Department of Cardiovascular Surgery of the First Affiliated Hospital & Institute for Cardiovascular Science, Soochow University, Suzhou, China

Correspondence should be addressed to Ziying Yang; skyinger@163.com, Junjie Yang; junjieyang2009@gmail.com, and Zhenya Shen; zhenyashen@sina.cn

Received 6 March 2018; Accepted 11 June 2018; Published 9 September 2018

Academic Editor: Marco Tatullo

Copyright © 2018 Teng Ma et al. This is an open access article distributed under the Creative Commons Attribution License, which permits unrestricted use, distribution, and reproduction in any medium, provided the original work is properly cited.

Background. To cure ischemic diseases, angiogenesis needs to be improved by various strategies in ischemic area. Considering that microRNA-132 (miR-132) regulates endothelial cell behavior during angiogenesis and the safe and efficacious delivery of microRNAs *in vivo* is rarely achieved, an ideal vehicle for miR-132 delivery could bring the promise for ischemic diseases. As a natural carrier of biological molecules, exosomes are more and more developed as an ideal vehicle for miRNA transfer. Meanwhile, mesenchymal stem cells could release large amounts of exosomes. Thus, this study aimed to investigate whether MSC-derived exosomes can be used for miR-132 delivery in the treatment of myocardial ischemia. *Methods*. MSC-derived exosomes were electroporated with miR-132 mimics and inhibitors. After electroporation, miR-132 exosomes were labelled with DiI and added to HUVECs. Internalization of DiI-labelled exosomes was examined by fluorescent microscopy. Expression levels of miR-132 in exosomes and HUVECs were quantified by real-time PCR. The mRNA levels of miR-132 target gene RASA1 in HUVECs were quantified by real-time PCR. Luciferase reporter assay was performed to examine the targeting relationship between miR-132 and RASA1. The effects of miR-132 exosomes on the angiogenic ability of endothelial cells were evaluated by tube formation assay. Matrigel plug assay and myocardial infarction model were used to determine whether miR-132 exosomes can promote angiogenesis *in vivo*. *Results*. miR-132 mimics were effectively electroporated and highly detected in MSC-derived exosomes. The expression level of miR-132 was high in HUVECs preincubated with miR-132 mimic-electroporated exosomes and low in HUVECs preincubated with miR-132 inhibitor-electroporated exosomes. The expression level of RASA1, miR-132 target gene, was reversely correlated with miR-132 expression in HUVECs pretreated with exosomes. Luciferase reporter assay further confirmed that RASA1 was a direct target of miR-132. Exosomes loaded with miR-132, as a vehicle for miRNA transfer, significantly increased tube formation of endothelial cells. Moreover, subcutaneous injection of HUVECs pretreated with miR-132 exosomes in nude mice significantly increased their angiogenesis capacity *in vivo*. In addition, transplantation of miR-132 exosomes in the ischemic hearts of mice markedly enhanced the neovascularization in the peri-infarct zone and preserved heart functions. *Conclusions*. The findings suggest that the export of miR-132 via MSC-derived exosomes represents a novel strategy to enhance angiogenesis in ischemic diseases.

1. Introduction

In acute ischemic diseases such as myocardial ischemia, blood flow to the heart is impaired. Vessels need to be regenerated to rescue the ischemic cascade. Neoangiogenesis can be improved by activating endogenous progenitor cells, supplying exogenous stem cells and/or therapeutic molecules such as angiogenic mRNA or microRNAs [1, 2].

MicroRNAs, a class of small noncoding RNAs (containing about 18–22 nucleotides), regulate gene expression by

direct binding to the 3′-untranslated region (3′-UTR) of their target mRNAs and inducing their translational inhibition and/or degradation. MicroRNAs are recognized to participate in biological development, cell differentiation, apoptosis, and many other physiological and pathological processes [3]. Recently, multiple lines of evidence indicate that miR-132 regulate many processes in endothelial cells including angiogenic responses [1, 4, 5]. In 2010, Anand et al. demonstrated that upregulation of miR-132 positively controls pathological angiogenesis in response to vascular endothelial growth factor A (VEGF-A) by suppressing p120RasGap (RASA1) [4]. Recently, a study conducted by Katare et al. reported pericyte progenitor cells constitutively expressed and secreted miR-132 and promoted endothelial angiogenesis via modulation of methyl-CpG-binding protein 2 (MeCP2) [1]. Moreover, the potent proangiogenic effect of miR-132 has been confirmed in a mouse hind limb ischemia model. The study suggested that miR-132 may exert their proangiogenic effect by enhancing the Ras-mitogen-activated protein kinases (MAPK) signaling pathway through direct inhibition of RASA1 and Spred1 [5].

Exosomes are nanosized extracellular vesicles (30–100 nm in diameter) and are positive for CD9, CD63, and CD81. As a type of membrane vesicle, exosomes now have been recognized as a vehicle to facilitate intercellular communication and modulate the function of recipient cells though delivery of proteins, RNA, and other molecular constituents [6]. Exosomes have many remarkable attributes, such as stability, biocompatibility, and low immunogenicity, that delivery vehicles should have. The wide distribution of exosomes in the blood, urine, bronchoalveolar lavage fluid, breast milk, synovial fluid, pleural effusions, and ascites demonstrated that exosomes are well tolerated in biological fluids [7]. Another highly desired attribute of delivery vehicles is the ability to home to target location. Accumulating evidence suggests that depending on their cell source, surface antigen, and contents, exosomes could target specific cell types [8, 9]. These attributes provide a rationale for the applications of exosomes as therapeutic delivery vehicles in a wide spectrum of diseases such as cardiovascular disease, kidney injury, immune disease, neurological diseases, and cancer [9, 10–13].

The contents of exosomes are cell type specific and vary from different pathological conditions [14, 15]. Appropriate cell types need to be considered to obtain optimal and plentiful exosomes. Recently, mesenchymal stem cells (MSCs) are reported to be capable of secreting a large amount of functional exosomes. Studies have also demonstrated that MSC-derived exosomes have a significant proangiogenic function in myocardial infarction (MI) and hind limb ischemia model [10, 16].

In this study, we proposed that miR-132, delivered by MSC-derived exosomes, could exert the angiogenic effect in myocardial infarction. We investigated the angiogenic effect of miR-132-electroporated exosomes derived from MSCs *in vitro* and *in vivo*, as well as the underlying mechanisms. We treated HUVECs with miR-132 exosomes and found that miR-132 was upregulated in recipient cells, while the target gene RASA1 was downregulated in HUVECs. miR-132 exosomes promoted angiogenesis of HUVECs both *in vitro* and *in vivo*. In addition, transplantation of miR-132 exosomes in the ischemic hearts of mice markedly enhanced the neovascularization in the peri-infarct zone and preserved heart functions. Our study represents a potential strategy for revascularization and has important implications for new therapeutic approaches to ischemic diseases.

2. Materials and Methods

2.1. Animals. The mice were purchased from the Laboratory Animal Center of Nanjing University (Nanjing, China). The animals were housed under specific pathogen-free conditions, with 12-hour light/dark cycles and free access to food and water. The animal experiment was approved by the Ethic Committee of Soochow University. All efforts were made to minimize animal suffering.

2.2. Cell Culture. Bone marrow-derived mesenchymal stem cells (BMSCs) were isolated based on a previously reported procedure [17]; bone marrow cells were flushed from the bone cavity of femurs and tibias using 1 ml syringe with low-glucose Dulbecco's modified eagle medium (DMEM). All bone marrow cells were passed through a 70 μm cell strainer. The obtained bone marrow cells were seeded onto a culture dish and incubated at 37°C in a humidified atmosphere containing 5% CO_2, with C57BL/6 mouse mesenchymal stem cell growth medium (Cyagen, Guangdong, China). The phenotype profile of BMSCs (P4–P6) was identified by flow cytometry, using antibodies against mouse CD31, CD44, and CD105 and Sca-1. Human umbilical venous endothelial cells (HUVECs; Cell Bank of Chinese Academy of Sciences, Shanghai, China) were cultured in EGM2 supplemented with 5% fetal bovine serum according to manufacturer's instructions. All experiments were performed before passage 7.

2.3. Isolation and Purification of MSC-Derived Exosomes. MSCs were cultured in DMEM/F12 supplemented with 10% exosome-free FBS. After 48 h, exosomes were isolated from BMSC supernatant as previously described [10]. Briefly, the supernatant was obtained and centrifuged at 200 ×g for 30 min at 4°C to remove cellular debris. Afterwards, the supernatants were mixed with total exosome isolation reagent (Invitrogen, USA) overnight at 4°C. After centrifuging at 10,000 ×g for 1 h, the pellet was then carefully resuspended in 200 μl of PBS and used immediately or stored at −80°C. To analyze these exosomes, the characteristic surface marker proteins of exosomes were analyzed by Western blot and the exosome morphologies were observed with a transmission electron microscope (TEM) (JEOL JEM-1230) as described previously in detail.

2.4. Loading miR-132 into Exosomes. Resuspended exosomes were diluted in the Gene Pulser electroporation buffer (Bio-Rad Laboratories, CA) in 1 : 1 ratio. 1 μmol of mouse miR-132 mimic (Ambion, NY) or inhibitor was added to 200 μl of exosome sample. The mixtures were transferred into cold 0.2 cm electroporation cuvettes and electroporated at 150 V/100 μF capacitance using a Gene Pulser II system (Bio-Rad Laboratories, CA) as described previously [18]. After removing the free-floating miRNA mimic, exosomes were reisolated

using ultracentrifugation. The final pellet (exosome) was resuspended in PBS and stored at −80°C.

2.5. Exosome Labelling and Internalization. Exosomes (250 μg) were labelled with 1 μM of DiI lipophilic dye (Invitrogen). After incubating at 37°C for 30 min, excess dye was removed by washing with PBS, and labelled exosomes were reisolated by ultracentrifugation (described above). Recipient HUVECs (3×10^5) were incubated with DiI-labelled exosomes (10 μg) for 2 h, fixed in 4% paraformaldehyde (PFA) for 10 min at room temperature, washed with PBS for three times, incubated with DAPI (1 : 500, Invitrogen) for 5 minutes at room temperature, and subjected to confocal microscopy using a Zeiss LSM 780 confocal microscope with 100x magnification ($n = 3$).

2.6. Tube-Like Structure Formation Assay. 2×10^4/well HUVECs (three replicates per group) were seeded on top of Matrigel (BD Biosciences) in a 96-well plate and treated with the blank exosomes, miR-132 mimic electroexosomes, or miR-132 inhibitor electroexosomes, respectively. After incubation at 37°C for 6 h, tube formation was observed by an inverted microscope (Leica DMI6000B, Germany), and the cumulative tube length of the network structure was quantified (4x magnification) using ImageJ software.

2.7. Matrigel Plug Angiogenesis Assay. Matrigel plug angiogenesis assays were performed as previously described [19]; 2.5×10^5 HUVECs were treated with 30 μg of exosomes, or vehicle control (DMEM), premixed with Matrigel (1 mg/ml, BD Biosciences) and DMEM, and injected subcutaneously into SCID male mice (6-week-old, $n = 6$) in both inguinal regions. After 14 days, the animals were sacrificed using overdose of anesthetic. Plugs were excised and performed to the subsequent immunofluorescence assay.

2.8. Acute MI Model and Assessment of Heart Functions. An acute myocardial infarction (AMI) was generated in mice as described previously [20]. Briefly, C57BL/6J mice (female, ~20 g) were anesthetized with ketamine (80 mg/kg, IP) and mechanically ventilated. The left anterior descending artery (LAD) was ligated with a 6-0 suture, and the animals were divided into four groups: saline control, miR-132, Exo-null, and Exo-132. After LAD ligation, each mouse received an intramyocardial injection of PBS, miR-132, normal exosome, or miR-132-electroporated exosome, respectively. A total of 20 μl saline containing PBS, miR-132, or exosomes (600 μg) was transplanted by myocardial injection near the ligation site in the free wall of the left ventricle.

Cardiac function was determined by performing echocardiography on days 3, 7, and 28 after MI, using the Vevo 2100 system (VisualSonics Inc., Toronto, ON, Canada) with an 80 MHz probe. The left ventricular parameters were recorded from two-dimensional images using the M-mode interrogation in the short-axis view. Finally, the mice were sacrificed to harvest the heart tissue for immunohistochemical analysis.

2.9. Immunohistochemical Analysis. Immunohistochemistry staining was performed to detect vessel density of Matrigel plug and heart tissue as described previously [21]. The fresh tissue samples were fixed in 4% paraformaldehyde (PFA) and then embedded in OCT and cut into 6 μm thick slices. After blocking with 3% bovine serum albumin (BSA) for 30 min, the sections were subsequently incubated overnight at 4°C with the primary antibody against CD31. Secondary antibody goat anti-mouse Alexa 594 (1 : 500; Life Technologies) was used for detection. The nuclei were counterstained with 4,6-diamidino-2-phenylindole (DAPI). Images were observed by using a fluorescence microscope (Olympus).

2.10. Dual-Luciferase Reporter Assay. To elucidate whether RASA1 was a target gene of miR-132, TargetScan (http://targetscan.org) was used to predict miRNA molecules that may regulate RASA1, and miR-132 was identified as a potential regulator of RASA1. Wild-type (WT) and mutant seed regions of miR-132 in the 3′-UTR of RASA1 gene were cloned into pMIR-REPORT luciferase reporter plasmids (Invitrogen, USA). Plasmids with WT or mutant 3′-UTR DNA sequences were cotransfected with miR-132 mimic (100 nM; Sangon Biotech Co. Ltd., Shanghai, China) or negative control mimics into HEK293T cells (ATCC, Manassas, VA, USA). After cultivation at 37°C for 24 hours, cells were assayed using the dual-luciferase assay system (Promega, Madison, USA) according to the manufacturer's instructions. All assays were repeated at least three times.

2.11. Quantitative RT-PCR Assay. Total RNA was isolated from exosomes or HUVECs using TRIzol reagent (Invitrogen, USA) as described previously [22], and reverse transcription was performed using the microRNA reverse transcription system (GenePharma, Shanghai, China) or the PrimeScript RT reagent kit (TAKARA, Japan). The expression level of miR-132 was analyzed by SYBR Green assay following the manufacturer's instruction, using U6 as control. For RASA1, quantitative RT-PCR (Q-PCR) was performed using SYBR PCR master mix in the ABI Step One-Plus Detection system (Applied Biosystems, USA) according to the manufacturer's instructions. The primers used for RASA1 are as follows: sense, 5′-TTATGATGGGAGGCCG CTATT-3′, and antisense: 5′-CTGCATTGGTACAGGT TCCTT-3′. GAPDH was used as an internal control. The $2-\Delta\Delta CT$ method was employed to determine the relative mRNA expression. Each assay was performed in triplicate.

2.12. Western Blot Analysis. Western blotting was performed to quantify specific protein expression levels in BMSCs and BMSC-derived exosomes. Samples were lysed with RIPA buffer containing protease inhibitor cocktail (Roche, USA), and the protein concentration was determined by BCA assay (Roche, USA). Equal quantities of protein were loaded and run on 10% SDS-PAGE gels and then transferred to polyvinylidene difluoride (PVDF) membranes. Each membrane was blocked in 5% BSA and subsequently incubated overnight at 4°C with anti-CD9 and anti-CD63, respectively. After washing, the membranes were incubated with peroxidase-conjugated goat anti-mouse secondary antibody (Invitrogen, USA). Image analysis and blot quantification

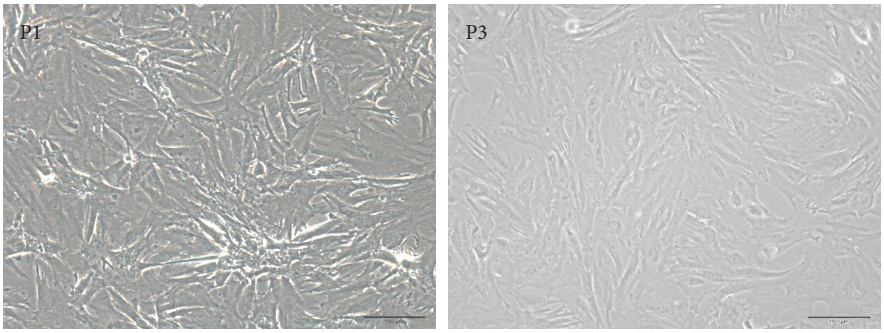

(a)

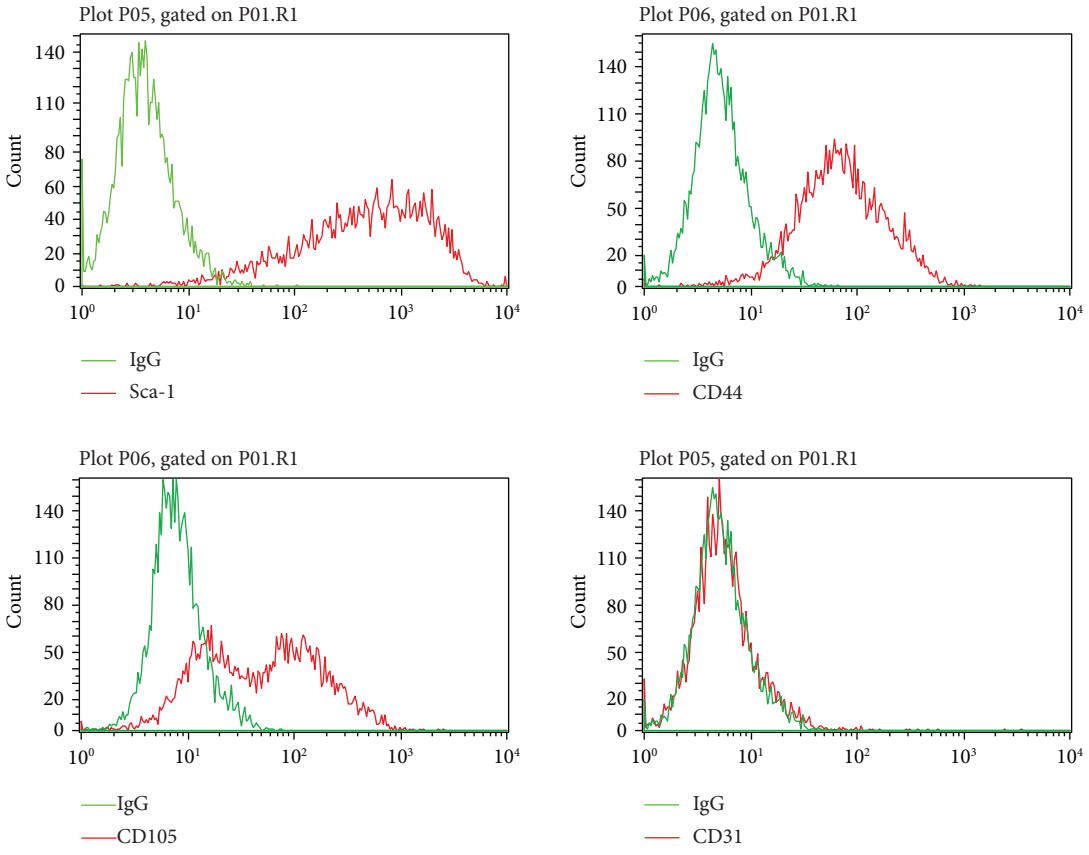

(b)

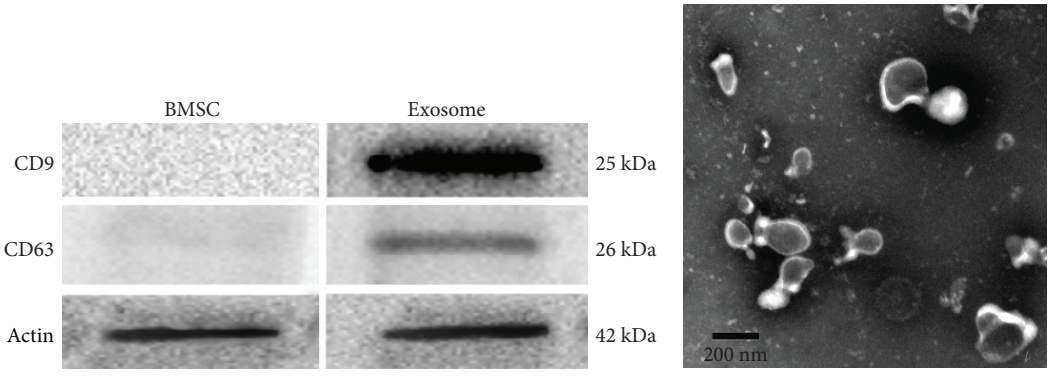

(c) (d)

Figure 1: Continued.

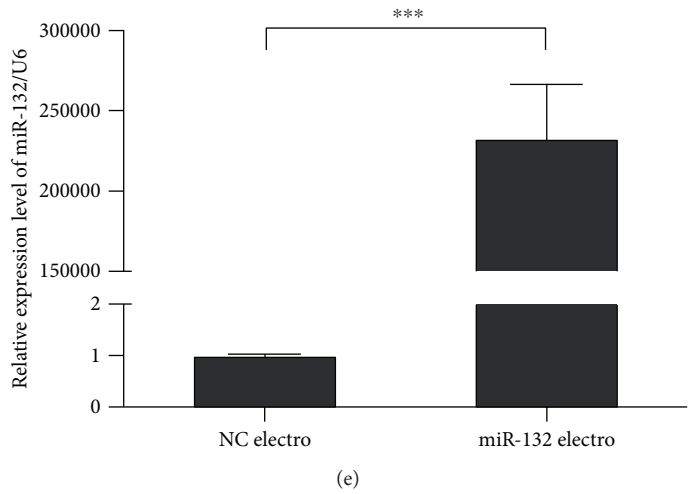

Figure 1: Characterization of BMSCs and BMSC-derived exosomes. (a) Morphology of MSCs (P1, P3) observed under an inverted fluorescence microscope. Scale bar: 100 μm. (b) Phenotypic analysis of cell surface antigens of MSCs by flow cytometry ($n = 3$). (c) Surface marker proteins of BMSCs and BMSC-derived exosomes analyzed by Western immunoblotting ($n = 3$). (d) Morphology of MSC-derived exosomes under transmission electron microscopy. Scale bar: 200 nm. (e) The expression level of miR-132 determined by Q-PCR ($n = 3$). $^{***}P < 0.001$. NC: negative control.

were performed with Image Quant LAS 4000 mini biomolecular imager (GE Healthcare, Uppsala, Sweden).

2.13. Statistical Analysis. All data of *in vitro* experiments were obtained from at least three independent experiments. In the *in vivo* study, more than 6 samples were used in each group. The results were presented as means ± SD unless otherwise indicated and were analyzed using GraphPad Prism 5 software. Statistical analyses were performed using a two-tailed Student *t*-test or one-way ANOVA with post hoc tests to determine significant differences between the groups. $P < 0.05$ was considered statistically significant.

3. Results

3.1. Characterization of BMSCs and BMSC-Derived Exosomes. MSCs were isolated from the bone marrow of C57BL/6 mice as described previously. MSCs were typically spindle-shaped and adherent to the plastic dishes (Figure 1(a)). Flow cytometry was used to identify the surface antigens of MSCs. Results showed that MSCs were negative for CD31, but positive for Sca-1, CD44, and CD105 (Figure 1(b)). The exosomes secreted from BMSCs were isolated as described in Materials and Methods and subjected to biochemical and biophysical analyses. Biochemical analysis of isolated exosomes showed the presence of the exosome proteins CD63 and CD9 (Figure 1(c)), while no expression of CD63 and CD9 was detected in BMSCs. Electron microscopy analysis of exosomes exhibited typical cup-shaped morphology and confirmed the size range of less than 150 nm (Figure 1(d)). Furthermore, a significant miR-132 overexpression was detected by qRT-PCR in electroporated MSCs with miR-132 (Figure 1(e)).

3.2. miR-132 Exosomes Are Efficiently Taken Up by HUVECs. Exosomes were labelled with CM-DiI dye and incubated with HUVECs *in vitro*. Using an inverted fluorescence microscope, we provided qualitative evidence that HUVECs take up DiI-labelled exosomes derived from BMSCs (Figure 2(a)). Next, we performed qPCR to evaluate the expression of miR-132 in HUVECs. We observed a significant increase of miR-132 expression in HUVECs taking up miR-132 mimic electro-Exos, when compared with both blank HUVECs and HUVECs taking up miR-132 inhibitor electro-Exos (Figure 2(b)). It is worthy of note that the expression of RASA1, a target gene of miR-132, was significantly downregulated (Figure 2(c)). Luciferase reporter assay was used to further confirm the targeting relationship between miR-132 and RASA1. Results showed that miR-132 significantly decreased the relative luciferase reporter activity of the wild-type RASA1 3′-UTR, whereas that of the mutant RASA1 3′-UTR did not change significantly, which suggests that miR-132 could directly bind to the 3′-UTR of RASA1 (Figure 2(d)).

3.3. miR-132-Electroporated Exosomes Promote Angiogenesis In Vitro. We investigated whether miR-132 electroexosomes could enhance the angiogenic behavior of endothelial cells *in vitro*. The tube length and the number of meshes were increased in HUVECs treated with miR-132 mimic electroexosomes for 12 h, compared to those treated with blank exosomes and miR-132 inhibitor electroexosomes (Figures 3(a)–3(c)). As evidenced by tube formation assay, our study suggests that overexpressed miR-132 could enhance the proangiogenic effects of exosome on endothelial cells.

3.4. miR-132-Electroporated Exosomes Promote Angiogenesis In Vivo. Finally, we utilized Matrigel plug to examine *in vivo* angiogenic behavior. Matrigel containing HUVECs, HUVECs treated with blank exosome, or HUVECs treated with miR-132 mimic electroexosome was injected subcutaneously into SCID male mice ($n = 6$) in the inguinal regions,

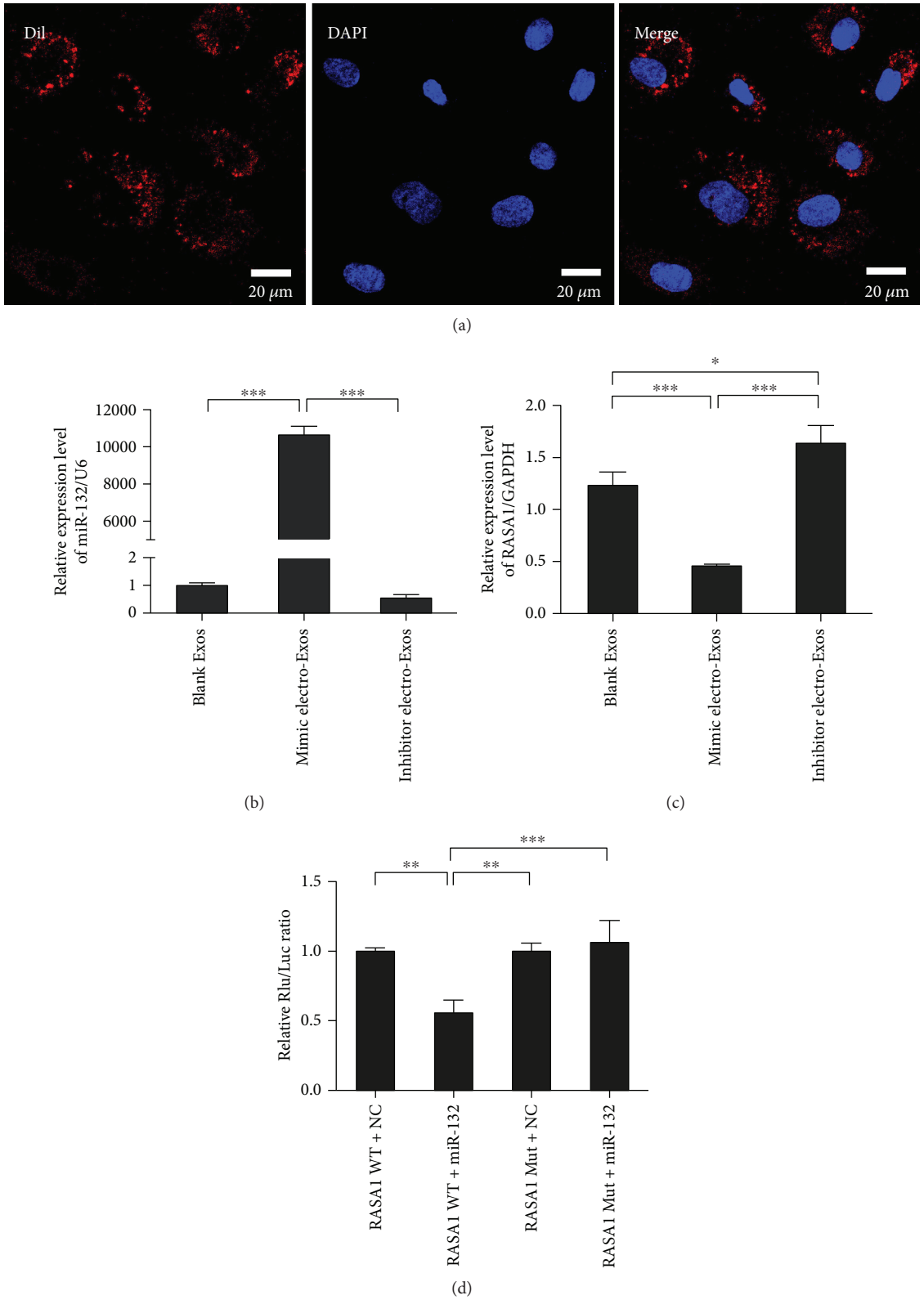

Figure 2: Internalization of miR-132-electroporated exosomes and detection of target gene RASA1. (a) Confocal images of DiI-labelled exosomes taken up by HUVECs. Scale bar: 20 μm. (b, c) HUVECs were incubated with miR-132 mimics or inhibitor-electroporated exosomes for 2 h. The relative expression level of miR-132 and its target gene RASA1 was detected by RT-PCR ($n = 3$). (d) 293T was cotransfected with miR-132 mimics or NC and firefly luciferase reporter plasmid containing wild-type or mutant-type 3′UTR of RASA1. After incubation for 48 h, the firefly luciferase activity of each sample was detected and normalized to the Renilla luciferase activity ($n = 3$). The data represent the mean ± SEM of triplicates. $^{*}P < 0.05$, $^{**}P < 0.01$, $^{***}P < 0.001$.

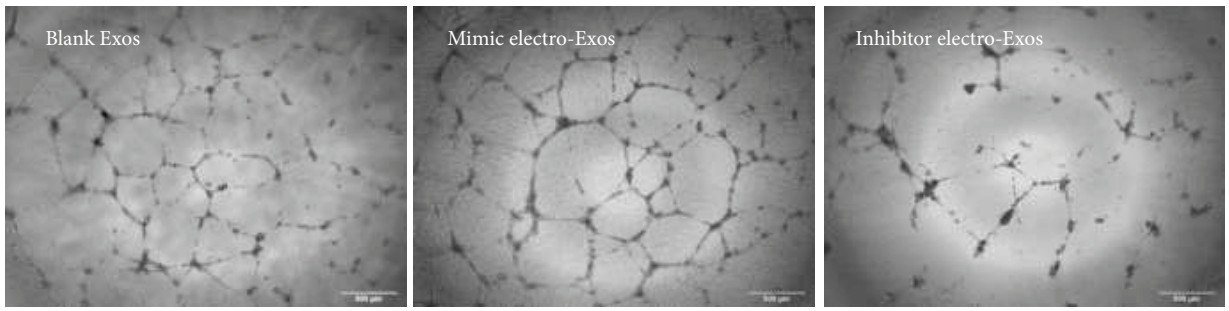

(a)

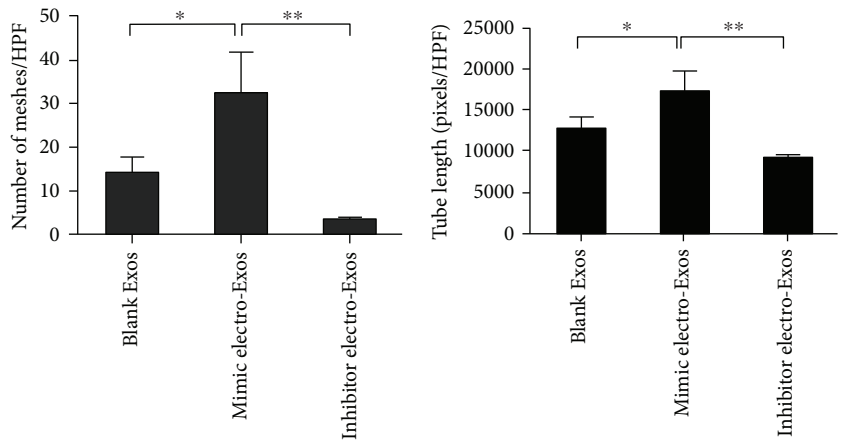

(b) (c)

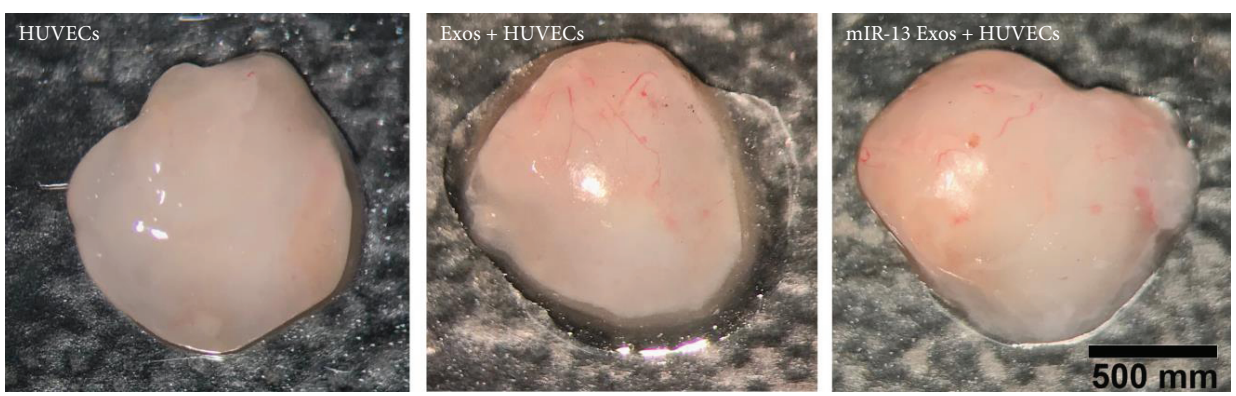

(d)

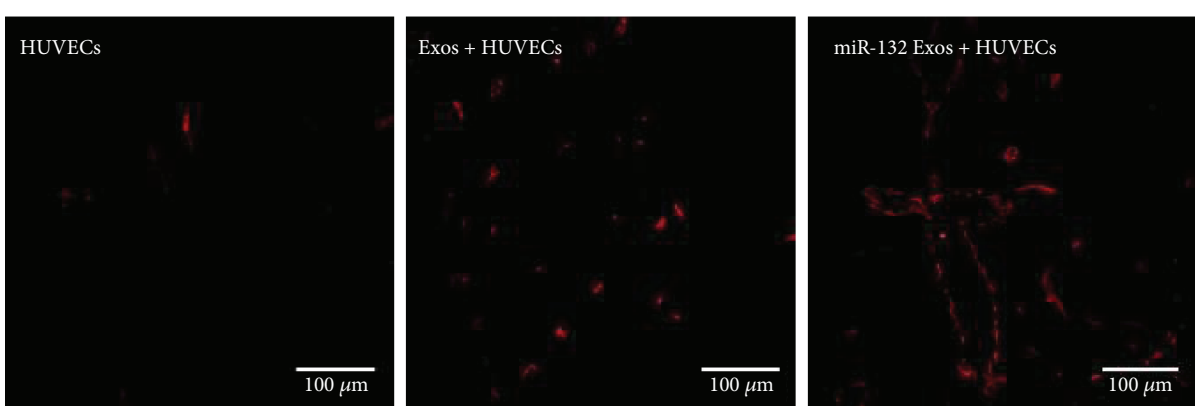

(e)

Figure 3: Continued.

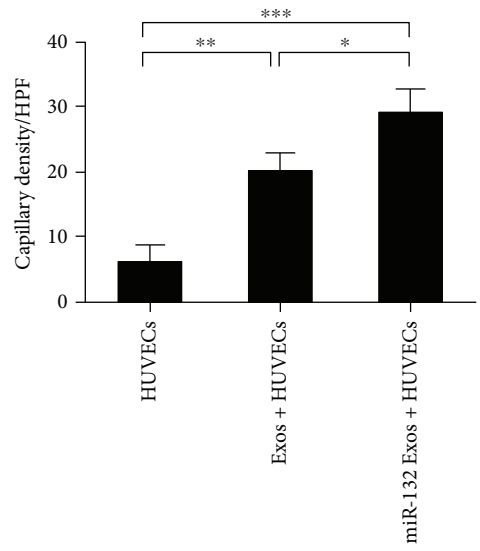

(f)

Figure 3: miR-132-electroporated exosomes promoted angiogenesis *in vitro* and *in vivo*. (a) Tube formation assay on Matrigel was assessed 6 h after seeding HUVECs pretreated with blank, miR-132 mimic-electroporated or miR-132 inhibitor-electroporated exosomes. Scale bar: 500 μm. (b, c) Quantitative assessment of the total number of meshes and tube length ($n = 3$). $^{*}P < 0.05$, $^{**}P < 0.01$. (d) Gross look of Matrigel plugs. (e, f) Immunofluorescence staining of vessels in the sections of Matrigel plugs and quantitative assessment of capillaries per high-power field in each group ($n = 3$). $^{*}P < 0.05$, $^{***}P < 0.001$.

respectively. After 14 days, Matrigel was excised and photographed to assess the presence of blood vessels. The Matrigel plugs containing miR-132 exosome exhibited bright red color indicating blood-perfused vessels, whereas blank exosome-containing plugs presented light yellowish color that is correlated with the limited formation of new vessels (Figure 3(d)). In addition, the immunofluorescence staining showed that the number of vessels in the plugs containing miR-132 exosomes (29.33 ± 2.86/HPF) was also significantly higher than that in the negative control (6.33 ± 2.05/HPF) and those containing blank exosomes (20.33 ± 2.05/HPF) (Figures 3(e) and 3(f)).

3.5. miR-132-Electroporated Exosomes Preserve Cardiac Function and Promote Angiogenesis in a Mouse MI Model. We assessed the *in vivo* therapeutic effects of miR-132 exosomes on a mouse MI model. Preinterventional left ventricular ejection fraction (LVEF) and fractional shortening (FS) values were similar in all groups (data not shown). Significant decreases in LVEF and FS in saline-treated mice were observed on day 7 and day 28 after MI. Compared with saline-treated mice, the miR-132 and normal exosome group partially rescued MI-induced decrease of LVEF and FS, while the miR-132-exosome group significantly increased LVEF (day 7: 30.18 ± 0.94 versus 48.04 ± 1.27, $P < 0.001$, and day 28: 31.56 ± 0.83 versus 51.97 ± 1.32, $P < 0.001$, resp.) and FS (day 7: 12.21 ± 1.16 versus 19.87 ± 1.17, $P < 0.01$, and day 28: 11.80 ± 0.25 versus 21.33 ± 0.64, $P < 0.0001$, resp.) compared with saline-treated mice on day 7 and day 28 after MI (Figures 4(a) and 4(b)). Hearts were excised on day 28 after MI. Capillary density of cardiac tissue was further examined by immunohistochemical stain. Compared with the saline-treated group (19 ± 2.45/HPF), both the miR-132 (33.33 ± 3.40/HPF) and normal exosome groups (32.67 ± 3.09/HPF) had a higher density of vessels. More importantly, the capillary density of the infarct area was significantly increased in the miR-132 exosome group (50 ± 1.63/HPF), (Figures 4(c) and 4(d)). These data demonstrate that miR-132-electroporated exosomes could effectively preserve cardiac function and promote angiogenesis in a mouse MI model.

4. Discussion

In this paper, we demonstrated that exosomes loaded with miR-132, as a vehicle for miRNA carriage and transfer, significantly increased tube formation *in vitro* and neoangiogenesis in Matrigel plug and myocardial infarction. Mechanistically, miR-132 promotes angiogenesis by downregulating the expression level of its target gene RASA1 in HUVECs. These findings greatly extend our current understanding of exosomes on angiogenesis and indicate that exosomes give an inspiring hope as vehicles of therapeutic molecules for the treatment of ischemic diseases.

Ischemic heart disease (IHD) is the leading cause of morbidity and mortality worldwide owing to aging, obesity, diabetes, and other comorbid diseases [23]. One potent therapeutic approach for IHD is to induce revascularization, therefore, increase oxygen supply, inhibit cardiomyocyte apoptosis, and reduce myocardial fibrosis. MicroRNAs are small noncoding RNAs that act as negative regulators of protein-coding genes. It has been well established that microRNAs promote both physiological and pathological angiogenesis [4, 24]. A large number of therapeutic strategies

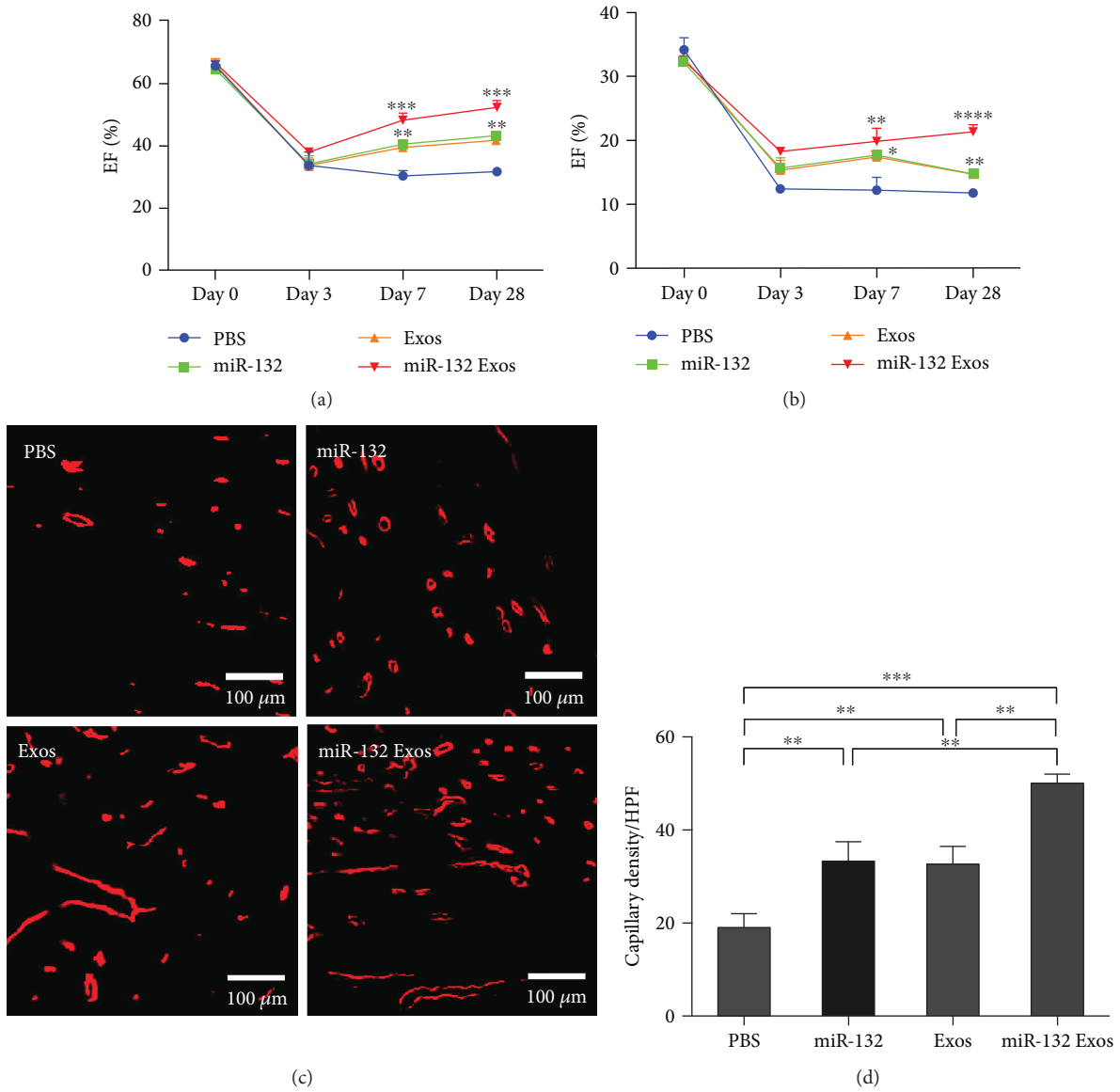

Figure 4: miR-132-electroporated exosomes preserve cardiac function and promoted angiogenesis in MI model. (a, b) Quantitative assessment of LVEF and FS value in each group after MI ($n = 3$). $^{*}P < 0.05$, $^{**}P < 0.01$, $^{***}P < 0.001$, $^{****}P < 0.0001$. (c, d) Immunofluorescence staining of vessels in the sections of heart tissue and quantitative assessment of capillaries per high-power field in each group. Scale bar: 500 μm ($n = 3$). $^{**}P < 0.01$, $^{***}P < 0.001$.

based on microRNAs have been carried out on the treatment of myocardial infarction and other ischemic diseases [2, 20, 22].

The intercellular communication occurs directly (between adjacent cells, via gap junctions) or indirectly (at long distances, via soluble factors and extracellular vesicles, including exosomes). These vesicles that act as the vehicles of proteins, RNA, and other molecular constituents modulate the intercellular communication. Previous studies reported that changing the miRNA expression in exosomes derived from MSCs could protect ischemia-reperfusion injury and promote angiogenesis in acute MI [10, 25]. All of these findings indicated that exosomes, as natural therapeutic delivery vehicles, play an important role in angiogenesis [10, 26]. In addition, exosomes can be easily stored at −20°C for at least 6 months without loss of biological activity [27]. Exosomes may be easier to manufacture and standardize in terms of dosage and biological activity.

According to previous researches, we selected miR-132 for gain and loss of function in HUVECs pretreated with electroporated exosomes, to investigate the role of exosome-transferred proangiomiRs in angiogenesis. Exogenous miR-132 mimics and inhibitors were successfully electroporated into MSC-derived exosomes, and it was shown that loaded exosomes can be taken up by HUVECs. The loaded exosomes effectively delivered miR-132 mimics into HUVECs, causing increase of miR-132, and functionally promoted tube formation and neoangiogenesis in Matrigel

plug and myocardial infarction. On the contrary, inhibiting the expression of miR-132 in exosomes derived from MSCs resulted in reduced angiogenesis. These findings indicate that the extracellular miR-132 was loaded into exosomes, transferred into endothelial cells, and played a critical role in angiogenesis.

Furthermore, to investigate the molecular mechanisms by which miR-132 might promote angiogenesis, we focus on its target gene RASA1. RASA1 has been reported to be an evolutionary conserved target of miR-132 [5]. Previous studies have demonstrated that RASA1 acts as a crucial negative regulator of vascular sprouting and vessel branching. Furthermore, other researches have revealed that RASA1 regulates endothelial cell behavior during angiogenesis in HUVECs by inactivating the Ras-mitogen-activated protein kinase (MAPK) signaling pathway [5]. Our results showed that increasing the expression of miR-132 led to a statistically significant decrease of RASA1 level in HUVECs. This observation is in agreement with previous data [4]. In order to confirm the interaction between miR-132 and RASA1, we performed dual-luciferase reporter assay which demonstrated that RASA1 is a real target of miR-132 in HUVECs.

In conclusion, we identified that miR-132-electroporated exosomes promoted angiogenesis *in vitro* and *in vivo*. MSC-derived exosomes could be considered as a potential candidate for therapeutic angiogenesis especially for ischemic diseases. Exosomes derived from MSCs have theoretical advantages as a medicinal product, and, in the future, exosomes may gain preference over whole cell-based therapy in the discipline of regenerative medicine.

Abbreviations

MSC: Mesenchymal stem cells
MI: Myocardial infarction
3′-UTR: 3′-untranslated region
VEGF-A: Vascular endothelial growth factor A
RASA1: p120RasGap
MeCP2: Methyl-CpG-binding protein 2
MAPK: Ras-mitogen-activated protein kinases
DMEM: Dulbecco's modified eagle medium
HUVECs: Human umbilical venous endothelial cells
TEM: Transmission electron microscope
PFA: Paraformaldehyde
LAD: Left anterior descending artery
DAPI: 4,6-Diamidino-2-phenylindole
BSA: Bovine serum albumin
WT: Wild-type
PVDF: Polyvinylidene difluoride
LVEF: Left ventricular ejection fraction
FS: Fractional shortening
IHD: Ischemic heart disease.

Data Availability

The data used to support the findings of this study are available from the corresponding author upon request.

Ethical Approval

The experiment protocols were approved by the Ethic Committee of Soochow University (Reference no. SZUM2008031233).

Conflicts of Interest

The authors declare that there is no conflict of interests regarding the publication of this paper.

Authors' Contributions

Teng Ma, Yueqiu Chen, Yihuan Chen, and Qingyou Meng contributed equally to this work. All authors have contributed to, read, and approved the final manuscript for submission.

Acknowledgments

This work was supported by the National Natural Science Foundation of China (nos. 81770260, 81400199), National Clinical Key Specialty of Cardiovascular Surgery, and Jiangsu Clinical Research Center for Cardiovascular Surgery (BL201451), and Natural Science Foundation of Jiangsu Province (BK20160346 and BK20151212).

References

[1] R. Katare, F. Riu, K. Mitchell et al., "Transplantation of human pericyte progenitor cells improves the repair of infarcted heart through activation of an angiogenic program involving micro-RNA-132," *Circulation Research*, vol. 109, no. 8, pp. 894–906, 2011.

[2] Z. Wen, W. Huang, Y. Feng et al., "MicroRNA-377 regulates mesenchymal stem cell-induced angiogenesis in ischemic hearts by targeting VEGF," *PLoS One*, vol. 9, no. 9, article e104666, 2014.

[3] J. Krol, I. Loedige, and W. Filipowicz, "The widespread regulation of microRNA biogenesis, function and decay," *Nature Reviews Genetics*, vol. 11, no. 9, pp. 597–610, 2010.

[4] S. Anand, B. K. Majeti, L. M. Acevedo et al., "MicroRNA-132–mediated loss of p120RasGAP activates the endothelium to facilitate pathological angiogenesis," *Nature Medicine*, vol. 16, no. 8, pp. 909–914, 2010.

[5] Z. Lei, A. van Mil, M. M. Brandt et al., "MicroRNA-132/212 family enhances arteriogenesis after hindlimb ischaemia through modulation of the Ras-MAPK pathway," *Journal of Cellular and Molecular Medicine*, vol. 19, no. 8, pp. 1994–2005, 2015.

[6] H. Valadi, K. Ekstrom, A. Bossios, M. Sjostrand, J. J. Lee, and J. O. Lotvall, "Exosome-mediated transfer of mRNAs and microRNAs is a novel mechanism of genetic exchange between cells," *Nature Cell Biology*, vol. 9, no. 6, pp. 654–659, 2007.

[7] R. J. Simpson, S. S. Jensen, and J. W. E. Lim, "Proteomic profiling of exosomes: current perspectives," *Proteomics*, vol. 8, no. 19, pp. 4083–4099, 2008.

[8] L. Alvarez-Erviti, Y. Seow, H. F. Yin, C. Betts, S. Lakhal, and M. J. A. Wood, "Delivery of siRNA to the mouse brain by

systemic injection of targeted exosomes," *Nature Biotechnology*, vol. 29, no. 4, pp. 341–345, 2011.

[9] J. L. Hood, R. S. San, and S. A. Wickline, "Exosomes released by melanoma cells prepare sentinel lymph nodes for tumor metastasis," *Cancer Research*, vol. 71, no. 11, pp. 3792–3801, 2011.

[10] Z. Zhang, J. Yang, W. Yan, Y. Li, Z. Shen, and T. Asahara, "Pretreatment of cardiac stem cells with exosomes derived from mesenchymal stem cells enhances myocardial repair," *Journal of the American Heart Association*, vol. 5, no. 1, article e002856, 2016.

[11] M. Morigi, B. Imberti, C. Zoja et al., "Mesenchymal stem cells are renotropic, helping to repair the kidney and improve function in acute renal failure," *Journal of the American Society of Nephrology*, vol. 15, no. 7, pp. 1794–1804, 2004.

[12] A. Mokarizadeh, N. Delirezh, A. Morshedi, G. Mosayebi, A. A. Farshid, and K. Mardani, "Microvesicles derived from mesenchymal stem cells: potent organelles for induction of tolerogenic signaling," *Immunology Letters*, vol. 147, no. 1-2, pp. 47–54, 2012.

[13] H. Xin, Y. Li, B. Buller et al., "Exosome-mediated transfer of miR-133b from multipotent mesenchymal stromal cells to neural cells contributes to neurite outgrowth," *Stem Cells*, vol. 30, no. 7, pp. 1556–1564, 2012.

[14] H. Tadokoro, T. Umezu, K. Ohyashiki, T. Hirano, and J. H. Ohyashiki, "Exosomes derived from hypoxic leukemia cells enhance tube formation in endothelial cells," *Journal of Biological Chemistry*, vol. 288, no. 48, pp. 34343–34351, 2013.

[15] B. Yu, H. W. Kim, M. Gong et al., "Exosomes secreted from GATA-4 overexpressing mesenchymal stem cells serve as a reservoir of anti-apoptotic microRNAs for cardioprotection," *International Journal of Cardiology*, vol. 182, pp. 349–360, 2015.

[16] G. W. Hu, Q. Li, X. Niu et al., "Exosomes secreted by human-induced pluripotent stem cell-derived mesenchymal stem cells attenuate limb ischemia by promoting angiogenesis in mice," *Stem Cell Research & Therapy*, vol. 6, no. 1, p. 10, 2015.

[17] M. Gnecchi and L. G. Melo, "Bone marrow-derived mesenchymal stem cells: isolation, expansion, characterization, viral transduction, and production of conditioned medium," *Methods in Molecular Biology*, vol. 482, pp. 281–294, 2009.

[18] F. Momen-Heravi, S. Bala, T. Bukong, and G. Szabo, "Exosome-mediated delivery of functionally active miRNA-155 inhibitor to macrophages," *Nanomedicine: Nanotechnology, Biology and Medicine*, vol. 10, no. 7, pp. 1517–1527, 2014.

[19] P. Mocharla, S. Briand, G. Giannotti et al., "AngiomiR-126 expression and secretion from circulating $CD34^+$ and $CD14^+$ PBMCs: role for proangiogenic effects and alterations in type 2 diabetics," *Blood*, vol. 121, no. 1, pp. 226–236, 2013.

[20] W. Huang, S. S. Tian, P. Z. Hang, C. Sun, J. Guo, and Z. M. Du, "Combination of microRNA-21 and microRNA-146a attenuates cardiac dysfunction and apoptosis during acute myocardial infarction in mice," *Molecular Therapy - Nucleic Acids*, vol. 5, article e296, 2016.

[21] A. K. Horst, W. D. Ito, J. Dabelstein et al., "Carcinoembryonic antigen–related cell adhesion molecule 1 modulates vascular remodeling in vitro and in vivo," *The Journal of Clinical Investigation*, vol. 116, no. 6, pp. 1596–1605, 2006.

[22] Y. Chen, Y. Zhao, W. Chen et al., "MicroRNA-133 overexpression promotes the therapeutic efficacy of mesenchymal stem cells on acute myocardial infarction," *Stem Cell Research & Therapy*, vol. 8, no. 1, p. 268, 2017.

[23] A. Saparov, V. Ogay, T. Nurgozhin et al., "Role of the immune system in cardiac tissue damage and repair following myocardial infarction," *Inflammation Research*, vol. 66, no. 9, pp. 739–751, 2017.

[24] M. Dews, A. Homayouni, D. Yu et al., "Augmentation of tumor angiogenesis by a Myc-activated microRNA cluster," *Nature Genetics*, vol. 38, no. 9, pp. 1060–1065, 2006.

[25] W. D. Gray, K. M. French, S. Ghosh-Choudhary et al., "Identification of therapeutic covariant microRNA clusters in hypoxia-treated cardiac progenitor cell exosomes using systems biology," *Circulation Research*, vol. 116, no. 2, pp. 255–263, 2015.

[26] S. Rontauroli, R. Norfo, V. Pennucci et al., "miR-494-3p overexpression promotes megakaryocytopoiesis in primary myelofibrosis hematopoietic stem/progenitor cells by targeting SOCS6," *Oncotarget*, vol. 8, no. 13, pp. 21380–21397, 2017.

[27] V. B. R. Konala, M. K. Mamidi, R. Bhonde, A. K. Das, R. Pochampally, and R. Pal, "The current landscape of the mesenchymal stromal cell secretome: a new paradigm for cell-free regeneration," *Cytotherapy*, vol. 18, no. 1, pp. 13–24, 2016.

Hindawi
Stem Cells International
Volume 2018, Article ID 4706943, 8 pages
https://doi.org/10.1155/2018/4706943

Research Article

GM1 Ganglioside Promotes Osteogenic Differentiation of Human Tendon Stem Cells

Sonia Bergante,[1] Pasquale Creo,[1] Marco Piccoli,[1] Andrea Ghiroldi,[1] Alessandra Menon,[1] Federica Cirillo,[1] Paola Rota,[1] Michelle M. Monasky,[2] Giuseppe Ciconte,[2] Carlo Pappone,[2] Pietro Randelli,[3,4] and Luigi Anastasia[1,4]

[1]*Laboratory of Stem Cells for Tissue Engineering, Scientific Institute for Research, Hospitalization, and Health Care (IRCCS) Policlinico San Donato, San Donato 20097, Italy*
[2]*Arrhythmology Department, Scientific Institute for Research, Hospitalization, and Health Care (IRCCS) Policlinico San Donato, San Donato Milanese, Italy*
[3]*Azienda Socio Sanitaria Territoriale Centro Specialistico Ortopedico Traumatologico Gaetano Pini-CTO, Milano 20122, Italy*
[4]*Department of Biomedical Sciences for Health (L.I.T.A.), Università degli Studi di Milano, Segrate 20090, Italy*

Correspondence should be addressed to Pietro Randelli; pietro.randelli@unimi.it and Luigi Anastasia; luigi.anastasia@unimi.it

Received 15 June 2018; Accepted 26 July 2018; Published 23 August 2018

Academic Editor: Salvatore Scacco

Copyright © 2018 Sonia Bergante et al. This is an open access article distributed under the Creative Commons Attribution License, which permits unrestricted use, distribution, and reproduction in any medium, provided the original work is properly cited.

Gangliosides, the sialic acid-conjugated glycosphingolipids present in the lipid rafts, have been recognized as important regulators of cell proliferation, migration, and apoptosis. Due to their peculiar localization in the cell membrane, they modulate the activity of several key cell receptors, and increasing evidence supports their involvement also in stem cell differentiation. In this context, herein we report the role played by the ganglioside GM1 in the osteogenic differentiation of human tendon stem cells (hTSCs). In particular, we found an increase of GM1 levels during osteogenesis that is instrumental for driving the process. In fact, supplementation of the ganglioside in the medium significantly increased the osteogenic differentiation capability of hTSCs. Mechanistically, we found that GM1 supplementation caused a reduction in the phosphorylation of the platelet-derived growth factor receptor-β (PDGFR-β), which is a known inhibitor of osteogenic commitment. These results were further corroborated by the observation that GM1 supplementation was able to revert the inhibitory effects on osteogenesis when the process was inhibited with exogenous PDGF.

1. Introduction

Injuries to the tendon-to-bone enthesis are common in the field of orthopedic medicine, and high failure rates are often associated with their repair [1]. The use of biologic adjuvants that promote tissue regeneration, such as growth factors, platelet-rich plasma, and stem cells, have shown great potential for improving healing rates and function after surgery [2]. Accordingly, the use of tendon stem cells to improve tendon-bone junction repair has been considered advantageous, as tendon stem cells already belong to the tendon environment and possess the plasticity to potentially recover the different tissues found in the tendon-to-bone enthesis [3]. Along these lines, we reported the first isolation of human tendon stem cells from the supraspinatus and long head of the biceps tendons, and we demonstrated that they can be induced to differentiate toward osteoblasts, adipocytes, and muscle cells [4]. Nonetheless, an open issue in the stem cell field is to perfect the differentiation strategies in order to drive the process toward a specific phenotype and to avoid undesired cell commitment or, even more detrimental, the uncontrolled proliferation of undifferentiated progenitor cells. In this context, herein we investigated the role of gangliosides, which are sialic acid-containing glycosphingolipids (GSLs) ubiquitously distributed in cell membranes [5], in the osteogenic differentiation of hTSCs. Numerous studies have confirmed that gangliosides and their expression levels are controlled during development [6] and are cell type-

specific [7], supporting the idea that these molecules are key players in cell commitment. While some biological roles of these lipids have been clearly recognized, as they have been shown to be involved in processes like cell proliferation [8], cell adhesion [9], apoptosis [10], and differentiation [11], less is known about their role in stem cell homeostasis and differentiation. Nonetheless, it has been shown that a reduction of ganglioside biosynthesis inhibits the neuronal differentiation of MSCs in the early stage of the process [12], and our group recently demonstrated that an increase of ganglioside GD1a is crucial for human bone marrow mesenchymal stem cell (MSC) differentiation [13]. Moreover, we demonstrated the pivotal role of sialidase NEU3 in regulating ganglioside GM3 content, which is a key in skeletal muscle cell differentiation and survival under hypoxia [14–17]. Clearly, as gangliosides are mainly distributed in the lipid rafts of cell plasma membranes, which are rich in key tyrosine kinase receptors, the present study further corroborates the notion that we are at the beginning of fully unveiling the role of these sphingolipids in stem cell biology.

2. Materials and Methods

2.1. Cell Isolation and Culture. Human tendon stem cells (hTSCs) were isolated from supraspinatus tendon specimens collected during arthroscopic rotator cuff repair, as previously reported [4]. The isolated hTSCs were cultured in minimal essential medium alpha modification (α-MEM) (Merck) supplemented with 2 mM L-glutamine (Euroclone), 1% antibiotic-antimycotic mixture (Euroclone), and 20% (v/v) fetal bovine serum (FBS) (HyClone, Thermo Fisher Scientific) at 37°C in a 5% CO_2 and 95% air-humidified atmosphere. The medium was changed every 2-3 days.

2.2. Osteogenic and Adipogenic Differentiation. hTSCs were seeded at a concentration of 3×10^4 cells/cm^2 in a growth medium, and after 24 hours, cells were switched to an osteogenic or adipogenic medium for 17 days or 21 days, respectively. Osteogenic differentiation was obtained by culturing cells in the presence of DMEM-low glucose (Merck) supplemented with 4 mM L-glutamine (Euroclone), 1% antibiotic-antimycotic mixture (Euroclone), 10% FBS (HyClone, Thermo Fisher Scientific), 10 nM cholecalciferol (Merck Millipore), and the mesenchymal stem cell osteogenesis kit (Merck Millipore) according to the manufacturer's instructions. Adipogenic differentiation was induced by culturing cells in the presence of DMEM-low glucose supplemented with 4 mM L-glutamine, 1% antibiotic-antimycotic mixture, 10% FBS, and the mesenchymal stem cell adipogenesis kit (Merck Millipore), according to the manufacturer's instructions. To evaluate the effects of ganglioside GM1 treatment (Santa Cruz Biotechnology) on differentiation, hTSCs were cultured for 17 days in an osteogenic medium or 21 days in adipogenic medium supplemented with 1, 10, 50, and 100 μM GM1. To evaluate the effects of the platelet-derived growth factor-BB (PDGF-BB, Thermo Fisher Scientific) on osteogenic differentiation, cells were cultured in an osteogenic medium containing PDGF-BB at the final concentration of 10 ng/ml. The differentiation medium was changed every 2-3 days.

2.3. Metabolic Radiolabeling of Cell Sphingolipids. The metabolic radiolabeling of cell sphingolipids was performed as previously described by Riboni et al. [18]. Briefly, [3-^{3}H]-sphingosine (D-erythro > 97%, 50 μCi, 1.85 MBq, PerkinElmer) was dissolved in DMEM-low glucose with 10% FBS to a final concentration of 2.4 nM sphingosine, corresponding to 110.000 dpm/ml radioactivity. The medium was added to the cells and incubated for 2 hours (pulse) at 37°C, then it was replaced with DMEM-low glucose with 10% FBS without [^{3}H]-sphingosine for 48 hours (chase). After the incubation, cells were harvested by cell scraping in phosphate-buffered saline (PBS). Cell suspensions were frozen and lyophilized.

2.4. Extraction and Chromatographic Separation of Radiolabeled Sphingolipids. Total lipid extraction was performed as previously described by Bergante et al. [13]. Briefly, lipids were first extracted with 20 : 10 : 1 (v/v) chloroform/methanol/water, dried under a nitrogen stream, and then a two-phase partitioning was carried out in chloroform/methanol 2 : 1 (v/v) and 20% (v/v) water. After partitioning, gangliosides of the aqueous phase were separated and analyzed by high-performance thin-layer chromatography (HPTLC), using as running solvent chloroform/methanol/0.2% aqueous $CaCl_2$ 60 : 40 : 9 ($v/v/v$) [19, 20]. Radiolabeled sphingolipids were visualized with a Beta-Imager 2000 (Biospace). The radioactivity associated with individual lipids was determined with β-Vision software (Biospace).

2.5. RNA Extraction and Real-Time PCR. Total RNA was isolated using TRIzol Reagent (Ambion, Life Technologies), and 1 μg of extracted RNA was reverse transcribed to cDNA using the iScript cDNA synthesis kit (Bio-Rad) according to the manufacturer's instructions. Real-time PCR was performed in a 96-well plate with 10 ng of cDNA as a template, 0.2 μM primers, and 2x Power SYBR Green PCR Master Mix (Promega) in 20 μL final volume per well, using a StepOnePlus Real-Time PCR System (Applied Biosystems). The following primers were used to amplify the corresponding target genes: human alkaline phosphatase (ALP) forward 5′-CGCACGGAACTCCTGACC-3′ and reverse 5′-GCCACCACCATCTCG-3′, peroxisome proliferator-activated receptor-γ (PPAR-γ) forward 5′-TTCCTTCACTGATACACTGTCTGC-3′ and reverse 5′-GGAGTGGGAGTGGTCTTCCATTAC-3′, lipoprotein lipase (LPL) forward 5′-AGAGAGAACCAGACTCCAATG-3′ and reverse 5′-GGCTCCAAGGCTGTATCC-3′, beta 1,3-galactosyltransferase (GM1 synthase) forward 5′-CGCCTTCCAGGACTCCTACC-3′ and reverse 5′-CCGTCTTGAGGACGTATCGG-3′, osteocalcin forward 5′-GCAGCGAGGTAGTGAAGAG-3′ and reverse 5′-GAAAGCCGATGTGGTCAGC-3′, and S14 (used as endogenous control in all real-time PCR experiments) forward 5′-GTGTGACTGGTGGGATGAAGG-3′ and reverse 5′-TTGATGTGTAGGGCGGTGATAC-3′.

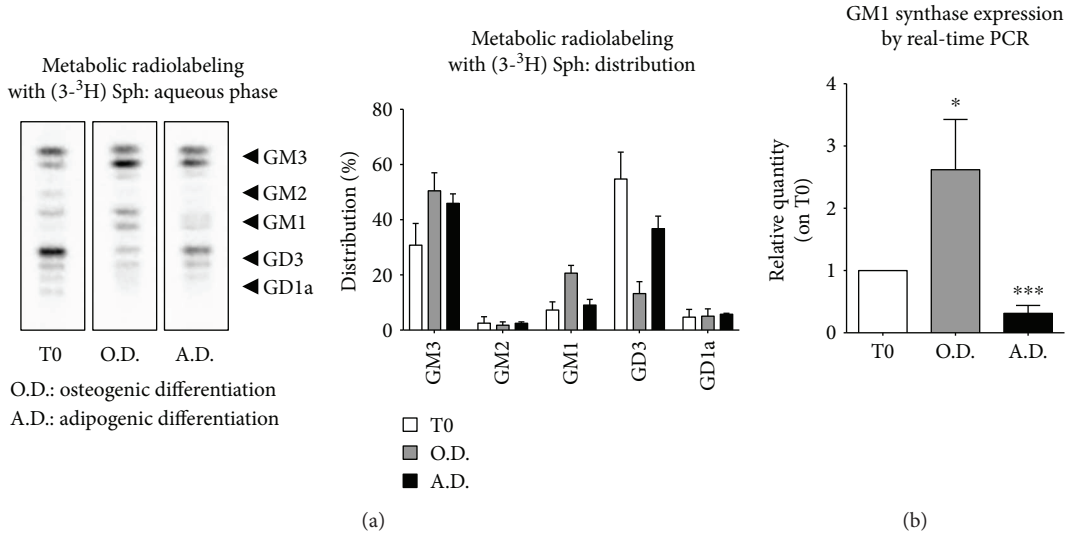

Figure 1: Ganglioside pattern upon differentiation of hTSCs to either osteoblasts or adipocytes. (a) Metabolic radiolabeled gangliosides separated by HPTLC and visualized with a Beta-Imager 2000 (Biospace). Doubled spots in cellular gangliosides correspond to the presence of species with different chain lengths of fatty acids. The graph on the right represents the percentage distribution of radiolabeled gangliosides. (b) Real-time PCR analysis of GM1 synthase gene expression in hTSCs differentiated toward osteoblasts (O.D.) or adipocytes (A.D.) as compared to that in undifferentiated cells (T0). Ribosomal protein S14 gene was used as housekeeper gene. All data are means ± SD of three different experiments. The statistical analysis was determined by Student's t-test. $^{*}p < 0.05$, $^{***}p < 0.001$.

2.6. Analysis of Mineralization. Matrix mineralization of hTSCs was evaluated at the 17th day of osteogenic differentiation using the osteogenesis assay kit (Merck Millipore). Briefly, cells were fixed with 4% paraformaldehyde at room temperature for 15 minutes. In order to detect mineral deposition in the extracellular matrix, cells were washed twice with PBS and incubated with alizarin red stain solution for 20 minutes. The dye was then extracted from the stained monolayer according to the manufacturer's instructions and quantified using a Victor 3 instrument (Perkin Elmer).

2.7. Immunoblotting. Cells were harvested in ice-cold PBS by cell scraping and centrifuged at 400 ×g for 10 minutes at 4°C. Cells were lysed in RIPA buffer (150 mM sodium chloride, 1% Triton X-100, 0.5% sodium deoxycholate, 0.1% sodium dodecyl sulphate, and 50 mM Tris pH 8) containing complete protease and phosphatase inhibitors (Merck). After cell lysis, the samples were centrifuged at 10,000 ×g for 15 minutes at 4°C. Protein amounts were measured using a Pierce BCA protein assay kit (Thermo Scientific). Proteins were loaded into a 10% SDS-PAGE gel, then transferred onto a nitrocellulose membrane (Trans-Blot, Bio-Rad Laboratories) by electroblotting. After blocking the membranes with 5% (*w*/*v*) of nonfat dry milk in Tris-buffered saline-Tween 0.1% (TBS-T) for 1 hour at room temperature, they were incubated overnight at 4°C with the following primary antibodies: rabbit phospho-PDGFR-β, 1 : 1000 dilution (Y751, Cell Signaling); rabbit PDGFR-β, 1 : 1000 dilution (Cell Signaling); and rabbit monoclonal early endosome antigen 1 (EEA1), 1 : 1000 dilution (Cell Signaling). The membranes were then washed in TBS-T three times and incubated for 1 hour at room temperature with specific secondary antibodies. In particular, phospho-PDGFR-β was incubated with the IRDye® 800CW goat anti-mouse IgG (LI-COR), the total PDGFR-β with the IRDye 680RD goat anti-rabbit IgG (Li-COR), and EEA1 with the HRP-conjugated anti-rabbit IgG (Amersham), diluted 1 : 5000 in 5% (*w*/*v*) nonfat dry milk in TBS-T. The membranes were analyzed by the Odyssey® FC imaging system (LI-COR), and the densitometric analysis was performed with the specific Image Studio™ software (LI-COR).

3. Results

3.1. Ganglioside Changes in hTSC Differentiation toward Osteoblasts and Adipocytes. To assess the ganglioside pattern distribution of hTSCs, cells were metabolically radiolabeled with the sphingolipid precursor [3-^{3}H]-sphingosine and quantitatively analyzed by HTPLC coupled with a radiochromatoscanner, as described in "Materials and Methods." The ganglioside distribution in proliferating hTSCs was as follows: GM3 (30.79% ± 7.85), GM2 (2.53% ± 2.33), GM1 (7.28% ± 2.94), GD3 (43.83% ± 19.35), and GD1a (4.71% ± 2.80), with GM3 and GD3 being the main gangliosides (Figure 1(a) and 1(b), T0).

Next, changes in ganglioside pattern were evaluated upon differentiation of hTSCs to either osteoblasts or adipocytes, as previously reported [4], by metabolic radiolabeling after 17 and 21 days of cell culturing in either osteogenic (O.D.) or adipogenic (A.D.) medium (Figure 1(a)). When hTSCs were differentiated toward osteoblasts, a 1.6- and 2.8-fold increase of GM3 and GM1 gangliosides was observed, respectively, as well as a 3.7-fold decrease of GD3, as compared to proliferating undifferentiated cells. When hTSCs were differentiated toward adipocytes, a 1.7-fold increase in GM3 and 1.5-fold decrease in GD3 relative distribution were observed, as compared to undifferentiated cells, while no significant changes in the relative quantity of GM1 could be observed (Figure 1(a)). To test whether the observed increase

of GM1 during osteogenesis was due to an upregulation of its biosynthesis, GM1 synthase expression was measured by real-time PCR, and a 2.6-fold increase could be observed at the end of the differentiation process, as compared to proliferating hTSCs. On the other hand, a 3.2-fold reduction of GM1 synthase expression was measured when hTSCs were induced to differentiate toward adipocytes (Figure 1(b)).

3.2. Effects of Exogenous GM1 on Osteogenic Differentiation of hTSCs. To test the role of GM1 increase during osteogenesis, exogenous 1, 10, 50, and 100 μM GM1 was supplemented in the osteogenic medium during the differentiation process. Osteogenic marker ALP gene expression was measured by real-time PCR after 17 days of differentiation and compared to undifferentiated cells (T0) and GM1-free osteogenic medium (O.D.). Results showed a significant 1.8- and 2.4-fold increase in ALP expression when cells were supplemented with 50 or 100 μM GM1 in addition to the osteogenic medium, respectively, as compared to O.D. (Figure 2(a)).

Afterward, cells were induced to differentiate to osteoblasts in the presence of 50 or 100 μM GM1 and were evaluated for their capacity to sustain the mineralization of the extracellular matrix using a standard alizarin red staining, as described in "Materials and Methods." Dye relative quantification showed an increase of red staining in hTSCs differentiated in the presence of GM1, which was significantly higher (1.7-fold) in 100 μM GM1-treated cells (Figure 2(b)). On the contrary, exogenous GM1 strongly inhibited the gene expression of the adipogenic markers LPL and PPAR-γ (Figures 2(c) and 2(d)).

3.3. Mechanism of GM1-Activated Osteogenesis. To test whether osteogenesis was activated by GM1 through the inhibition of PDGFR-β, hTSCs were induced to differentiate in the presence of the ganglioside and then subjected to PDGFR-β analysis by Western blot. Results revealed that GM1-treated cells showed a 40% decrease in PDGFR-β phosphorylation, measured as the pPDGFR/PDGFR ratio, as compared to untreated cells, supporting the hypothesis of a GM1-induced inhibition of PDGFR-β (Figure 3(a)). Furthermore, it was assessed whether exogenous GM1 was able to counteract PDGF-induced activation of PDGFR-β, which is known to inhibit osteogenesis [21]. To this purpose, hTSCs were induced to differentiate for 17 days in normal osteogenic medium in the presence of 10 ng/ml PDGF-BB, which caused a 43% decrease in ALP expression (Figure 3(b)) and a 40% decrease in osteocalcin expression by real-time PCR (Figure 3(c)). On the other hand, addition of 100 μM GM1 to the osteogenic medium containing 10 ng/ml PDGF-BB completely restored the differentiation capability of hTSCs, as ALP and osteocalcin expression levels were comparable to differentiated untreated controls (Figure 3(b) and 3(c)).

4. Discussion

In this work, we investigated the role of gangliosides in the osteogenic differentiation of adult human tendon stem cells that we isolated and characterized for the first time from human supraspinatus tendons [4]. The method used for ganglioside pattern analysis required an initial metabolic radiolabeling of cell sphingolipids by adding [3-^{3}H]-sphingosine in the culture medium that has been effectively used in our laboratories for many years [13–15]. As a result, cells synthesize radiolabeled sphingolipids that can be separated by HPTLC chromatography and accurately measured with a radiochromatoscanner. The use of metabolic radiolabeling significantly improves the sensitivity of the method, reducing the number of stem cells required for each analysis. Results demonstrated that the two main gangliosides of hTSCs, GM3 and GD3, increased and decreased, respectively, when cells were differentiated toward osteoblasts or adipocytes, suggesting that the modulation of these gangliosides is possibly linked to a general change of the biological status of the cell and not to the commitment toward a specific cell lineage. On the other hand, a marked increase of ganglioside GM1 was observed only during osteogenesis, supporting the possible role of this ganglioside in driving the process (Figure 1). The increase in GM1 content was accompanied by an increase of its synthase, which was instead reduced during adipogenesis (Figure 1). Interestingly, the addition of exogenous GM1 to the differentiation medium improved osteogenesis, as confirmed by a significant increase of ALP gene expression, which is a specific osteoblast marker, as well as by an increase of the extracellular matrix mineralization, as assessed by alizarin red staining (Figure 2). On the contrary, gene expression of the adipogenic markers PPAR-γ and LPL decreased upon GM1 supplementation to the adipogenic differentiation medium, supporting the idea that the ganglioside could inhibit the process (Figure 2). We then investigated the mechanism of GM1-induced increase of osteogenesis in hTSCs. Along this line, it has been reported that gangliosides can regulate the activity of the epidermal growth factor receptor [22], the fibroblast growth factor receptor [23], the nerve growth factor receptor (NGF) [24], the platelet-derived growth factor receptor (PDGFR) [25], and the insulin receptor (IR) [26]. In particular, it has been shown that GM1 is crucial in PDGFR regulation through different mechanisms of action that appear to be cell type-dependent. In this context, it has been demonstrated that, in fibroblasts, GM1 is able to inhibit the ligand-mediated phosphorylation of tyrosine residues of the cytoplasmic tail of the receptor [27], as well as the ligand-induced intracellular association of SH2-containing proteins with PDGFR in human glioma cells [28]. On the contrary, in Swiss-3T3 cells, it has been demonstrated that GM1-mediated inhibition of PDGFR requires the extracellular and/or the transmembrane domains of the receptor [29]. Moreover, in the same cell line, it has been shown that GM1 regulates PDGFR signaling by controlling the distribution of the receptor in- and outside of lipid rafts and that PAG regulates the membrane partitioning and the mitogenic signaling of PDGFR through an increase in GM1 levels in caveolae [30, 31]. PDGF/PDGFR signaling is reported to be involved in the regulation of various cell functions, including osteogenesis and adult stem cell differentiation toward osteoblasts. In particular, it has been observed that the downregulation of PDGRα promotes osteogenic differentiation of MSCs through the BMP/smad signaling pathway [32], and the blocking of the PDGFR-β

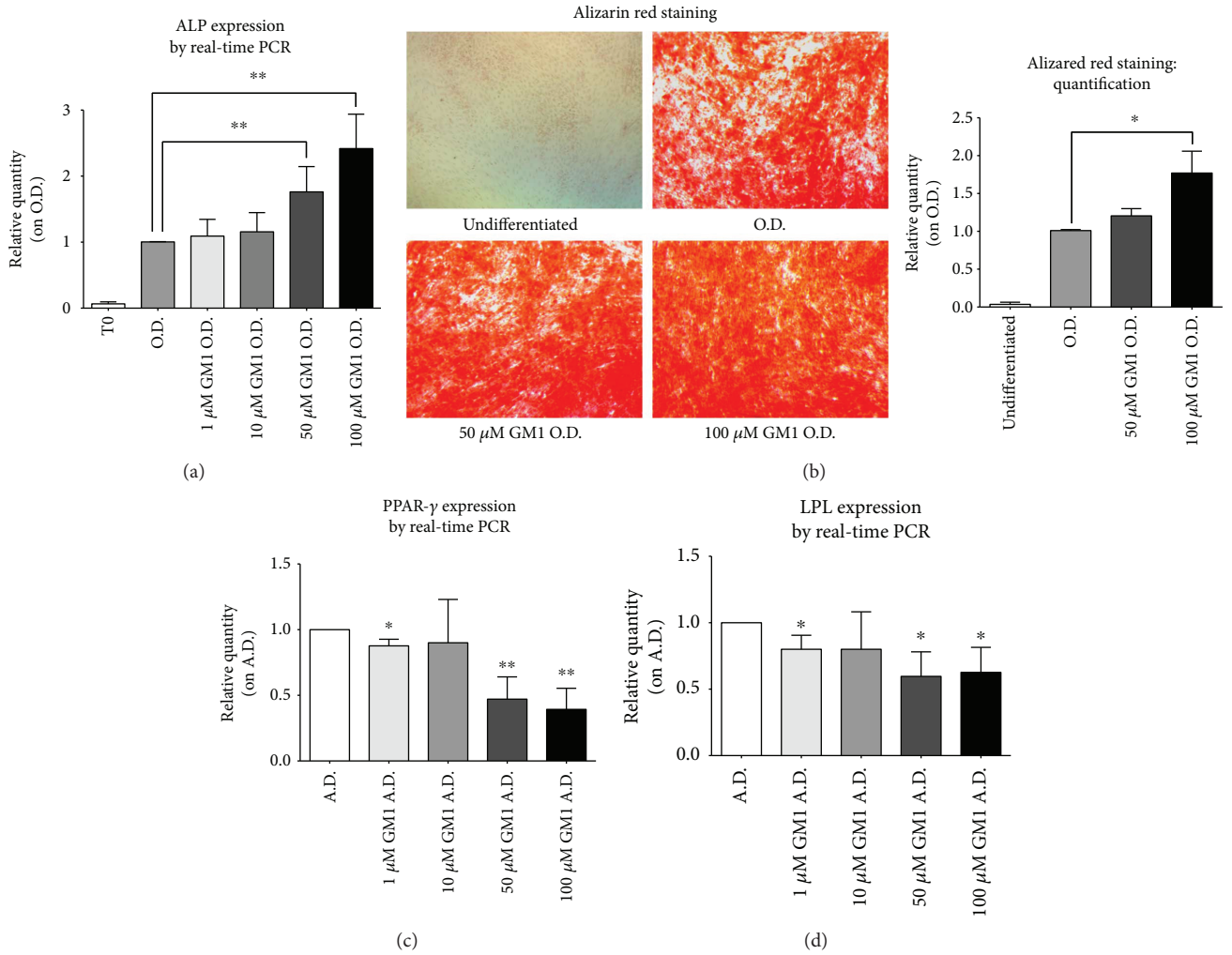

FIGURE 2: Evaluation of hTSC differentiation either to osteoblasts and adipocytes upon GM1 treatment. (a) Gene expression of the osteogenic marker ALP by real-time PCR. hTSCs were differentiated toward osteoblasts for 17 days in osteogenic medium supplemented with exogenous 1, 10, 50, and 100 μM GM1. The results were compared to hTSCs differentiated in GM1-free osteogenic medium (O.D.). Ribosomal protein S14 gene was used as endogenous control. (b) Analysis and quantification of calcium deposits in hTSCs after osteogenic differentiation by alizarin red staining. Undifferentiated hTSCs and hTSCs differentiated in the presence of 50 μM and 100 μM GM1 were compared to hTSCs differentiated in GM1-free osteogenic medium (O.D.) and considered as controls. (c, d) Gene expression analysis of adipogenic markers, PPAR-γ and LPL, by real-time PCR. hTSCs were differentiated toward adipocytes for 21 days in adipogenic medium supplemented with exogenous 1, 10, 50, and 100 μM GM1. The results were compared to hTSCs differentiated in GM1-free adipogenic medium (A.D.). Ribosomal protein S14 gene was used as endogenous control. All data are means ± SD of four different experiments. The statistical analysis was determined by Student's t-test. $^{*}p < 0.05$, $^{**}p < 0.01$.

pathway markedly promotes osteoblast differentiation and matrix mineralization in mouse osteoblastic MC3T3-E1 cells [33]. Moreover, PDGFR-β inhibition increases the osteogenic differentiation of primary rat osteoblastic cells [34] and human MSCs [21]. Altogether, these results support the hypothesis that GM1 could exert its effects on osteogenesis through the inhibition of the PDGF receptor also in hTSCs. To test this hypothesis, we assessed the activation levels of the PDGFR-β receptor during osteogenesis in the presence of exogenous GM1 in the culture medium. Indeed, we observed a significant decrease in the activation of the receptor when GM1 was added to the differentiation medium (Figure 3). To further confirm our hypothesis, we assessed whether GM1 was able to counteract the inhibition of osteogenesis caused by the activation of PDGFR-β upon addition of its ligand (PDGF-BB) in the differentiation medium. Results showed that PDGF-BB stimulation inhibited osteogenesis, as confirmed by a significant decrease of ALP and osteocalcin gene expression. As anticipated, the addition of GM1 to the osteogenic medium containing PDGF-BB completely restored the differentiation capabilities of hTSCs, as we could observe ALP and osteocalcin expression levels similar to untreated control cells (Figure 3).

5. Conclusions

In conclusion, our results show that ganglioside GM1 significantly increases during osteogenic differentiation of hTSCs. Most importantly, the ganglioside increase is instrumental for driving the process through the inhibition of PDGFR-β.

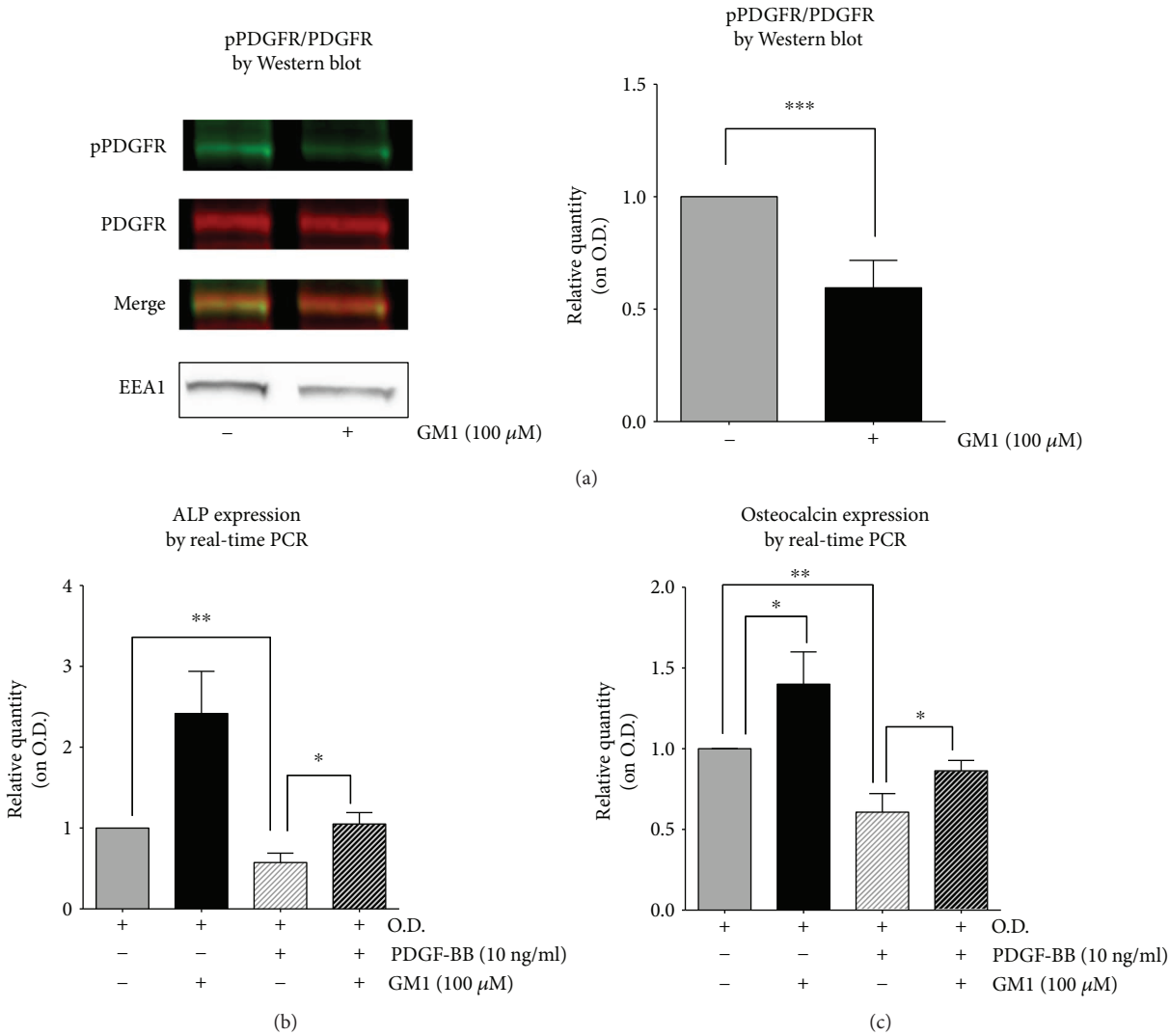

Figure 3: Effects of GM1 treatment on PDGFR activation. (a) Western blot analysis and quantification of PDGFR-β activation. hTSCs were differentiated toward osteoblasts in osteogenic medium supplemented with 100 μM GM1, as compared to hTSCs differentiated in GM1-free osteogenic medium (O.D.). Total proteins were extracted and analyzed with anti-phosphorylated-PDGFR-β (Tyr 751) antibody (green) and anti-PDGFR-β (28E1) antibody (red). EEA1 expression was used as internal control. Data are means ± SD of four different experiments. (b, c) Gene expression analysis of the osteogenic markers ALP and osteocalcin by real-time PCR. hTSCs were differentiated toward osteoblasts in osteogenic medium supplemented with 100 μM GM1 or 10 ng/ml PDGF-BB or with both 100 μM GM1 and 10 ng/ml PDGF-BB. The results were compared to hTSCs differentiated in free osteogenic medium (O.D.). Ribosomal protein S14 gene was used as housekeeper. All data are means ± SD of three different experiments. The statistical analysis was determined by Student's t-test. $^{*}p < 0.05$, $^{**}p < 0.01$, $^{***}p < 0.001$.

Indeed, the addition of exogenous GM1 to the differentiation medium greatly increased the osteogenic capabilities of hTSCs, supporting its possible use as a new factor to be added in the differentiation medium to improve this process. Further studies are ongoing in our laboratories to fully elucidate the mechanism of GM1 regulation of PDGFR-β activation and the possible therapeutic application of GM1 in regenerative medicine.

Data Availability

The data used to support the findings of this study are available from the corresponding author upon request.

Conflicts of Interest

The authors declare that there is no conflict of interest regarding the publication of this paper.

Acknowledgments

This work was partially supported by the "Line 2 Grants, Type B" from the Department of Biomedical Sciences for Health, University of Milan (Italy) and by the local research funds of the IRCCS Policlinico San Donato, a clinical research hospital partially funded by the Italian Ministry of Health.

References

[1] J. Apostolakos, T. J. Durant, C. R. Dwyer et al., "The enthesis: a review of the tendon-to-bone insertion," *Muscles, Ligaments and Tendons Journal*, vol. 4, no. 3, pp. 333–342, 2014.

[2] P. Randelli, F. Randelli, V. Ragone et al., "Regenerative medicine in rotator cuff injuries," *BioMed Research International*, vol. 2014, Article ID 129515, 9 pages, 2014.

[3] J. A. Cadby, E. Buehler, C. Godbout, P. R. van Weeren, and J. G. Snedeker, "Differences between the cell populations from the peritenon and the tendon core with regard to their potential implication in tendon repair," *PLoS One*, vol. 9, no. 3, article e92474, 2014.

[4] P. Randelli, E. Conforti, M. Piccoli et al., "Isolation and characterization of 2 new human rotator cuff and long head of biceps tendon cells possessing stem cell-like self-renewal and multipotential differentiation capacity," *The American Journal of Sports Medicine*, vol. 41, no. 7, pp. 1653–1664, 2013.

[5] P. H. Lopez and R. L. Schnaar, "Gangliosides in cell recognition and membrane protein regulation," *Current Opinion in Structural Biology*, vol. 19, no. 5, pp. 549–557, 2009.

[6] R. K. Yu, "Chapter 3 development regulation of ganglioside metabolism," *Progress in Brain Research*, vol. 101, pp. 31–44, 1994.

[7] J. Inokuchi, M. Nagafuku, I. Ohno, and A. Suzuki, "Heterogeneity of gangliosides among T cell subsets," *Cellular and Molecular Life Sciences*, vol. 70, no. 17, pp. 3067–3075, 2013.

[8] D. H. Kwak, S. Lee, S. J. Kim et al., "Ganglioside GM3 inhibits the high glucose- and TGF-β1-induced proliferation of rat glomerular mesangial cells," *Life Sciences*, vol. 77, no. 20, pp. 2540–2551, 2005.

[9] T. Kazarian, A. A. Jabbar, F. Q. Wen, D. A. Patel, and L. A. Valentino, "Gangliosides regulate tumor cell adhesion to collagen," *Clinical & Experimental Metastasis*, vol. 20, no. 4, pp. 311–319, 2003.

[10] F. Malisan and R. Testi, "GD3 in cellular ageing and apoptosis," *Experimental Gerontology*, vol. 37, no. 10-11, pp. 1273–1282, 2002.

[11] S. M. Kim, J. U. Jung, J. S. Ryu et al., "Effects of gangliosides on the differentiation of human mesenchymal stem cells into osteoblasts by modulating epidermal growth factor receptors," *Biochemical and Biophysical Research Communications*, vol. 371, no. 4, pp. 866–871, 2008.

[12] G. Moussavou, D. H. Kwak, M. U. Lim et al., "Role of gangliosides in the differentiation of human mesenchymal-derived stem cells into osteoblasts and neuronal cells," *BMB Reports*, vol. 46, no. 11, pp. 527–532, 2013.

[13] S. Bergante, E. Torretta, P. Creo et al., "Gangliosides as a potential new class of stem cell markers: the case of GD1a in human bone marrow mesenchymal stem cells," *Journal of Lipid Research*, vol. 55, no. 3, pp. 549–560, 2014.

[14] L. Anastasia, N. Papini, F. Colazzo et al., "NEU3 sialidase strictly modulates GM3 levels in skeletal myoblasts C2C12 thus favoring their differentiation and protecting them from apoptosis," *The Journal of Biological Chemistry*, vol. 283, no. 52, pp. 36265–36271, 2008.

[15] R. Scaringi, M. Piccoli, N. Papini et al., "NEU3 sialidase is activated under hypoxia and protects skeletal muscle cells from apoptosis through the activation of the epidermal growth factor receptor signaling pathway and the hypoxia-inducible factor (HIF)-1α," *The Journal of Biological Chemistry*, vol. 288, no. 5, pp. 3153–3162, 2013.

[16] N. Papini, L. Anastasia, C. Tringali et al., "MmNEU3 sialidase over-expression in C2C12 myoblasts delays differentiation and induces hypertrophic myotube formation," *Journal of Cellular Biochemistry*, vol. 113, no. 9, pp. 2967–2978, 2012.

[17] M. Piccoli, E. Conforti, A. Varrica et al., "NEU3 sialidase role in activating HIF-1α in response to chronic hypoxia in cyanotic congenital heart patients," *International Journal of Cardiology*, vol. 230, pp. 6–13, 2017.

[18] L. Riboni, P. Viani, and G. Tettamanti, "[51] Estimating sphingolipid metabolism and trafficking in cultured cells using radiolabeled compounds," *Methods in Enzymology*, vol. 311, pp. 656–682, 2000.

[19] N. Papini, L. Anastasia, C. Tringali et al., "The plasma membrane-associated sialidase MmNEU3 modifies the ganglioside pattern of adjacent cells supporting its involvement in cell-to-cell interactions," *The Journal of Biological Chemistry*, vol. 279, no. 17, pp. 16989–16995, 2004.

[20] R. K. Yu and T. Ariga, "Ganglioside analysis by high-performance thin-layer chromatography," *Methods in Enzymology*, vol. 312, pp. 115–134, 2000.

[21] F. Fierro, T. Illmer, D. Jing et al., "Inhibition of platelet-derived growth factor receptorβ by imatinib mesylate suppresses proliferation and alters differentiation of human mesenchymal stem cells *in vitro*," *Cell Proliferation*, vol. 40, no. 3, pp. 355–366, 2007.

[22] E. G. Bremer, J. Schlessinger, and S. Hakomori, "Ganglioside-mediated modulation of cell growth. Specific effects of GM3 on tyrosine phosphorylation of the epidermal growth factor receptor," *The Journal of Biological Chemistry*, vol. 261, no. 5, pp. 2434–2440, 1986.

[23] E. Meuillet, G. Cremel, D. Hicks, and H. Dreyfus, "Ganglioside effects on basic fibroblast and epidermal growth factor receptors in retinal glial cells," *Journal of Lipid Mediators and Cell Signalling*, vol. 14, no. 1-3, pp. 277–288, 1996.

[24] G. Ferrari, B. L. Anderson, R. M. Stephens, D. R. Kaplan, and L. A. Greene, "Prevention of apoptotic neuronal death by G_{M1} ganglioside. Involvement of Trk neurotrophin receptors," *The Journal of Biological Chemistry*, vol. 270, no. 7, pp. 3074–3080, 1995.

[25] J. Brooklyn, E. G. Bremer, and A. J. Yates, "Gangliosides inhibit platelet-derived growth factor-stimulated receptor dimerization in human glioma U-1242MG and Swiss 3T3 cells," *Journal of Neurochemistry*, vol. 61, no. 1, pp. 371–374, 1993.

[26] X. Q. Wang, S. Lee, H. Wilson et al., "Ganglioside GM3 depletion reverses impaired wound healing in diabetic mice by activating IGF-1 and insulin receptors," *The Journal of Investigative Dermatology*, vol. 134, no. 5, pp. 1446–1455, 2014.

[27] A. J. Yates, H. E. Saqr, and J. Van Brocklyn, "Ganglioside modulation of the PDGF receptor. A model for ganglioside functions," *Journal of Neuro-Oncology*, vol. 24, no. 1, pp. 65–73, 1995.

[28] T. Farooqui, T. Kelley, K. M. Coggeshall, A. A. Rampersaud, and A. J. Yates, "GM1 inhibits early signaling events mediated by PDGF receptor in cultured human glioma cells," *Anticancer Research*, vol. 19, no. 6B, pp. 5007–5013, 1999.

[29] J. L. Oblinger, C. L. Boardman, A. J. Yates, and R. W. Burry, "Domain-dependent modulation of PDGFRβ by ganglioside GM1," *Journal of Molecular Neuroscience*, vol. 20, no. 2, pp. 103–114, 2003.

[30] T. Mitsuda, K. Furukawa, S. Fukumoto, H. Miyazaki, T. Urano, and K. Furukawa, "Overexpression of ganglioside GM1 results in the dispersion of platelet-derived growth factor receptor from glycolipid-enriched microdomains and in the suppression of cell growth signals," *The Journal of Biological Chemistry*, vol. 277, no. 13, pp. 11239–11246, 2002.

[31] L. Veracini, V. Simon, V. Richard et al., "The Csk-binding protein PAG regulates PDGF-induced Src mitogenic signaling via GM1," *The Journal of Cell Biology*, vol. 182, no. 3, pp. 603–614, 2008.

[32] A. Li, X. Xia, J. Yeh et al., "PDGF-AA promotes osteogenic differentiation and migration of mesenchymal stem cell by down-regulating PDGFRα and derepressing BMP-Smad1/5/8 signaling," *PLoS One*, vol. 9, no. 12, article e113785, 2014.

[33] Y. Y. Zhang, Y. Z. Cui, J. Luan, X. Y. Zhou, G. L. Zhang, and J. X. Han, "Platelet-derived growth factor receptor kinase inhibitor AG-1295 promotes osteoblast differentiation in MC3T3-E1 cells via the Erk pathway," *Bioscience Trends*, vol. 6, no. 3, pp. 130–135, 2012.

[34] S. O'Sullivan, D. Naot, K. Callon et al., "Imatinib promotes osteoblast differentiation by inhibiting PDGFR signaling and inhibits osteoclastogenesis by both direct and stromal cell-dependent mechanisms," *Journal of Bone and Mineral Research*, vol. 22, no. 11, pp. 1679–1689, 2007.

Hindawi
Stem Cells International
Volume 2018, Article ID 3208285, 17 pages
https://doi.org/10.1155/2018/3208285

Review Article

In Vitro Weight-Loaded Cell Models for Understanding Mechanodependent Molecular Pathways Involved in Orthodontic Tooth Movement: A Systematic Review

Mila Janjic,[1] **Denitsa Docheva**,[2] **Olivera Trickovic Janjic**,[3] **Andrea Wichelhaus**,[1] **and Uwe Baumert**[1]

[1]*Department of Orthodontics and Dentofacial Orthopedics, University Hospital, LMU Munich, 80336 Munich, Germany*
[2]*Experimental Trauma Surgery, Department of Trauma Surgery, University Regensburg Medical Centre, 93053 Regensburg, Germany*
[3]*Department of Preventive and Pediatric Dentistry, Faculty of Medicine, University of Niš, 18000 Niš, Serbia*

Correspondence should be addressed to Uwe Baumert; uwe.baumert@med.uni-muenchen.de

Received 26 January 2018; Accepted 9 May 2018; Published 31 July 2018

Academic Editor: Andrea Ballini

Copyright © 2018 Mila Janjic et al. This is an open access article distributed under the Creative Commons Attribution License, which permits unrestricted use, distribution, and reproduction in any medium, provided the original work is properly cited.

Cells from the mesenchymal lineage in the dental area, including but not limited to PDL fibroblasts, osteoblasts, and dental stem cells, are exposed to mechanical stress in physiological (e.g., chewing) and nonphysiological/therapeutic (e.g., orthodontic tooth movement) situations. Close and complex interaction of these different cell types results in the physiological and nonphysiological adaptation of these tissues to mechanical stress. Currently, different *in vitro* loading models are used to investigate the effect of different types of mechanical loading on the stress adaptation of these cell types. We performed a systematic review according to the PRISMA guidelines to identify all studies in the field of dentistry with focus on mechanobiology using *in vitro* loading models applying uniaxial static compressive force. Only studies reporting on cells from the mesenchymal lineage were considered for inclusion. The results are summarized regarding gene expression in relation to force duration and magnitude, and the most significant signaling pathways they take part in are identified using protein-protein interaction networks.

1. Introduction

The aim of orthodontics is to move an abnormally positioned tooth through the application of a continuous force on its surface. This force stimulates bone remodelling in the surrounding tissue, namely, the periodontal ligament (PDL) and the alveolar bone, resulting in the bone removal in the direction of the tooth movement and bone apposition in the opposite direction (Figure 1). Thus, the underlying mechanism of orthodontic tooth movement (OTM) is the stimulation of bone remodelling by the application of an orthodontic force [1].

Histologically, the effects of orthodontic force on the tooth and its surrounding tissues are now well understood and the underlying stages in OTM are identified [2]. Human periodontal ligament cells (hPDLCs) and human osteoblasts (hOBs) are recognized as the cell types originating from the mesenchymal lineage, which play the most dominant role during OTM. Unlike hOBs, which represent well a characterized cell type, hPDLCs represent a mixed population of mostly fibroblast-like cells [3]. Among them, mesenchymal stem cells are of special importance as the source of progenitors responsible for the regeneration and remodulation of not only PDL itself but also alveolar bone [4].

In order to better understand morphological changes during OTM, it is important to elucidate molecular and cellular signaling mechanisms between and within these cell types. The complex *in vivo* structure of the tissues involved

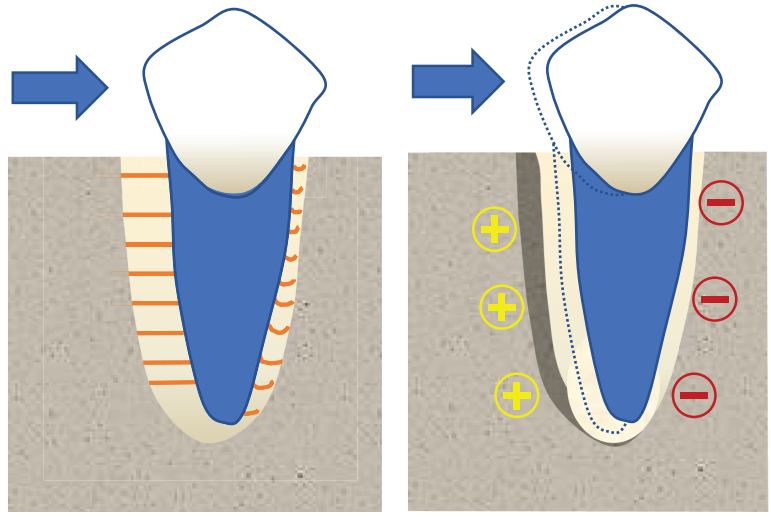

(a) (b)

Figure 1: Bone remodelling during orthodontic tooth movement. (a) Initial displacement of the tooth due to stretching of the fibres within the PDL on the tension side and compression on the opposite with the application of the orthodontic force. (b) Bone apposition on the tension side and resorption on the compression side as the result of the long-term force application.

makes it impossible to investigate force sensing and cellular communication of individual cells. Therefore, *in vitro* models using cells isolated from the PDL or from alveolar bone were established and different types of forces mimicking those found during OTM were applied [5]. These *in vitro* models are used to answer open questions including but not limited to how cells sense force, how they convert mechanical stress into molecular signals, and how these molecular signals influence the specific response of these cells to that specific force.

On the basis of the most commonly used approaches to apply mechanical stress on cells, present *in vitro* loading models can be classified into those using substrate deformation-based approaches, hydrostatic pressure approach, centrifugation approach, fluid flow approach, vibration approach, and weight approach [6]. Also, there has been increasing interest in moving from conventional monolayer, two-dimensional (2D) *in vitro* loading models to three-dimensional (3D) *in vitro* loading models.

Weight-based *in vitro* loading models have been successfully used over several years to investigate the effect of static, compressive, unidirectional force on the cells. In models using 2D cell cultures, cells are precultured in cell culture dishes (e.g., 6-well plates). After reaching the desired confluency, the cells are subjected to weight-based compression. In most cases, a glass slide is laid on top of the cell monolayer. Then, a weight is applied by positioning a glass cylinder filled with lead granules on top of this slide. The glass slide is used to secure even distribution of the force [7]. Increasing or reducing the number of granules in the glass cylinder adjusts the level of compressive force (Figure 2(a)). The same type of force is applied by slight modifications of this model: some authors used a stack of glass slides of different heights (e.g., [8]) or glass discs of different thicknesses (e.g., [9]) replacing the glass cylinder filled with lead granules. This *in vitro* loading model can also be used to apply static compressive force on 3D cell cultures. In this case, the same principle is used, except that the cells are embedded in a 3D matrix that is then compressed in the described manner (Figure 2(b)). Yang et al. [6] coined the term "weight approach"-based (WAB) for this *in vitro* model. To refer to this specific setup, we will also use WAB throughout this publication.

The primary aim of this review was to identify all articles related to the field of orthodontics using either a 2D or 3D WAB *in vitro* loading model and provide an overview of the details of their use: the most commonly used loading durations, force magnitudes, and scaffolds and their findings regarding gene expression and substance secretion in relation to force application. The secondary objective was to discover most commonly examined genes and to identify important pathways in OTM that most of the identified genes from these studies are involved in, focusing especially on hPDLCs.

2. Materials and Methods

To conduct this review, the "Preferred Reporting Items for Systematic Review and Meta-Analysis Protocols" (PRISMA-P) 2015 statement was consulted [10].

2.1. Defining the Eligibility Criteria. Inclusion criteria were as follows:

(i) Studies in the field of dentistry that examined the effect of mechanical stress on tooth surrounding tissues

(ii) Application of the 2D or 3D WAB *in vitro* loading model…

(iii) …on hPDLCs, hOBs, or all bone-like cell types/lines of human or animal origin

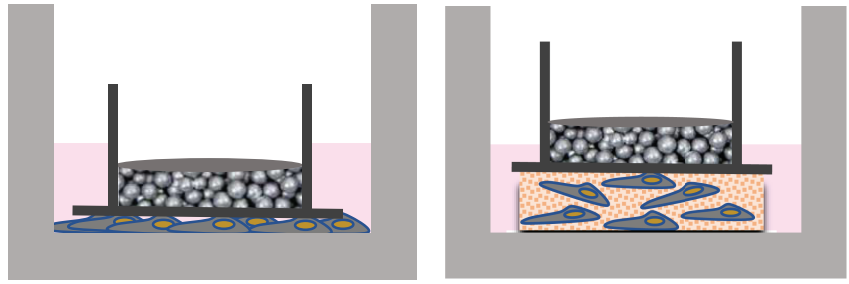

(a) (b)

Figure 2: Schematic illustration of the static 2D (a) and 3D (b) *in vitro* loading model based on the weight approach applied in the literature (details are found in the text).

(iv) Only studies written in English language, identified on the PubMed database until 01.12.2017, were taken into consideration

2.2. Literature Search and Study Selection Process. Separate search strategies were created for studies using either the 2D or the 3D *in vitro* setup for mechanical cell loading (Supplement 1). Searches were performed in the PubMed database following these predefined search strategies.

After identification of relevant studies in the PubMed database, the downloaded records from each search were imported into the bibliographic software EndNote X8 (Clarivate Analytics, Philadelphia, Pennsylvania, USA). All records were examined by two reviewers independently (MJ and UB), according to predefined inclusion and exclusion criteria (see above): first by title, then by abstract. If the abstract was not available, the full text of the report was obtained. Records that were obviously irrelevant were excluded, and the full texts of all remaining records were acquired. After the full-text assessment, the final list of included articles was generated. Any disagreements during this process were dissolved through discussion with another review author (DD) until reaching a consensus. The articles that did not meet all inclusion criteria after full-text assessment were excluded from further examination. Additional relevant studies were further identified through forward and backward reference chaining and hand-search of specific journals. Study quality assessment of the included studies was not performed, since the goal of this article was to provide an overview of all findings in the field only.

2.3. Data Extraction. The following information was extracted from each study obtained in full length: author, journal, year of publication, and used cell type. Force magnitude and duration, examined genes or substances, gene expression, or substance secretion details were recorded only if their response was directly connected to mechanical force stimulus. Gene symbols were used in the tables whenever possible. In case the identity or variant of a gene was doubtful or not clear primer sequences were examined using Primer-BLAST (URL: https://www.ncbi.nlm.nih.gov/tools/primer-blast/) [11]. If Western blot, ELISA, or inhibition experiments were reported, we tried to verify the antibodies and/or inhibitor specificity to determine the exact protein species (variant). Additionally, the method used for evaluation of the gene/substance expression was recorded. Data regarding the used scaffolds were collected for studies applying 3D WAB *in vitro* setups.

The following tables were prepared to summarize the findings: (1) studies applying the 2D WAB *in vitro* loading model on human primary cells from the orofacial region (i.e., hPDLCs, hOBs, and human oral bone marrow cells), (2) studies applying the 2D WAB *in vitro* loading model on human and nonhuman cells and cell lines not included in the first table, and (3) studies applying the 3D WAB *in vitro* loading model on human and nonhuman cells and cell lines.

2.4. STRING Analysis. The examined genes and metabolites using the 2D approach were summarized in two separate lists: one for hPDLFs and one for hOBs and other human bone-derived cell lines. Protein-protein interaction (PPI) networks were generated for both lists separately using the STRING database (10.5, URL: https://string-db.org/) [12]. From within STRING, the KEGG database [13] was queried to identify the main pathways involved. Only pathways with a false discovery rate below 1.00*E*−05 were considered.

3. Results

3.1. Study Selection Process. Figure 3 summarises the results of both 2D and 3D searches using a flow chart according to PRISMA. Separate searches were conducted for the studies applying either the 2D or 3D (Supplement 1) WAB *in vitro* loading models.

The search formula applied to identify 2D WAB *in vitro* loading studies is shown in Supplement 1. Altogether, 2284 abstracts were identified in the PubMed database (Figure 3).

Additionally, 7 articles were identified through forward and backward reference chaining and hand-search of specific journals. After reading the titles and abstracts of all identified studies, we excluded 2184. The remaining 107 articles were then checked by full-text reading. Fifty-six of them meet our inclusion criteria and were included for further analysis. The remaining did not meet the inclusion criteria. Reasons for their exclusion are listed in Supplement 1.

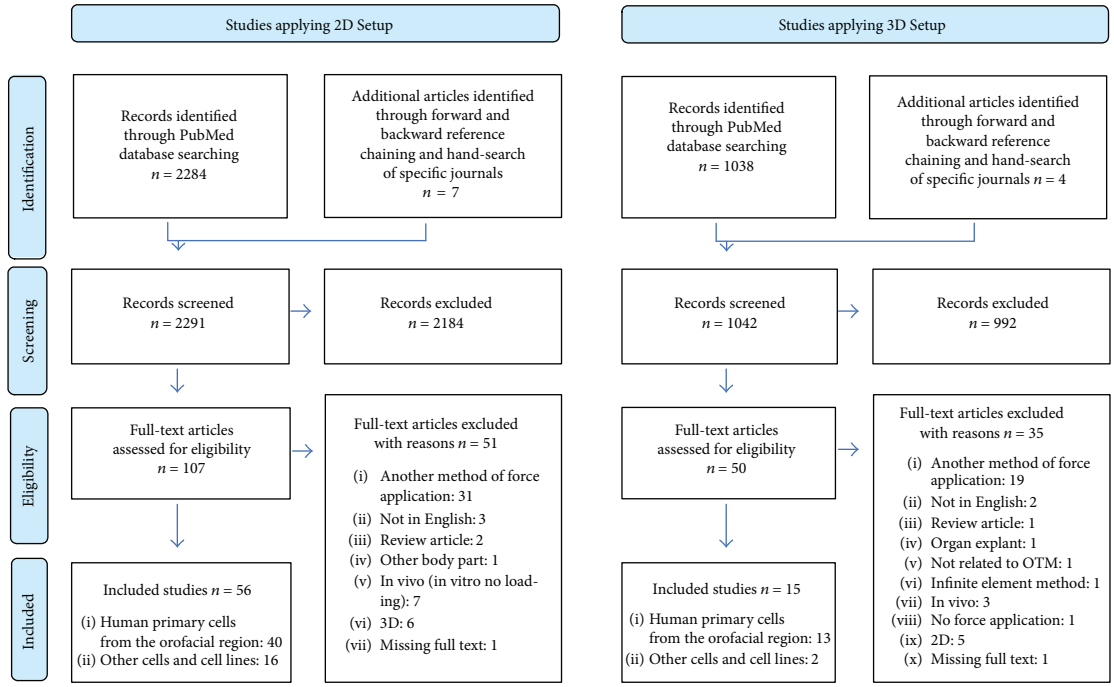

Figure 3: PRISMA flow diagram of the review process.

The search formula applied to identify 3D WAB *in vitro* loading studies is shown in Supplement 1. We identified a total of 1038 articles in PubMed (Figure 3). Additional 4 articles were discovered through forward and backward reference chaining and hand-search of specific journals. After initial screening, we excluded 992 articles and proceeded with full-text reading of the 50 articles. Finally, 17 of them meet our inclusion criteria. The remaining articles were excluded from further analysis. Reasons for their exclusion are summarized in Supplement 1.

All studies fulfilling the inclusion criteria were organised into three different supplementary tables: Supplement 2 summarises 2D WAB *in vitro* loading studies using human primary cells from the orofacial region. In Supplement 3, the two-dimensional WAB *in vitro* loading studies using human nonorofacial-derived cells and animal cells and cell lines are found. Supplement 4 summarises the 3D WAB *in vitro* loading studies.

3.2. Force Durations and Force Magnitudes Used in the Studies

3.2.1. 2D WAB In Vitro Loading Model. In these studies, compression forces ranging from 0.25 g/cm^2 to 5 g/cm^2 were applied on cells in 2D culture. The most commonly used compressive force was 2 g/cm^2, irrespectively which cell type was used in the study. In most of the studies, the force was applied for 24 h (Supplements 2 and 3).

3.2.2. 3D WAB In Vitro Loading Model. Force duration and magnitude depended on the scaffold used (Supplement 4). In most of the studies, scaffolds made from collagen gel and the polylactic-co-glycolic acid (PLGA) were applied. One of the studies [14] used a hydrophilically modified poly-L-lactide (PLLA) matrix. Collagen gel scaffolds were used with force magnitudes varying between 0.5 g/cm^2 and 9.5 g/cm^2; the most commonly used force was 6 g/cm^2. Force was applied for 0.5 to 72 h. Most commonly used force application periods were 12 and 24 h. Force levels between 5 and 35 g/cm^2 were applied to cells embedded in PLGA scaffolds. The most commonly applied force was 25 g/cm^2. The duration of force application was from 3 to 72 h. The study using the hydrophilically modulated PLLA matrix [14] applied force magnitudes from 5 to 35 g/cm^2. The duration of force application varied between one day and 14 days.

3.3. Cell Types Used in the Studies

3.3.1. 2D WAB In Vitro Loading Model. Forty of these studies used human primary cells isolated from the tooth surrounding tissues (Supplement 2): hPDLCs, hOBs, and human orofacial bone marrow-derived cells (hOBMC). The remaining studies used other cells and cell lines from human and animal sources: MG63, RAW264.7, ST-2, Saos-2, OCCM-30, MC3T3-E1, C2C12, U2OS, rat-derived PDLCs, or bone marrow-derived osteoblasts and the cementoblast cell line HCEM-SV40 (Supplement 3).

3.3.2. 3D WAB In Vitro Loading Model. hPDLCs and human gingival fibroblasts were used in 13 studies (Supplement 4). The remaining two studies used cell types and lines from the nonoral region or nonhuman origin (Supplement 4): the murine cell line MC3T3-E1 and murine osteoblasts.

Taken together, the most commonly used cells were hPDLCs. They were used in total 51 studies (2D: 38; 3D: 13) (Supplements 2 and 4). According to the isolation

method applied, we distinguished between the following sources: "explant method" [15, 16] (2D: 18; 3D: 4), "enzyme digestion method" [4] (2D: 9; 3D: 6), commercial sources (2D: 3; 3D: 1), or "no detailed information of isolation available" (2D: 8; 3D: 2).

3.4. Genes and Substances Examined in the Studies. A complete overview of genes and metabolites examined in 2D and 3D WAB studies and details of their expression can be found in Supplements 2 and 3 (2D) and Supplement 4 (3D).

In this review, special attention was paid to hPDLCs as the most examined cell type among studies and their prominent role in OTM. The most examined genes and metabolites in relation to hPDLCs were TNF superfamily member 11 (TNFSF11), TNF receptor superfamily member 11B (TNFRSF11B), prostaglandin-endoperoxide synthase 2 (PTGS2), and prostaglandin E_2 (PGE_2). In Table 1, details regarding their expression/secretion, including the information at which time points or force magnitudes the highest/lowest value was reached, is summarized.

3.5. STRING Analysis and KEGG Pathways

3.5.1. Construction of Protein-Protein Interaction (PPI) Network. In order to elucidate the molecular mechanisms of OTM and the role of the hPDLCs and bone cells in this process, we used STRING to construct PPI networks. Two separate gene lists were compiled from those studies using hPDLCs ("hPDLC list"; data from Supplement 3) and from those using hOBs or human bone-cells and cell lines ("hOB list"; data from Supplements 2 and 3). The hPDLC list contained 48 different genes (Figure 4(a)) and the hOB list 51 different genes (Figure 4(b)).

Two separate PPI networks were obtained, based on the interactions with a high level of confidence (>0.700) (Figure 4). Nodes in the networks represent the proteins produced by a single protein-coding gene locus; edges represent protein-protein interaction. Based on the colour of the edge, eight different interactions based on "gene neighbourhood," "gene fusion," "cooccurrence," "coexpression," "experiments," "databases," and "text mining" can be differentiated [12]. The top 10 nodes with the highest degree of connections from each of the two gene lists are also shown in Figure 4. PPI enrichment p values for each constructed network were calculated in STRING. These show that both PPI networks had significantly more interactions than expected and that the nodes are not random (PP enrichment p value $< 1.0E{-}16$).

3.5.2. Identification of KEGG Pathways. According to our STRING analysis, KEGG pathways relevant for OTM for each set of genes are listed in Table 2.

4. Discussion

In vivo bone remodelling during OTM represents a complex biological process, triggered by mechanical stimuli. OTM involves numerous events, spatially and temporary orchestrated and coordinated by different cell types, signaling factors, and networks [1]. Systematic breakdown and analysis of individual components of this complex process is the key for understanding its molecular background and a possible way to accelerate and improve it. Therefore, a variety of *in vitro* mechanical loading models have been established [5, 6]. The *in vitro* loading model based on the weight approach has been considered as the most appropriate loading model for the stimulation of the orthodontic force on the compressive site [6].

4.1. Characteristics of 2D and 3D WAB In Vitro Loading Models

4.1.1. Conventional 2D WAB. In vitro *loading model*, initially described by Kanai et al. [7], has been used for more than two decades for studying the compression-induced osteoclastogenesis and is still considered as the gold standard. It represents a simple and effective method for application of static compressive, unidirectional force to a cell monolayer.

The advantages of WAB *in vitro* loading model are the following:

(i) It reduces the need for animal studies, which are costly and time consuming.

(ii) It enables the analysis of specific cell types independently or in cocultures with other cells of interest.

(iii) Human primary cells can be used for better approximation to clinical situation.

From our point of view, the main disadvantage is its missing impact of the natural surrounding environment. There has been an increasing interest in the development of the 3D cell culture WAB *in vitro* loading model during the last years, in order to approximate the *in vitro* situation to the *in vivo* situation.

4.1.2. 3D WAB In Vitro Loading Model. During the last years, more studies have been using cells incorporated into biological scaffolds instead of monolayer cultures. This is due to the demand of mimicking an extracellular matrix, which is beneficial for cell behaviour, instead of growing cells on artificial plastic cell culture surface [46]. According to our data, three types of scaffolds have been used so far in combination with the 3D WAB *in vitro* loading model. The first identified studies used collagen I scaffolds [26, 47, 48]. Although the collagen gels are still widely used for this purpose, there is the increasing interest in the development of scaffolds composed of synthetic polymers. In 2011, Li et al. [33] introduced the PLGA scaffolds that had a higher stiffness in comparison to collagen gels and an elastic modulus very close to that of human PDL. The only disadvantage was that cells growing in PLGA displayed a disordered grow pattern that differs from the one in natural PDL [33]. Liao et al. [14] went one step further and introduced a hydrophilically modified PLLA matrix. This matrix displayed several advantages: higher nutrient and oxygen permeability and a better cell attachment, making it more suitable for long-term force application [14].

4.2. Force Magnitude Used in the Studies. According to Schwarz [49], optimal orthodontic force (OOF) in clinical

Table 1: Top four examined genes or substances in studies applying 2D or 3D *in vitro* WAB loading model on hPDLCs. For each gene or substance, cell culture type and literature reference are given. Additionally, examined force durations and magnitudes are summarized. Force effect on gene expression/substance secretion was evaluated (increase/decrease/no change). In all cases, the most prominent changes (increase/decrease) or "no change" are noted. For each change of expression/secretion, the corresponding maximum (increase/decrease) of force duration and magnitudes are additionally provided.

Gene symbol or metabolite	Cell culture	Reference	Examined force applied		Gene expression			Substance secretion		
			Duration (h)	Magnitude (g/cm^2)	Increase/decrease/no change	Change in relation to force duration (h)	Change in relation to force magnitude (g/cm^2)	Increase/decrease/no change	Change in relation to force duration (h)	Change in relation to force magnitude (g/cm^2)
PGE_2	2D	Benjakul et al. in press [17]	48	1.5	na			Increase (qPCR: GAPDH)	48	1.5
		Jin et al. 2015 [18]	0; 0.5; 3; 6; 12	2.0	na			Increase (ELISA)	12	2.0
		Kang et al. 2010 [19]	0.5; 2; 6; 24; 48	2.0	na			Increase (ELISA)	48	2.0
		Kanzaki et al. 2002 [20]	0.5; 1.5; 6; 24; 48 (+ELISA: 60)	0.5; 1.0; 2.0; 3.0; 4.0 (ELISA: 2.0)	na			Increase (ELISA)	60	2.0
		Kirschneck et al. 2015 [21]	24	2.0	na			Not explicitly stated (ELISA)		
		Liu et al. 2006 [22]	48	2.0	na			Increase (ELISA)	48	2.0
		Mayahara et al. 2007 [23]	3; 6; 12; 24; 48	2	na			Increase (ELISA)	48	2
		Premaraj et al. 2013 [24]	0.5; 1; 3; 6	5.0	na			Increase (ELISA)	1	5.0
		Proff et al. 2014 [9]	24	2	na			Increase (ELISA)	24	2
		Römer et al. 2013 [25]	24	2	na			Increase (ELISA)	24	2
	3D (Coll. gel)	de Araujo et al. 2007 [26]	3; 12; 24; 48; 72	6.0				Increase (EIA)	72	6.0
	3D (PLGA)	Li et al. 2016 [27]	6; 24; 72	5.0; 15.0; 25.0	na			Increase (ELISA)	24	15.0…25.0
		Yi et al. 2016 [28]	24	25.0				Increase (ELISA)	24	25.0
PTGS2	2D	Jin et al. 2015 [18]	0; 0.5; 3; 6; 12	2.0	Increase (qPCR: GAPDH)	12	2.0			
		Kang et al. 2010 [19]	0.5; 2; 6; 24; 48	2.0	Increase (qPCR: GAPDH)	48				
		Kanzaki et al. 2002 [20]	0.5; 1.5; 6; 24; 48	0.5; 1.0; 2.0; 3.0; 4.0	Increase (sqPCR: ACTNB)	6	2.0			
		Kirschneck et al. 2015 [21]	24	2.0	Increase (qPCR: POL2RA)	24	2.0			
		Liu et al. 2006 [22]	48	2.0	Increase (sqPCR: ACTNB)	48	2.0			
		Mayahara et al. 2007 [23]	3; 6; 12; 24; 48	2	Increase (qPCR: GAPDH)	48	2			
		Mayahara et al. 2010 [29]	3; 6; 12; 24; 48	2.0	Increase (qPCR: GAPDH)	48	2			
		Premaraj et al. 2013 [24]	6	0.2; 2.2; 5.0	nd			Increase (WB)	6	5.0
		Proff et al. 2014 [9]	24	2	Increase (qPCR: POL2RA)	24	2	Increase (WB)	24	2
		Römer et al. 2013 [25]	24	2	Increase (qPCR: POL2RA)	24	2			
		Wongkhantee et al. 2007 [30]	24	0; 1.25; 2.5	Increase (sqPCR: GAPDH)	24	2.5			
	3D (Coll. gel)	de Araujo et al. 2007 [26]	1; 3; 6; 12; 24; 48; 72	3.6; 6.0; 7.1; 9.5	Increase (sqPCR: GAPDH)	6	7.1			

Table 1: Continued.

Gene symbol or metabolite	Cell culture	Reference	Examined force applied		Gene expression			Substance secretion		
			Duration (h)	Magnitude (g/cm^2)	Increase/decrease/no change	Change in relation to force duration (h)	Change in relation to force magnitude (g/cm^2)	Increase/decrease/no change	Change in relation to force duration (h)	Change in relation to force magnitude (g/cm^2)
	3D (PLGA)	Li et al. 2016 [31]	6; 24; 72	25.0	Increase (qPCR: GAPDH)	6	25.0			
		Li et al. 2013 [32]	6; 24; 72	25.0	Increase (qPCR: GAPDH)	6	25.0			
		Li et al. 2016 [27]	6; 24; 72	5.0; 15.0; 25.0	Increase (qPCR: GAPDH)	6	25.0			
		Li et al. 2011 [33]	6	5; 15; 25; 35	Increase (qPCR: GAPDH)	6	35.0			
		Yi et al. 2016 [28]	24	25.0	Increase (qPCR: GAPDH)	24	25.0	Increase (WB)	24	25.0
TNFRSF11B	2D	Benjakul et al. in press [17]	48	1.5	No change (qPCR: GAPDH)			No change		
		Jin et al. 2015 [18]	0; 0.5; 3; 6; 12	2.0	No change (qPCR: GAPDH)					
		Kanzaki et al. 2002 [20]	0.5; 1.5; 6; 24; 48	0.5; 1.0; 2.0; 3.0; 4.0	No change (sqPCR: ACTNB)					
		Kim et al. 2013 [8]	0.5; 2; 6; 24; 48	2.0	Transitory downregulated. (qPCR: GAPDH)	6	2.0	Transitory downregulation (ELISA)	6	2.0
		Kirschneck et al. 2015 [21]	24	2.0	No change (qPCR: POL2RA)					
		Lee et al. 2015 [34]	0; 2; 4; 8; 24; 48	2.5	No change (qPCR: ACTNB)					
		Liu et al. 2017 [35]	6; 12; 24	0.5; 1.0; 1.5	nd			Decrease (WB)	n. g.	1.5
		Luckprom et al. 2011 [36]	2; 4	2.5	No change (sqPCR: GAPDH)					
		Mitsuhashi et al. 2011 [37]	1; 3; 6; 9; 12; 24	4.0	No change (qPCR: ACTNB)					
		Nakajima et al. 2008 [38]	0; 1; 3; 6; 9; 12; 24	0.5; 1.0; 2.0; 3.0; 4.0	nd			Increase (ELISA)	24	0.5
		Nishijima et al. 2006 [39]	48	0; 0.5; 1.0; 2.0; 3.0	nd			Decrease (ELISA)	48	2.0
		Römer et al. 2013 [25]	24	2	No change (qPCR: RNA-polymerase-2-polypeptide A)					
		Yamada et al. 2013 [40]	12	4.0	Decrease (qPCR: GAPDH)	12	4.0	Decrease (ELISA)	12	4.0
		Yamaguchi et al. 2006 [41]	0; 3; 6; 9; 12; 24; 48	0.5; 1.0; 2.0; 3.0	n. d.			Decrease (ELISA)	12…48	2.0
	3D (Coll. gel)	Kaku et al. 2016 [42]	12; 24	0.5; 1.0; 2.0	Increase (qPCR: GAPDH)	12	1.0			
	3D (PLLA modif.)	Liao et al. 2016 [14]	1 d; 3 d; 7 d; 14 d	5.0; 15.0; 25.0; 35.0	No change (qPCR: GAPDH)					

Table 1: Continued.

Gene symbol or metabolite	Cell culture	Reference	Examined force applied		Gene expression		Substance secretion		
			Duration (h)	Magnitude (g/cm^2)	Increase/decrease/no change	Change in relation to force duration (h)	Change in relation to force magnitude (g/cm^2)	Increase/decrease/no change	Change in relation to force duration (h)	Change in relation to force magnitude (g/cm^2)
	3D (PLGA)	Jianru et al. 2015 [43]	3; 6; 12 (WB: 12)	25.0	Decrease followed by increase (qPCR: GAPDH)	3 (decrease) 12 (increase)	25.0	Increase (WB)	12	25.0
		Li et al. 2016 [31]	6; 24; 72	25.0	Decrease followed by Increase (qPCR: GAPDH)	6 (decrease) 72 (increase)	25.0			
		Li et al. 2016 [27]	6; 24; 72	5.0; 15.0; 25.0	Decrease followed by increase (qPCR: GAPDH)	6 (decrease) 72 (increase)	15.0 (decrease) 25.0 (increase)	Decrease followed by Increase (qPCR: GAPDH)	6 (decrease) 72 (increase)	25.0 (decrease) 25.0 (increase)
		Li et al. 2011 [33]	6; 24; 72	25	Decrease followed by increase (qPCR: GAPDH)	6 (decrease) 72 (increase)	25.0			
		Yi et al. 2016 [28]	24	25.0	Decrease (qPCR: GAPDH)	24	25.0	No change (WB)		
TNFSF11	2D	Benjakul et al. in press [17]	48	1.5	Increase (qPCR: GAPDH)	48	1.5	Increase (qPCR: GAPDH)	48	1.5
		Jin et al. 2015 [18]	0; 0.5; 3; 6; 12	2.0	Increase (qPCR: GAPDH)	12	2.0			
		Kang et al. 2013 [44]	2; 48	2.0	Increase (qPCR: GAPDH)	48	2.0			
		Kanzaki et al. 2002 [20]	0.5; 1.5; 6; 24; 48	0.5; 1.0; 2.0; 3.0; 4.0	Increase (sqPCR: ACTNB)	48	2.0	Increase (WB): 40-kDa+ 55-kDa	48	2.0
		Kikuta et al. 2015 [45]	1; 3; 6; 9; 12; 24 (+ELISA: 48)	4.0	Increase (qPCR: GAPDH)	12	4.0	Increase (ELISA)	24	4.0
		Kim et al. 2013 [8]	0.5; 2; 6; 24; 48	2.0 ++	Increase (qPCR: GAPDH)	24	2.0	Increase (ELISA)	48	2.0
		Kirschneck et al. 2015 [21]	24	2.0	Increase (qPCR: POL2RA)	24	2.0			
		Lee et al. 2015 [34]	0; 2; 4; 8; 24; 48	2.5	Increase (qPCR: ACTNB)	24	2.5			
		Liu et al. 2017 [35]	6, 12, 24	0.5; 1.0; 1.5	nd			Increase (WB: GAPDH)	ng	1.5
		Liu et al. 2006 [22]	48	2.0	Increase (sqPCR: ACTNB)	48	2.0			
		Luckprom et al. 2011 [36]	2; 4	2.5	Increase (sqPCR: GAPDH)	2	2.5	Increase (WB)	4	2.5
		Mitsuhashi et al. 2011 [37]	1; 3; 6; 9; 12; 24	4.0	Temporary increase (qPCR: ACTNB)	6…9	4.0			
		Nakajima et al. 2008 [38]	0; 1; 3; 6; 9; 12; 24	0.5; 1.0; 2.0; 3.0; 4.0	nd			Increase (ELISA)	24	4.0
		Nishijima et al. 2006 [39]	48	0; 0.5; 1.0; 2.0; 3.0	nd			Increase (ELISA)	12…48	2.0
		Römer et al. 2013 [25]	24	2	Increase (qPCR: RNA-polymerase-2-polypeptide A)	24	2			

Table 1: Continued.

Gene symbol or metabolite	Cell culture	Reference	Examined force applied		Gene expression			Substance secretion		
			Duration (h)	Magnitude (g/cm^2)	Increase/decrease/no change	Change in relation to force duration (h)	Change in relation to force magnitude (g/cm^2)	Increase/decrease/no change	Change in relation to force duration (h)	Change in relation to force magnitude (g/cm^2)
		Wongkhantee et al. 2007 [30]	24	0; 1.25; 2.5	Increase (sqPCR: GAPDH)	24	2.5	Increase (WB; ACTNB)	24	2.5
		Yamada et al. 2013 [40]	12	4.0	Increase (qPCR: GAPDH)	12	4.0	Increase (ELISA)	12	4.0
		Yamaguchi et al. 2006 [41]	0; 3; 6; 9; 12; 24; 48	0.5; 1.0; 2.0; 3.0	nd			Increase (ELISA): sRANKL Increase (WB)	12…48 12	2.0 2.0
	3D (Coll. gel)	Kang et al. 2013 [44]	2; 48	2.0	Increase (qPCR: GAPDH)	2	2.0			
	3D (PLLA modif.)	Liao et al. 2016 [14]	1 d; 3 d; 7 d; 14 d	5.0; 15.0; 25.0; 35.0	Increase (qPCR: GAPDH)	Day 14	35.0			
		Jianru et al. 2015 [43]	3; 6; 12 (WB: 12)	25.0	Increase (qPCR: GAPDH)	6	25.0	Increase (WB)	12	25.0
		Li et al. 2016 [31]	6; 24; 72	25.0	Increase (qPCR: GAPDH)	6	25.0			
		Li et al. 2016 [27]	6; 24; 72	5.0; 15.0; 25.0	Increase (qPCR: GAPDH)	6	25.0	Decrease (ELISA)	72	25.0
	3D (PLGA)	Li et al. 2011 [33]	6; 24; 72	5; 15; 25; 35	Increase (qPCR: GAPDH) Increase followed by no change (qPCR: GAPDH)	6 6 (increase) 72 (no change)	25…35.0 25 25			
		Yi et al. 2016 [28]	24	25.0	Increase (qPCR: GAPDH)	24	25.0	Increase (WB)	24	25.0

2D: two-dimensional cell culture; 3D (Coll. gel): three-dimensional cell culture, collagen gel; 3D (PLGA): three-dimensional cell culture using PLGA scaffolds; 3D (PLLA modif.): three-dimensional cell culture, hydrophilically modified PLLA scaffolds; qPCR: quantitative polymerase chain reaction (e.g., real-time PCR); sqPCR: semiquantitative polymerase chain reaction, followed by reference gene used; nr: not reported; na: not applicable; ELISA: enzyme-linked immune absorbent assay; WB: Western blot; IF: immunofluorescence; FLM: fluorescence microscopy; EIA: enzyme immunoassay.

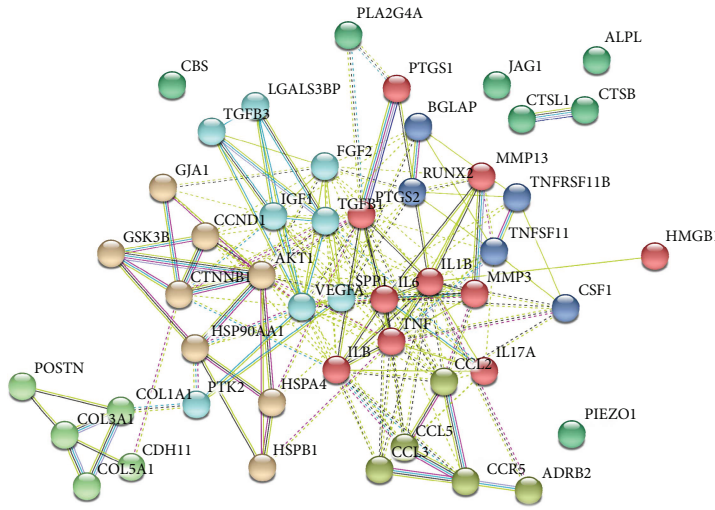

hPDLC list:

ADRB2, AKT1, ALPL, BGLAP, CBS, CCL2, CCL3, CCL5, CCND1, CCR5, CDH11, COL1A1, COL3A1, COL5A1, CSF1, CTNNB1, CTSB, CTSL, CXCL8, FGF2, GJA1, GSK3B, HMGB1, HSP90AA1, HSPA4, HSPB1, IGF1, IL17A, IL1B, IL6, JAG1, LGALS3BP, MMP13, MMP3, PIEZO1, PLA2G4A, POSTN, PTGS1, PTGS2, PTK2, RUNX2, SPP1, TGFB1, TGFB3, TNF, TNFRSF11B, TNFSF11, VEGFA

Gene	Number of interactions
VEGFA	24
IL6	23
IL1B	21
TNF	18
AKT1	18
TGFB1	18
CXCL8 (IL8)	17
IGF1	17
FGF2	16
PTGS2	15

(a)

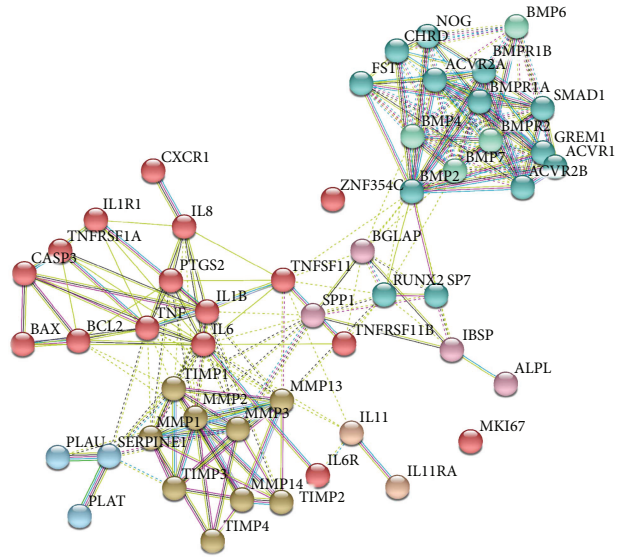

hOB list:

ACVR1, ACVR2A, ACVR2B, ALPL, BAX, BCL2, BGLAP, BMP2, BMP4, BMP6, BMP7, BMPR1A, BMPR1B, BMPR2, Casp3, CHRD, CXCR1, FST, GREM1, IBSP, IL11, IL11RA, IL1B, IL1R1, IL6, IL6R, IL8, MKI67, MMP1, MMP13, MMP14, MMP2, MMP3, NOG, PLAT, PLAU, PTGS2, RUNX2, SERPINE1, SMAD1, SP7, SPP1, TIMP1, TIMP2, TIMP3, TIMP4, TNF, TNFRSF11B, TNFRSF1A, TNFSF11, ZNF354C

Gene	Number of interactions
IL6	22
BMP2	19
TNF	16
BMP4	15
BMP7	15
IL1B	15
MMP2	15
BMPR1A	14
BMPR1B	14
BMPR2	14

(b)

Figure 4: Protein-protein interaction networks for the (a) "hPDLC list" and the (b) "hOB list". The gene lists are shown in the lower left part of each subfigure. Those genes with the highest number of interactions ("top 10") are given in tables in the lower right part of each subfigure.

Table 2: KEGG pathways relevant for OTM with false discovery rates below $1.00E-05$ derived from STRING analysis using the set of examined genes from human periodontal ligament cells ("hPDLC list"; top panel) and human bone and bone-related cells and cell lines ("hOB list"; bottom panel). "X", gene involved in that specific pathway.

(a)

KEGG ID	4060	4668	4510	4620	4370	4062	4380	4010	4064
KEGG name	Cytokine-cytokine receptor interaction	TNF signaling pathway	Focal adhesion	Toll-like receptor signaling pathway	VEGF signaling pathway	Chemokine signaling pathway	Osteoclast differentiation	MAPK signaling pathway	NF-kappa B signaling pathway
False discovery rate	2.62*E*–15	2.06*E*–12	3.90*E*–11	2.04*E*–09	9.47*E*–08	1.33*E*–07	2.29*E*–07	1.42*E*–06	1.86*E*–05
ADRB2									
AKT1		X	X	X	X	X	X	X	
ALPL									
BGLAP									
CBS									
CCL2	X	X				X			
CCL3	X			X		X			
CCL5	X	X		X		X			
CCND1			X						
CCR5	X					X			
CDH11									
COL1A1			X						
COL3A1			X						
COL5A1			X						
CSF1	X	X					X		
CTNNB1			X						
CTSB									
CTSL									
CXCL8 (= IL8)	X			X		X			X
FGF2								X	
GJA1									
GSK3b			X			X			
HMGB1									
HSP90AA1									
HSPA4									
HSPB1					X			X	
IGF1			X						
IL17A	X								
IL1B	X	X		X			X	X	X
IL6	X	X		X					
JAG1		X							
LGALS3BP									
MMP13									
MMP3		X							
PIEZO1									
PLA2G4A					X			X	
POSTN									
PTGS1									
PTGS2		X			X				X

Table 2: Continued.

KEGG ID	4060	4668	4510	4620	4370	4062	4380	4010	4064
KEGG name	Cytokine-cytokine receptor interaction	TNF signaling pathway	Focal adhesion	Toll-like receptor signaling pathway	VEGF signaling pathway	Chemokine signaling pathway	Osteoclast differentiation	MAPK signaling pathway	NF-kappa B signaling pathway
False discovery rate	2.62*E*–15	2.06*E*–12	3.90*E*–11	2.04*E*–09	9.47*E*–08	1.33*E*–07	2.29*E*–07	1.42*E*–06	1.86*E*–05
PTK2			X		X	X			
RUNX2									
SPP1			X	X					
TGFB1	X							X	
TGFB3	X						X	X	
TNF	X	X		X			X	X	X
TNFRSF11B	X						X		
TNFSF11	X						X		X
VEGFA	X		X		X				

(b)

KEGG ID	4350	4060	4064	4390	4668	4210	4380	4620	4066
KEGG name	TGF-beta signaling pathway	Cytokine-cytokine receptor interaction	NF-kappa B signaling pathway	Hippo signaling pathway	TNF signaling pathway	Apoptosis	Osteoclast differentiation	Toll-like receptor signaling pathway	HIF-1 signaling pathway
False discovery rate	8.33*E*–23	2.37*E*–21	8.32*E*–11	5.07*E*–09	1.01*E*–08	6.26*E*–08	1.02*E*–05	6.79*E*–05	7.16*E*–05
ACVR1	X	X							
ACVR2A	X	X							
ACVR2B	X	X							
ALPL									
BAX						X			
BCL2			X			X			X
BGLAP									
BMP2	X	X		X					
BMP4	X			X					
BMP6	X			X					
BMP7	X	X		X					
BMPR1A	X	X		X					
BMPR1B	X	X		X					
BMPR2	X	X		X					
Casp3					X	X			
CHRD	X								
CXCR1		X							
FST	X								
GREM1									
IBSP									
IL11		X							
IL11RA									
IL1b		X	X		X	X	X	X	
IL1r1		X	X		X	X			

Table 2: Continued.

KEGG ID	4350	4060	4064	4390	4668	4210	4380	4620	4066
KEGG name	TGF-beta signaling pathway	Cytokine-cytokine receptor interaction	NF-kappa B signaling pathway	Hippo signaling pathway	TNF signaling pathway	Apoptosis	Osteoclast differentiation	Toll-like receptor signaling pathway	HIF-1 signaling pathway
False discovery rate	8.33*E*–23	2.37*E*–21	8.32*E*–11	5.07*E*–09	1.01*E*–08	6.26*E*–08	1.02*E*–05	6.79*E*–05	7.16*E*–05
IL6		X					X	X	X
IL6R		X							X
IL8		X	X				X	X	
MKI67									
MMP1									
MMP13									
MMP14									
MMP2									
MMP3									
NOG	X								
PLAT									
PLAU			X						
PTGS2			X						
RUNX2									
SERPINE1				X					X
SMAD1	X			X					
SP7									
SPP1							X	X	
TIMP1									X
TIMP2									
TIMP3									
TIMP4									
TNF	X	X	X		X	X	X	X	
TNFRSF11B		X							
TNFRSF1A		X	X		X	X			
TNFSF11		X	X						
ZNF354C									

orthodontics should be equal to capillary blood vessel pressure (≈25 g/cm^2) [49]. On a tissue level, OOF should enable the desired clinical outcome without causing the unwanted side effects, for example, root resorption. On the cellular level, it should evoke best biologic cellular response without inhibiting the cell proliferation significantly [27]. Optimal orthodontic force *in vitro* varies between different models. Estimation of OOF for each *in vitro* model is of crucial importance for their successful application in OTM simulation [20, 33].

In 2D cell culture WAB *in vitro* loading models, applied forces varied between 0.2 and 5.0 g/cm^2. Our data suggest that 2.0 g/cm^2 was the most commonly used force magnitude in the studies so far. According to Kanzaki et al. [20], this force magnitude proved to induce the best cellular response. Few studies reported a decrease in cell viability in a force-dependent manner, especially with the application of 4 g/cm^2 force [20, 37, 50, 51].

In studies applying the 3D WAB *in vitro* loading models, the force magnitude used was chosen depending on the stiffness of the scaffold. Studies using collagen gel scaffolds most commonly applied 6 g/cm^2 force onto their *in vitro* models. According to Araujo et al. [47], this force was corresponding to the therapeutic orthodontic force, giving the best cellular response. For PLGA scaffolds, the force magnitude showing the best performance was 25 g/cm^2 (range: 5–35 g/cm^2). The same range of forces were applied in the study of Liao et al. [14] using a hydrophilically modified PLLA scaffold matrix. This range also corresponds to the one used in clinical settings, which indicates that these scaffolds are closest to the mechanical properties of *in vivo* PDL [14, 33]. This qualifies them also as a suitable model for investigation of light and

heavy forces, which are considered as a cause of orthodontic treatment failure.

4.3. Duration of the Force Application. The length of the force application in the studies rarely exceeded 72 h. In most of the cases, force was applied up to 24 and 48 h. Considering the fact that the first 10 days are of crucial importance for OTM ([52], p. 303), the duration of force application in most of the conducted studies is insufficient to fully understand the molecular background of OTM. Additionally, we would like to point out that only a few studies observed cell viability during the experiment. Most of them confirmed a reduction of cell viability, not only due to the force level but also depending on time [19, 50, 51]. We assume that one of the limitations, especially in the 2D WAB *in vitro* models, is compromised nutrient and oxygen supply in the pressure area. To overcome especially the time limitation of previous models, Liao et al. [14] introduced the hydrophilically modified PLLA matrix as a new scaffold for 3D cultures. They have shown that this scaffold can be used for up to 14 days without affecting cell viability, claiming that it provides good perfusion of the nutrients and oxygen over longer periods of time [14]. Establishing an *in vitro* model suitable for long-term force application (up to or more than 10 days) is beneficial for progress in this research field.

4.4. Role of PDL and hPDLCs in OTM. Due to lack of PDL, ankylosed teeth and implants cannot undergo OTM, which depict best PDL's key role in transmitting the mechanical stimulus and initiating the process of bone remodelling [1, 53]. Beside its mechanotransduction properties, it also contributes to tissue homoeostasis and repair, mostly due to the presence of mesenchymal stem cells which are an important part in the normal hPDLC population [4]. This portion of hPDLCs is known to be present in a higher extent in hPDLCs isolated with the "enzyme digestion method" [54], commonly used among the studies in this review, especially in the 3D group.

4.5. Most Examined Genes in the Studies That Used hPDLCs. To explain the contribution of hPDLCs in OTM on the molecular level, we summarised all data regarding the most commonly examined genes and substances in this cell type (Table 1). These were *TNFSF11*, *PTGS2*, and PGE_2, known as osteoclastogenesis inducers, and *TNFRSF11B*, known as an osteoclastogenesis inhibitor.

TNFSF11 (also known as "RANKL") [55] plays a crucial role in bone resorption on the compression side during OTM, inducing the osteoclast formation. *TNFSF11* showed an increased gene expression in all studies that used the 2D WAB *in vitro* loading model (Table 1). In most of the studies using this model, *TNFSF11* gene expression, as well as protein secretion, was positively correlated with both force duration and magnitude reaching the maximum expression level after 12–24 hours of force application. Studies using the 3D WAB *in vitro* loading model also reported an increase in the TNFSF11 secretion, most of them after 6 hours of force application (Table 1). In cells grown in PLGA scaffolds, a positive correlation between force magnitude and gene expression but a negative correlation between force duration and gene expression was noticed.

TNFRSF11B, also referred to as osteoprotegerin (OPG), is TNFSF11's antagonist that inhibits osteoclastogenesis [55]. Most of the studies applying the 2D WAB *in vitro* loading model reported no observed change in gene expression ($n = 8$), with exception of two studies that reported downregulation [40] or transitory downregulation [8] (Table 1). Considering protein secretion, results were contradictory. Most studies, however, reported a decrease in protein secretion or did not report any change. Results from studies using 3D WAB *in vitro* loading were also contrary, depending on the scaffold used. In a study using collagen gel scaffolds, an increase in *TNFRSF11B* gene expression was observed [26]. In all studies applying PLGA scaffolds, a decrease in TNFRSF11B secretion was positively correlated with force magnitude and negatively correlated with force duration [27, 28, 31, 33, 43]. With one exception [28], a comparison of *TNFSF11* and *TNFRSF11B* gene expression in the aforementioned studies showed that a rapid down/regulation of *TNFRSF11B* appears parallel to a rapid upregulation of *TNFSF11* in 3D WAB *in vitro* loading. Since both genes represent antagonists in bone turnover regulation, this was explained as a good representation of the cyclic changes in the bone metabolism on the compression side during OTM [31, 33]. It was also suggested that downregulation of *TNFSF11* in later stages might have something to do with other inducers for prolonged osteoclastogenesis promotion [33].

Gene expression of *PTGS2* was increased upon force application in both 2D and 3D studies. In most of the 2D WAB studies, *PTGS2* showed a positive correlation between the duration of the experiment and gene expression (Table 1). In those studies, using the 3D WAB *in vitro* loading model, *PTGS2* seemed to be negatively correlated with force duration and positively correlated with force magnitude. On the other hand, PTGS2 protein quantity was shown to be in positive correlation with both duration and force magnitude using Western blotting (Table 1). Since PTGS2 is involved in prostaglandin E_2 metabolism, an upregulation of *PTGS2* gene expression (maximum at 24 to 48 h after force application) is correlated with an upregulation of PGE_2 secretion (maximum at 48 h after force application) in all studies (Table 1).

Taken together, there seems to be some inconsistency between studies using the 2D and the 3D WAB *in vitro* loading model. The results within the 2D WAB group of studies are quite similar and comparable. However, a noticeable higher heterogeneity among those studies using the 3D WAB *in vitro* loading model is recognizable. This heterogeneity can be related to the type of scaffolds used.

4.6. STRING PPI Analysis. We performed STRING PPI analysis for two selected sets of genes ("hPDLC list" and "hOB list"). PPI enrichment p values obtained from both PPI networks (Figure 4) had significantly more interactions than expected. This implicates that the genes examined in the studies were not chosen randomly. From our point of view, this is not surprising, since most of the

studies were selecting "the genes of interest" for their analysis, all previously known or suspected to be involved in bone metabolism. Just a few of the studies performed microarray analysis in order to identify all genes responding to force application [26, 32, 44, 48].

In addition, KEGG pathways relevant for OTM, identified for each set of genes in STRING analysis (Table 2), can be useful source for discovering new genes that might influence OTM.

5. Conclusions

In summary, the WAB *in vitro* loading model represents a simple and very efficient way to investigate molecular events during OTM. The purpose of this review was to provide an overview of all used forms of the WAB *in vitro* loading model (2D and 3D in combination with different scaffolds), present all current findings, and point out at certain questions for their further improvement.

3D WAB *in vitro* loading models have shown to be promising for use in future research by bringing a more real environment in *in vitro* setups. However, unlike well-established 2D models that provide comparable results, 3D models show inconsistency in results. Obviously, there is a need for further improvement in order to establish standardised *in vitro* models that will provide comparable results. Also, there is a need to elucidate molecular events during longer periods of force application. Therefore, the future goal is to establish both 2D and 3D loading models that will allow us to conduct long-term investigations. The study of Liao et al. [14] is a good example for this, and there should be more research in that direction.

Abbreviations

2D: Two-dimensional
3D: Three-dimensional
ATP: Adenosine triphosphate
cAMP: Cyclic adenosine monophosphate
ECM: Extracellular matrix
ELISA: Enzyme-linked immunosorbent assay
H_2S: Hydrogen sulfide
hOBMCs: Human oral bone marrow cells
hOBs: Human osteoblasts
hPDLCs: Human periodontal ligament cells
KEGG: Kyoto encyclopedia of genes and genomes
NO: Nitric oxide
OOF: Optimal orthodontic force
OPG: Osteoprotegerin
OTM: Orthodontic tooth movement
PDL: Periodontal ligament
PGE_2: Prostaglandin E_2
PLGA: Polylactic-co-glycolic acid
PLLA: Poly-L-lactide acid
PPI: Protein-protein interaction
PTGS2: Prostaglandin-endoperoxide synthase 2
RANKL: Receptor activator of nuclear factor kappa-*B* ligand
ROS: Reactive oxygen species
STRING: Search tool for the retrieval of interacting genes/proteins
TNF: Tumor necrosis factor
TNFRSF11B: TNF receptor superfamily member 11b
TNFSF11: TNF superfamily member 11
WAB: Weight approach based.

Conflicts of Interest

The authors declare that there is no conflict of interest regarding the publication of this manuscript.

Acknowledgments

Mila Janjic received a study grant from BAYHOST (Bayerisches Hochschulzentrum für Mittel-, Ost- und Südosteuropa, Regensburg, Germany) and from the Fund for Young Talents of the Republic of Serbia (Government of the Republic of Serbia, Ministry of Youth and Sports, Belgrade, Serbia).

Supplementary Materials

Supplementary 1. Search strategy designed for the studies applying the *in vitro* loading model based on a weight approach on cells in 2D or 3D cell culture and lists the excluded studies after full-text reading with reasons.

Supplementary 2. Studies applying the 2D weight approach on human primary cells from the orofacial region, that is, human periodontal ligament cells (hPDLC), human oral bone marrow cells (hOBMC), and human alveolar bone osteoblasts (hOB). For each gene or metabolite force magnitude and force duration, the change in gene expression or substance secretion (increase, decrease, and no change) and the techniques applied are given.

Supplementary 3. Studies applying the 2D weight approach on human and nonhuman cells and cell lines not included in Supplement 2 (i.e., human primary cells from the orofacial region). For each gene or metabolite force magnitude and force duration, the change in gene expression or substance secretion (increase, decrease, and no change) and the techniques applied are given.

Supplementary 4. Studies applying the 3D weight approach on human and nonhuman cells and cell lines. For each gene or metabolite force magnitude and force duration, the change in gene expression or substance secretion (increase, decrease, and no change) and the techniques applied are given.

References

[1] A. Wichelhaus, *Orthodontic Therapy - Fundamental Treatment Concepts*, Georg Thieme, New York, 2017.

[2] Z. Davidovitch and V. Krishnan, "Biological basis of orthodontic tooth movement: an historical perspective," in *Biological Mechanisms of Tooth Movement, V. Krishnan and Z. Davidovitch Eds*, pp. 3–14, Wiley, Chichester, West Sussex, UK, 2015.

[3] Z. Davidovitch, "Tooth movement," *Critical Reviews in Oral Biology and Medicine*, vol. 2, no. 4, pp. 411–450, 1991.

[4] B. M. Seo, M. Miura, S. Gronthos et al., "Investigation of multipotent postnatal stem cells from human periodontal ligament," *The Lancet*, vol. 364, no. 9429, pp. 149–155, 2004.

[5] U. Baumert, I. Golan, B. Becker et al., "Pressure simulation of orthodontic force in osteoblasts: a pilot study," *Orthodontics and Craniofacial Research*, vol. 7, no. 1, pp. 3–9, 2004.

[6] L. Yang, Y. Yang, S. Wang, Y. Li, and Z. Zhao, "*In vitro* mechanical loading models for periodontal ligament cells: from two-dimensional to three-dimensional models," *Archives of Oral Biology*, vol. 60, no. 3, pp. 416–424, 2015.

[7] K. Kanai, H. Nohara, and K. Hanada, "Initial effects of continuously applied compressive stress to human periodontal ligament fibroblasts," *The Journal of Japan Orthodontic Society*, vol. 51, pp. 153–163, 1992.

[8] S. J. Kim, K. H. Park, Y. G. Park, S. W. Lee, and Y. G. Kang, "Compressive stress induced the up-regulation of M-CSF, RANKL, TNF-α expression and the down-regulation of OPG expression in PDL cells via the integrin-FAK pathway," *Archives of Oral Biology*, vol. 58, no. 6, pp. 707–716, 2013.

[9] P. Proff, C. Reicheneder, A. Faltermeier, D. Kubein-Meesenburg, and P. Römer, "Effects of mechanical and bacterial stressors on cytokine and growth-factor expression in periodontal ligament cells," *Journal of Orofacial Orthopedics / Fortschritte der Kieferorthopädie*, vol. 75, no. 3, pp. 191–202, 2014.

[10] D. Moher, PRISMA-P Group, L. Shamseer et al., "Preferred reporting items for systematic review and meta-analysis protocols (PRISMA-P) 2015 statement," *Systematic Reviews*, vol. 4, no. 1, 2015.

[11] J. Ye, G. Coulouris, I. Zaretskaya, I. Cutcutache, S. Rozen, and T. L. Madden, "Primer-BLAST: a tool to design target-specific primers for polymerase chain reaction," *BMC Bioinformatics*, vol. 13, no. 1, p. 134, 2012.

[12] D. Szklarczyk, J. H. Morris, H. Cook et al., "The STRING database in 2017: quality-controlled protein-protein association networks, made broadly accessible," *Nucleic Acids Research*, vol. 45, no. D1, pp. D362–D368, 2016.

[13] J. Du, Z. Yuan, Z. Ma, J. Song, X. Xie, and Y. Chen, "KEGG-PATH: Kyoto encyclopedia of genes and genomes-based pathway analysis using a path analysis model," *Molecular BioSystems*, vol. 10, no. 9, pp. 2441–2447, 2014.

[14] W. Liao, M. Okada, K. Inami, Y. Hashimoto, and N. Matsumoto, "Cell survival and gene expression under compressive stress in a three-dimensional in vitro human periodontal ligament-like tissue model," *Cytotechnology*, vol. 68, no. 2, pp. 249–260, 2016.

[15] B. Ragnarsson, G. Carr, and J. C. Daniel, "Basic biological sciences isolation and growth of human periodontal ligament cells in vitro," *Journal of Dental Research*, vol. 64, no. 8, pp. 1026–1030, 1985.

[16] M. J. Somerman, S. Y. Archer, G. R. Imm, and R. A. Foster, "A comparative study of human periodontal ligament cells and gingival fibroblasts *in vitro*," *Journal of Dental Research*, vol. 67, no. 1, pp. 66–70, 1988.

[17] S. Benjakul, S. Jitpukdeebodintra, and C. Leethanakul, "Effects of low magnitude high frequency mechanical vibration combined with compressive force on human periodontal ligament cells *in vitro*," *European Journal of Orthodontics*, In press.

[18] Y. Jin, J. Li, Y. Wang et al., "Functional role of mechanosensitive ion channel Piezo1 in human periodontal ligament cells," *The Angle Orthodontist*, vol. 85, no. 1, pp. 87–94, 2015.

[19] Y. G. Kang, J. H. Nam, K. H. Kim, and K. S. Lee, "FAK pathway regulates PGE2 production in compressed periodontal ligament cells," *Journal of Dental Research*, vol. 89, no. 12, pp. 1444–1449, 2010.

[20] H. Kanzaki, M. Chiba, Y. Shimizu, and H. Mitani, "Periodontal ligament cells under mechanical stress induce osteoclastogenesis by receptor activator of nuclear factor κB ligand up-regulation via prostaglandin E2 synthesis," *Journal of Bone and Mineral Research*, vol. 17, no. 2, pp. 210–220, 2002.

[21] C. Kirschneck, P. Proff, M. Maurer, C. Reicheneder, and P. Römer, "Orthodontic forces add to nicotine-induced loss of periodontal bone : An in vivo and in vitro study," *Journal of Orofacial Orthopedics*, vol. 76, no. 3, pp. 195–212, 2015.

[22] L. Liu, K. Igarashi, H. Kanzaki, M. Chiba, H. Shinoda, and H. Mitani, "Clodronate inhibits PGE2 production in compressed periodontal ligament cells," *Journal of Dental Research*, vol. 85, no. 8, pp. 757–760, 2006.

[23] K. Mayahara, Y. Kobayashi, K. Takimoto, N. Suzuki, N. Mitsui, and N. Shimizu, "Aging stimulates cyclooxygenase-2 expression and prostaglandin E_2 production in human periodontal ligament cells after the application of compressive force," *Journal of Periodontal Research*, vol. 42, no. 1, pp. 8–14, 2007.

[24] S. Premaraj, I. Souza, and T. Premaraj, "Focal adhesion kinase mediates β-catenin signaling in periodontal ligament cells," *Biochemical and Biophysical Research Communications*, vol. 439, no. 4, pp. 487–492, 2013.

[25] P. Römer, J. Köstler, V. Koretsi, and P. Proff, "Endotoxins potentiate COX-2 and RANKL expression in compressed PDL cells," *Clinical Oral Investigations*, vol. 17, no. 9, pp. 2041–2048, 2013.

[26] R. M. S. de Araujo, Y. Oba, and K. Moriyama, "Identification of genes related to mechanical stress in human periodontal ligament cells using microarray analysis," *Journal of Periodontal Research*, vol. 42, no. 1, pp. 15–22, 2007.

[27] M. Li, J. Yi, Y. Yang, W. Zheng, Y. Li, and Z. Zhao, "Investigation of optimal orthodontic force at the cellular level through three-dimensionally cultured periodontal ligament cells," *The European Journal of Orthodontics*, vol. 38, no. 4, pp. 366–372, 2016.

[28] J. Yi, B. Yan, M. Li et al., "Caffeine may enhance orthodontic tooth movement through increasing osteoclastogenesis induced by periodontal ligament cells under compression," *Archives of Oral Biology*, vol. 64, pp. 51–60, 2016.

[29] K. Mayahara, A. Yamaguchi, M. Sakaguchi, Y. Igarashi, and N. Shimizu, "Effect of Ga-Al-As laser irradiation on *COX-2* and *cPLA$_2$-α* expression in compressed human periodontal ligament cells," *Lasers in Surgery and Medicine*, vol. 42, no. 6, pp. 489–493, 2010.

[30] S. Wongkhantee, T. Yongchaitrakul, and P. Pavasant, "Mechanical stress induces osteopontin expression in human periodontal ligament cells through rho kinase," *Journal of Periodontology*, vol. 78, no. 6, pp. 1113–1119, 2007.

[31] M. Le Li, J. Yi, Y. Yang et al., "Compression and hypoxia play independent roles while having combinative effects in the

osteoclastogenesis induced by periodontal ligament cells," *The Angle Orthodontist*, vol. 86, no. 1, pp. 66–73, 2016.

[32] Y. Li, M. Li, L. Tan et al., "Analysis of time-course gene expression profiles of a periodontal ligament tissue model under compression," *Archives of Oral Biology*, vol. 58, no. 5, pp. 511–522, 2013.

[33] Y. Li, W. Zheng, J. S. Liu et al., "Expression of osteoclastogenesis inducers in a tissue model of periodontal ligament under compression," *Journal of Dental Research*, vol. 90, no. 1, pp. 115–120, 2010.

[34] S. Y. Lee, H. I. Yoo, and S. H. Kim, "CCR5-CCL axis in PDL during orthodontic biophysical force application," *Journal of Dental Research*, vol. 94, no. 12, pp. 1715–1723, 2015.

[35] F. Liu, F. Wen, D. He et al., "Force-induced H_2S by PDLSCs modifies osteoclastic activity during tooth movement," *Journal of Dental Research*, vol. 96, no. 6, pp. 694–702, 2017.

[36] P. Luckprom, K. Kanjanamekanant, and P. Pavasant, "Role of connexin43 hemichannels in mechanical stress-induced ATP release in human periodontal ligament cells," *Journal of Periodontal Research*, vol. 46, no. 5, pp. 607–615, 2011.

[37] M. Mitsuhashi, M. Yamaguchi, T. Kojima, R. Nakajima, and K. Kasai, "Effects of HSP70 on the compression force-induced TNF-α and RANKL expression in human periodontal ligament cells," *Inflammation Research*, vol. 60, no. 2, pp. 187–194, 2011.

[38] R. Nakajima, M. Yamaguchi, T. Kojima, M. Takano, and K. Kasai, "Effects of compression force on fibroblast growth factor-2 and receptor activator of nuclear factor kappa B ligand production by periodontal ligament cells *in vitro*," *Journal of Periodontal Research*, vol. 43, no. 2, pp. 168–173, 2008.

[39] Y. Nishijima, M. Yamaguchi, T. Kojima, N. Aihara, R. Nakajima, and K. Kasai, "Levels of RANKL and OPG in gingival crevicular fluid during orthodontic tooth movement and effect of compression force on releases from periodontal ligament cells *in vitro*," *Orthodontics and Craniofacial Research*, vol. 9, no. 2, pp. 63–70, 2006.

[40] K. Yamada, M. Yamaguchi, M. Asano, S. Fujita, R. Kobayashi, and K. Kasai, "Th17-cells in atopic dermatitis stimulate orthodontic root resorption," *Oral Diseases*, vol. 19, no. 7, pp. 683–693, 2013.

[41] M. Yamaguchi, N. Aihara, T. Kojima, and K. Kasai, "RANKL increase in compressed periodontal ligament cells from root resorption," *Journal of Dental Research*, vol. 85, no. 8, pp. 751–756, 2006.

[42] M. Kaku, J. M. Rosales Rocabado, M. Kitami et al., "Mechanical loading stimulates expression of collagen cross-linking associated enzymes in periodontal ligament," *Journal of Cellular Physiology*, vol. 231, no. 4, pp. 926–933, 2016.

[43] Y. I. Jianru, L. I. MeiLe, Y. YANG, W. ZHENG, L. I. Yu, and Z. ZHAO, "Static compression regulates OPG expression in periodontal ligament cells via the CAMK II pathway," *Journal of Applied Oral Science*, vol. 23, no. 6, pp. 549–554, 2015.

[44] K. L. Kang, S. W. Lee, Y. S. Ahn, S. H. Kim, and Y. G. Kang, "Bioinformatic analysis of responsive genes in two-dimension and three-dimension cultured human periodontal ligament cells subjected to compressive stress," *Journal of Periodontal Research*, vol. 48, no. 1, pp. 87–97, 2013.

[45] J. Kikuta, M. Yamaguchi, M. Shimizu, T. Yoshino, and K. Kasai, "Notch signaling induces root resorption via RANKL and IL-6 from hPDL cells," *Journal of Dental Research*, vol. 94, no. 1, pp. 140–147, 2014.

[46] M. Weinreb and C. E. Nemcovsky, "*In vitro* models for evaluation of periodontal wound healing/regeneration," *Periodontology*, vol. 68, no. 1, pp. 41–54, 2015.

[47] R. M. Santos de Araujo, Y. Oba, and K. Moriyama, "Role of regulator of G-protein signaling 2 (RGS2) in periodontal ligament cells under mechanical stress," *Cell Biochemistry and Function*, vol. 25, no. 6, pp. 753–758, 2007.

[48] Y. H. Lee, D. S. Nahm, Y. K. Jung et al., "Differential gene expression of periodontal ligament cells after loading of static compressive force," *Journal of Periodontology*, vol. 78, no. 3, pp. 446–452, 2007.

[49] A. M. Schwarz, "Tissue changes incidental to orthodontic tooth movement," *International Journal of Orthodontia, Oral Surgery and Radiography*, vol. 18, no. 4, pp. 331–352, 1932.

[50] K. Kanjanamekanant, P. Luckprom, and P. Pavasant, "Mechanical stress-induced interleukin-1beta expression through adenosine triphosphate/P2X7 receptor activation in human periodontal ligament cells," *Journal of Periodontal Research*, vol. 48, no. 2, pp. 169–176, 2013.

[51] P. Tripuwabhrut, K. Mustafa, P. Brudvik, and M. Mustafa, "Initial responses of osteoblasts derived from human alveolar bone to various compressive forces," *European Journal of Oral Sciences*, vol. 120, no. 4, pp. 311–318, 2012.

[52] W. R. Proffit and H. W. Fields Jr., *Contemporary Orthodontics*, Mosby, St. Louis, 2000.

[53] G. J. King, S. D. Keeling, and T. J. Wronski, "Histomorphometric study of alveolar bone turnover in orthodontic tooth movement," *Bone*, vol. 12, no. 6, pp. 401–409, 1991.

[54] K. Tanaka, K. Iwasaki, K. E. Feghali, M. Komaki, I. Ishikawa, and Y. Izumi, "Comparison of characteristics of periodontal ligament cells obtained from outgrowth and enzyme-digested culture methods," *Archives of Oral Biology*, vol. 56, no. 4, pp. 380–388, 2011.

[55] M. Yamaguchi, "RANK/RANKL/OPG during orthodontic tooth movement," *Orthodontics & Craniofacial Research*, vol. 12, no. 2, pp. 113–119, 2009.

Hindawi
Stem Cells International
Volume 2018, Article ID 5402853, 11 pages
https://doi.org/10.1155/2018/5402853

Research Article

Osteogenic Effect and Cell Signaling Activation of Extremely Low-Frequency Pulsed Electromagnetic Fields in Adipose-Derived Mesenchymal Stromal Cells

Patrina S. P. Poh,[1] Claudine Seeliger,[1] Marina Unger,[1] Karsten Falldorf,[2] Elizabeth R. Balmayor,[1] and Martijn van Griensven[1]

[1]*Experimental Trauma Surgery, Department of Trauma Surgery, Klinikum Rechts der Isar, Technical University of Munich, Ismaninger Strasse 22, 81675 Munich, Germany*
[2]*Sachtleben GmbH, Hamburg, Germany*

Correspondence should be addressed to Martijn van Griensven; martijn.vangriensven@tum.de

Received 20 April 2018; Accepted 6 June 2018; Published 12 July 2018

Academic Editor: Andrea Ballini

Copyright © 2018 Patrina S. P. Poh et al. This is an open access article distributed under the Creative Commons Attribution License, which permits unrestricted use, distribution, and reproduction in any medium, provided the original work is properly cited.

Extremely low-frequency pulsed electromagnetic field (ELF-PEMF) devices have been used in the clinic for the treatment of bone disorders over the past 30 years. However, the underlying mechanism of which ELF-PEMFs exert an effect on tissues at a cellular level is not well understood. Hence, in this study, we explored the potential of different ELF-PEMF signals in modulating human adipose-derived mesenchymal stromal cells' (hAMSC) osteogenic capability. The cell proliferation rate was assessed using carboxyfluorescein succinimidyl ester (CFSE) method. The osteogenesis potential of cells was determined by alkaline phosphatase (ALP) activity, Alizarin-Red S staining, and RT-qPCR. Finally, the intracellular signaling pathway of a selected ELF-PEMF signal was examined using the PathScan Intracellular Signaling Array. Among the tested ELF-PEMF signals, program 20 (26 Hz) showed activation of the Akt and MAPK/ERK signaling cascade and significant upregulations of collagen I, alkaline phosphatase, and osteocalcin when compared to nonstimulated cells. This study demonstrates the potential of certain ELF-PEMF signal parameters to induce osteogenic differentiation of hAMSC and provides important clues in terms of the molecular mechanisms for the stimulation of osteogenic effects by ELF-PEMF on hAMSC.

1. Introduction

Clinical intervention of large bone defects is limited. Autografts (transplantation of patient's own tissue) remain the gold standard for treating large bone defects. Despite exhibiting high healing rates, autografts have associated disadvantages; approximately 20–30% of autograft patients experienced donor site morbidity and are complicated by fracture, nonunion, and infection. Therefore, effective treatments for such bone defects are urgently needed.

Over the years, cell therapy has been proven to be a viable strategy that can aid the process of bone regeneration [1]. Autologous adipose-derived mesenchymal stromal cells (AMSC) are a promising tool in cell therapy due to their relative ease to harvest compared to other sources of mesenchymal stromal cells (MSC) and have been indicated as a cell source with high regenerative potential [1, 2]. However, the efficacy of AMSC therapy depends upon how effectively transplanted AMSC can be targeted persistently to the diseased area and how functional these cells are in terms of the regeneration process. Bone regeneration is a very dynamic and complex process involving diversity of cell types whose functions are regulated by intricate networks of biochemical signals. One crucial phase of bone regeneration is the proliferation and differentiation of precursor cells (i.e., MSC) into osteoblasts (bone-forming cells) that would build up the mineralized bone matrix. Hence, there have been tremendous efforts in the development of noninvasive strategies, which could complement cell therapy by stimulating proliferation and guiding differentiation of MSC within the injured sites

to promote bone regeneration [3, 4]. Among these, ELF-PEMFs present a potential technology platform, which can be applied noninvasively to regulate desirable cellular responses. ELF-PEMF-generating devices can produce electromagnetic signals with specific amplitudes, frequencies, and waveforms [5]. These signals can be transduced into soft tissue through an external coil applied at the intended injury sites, resulting in localized induced electric and magnetic fields [6]. Some studies suggested improved bone regenerative capabilities favoring osteoblast proliferation, differentiation, and production of calcified extracellular matrix (ECM) as a result of exposures to ELF-PEMF signals [7–12].

ELF-PEMF therapies aimed at aiding fracture repair have been investigated clinically for more than 30 years. Many efforts have been geared towards understanding the fundamental mechanism of ELF-PEMF stimulation on MSC harvested from different sources (i.e., alveolar bone-derived MSC [13], bone marrow-derived MSC (BMSC), and AMSC [14, 15]) and the associated implications on bone regeneration. However, while promising results have been obtained, there is still no clarity on the nature of such mechanism of action or on the optimal ELF-PEMF signal parameters which can be utilized to enhance osteogenic capabilities. Because of this, the optimal ELF-PEMF signal configurations required to enhance osteogenic potential of hAMSC [14–17] are uncertain. In most studies, the amplitude and frequency of the ELF-PEMF signal used to induce osteogenesis varied from 0.1 to 3 mT and from 7.5 to 75 Hz, respectively [4, 16], showing varying outcomes depending on the ELF-PEMF configurations (i.e., frequency, amplitude, and waveforms), ELF-PEMF devices (i.e., shape and size of applicator/field coil), method of application (i.e., position of the applicator in respect to the cells'/tissues' position), and duration of exposure. In this regard, for example, exposure durations found in the literature vary from 5 mins to 14 hours per day [5, 18] with no consensus on the optimal treatment duration. However, at present, long-term exposure of organs and tissues to ELF-PEMF is still highly debatable [19]. *In vivo* studies have illustrated that long-term exposure to ELF-PEMF can cause negative side effects, such as reduced sperm motility and testosterone level (1 mT, 50 Hz EMF, 24 hrs for 85 days) [20] and enhanced oxidative stress in liver tissue (1 mT, 50 Hz EMF, 4 hrs per day for 45 days) [21]. On the other hand, short exposures have shown promising benefits in line with those expected from potential therapies [22].

Within this context, we performed this study in an attempt to identify further potential ELF-PEMF signals that can potentially guide or enhance the osteogenic capabilities of hAMSC. Subsequently, the intracellular signaling pathways activated in hAMSC due to exposure of ELF-PEMF were examined.

2. Materials and Methods

2.1. Isolation of hAMSC. Isolation of hAMSC from 6 donors ($N = 6$) was performed with written informed patient's consent (acquired prior to tissue collection) and with approval of the local ethical committee of the University Hospital "Klinikum Rechts der Isar", Technical University of Munich, Germany, and according to the ethical guidelines established by this institution as well as the Declaration of Helsinki in its latest amendment. Briefly, solid fat samples (manually minced into smaller pieces) or liposuctions were digested with 0.075% (w/v) collagenase type II (Biochrom, Germany) in PBS at 37°C for 30 min. The digestion was terminated using DMEM-high glucose supplemented with 100 U/ml penicillin, 100 μg/ml streptomycin, and 10% (v/v) fetal calf serum (FCS). Detailed cell isolation procedures have been described by Schneider et al. [23]. The isolated cells were incubated at 37°C, 5% CO_2, and 95% air humidity. Cells of passage 3 were used for cell proliferation and mineralization assays, while gene expression and intracellular signaling arrays were performed with cells of passage 4.

2.2. ELF-PEMF Exposure. To evaluate the proliferative and osteogenic differentiation behavior of hAMSC when exposed to different ELF-PEMF signals, cell culture plates/flasks were placed onto the applicator (Figure 1). The applicator was connected to the Somagen® device (CE 0482, compliant with EN ISO 13485:2012 + AC:2012, Sachtleben GmbH, Germany) where ELF-PEMF signals were generated as previously described [24–26]. For the present study, 10 different ELF-PEMF signals (termed "CIT programs" by the manufacturer) were used. Briefly, all the ELF-PEMF signals generated by the device were constituted by a fundamental pulse, which was arranged into a pulse train with different fundamental frequencies as listed in Table 1.

Figure 1 shows the distribution of the peak ELF-PEMF magnetic field magnitude as a measure of the field homogeneity over the cell culture plate.

2.3. Cell Culture. The cell culture studies were divided into two sequential parts. In the first part (study 1), hAMSCs were trypsinised and plated with a density of 1×10^4 cells/cm^2 in 1 96-well plate. The osteogenic differentiation of hAMSC was induced using DMEM-low glucose supplemented with 100 U/ml penicillin, 100 μg/ml streptomycin, 5% (v/v) FCS, 100 nM dexamethasone, 1.6 mM calcium chloride ($CaCl_2$), 25 mM HEPES, 0.2 mM ascorbic acid, and 10 mM β-glycerol phosphate (hereafter referred as osteogenic medium). Then, cells were separately treated with each one of the ELF-PEMF signals listed in Table 1, once a day for 7 mins over 2 weeks. At days 3, 7, and 14, immediately after the ELF-PEMF exposure, cells were harvested for cell proliferation and mineralization assays.

In the second part (study 2), hAMSCs were identically plated at a density of 1×10^4 cells/cm^2 and cultured in osteogenic medium. The cells were exposed to one ELF-PEMF signal identified in study 1 also for 7 mins (single exposure). After a defined resting period (of 30 mins, 1, 2, 3, 4, and 6 hrs), samples were collected for intracellular cell signaling arrays. In both studies, hAMSCs cultured in osteogenic medium without ELF-PEMF exposure were used as control.

2.4. Carboxyfluorescein Succinimidyl Ester (CFSE) Labelling of Cells. Cell proliferation was assessed using CFSE (Abcam®, ab113853, UK). Briefly, cells were fluorescence labelled with

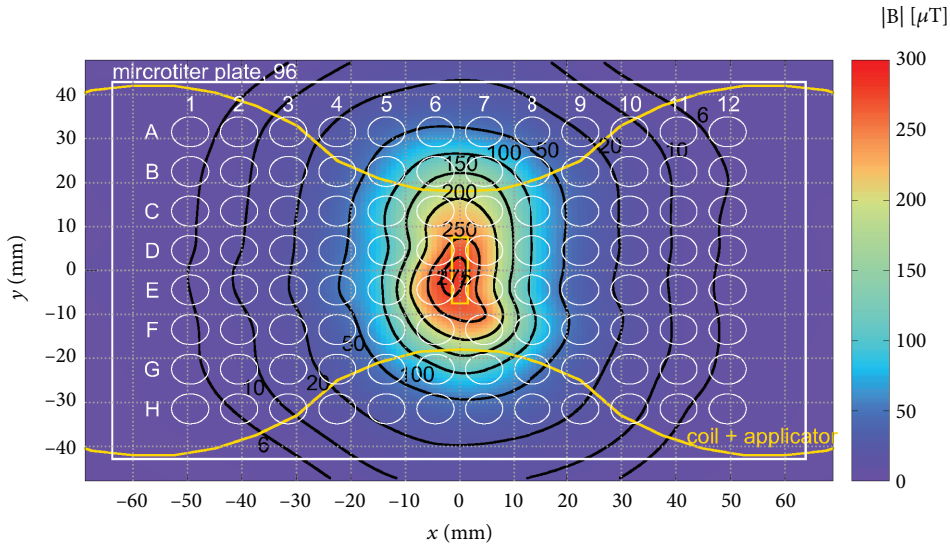

Figure 1: Peak magnetic field magnitude distribution across the cell culture plate (6 mm above the applicator). Yellow line outlined the contour of the applicator.

Table 1: ELF-PEMF signals utilized in the study. Frequencies (pulse repetition rate) of the ELF-PEMF signals investigated.

"CIT program number"	Pulse repetition rates (Hz)
4	10.0
16	16.0
10	20.6
18	23.8
20	26.0
64	33.0
31	49.9
81	52.3
114	75.6
124	90.6

1 μM CFSE in culture media for 15 mins at 37°C. Then, the cells were washed with culture media to remove nonincorporated dye and topped up with fresh culture media. On days 3, 7, and 14, cells were harvested and CFSE fluorescence absorbance was detected using a flow cytometer (MACSQuant, Miltenyi Biotec, Germany) using the blue laser (488 nm) and a 525/50 nm filter.

2.5. Sulforhodamine B (SRB) Staining of Cellular Protein. At days 3, 7, and 14, cells were fixed with ice-cold methanol for 15 mins and incubated in SRB solution for 30 mins. Subsequently, cells were washed with 1% acetic acid solution to remove unbound SRB. Then, SRB was incubated with 10 mM unbuffered Tris solution for 15 mins to dissolve bound SRB. Finally, absorbance was measured at 565/690 nm using a plate reader (BMG Labtech, Germany). A standard curve with known protein amount was generated and used for the calculation of corresponding value for all samples.

2.6. Alkaline Phosphatase (ALP) Activity. On days 3, 7, and 14, cell culture medium was aspirated, and cells were washed once with PBS. Then, cells were covered with ALP substrate solution (i.e., 3.5 mM 4-disodium-4-nitrophenyl phosphate prepared in 0.1 M AP-buffer consisting of 50 mM glycine, 100 mM Tris-base, and 2 mM magnesium chloride at pH 10.5) for 30 min at 37°C. Subsequently, 100 μl of reaction mixture was transferred into a 96-well plate in triplicate. Absorption of the reaction product was measured at 405 nm using a plate reader (BMG Labtech, Germany). Presented data were normalized to protein content.

2.7. Von Kossa Staining for Matrix Mineralization. At different time points (3, 7, and 14 days), the culture was washed twice with PBS and fixed with ice-cold methanol for 15 mins. Subsequently, culture was stained with 3% (w/v) silver nitrate solution (Fisher, Germany) for 30 mins, followed by three rinses with dH_2O. Stain was developed in 1% (w/v) pyrogallol solution for 3 mins, followed by two rinses with dH_2O (5 mins each). Then, culture was incubated with 5% sodium thiosulfate solution for 5 mins, washed in running tap water for 15 mins, and incubated with Kernecht-red solution for 5 mins. After washing, culture was treated with 96% ethanol for 1 min, air dried, and imaged using light microscopy (BZ-9000, Keyence, Japan).

2.8. Alizarin Red S Staining for Semiquantification of Matrix Mineralization. This procedure was performed for semiquantification of the extent of matrix mineralization. Briefly, on days 3, 7, and 14, cells were washed with PBS and fixed with ice-cold ethanol for 30 mins at room temperature. Then, cells were washed with distilled water (dH_2O) and incubated with 0.5% (w/v) Alizarin Red S in dH_2O, pH 4 for 10 min. After that, unincorporated dye was washed away using several rinses of dH_2O. The precipitates were dissolved using 10% hexadecylpyridinium chloride, and 100 μl of the solution was transferred to a 96-well plate in triplicate. The

Table 2: Forward and reverse primer sequences and annealing temperature for the respective genes.

Gene	Forward primer	Reverse primer	Annealing temperature (°C)
RunX2	TGCCTAGGCGCATTTCAGGTGC	TGAGGTGATGGCGGGGTGT	60
Osteocalcin	CCAGCGGTGCAGAGTCCAGC	GACACCCTAGACCGGGCCGT	60
Osteopontin	CTCCATTGACTCGAACGACTC	CGTCTGTAGCATCAGGGTACTG	60
Alkaline phosphatase	ACGTGGCTAAGAATGTCATC	CTGGTAGGCGATGTCCTTA	57.5
Collagen I	AGCGGACGCTAACCCCCTCC	CAGACGGGACAGCACTCGCC	60
Beta-tubulin	GAGGGCGAGGACGAGGCTTA	TCTAACAGAGGCAAAACTGAGCACC	60

absorption of the reaction product was measured at 562 nm using a plate reader. Presented data were normalized to protein content.

2.9. RT-qPCR. On days 3, 7, and 14, the cells were harvested, and mRNA was extracted using Tri Reagent (Sigma-Aldrich, Germany) according to manufacturer's recommendations. RNA quantification and quality control were done with NanoDrop (Nanodrop Tech, USA). Reverse transcription to cDNA was performed in a C1000 Touch Thermal Cycler (Eppendorf, Germany) using a first strand cDNA synthesis kit (Thermo Scientific, USA) and following the instructions of the manufacturer. qPCR was performed in a CFX96 Real-Time System thermocycler using SsoFast EvaGreen supermix (Bio-Rad, Hercules, CA, USA) as a detection reagent for the gene expression of RunX2, osteocalcin, osteopontin, osterix, ALP, and collagen type I (COLIAI). Primer sequences used are listed in Table 2. Gene expression is expressed as $2^{-\mathrm{ddCT}}$ relative to the housekeeper (β-tubulin) and to the control group.

2.10. Intracellular Cell Signaling Array. The intracellular cell signaling pathway was examined using the PathScan Intracellular Signaling Array Kit (Cell Signaling Technology, The Netherlands) following the manufacturer's protocol. Briefly, cells were lysed using ice-cold lysis buffer and the lysates were diluted to 1 mg protein per ml solution using array diluent buffer. Following that, 75 μl of lysate was added to nitrocellulose-coated glass slides precoated with primary antibodies. The plate was incubated overnight at 4°C. Following washing using the array wash buffer, 75 μl of detection antibody cocktail was added to each well and incubated for an hour at room temperature on an orbital shaker. Following washing steps, 75 μl of HRP-linked streptavidin was added to each well and incubated at room temperature for 30 mins on an orbital shaker. Lastly, 1x LumiGLO®/peroxide reagent was added and chemiluminescence was detected using a chemiluminescence imager (Bio-Rad, USA).

2.11. Statistical Analysis. Cell proliferation, protein content, ALP activity, and Alizarin Red S data were represented as mean ± standard error of mean (SEM). Cell signaling protein array data was represented as mean ± standard deviation (SD). The cell proliferation, protein content, ALP activity, and Alizarin Red S data were subjected to two-way analysis of variance (two-way ANOVA) and Tukey's post hoc test (GraphPad Prism 7.0). Significance level was set at $p < 0.05$. On the other hand, RT-qPCR and cell signaling array data were subjected to one-way analysis of variance (one-way ANOVA) and Student's unpaired two-tailed t-test.

3. Results

3.1. Impact of ELF-PEMF Exposure on hAMSC Proliferation. Cell proliferation was assessed by CFSE and SRB (protein content). CFSE is a membrane-permeant fluorescent dye that covalently attaches to free amines of cytoplasmic proteins, and the CFSE fluorescence within daughter cells progressively halved following each cell division [27]. On the other hand, SRB binds stoichiometrically to cellular proteins and can be easily eluted and used as a proxy for cell proliferation [28]. In all groups, cell proliferation increased steadily from day 3 to day 14. However, when compared to the control group of the same culture period, cell proliferation slightly decreased after 3 days of ELF-PEMF exposure. However, no significant differences on cell proliferation were detected between groups (Figures 2(a) and 2(b)).

3.2. Osteogenic Capabilities of hAMSC When Treated with ELF-PEMF. All cells were cultured under osteogenic media to determine if the application of ELF-PEMF would enhance the differentiation of hAMSC towards osteogenic lineage. ALP activity slightly increased for control, ELF-PEMF groups 4, 31, and 114 at day 7 compared to the respective day 3 of the group (Figure 3(a)). However, only CIT number 20 exposed group showed slight increase in ALP activity compared to control on day 3 (Figure 3(a)).

Generally, Alizarin Red S and von Kossa assays (Figures 3(b) and 4) showed that increasing the amount of mineralized matrix was formed over time in all groups, with or without ELF-PEMF exposure. It was noted that the effect of ELF-PEMF on matrix mineralization was more prominent on day 3, as all ELF-PEMF-treated groups showed 1.5- to 2.5-fold increase in Alizarin Red S staining compared to control (Figure 3(b)).

Of the ten different ELF-PEMF signals, seven (e.g., CIT numbers 10, 16, 18, 20, 64, 114, and 124) were further investigated in terms of osteogenic gene expression (Figure 5).

Cells treated with CIT numbers 20 and 124 showed significant upregulation of COLIAI after 3 days of exposure compared to control. Moreover, CIT number 20 also resulted in a significant upregulation of ALP and osteocalcin for the same time of observation. On the other hand, CIT number 18-treated cells showed significant upregulation of RunX2 expression after 7 days compared to control. Osteopontin expression levels were slightly, but not significantly, elevated

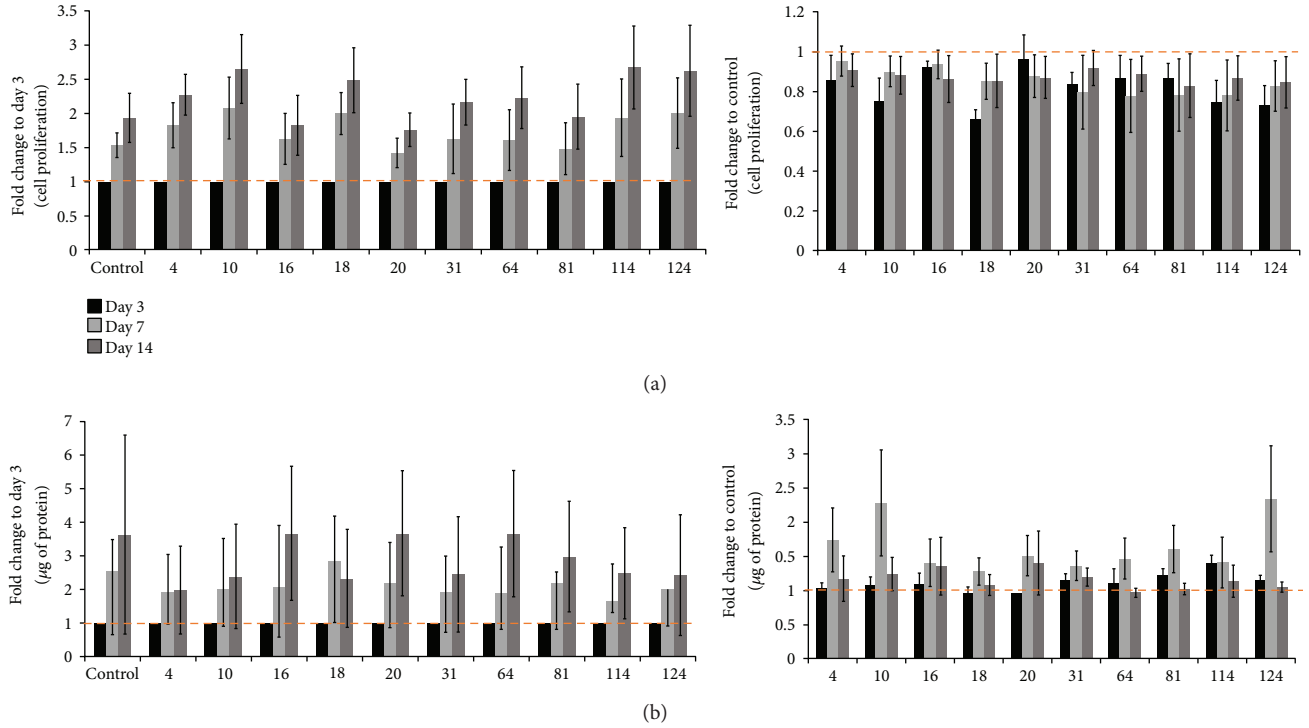

Figure 2: Graphs show fold change of (a) cell proliferation and (b) protein content to the respective day 3 of the group (left graphs) and to the control group (without ELF-PEMF exposure) of the same culture period (e.g., 3 versus 3 days, 7 versus 7 days, and 14 versus 14 days) (right graphs). Mean ± SEM, $N = 6$ donors, $n = 3$ triplicates.

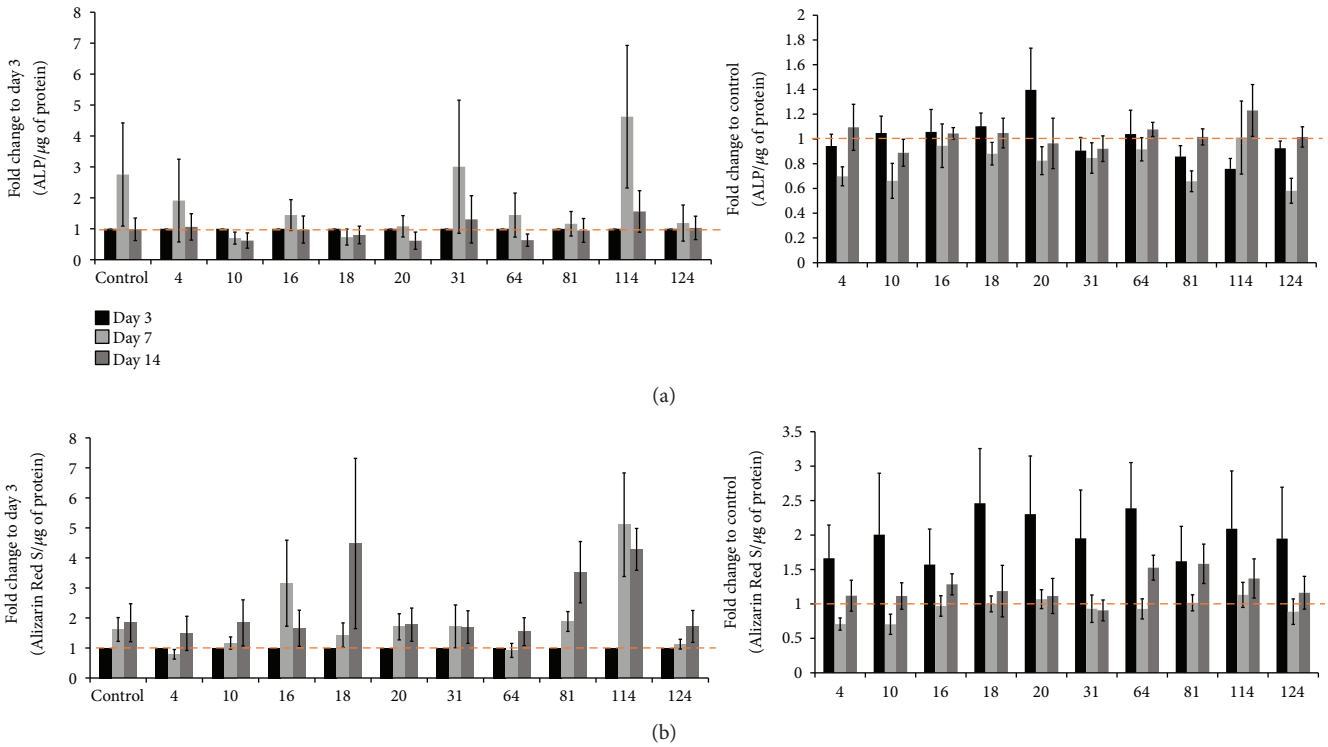

Figure 3: Graph shows fold change of (a) alkaline phosphatase (ALP) and (b) Alizarin Red S content to the respective day 3 cultured group and to the control (without ELF-PEMF exposure) of the same culture period (e.g., 3 versus 3 days, 7 versus 7 days, and 14 versus 14 days). Mean ± SEM, $N = 6$ donors, $n = 3$ triplicates.

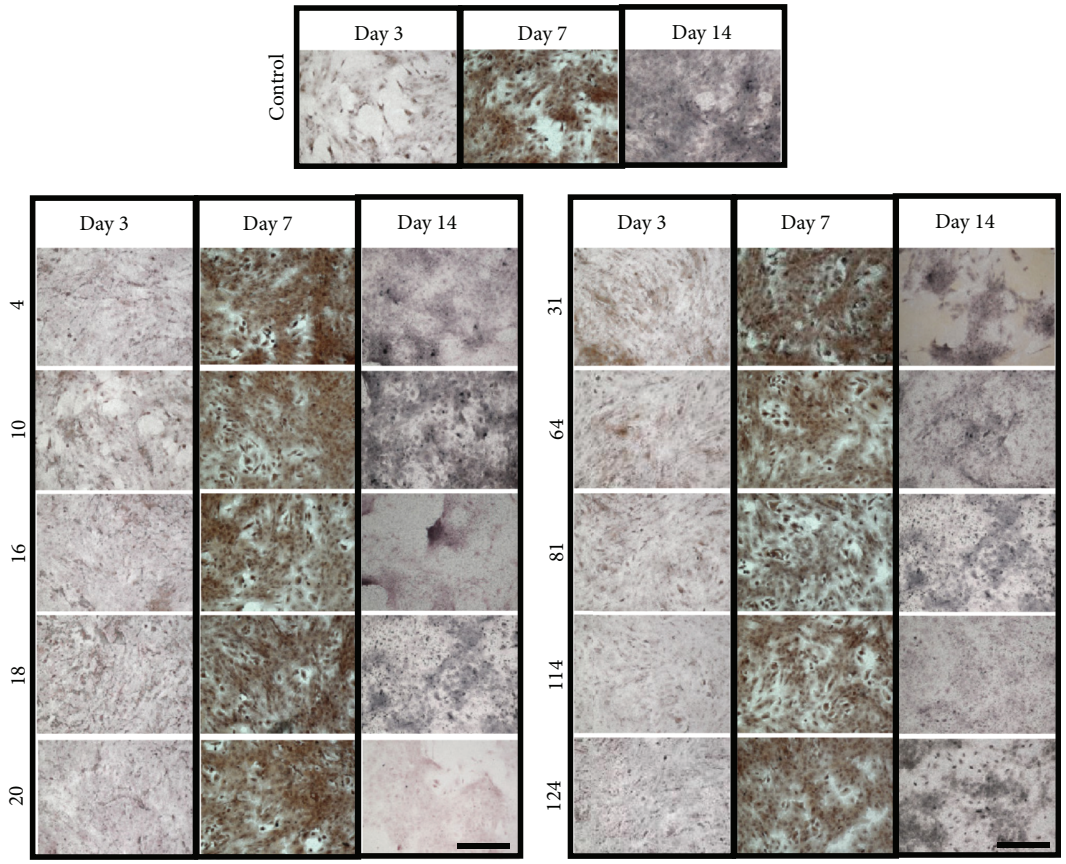

Figure 4: Representative images of culture stained with von Kossa on days 3, 7, and 14 immediately after exposure with ELF-PEMF. Control: cells without ELF-PEMF exposure. Scale bar = 500 μm.

for all ELF-PEMF groups except for CIT number 114 on both days 3 and 7 compared to control.

3.3. Effect of 26 Hz ELF-PEMF on Intracellular Cell Signaling of hAMSC. Based on the observations from part 1 of the study, it was indicated that 26 Hz ELF-PEMF (CIT number 20) shows potential of triggering osteogenesis of hAMSC (upregulation of COL1A1, ALP, and osteocalcin genes at day 3) as compared to other ELF-PEMF signals. Thus, this signal was selected for the elucidation of intracellular cell signaling pathways using a protein array. The system used allowed for the detection of 18 different proteins involved in proliferation, growth, apoptosis, and/or stress signaling when phosphorylated or cleaved. Figure 6 shows the state of various intracellular proteins measured in hAMSC treated with CIT number 20 for 7 mins. Measurements were performed either immediately (without resting period) or after 0.5, 1, 2, 3, 4, and 6 hours of resting period.

Generally, it was observed that the amount of phosphorylated Akt, AMPKα, BAD, ERK1/2, HSP27, p53, p70 S6 kinase, PRAS 40, and s6 ribosomal protein increased during exposure and gradually returned to baseline as hAMSCs were left at resting state (Figure 6). Conversely, cleavage of caspase-3 and PARP as well as phosphorylation of GSK 3β, mammalian target of rapamycin (mTOR), p38, JNK, and STAT1 did not change significantly throughout the experimental period (Figure 6). Notably, the amount of phosphorylated STAT3 significantly increased compared to the control sample and was kept almost constant for up to 6 hours after the completion of the exposure (Figure 6).

4. Discussion

Across all tested ELF-PEMF programs, none caused irreversible cytotoxicity to hAMSC as evidenced by the increasing cell proliferation and protein production over time. This observation was in line with that of intracellular signaling array. When exposed to 26 Hz ELF-PEMF (CIT number 20), a stress-related pathway was activated. This is evidenced by the increase in HSP27 activation, which has been shown to protect cells from undergoing apoptosis under stress conditions [29] through interactions with cytochrome-c or caspase-3 [30]. Additionally, p53, an antioncogenic protein, which plays an important role in response to DNA damage [31], was also activated. Notably, apoptosis was repressed, as shown by the activation of the prosurvival Akt pathway due to the lack of activation of the proapoptotic effectors caspase-3 [32] and PARP and the inactivation of the proapoptotic protein BAD.

In this study, ELF-PEMFs were applied to hAMSC cultured in osteogenic-conditioned media to elucidate the potential of ELF-PEMF in acceleration of hAMSC osteogenesis differentiation. All groups (including control) show a general increase of mineralized matrix over time. However,

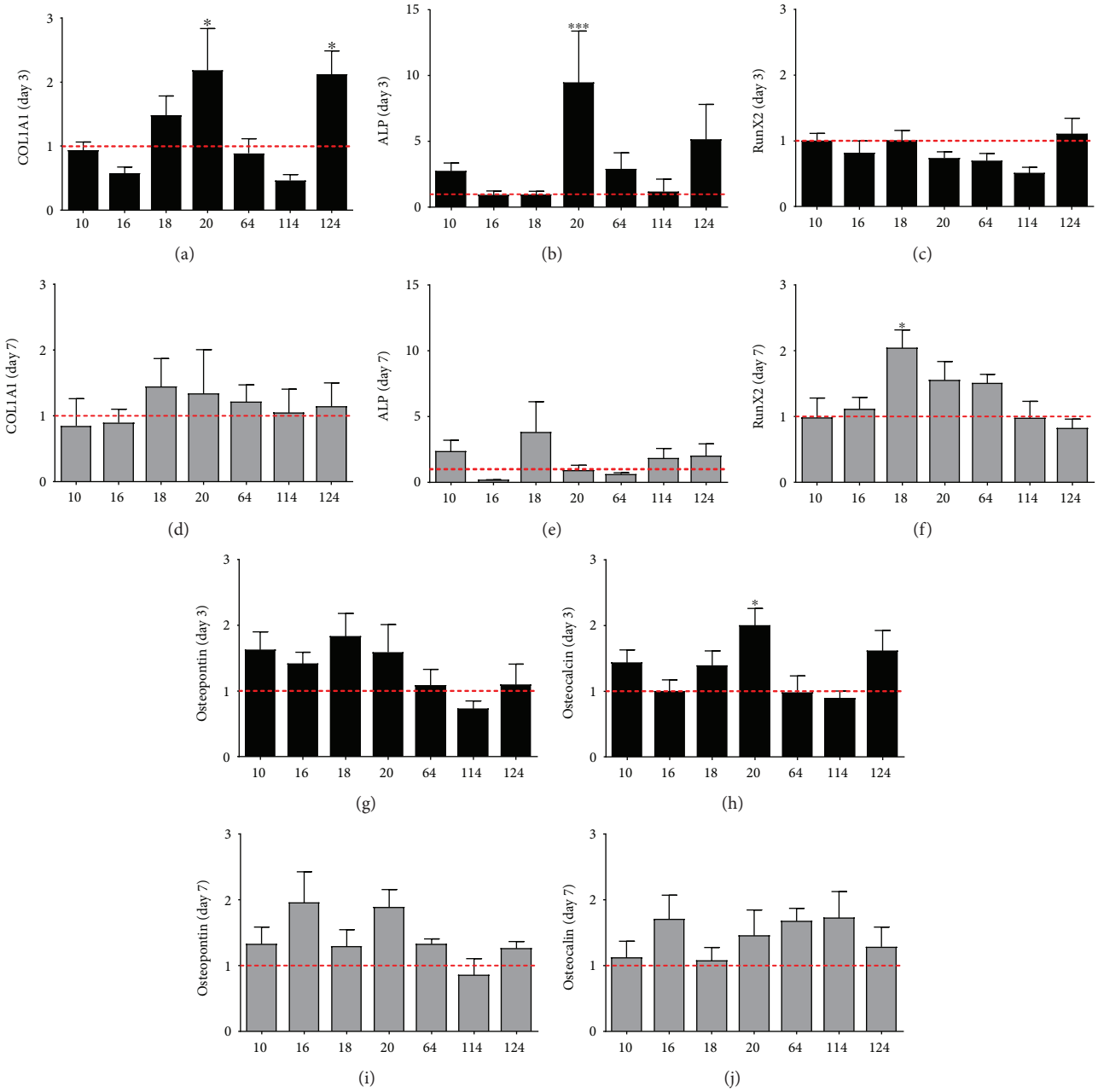

FIGURE 5: Graph showing the relative gene expression of (a, d) COLIAI, (b, e) alkaline phosphatase (ALP), (c, f) RunX2, (g, i) osteopontin, and (h, j) osteocalcin after (a–c, g, h) 3 and (d–f, i, j) 7 days in culture under the various ELF-PEMF signals. Data were plotted as fold change to control of the same culture period, represented by the dotted line ($y = 1$). Mean ± SEM, $N = 5$ donors, $n = 3$ triplicates ($^{*}p < 0.05$ and $^{***}p < 0.001$).

only prominent differences in terms of extent of mineralization were observed on day 3 in ELF-PEMF-treated groups compared to control. This indicated that ELF-PEMFs do elicit a positive response towards hAMSC matrix mineralization. However, in our experiments, we noted a dramatic difference in terms of the capability to form mineralized matrix among the different donor hAMSC as reflected in the relatively large deviation (Figure 3) and von Kossa staining of different donor hAMSC with and without ELF-PEMF exposures (Figure 4).

At the gene level, it was observed that hAMSC exposed to 26 Hz ELF-PEMF (CIT number 20) exhibited a more prominent differentiation into osteogenic lineage compared to other exposure groups as evidenced by the increase in ALP (an early marker for osteoblast progenitors), COLIAI (collagen type I, the most abundant ECM protein in bone tissue), and osteocalcin (secreted by mature osteoblasts and commonly used to represent terminal osteoblast differentiation) gene expression after 3 days of exposure. The temporal expression of osteogenic-related genes can be utilized to

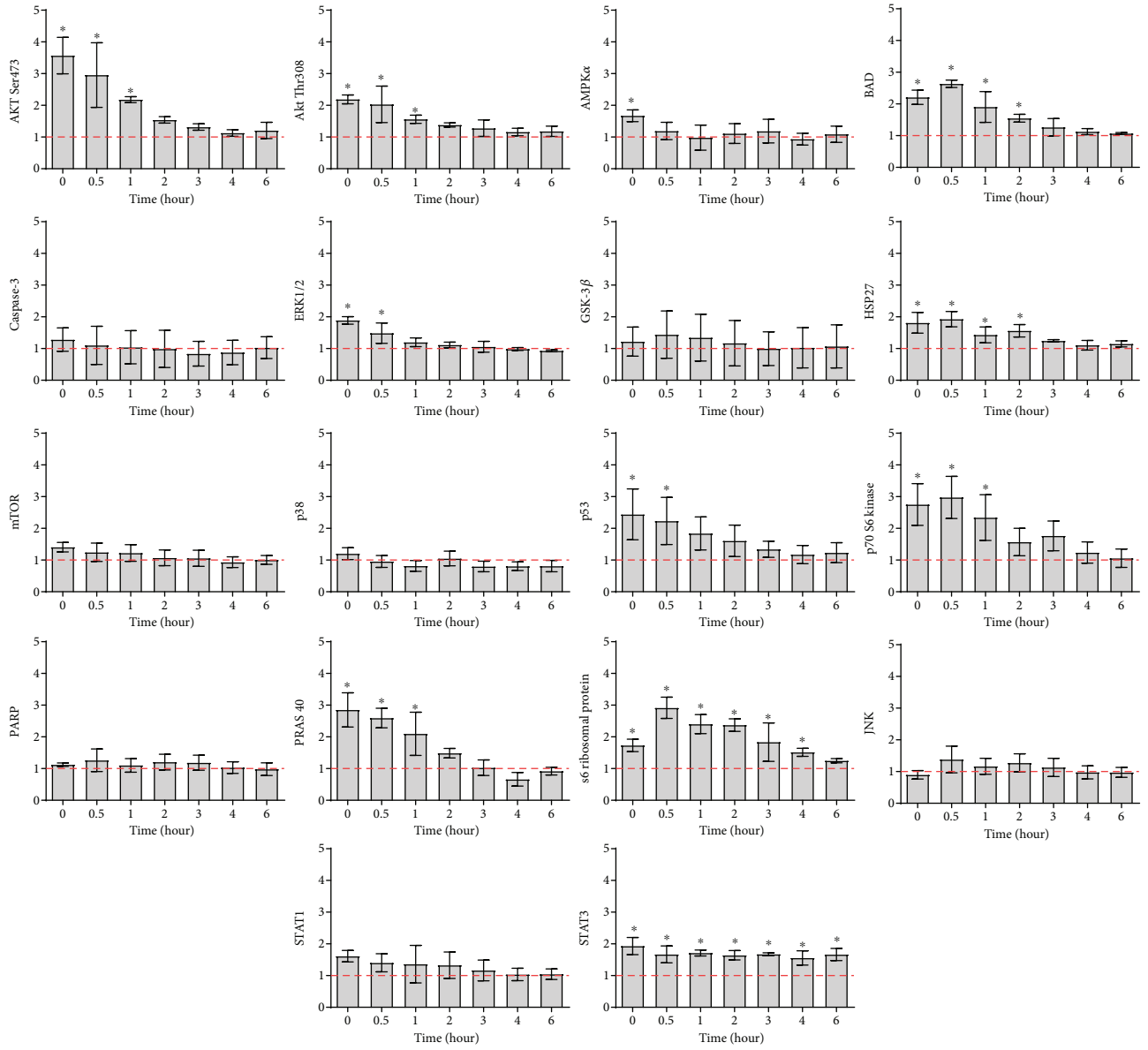

Figure 6: Graph shows the levels of key phosphorylated/cleaved proteins involved in the Akt, MAPK/ERK, and caspase signaling pathways in hAMSC subjected to 26 Hz ELF-PEMF (CIT number 20) exposure in osteogenic media. Protein quantification was examined immediately, 0.5, 1, 2, 3, 4, or 6 hours after the completion of the ELF-PEMF exposure. Data were plotted as fold change to control (hAMSC culture in osteogenic media without ELF-PEMF exposure), represented by the line ($y = 1$). Mean ± SD, $N = 2$ donors, $n = 4$ replicates. $^{*}p < 0.05$ compared to control.

characterize osteoblasts' maturation process [33]. This indicated that CIT program number 20 is relatively more effective when compared to other tested ELF-PEMF programs in inducing hAMSC towards the osteogenic lineage.

Based on the gene expression profiles, a protein array was chosen to further elucidate the underlying intercellular signaling pathways that lead to enhanced hAMSC potential for osteogenic differentiation. Akt signaling cascade was activated in hAMSC when exposed to 26 Hz ELF-PEMF (CIT number 20), marked by the increased levels of phosphorylated Akt at Ser473 and Thr308, p70 S6 kinase, and S6 ribosomal protein [34]. On the other hand, there were no significant changes in the levels of phosphorylated mTOR after exposure. However, it is well established that mTOR regulates protein synthesis through the phosphorylation and activation of S6 kinase, which is used as a readout of mTOR activity [34].

Our results also suggest coactivation of ERK 1/2 signaling pathway in hAMSC exposed to 26 Hz ELF-PEMF, as shown by the increased levels of phosphorylated ERK1/2 shortly after exposure. Studies have reported that the Akt [35] and ERK1/2 [36] signaling pathways can be activated during cell stress to prevent cell death and work synergistically to promote cell proliferation and protein translation [37]. This happens because Akt activation promotes nuclear export of p21cip1 into the cytoplasm, where it is degraded by the

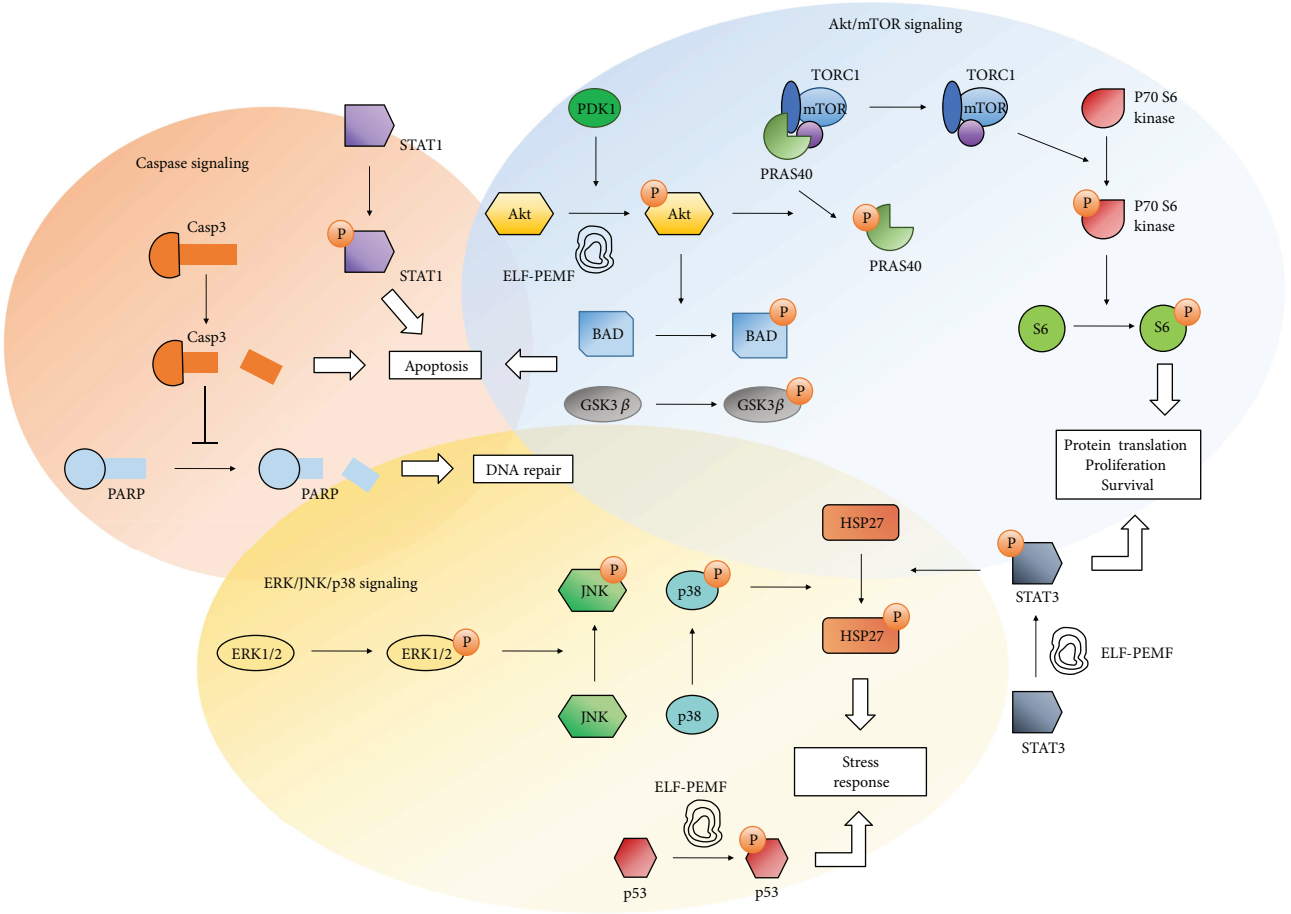

Figure 7: Illustration of the intracellular signaling pathways investigated on human adipose-derived mesenchymal stromal cells when subjected to ELF-PEMF. The coactivation of ERK and Akt in response to CIT program number 20 exposure promoted cell growth and survival and prevented apoptosis despite of certain levels of cellular stress.

proteasome. As a result, p21cip1 levels decrease and the cell cycle arrest ceases [38]. These observations suggest that a combination of ERK and Akt activation (Figure 7) in response to 26 Hz ELF-PEMF promoted hAMSC growth and survival and prevented apoptosis despite of certain levels of cellular stress. This hypothesis is supported by the observed long-lasting phosphorylation of STAT3, a crucial transcription factor implicated in the maintenance and antiapoptotic status of cells [22]. It is noted that further experiments are required to confirm these initial observations.

Recently, using the same ELF-PEMF device, Ehnert et al. [24] demonstrated that primary human osteoblasts subjected to 16 Hz ELF-PEMF (CIT number 16) exposure showed better viability and maturation through the activation of the ERK1/2 signaling cascade. On the contrary, it did not affect osteoclast viability and maturation. Furthermore, antioxidative defense mechanisms could be induced by the same ELF-PEMF signal as reported by Ehnert et al. [24]. More recently, Ehnert et al. [26] also showed the potential of ELF-PEMF 16 Hz (CIT number 16) and 26 Hz (CIT number 20) in promoting osteogenesis in coculture of osteoblasts and MSCs and an increase in osteoclast activity when exposed to 26 Hz ELF-PEMF (CIT number 20). Collectively, these data indicate how cells of different lineages respond differently to ELF-PEMF signals. Future studies will be performed on a more complex culture system (e.g., co-/triculture model incorporating osteoblasts, osteoclasts, and monocytes/macrophages) to elucidate a more effective ELF-PEMF signal and spatial configuration, which can exert a net positive bone formation response.

Data Availability

The quantitative data from, that is, ALP, RT-qPCR, and intracellular signaling pathway array used to support the findings of this study are available from the corresponding author upon reasonable request. The ELF-PEMF signal pattern data used to support the findings of this study were supplied by Sachtleben GmbH, Hamburg, Germany, and so cannot be made freely available. Requests for access to these data should be made to Karsten Falldorf at falldorf@citresearch.de.

Conflicts of Interest

Karsten Falldorf is an employee of Sachtleben GmbH. All other authors declare that they have no conflicts of interest.

Acknowledgments

This study was funded by Sachtleben GmbH. This work was supported by the German Research Foundation (DFG) and the Technical University of Munich (TUM) in the framework of the Open Access Publishing Program.

References

[1] R. C. Nordberg and E. G. Loboa, "Our fat future: translating adipose stem cell therapy," *Stem Cells Translational Medicine*, vol. 4, no. 9, pp. 974–9, 2015.

[2] M. W. Morcos, H. Al-Jallad, and R. Hamdy, "Comprehensive review of adipose stem cells and their implication in distraction osteogenesis and bone regeneration," *BioMed Research International*, vol. 2015, Article ID 842975, 20 pages, 2015.

[3] H. J. Yang, R. Y. Kim, and S. J. Hwang, "Pulsed electromagnetic fields enhance bone morphogenetic protein-2 dependent-bone regeneration," *Tissue Engineering Part A*, vol. 21, no. 19-20, pp. 2629–2637, 2015.

[4] M. Hronik-Tupaj and D. L. Kaplan, "A review of the responses of two- and three-dimensional engineered tissues to electric fields," *Tissue Engineering Part B, Reviews*, vol. 18, no. 3, pp. 167–180, 2012.

[5] R. K. Aaron, D. M. Ciombor, and B. J. Simon, "Treatment of nonunions with electric and electromagnetic fields," *Clinical Orthopaedics and Related Research*, vol. 419, no. 419, pp. 21–29, 2004.

[6] S. B. Behrens, M. E. Deren, and K. O. Monchik, "A review of bone growth stimulation for fracture treatment," *Current Orthopaedic Practice*, vol. 24, no. 1, pp. 84–91, 2013.

[7] M.-T. Tsai, W.-J. Li, R. S. Tuan, and W. H. Chang, "Modulation of osteogenesis in human mesenchymal stem cells by specific pulsed electromagnetic field stimulation," *Journal of orthopaedic research*, vol. 27, no. 9, pp. 1169–1174, 2009.

[8] L. Fassina, L. Visai, F. Benazzo et al., "Effects of electromagnetic stimulation on calcified matrix production by SAOS-2 cells over a polyurethane porous scaffold," *Tissue Engineering*, vol. 12, no. 7, pp. 1985–1999, 2006.

[9] N. Selvamurugan, S. Kwok, A. Vasilov, S. C. Jefcoat, and N. C. Partridge, "Effects of BMP-2 and pulsed electromagnetic field (PEMF) on rat primary osteoblastic cell proliferation and gene expression," *Journal of Orthopaedic Research*, vol. 25, no. 9, pp. 1213–1220, 2007.

[10] M. T. Tsai, W. H. S. Chang, K. Chang, R. J. Hou, and T. W. Wu, "Pulsed electromagnetic fields affect osteoblast proliferation and differentiation in bone tissue engineering," *Bioelectromagnetics*, vol. 28, no. 7, pp. 519–528, 2007.

[11] P. Diniz, K. Shomura, K. Soejima, and G. Ito, "Effects of pulsed electromagnetic field (PEMF) stimulation on bone tissue like formation are dependent on the maturation stages of the osteoblasts," *Bioelectromagnetics*, vol. 23, no. 5, pp. 398–405, 2002.

[12] S. D. McCullen, J. P. McQuilling, R. M. Grossfeld, J. L. Lubischer, L. I. Clarke, and E. G. Loboa, "Application of low-frequency alternating current electric fields via interdigitated electrodes: effects on cellular viability, cytoplasmic calcium, and osteogenic differentiation of human adipose-derived stem cells," *Tissue Engineering Part C, Methods*, vol. 16, no. 6, pp. 1377–1386, 2010.

[13] K. Lim, J. Hexiu, J. Kim et al., "Effects of electromagnetic fields on osteogenesis of human alveolar bone-derived mesenchymal stem cells," *BioMed Research International*, vol. 2013, Article ID 296019, 14 pages, 2013.

[14] G. Ceccarelli, N. Bloise, M. Mantelli et al., "A comparative analysis of the *in vitro* effects of pulsed electromagnetic field treatment on osteogenic differentiation of two different mesenchymal cell lineages," *BioResearch Open Access*, vol. 2, no. 4, pp. 283–294, 2013.

[15] A. Ongaro, A. Pellati, L. Bagheri, C. Fortini, S. Setti, and M. De Mattei, "Pulsed electromagnetic fields stimulate osteogenic differentiation in human bone marrow and adipose tissue derived mesenchymal stem cells," *Bioelectromagnetics*, vol. 35, no. 6, pp. 426–436, 2014.

[16] K. S. Kang, J. M. Hong, J. A. Kang, J. W. Rhie, Y. H. Jeong, and D. W. Cho, "Regulation of osteogenic differentiation of human adipose-derived stem cells by controlling electromagnetic field conditions," *Experimental & Molecular Medicine*, vol. 45, no. 1, article e6, 2013.

[17] K. S. Kang, J. M. Hong, Y. J. Seol, J. W. Rhie, Y. H. Jeong, and D. W. Cho, "Short-term evaluation of electromagnetic field pretreatment of adipose-derived stem cells to improve bone healing," *Journal of Tissue Engineering and Regenerative Medicine*, vol. 9, no. 10, pp. 1161–1171, 2015.

[18] N. A. Walker, C. R. Denegar, and J. Preische, "Low-intensity pulsed ultrasound and pulsed electromagnetic field in the treatment of tibial fractures: a systematic review," *Journal of Athletic Training*, vol. 42, no. 4, pp. 530–535, 2007.

[19] National Research Council, *Assessment of the Possible Health Effects of Ground Wave Emergency Network*, The National Academies Press, Washington, DC, USA, 1993.

[20] A. Bahaodini, M. Owjfard, A. Tamadon, and S. M. Jafari, "Low frequency electromagnetic fields long-term exposure effects on testicular histology, sperm quality and testosterone levels of male rats," *Asian Pacific Journal of Reproduction*, vol. 4, no. 3, pp. 195–200, 2015.

[21] N. Erdal, S. Gürgül, L. Tamer, and L. Ayaz, "Effects of long-term exposure of extremely low frequency magnetic field on oxidative/nitrosative stress in rat liver," *Journal of Radiation Research*, vol. 49, no. 2, pp. 181–187, 2008.

[22] H. Song, S. P. Ethier, M. L. Dziubinski, and J. Lin, "Stat3 modulates heat shock 27 kDa protein expression in breast epithelial cells," *Biochemical and Biophysical Research Communications*, vol. 314, no. 1, pp. 143–150, 2004.

[23] S. Schneider, M. Unger, M. van Griensven, and E. R. Balmayor, "Adipose-derived mesenchymal stem cells from liposuction and resected fat are feasible sources for regenerative medicine," *European Journal of Medical Research*, vol. 22, no. 1, p. 17, 2017.

[24] S. Ehnert, K. Falldorf, A.-K. Fentz et al., "Primary human osteoblasts with reduced alkaline phosphatase and matrix mineralization baseline capacity are responsive to extremely low frequency pulsed electromagnetic field exposure — clinical implication possible," *Bone Reports*, vol. 3, pp. 48–56, 2015.

[25] S. Ehnert, A.-K. Fentz, A. Schreiner et al., "Extremely low frequency pulsed electromagnetic fields cause antioxidative defense mechanisms in human osteoblasts via induction of $\bullet O_2^-$ and H_2O_2," *Scientific Reports*, vol. 7, no. 1, article 14544, 2017.

[26] S. Ehnert, M. van Griensven, M. Unger et al., "Co-culture with human osteoblasts and exposure to extremely low frequency pulsed electromagnetic fields improve osteogenic

differentiation of human adipose-derived mesenchymal stem cells," *International Journal of Molecular Sciences*, vol. 19, no. 4, p. 944, 2018.

[27] A. B. Lyons, "Analysing cell division in vivo and in vitro using flow cytometric measurement of CFSE dye dilution," *Journal of Immunological Methods*, vol. 243, no. 1-2, pp. 147–154, 2000.

[28] E. A. Orellana and A. L. Kasinski, "Sulforhodamine B (SRB) assay in cell culture to investigate cell proliferation," *Bio-protocol*, vol. 6, no. 21, article e1984, 2016.

[29] D. Lanneau, A. de Thonel, S. Maurel, C. Didelot, and C. Garrido, "Apoptosis versus cell differentiation: role of heat shock proteins HSP90, HSP70 and HSP27," *Prion*, vol. 1, no. 1, pp. 53–60, 2007.

[30] P. Pandey, R. Farber, A. Nakazawa et al., "Hsp27 functions as a negative regulator of cytochrome c-dependent activation of procaspase-3," *Oncogene*, vol. 19, no. 16, pp. 1975–1981, 2000.

[31] D. Lane and S. Benchimol, "p53: oncogene or anti-oncogene?," *Genes & Development*, vol. 4, no. 1, pp. 1–8, 1990.

[32] A. G. Porter and R. U. Jänicke, "Emerging roles of caspase-3 in apoptosis," *Cell Death and Differentiation*, vol. 6, no. 2, pp. 99–104, 1999.

[33] T. A. Owen, M. Aronow, V. Shalhoub et al., "Progressive development of the rat osteoblast phenotype in vitro: reciprocal relationships in expression of genes associated with osteoblast proliferation and differentiation during formation of the bone extracellular matrix," *Journal of Cellular Physiology*, vol. 143, no. 3, pp. 420–430, 1990.

[34] N. Hay and N. Sonenberg, "Upstream and downstream of mTOR," *Genes & Development*, vol. 18, no. 16, pp. 1926–1945, 2004.

[35] D. Vauzour, K. Vafeiadou, C. Rice-Evans, R. J. Williams, and J. P. E. Spencer, "Activation of pro-survival Akt and ERK1/2 signalling pathways underlie the anti-apoptotic effects of flavanones in cortical neurons," *Journal of Neurochemistry*, vol. 103, no. 4, pp. 1355–1367, 2007.

[36] K. Balmanno and S. J. Cook, "Tumour cell survival signalling by the ERK1/2 pathway," *Cell Death and Differentiation*, vol. 16, no. 3, pp. 368–377, 2008.

[37] J.-C. Chambard, R. Lefloch, J. Pouysségur, and P. Lenormand, "ERK implication in cell cycle regulation," *Biochimica et Biophysica Acta (BBA) - Molecular Cell Research*, vol. 1773, no. 8, pp. 1299–1310, 2007.

[38] A. M. Mirza, S. Gysin, N. Malek, K. I. Nakayama, J. M. Roberts, and M. McMahon, "Cooperative regulation of the cell division cycle by the protein kinases RAF and AKT," *Molecular and Cellular Biology*, vol. 24, no. 24, pp. 10868–10881, 2004.

Hindawi
Stem Cells International
Volume 2018, Article ID 7146384, 11 pages
https://doi.org/10.1155/2018/7146384

Research Article

Treatment of Full-Thickness Rotator Cuff Tendon Tear Using Umbilical Cord Blood-Derived Mesenchymal Stem Cells and Polydeoxyribonucleotides in a Rabbit Model

Dong Rak Kwon,[1] **Gi-Young Park**,[1] **and Sang Chul Lee**[2]

[1]*Department of Rehabilitation Medicine, Catholic University of Daegu School of Medicine, Daegu, Republic of Korea*
[2]*Department and Research Institute of Rehabilitation Medicine, Yonsei University College of Medicine, Seoul, Republic of Korea*

Correspondence should be addressed to Sang Chul Lee; bettertomo@yuhs.ac

Received 27 December 2017; Revised 29 March 2018; Accepted 11 April 2018; Published 15 May 2018

Academic Editor: Andrea Ballini

Copyright © 2018 Dong Rak Kwon et al. This is an open access article distributed under the Creative Commons Attribution License, which permits unrestricted use, distribution, and reproduction in any medium, provided the original work is properly cited.

Objective. The aim of this study was to investigate regenerative effects of ultrasound- (US-) guided injection with human umbilical cord blood-derived mesenchymal stem cells (UCB-MSCs) and/or polydeoxyribonucleotide (PDRN) injection in a chronic traumatic full-thickness rotator cuff tendon tear (FTRCTT) in a rabbit model. *Methods*. Rabbits ($n = 32$) were allocated into 4 groups. After a 5 mm sized FTRCTT just proximal to the insertion site on the subscapularis tendon was created by excision, the wound was immediately covered by a silicone tube to prevent natural healing. After 6 weeks, 4 injectants (0.2 mL normal saline, G1-SAL; 0.2 mL PDRN, G2-PDRN; 0.2 mL UCB-MSCs, G3-MSC; and 0.2 mL UCB-MSCs with 0.2 ml PDRN, G4-MSC + PDRN) were injected into the FTRCTT under US guidance. We evaluated gross morphologic changes on all rabbits after sacrifice. Masson's trichrome, anti-type 1 collagen antibody, bromodeoxyuridine, proliferating cell nuclear antigen, vascular endothelial growth factor, and platelet endothelial cell adhesion molecule stain were performed to evaluate histological changes. Motion analysis was also performed. *Results*. The gross morphologic mean tendon tear size in G3-MSC and G4-MSC + PDRN was significantly smaller than that in G1-SAL and G2-PDRN ($p < 0.05$). However, there were no significant differences in the tendon tear size between G3-MSC and G4-MSC + PDRN. In G4-MSC + PDRN, newly regenerated collagen type 1 fibers, proliferating cell activity, angiogenesis, walking distance, fast walking time, and mean walking speed were greater than those in the other three groups on histological examination and motion analysis. *Conclusions*. Coinjection of UCB-MSCs and PDRN was more effective than UCB-MSC injection alone in histological and motion analysis in a rabbit model of chronic traumatic FTRCTT. However, there was no significant difference in gross morphologic change of tendon tear between UCB-MSCs with/without PDRN injection. The results of this study regarding the combination of UCB-MSCs and PDRN are worth additional investigations.

1. Introduction

Rotator cuff tendon tears (RCTTs) are the most common tendon injury in adults and affect about 30% of people over 60 years of age [1]. Although surgical repair of a RCTT is one of the most common orthopedic procedures, the failure rate for rotator cuff tendon repair ranges widely from 20% to 90% [2]. The current therapeutic approaches do not achieve physiological restoration of the RCTT, and the quality of the repaired tendon is not optimal [3]. These deficiencies have driven attempts to regenerate RCTT with the use of biological adjuvants. Mesenchymal stem cells (MSCs) have been proposed as an attractive alternative to overcome the limitations of the current treatments [4]. Of the various MSCs, human umbilical cord blood-derived MSCs (UCB-MSC) have a greater therapeutic potential than MSCs derived from other tissues because of attributes that include the ability to home in on injured tissue, low immunogenicity, multidirectional differentiation, and extensive secretion profiles [5]. The function of autologous MSCs in patients with advanced age or significant comorbidities is impaired, and allogeneic UCB-MSCs may therefore be of particular benefit

in the elderly or those with multiple comorbidities [6]. In addition, UCB-MSCs can be produced commercially in larger quantities with the same quality.

Polydeoxyribonucleotide (PDRN) is a biological adjuvant which has the same advantages as UCB-MSCs in terms of commercial mass production. PDRN is a mixture of DNA polymers featuring a chain with length ranging from 50 to 2000 bp. It is extracted from the trout sperm and purified as a preparation containing a high percentage of DNA. PDRN is a source of pyrimidines and purines and stimulates nucleic acid synthesis through the salvage pathway [7]. PDRN can induce angiogenesis and collagen synthesis and also has an anti-inflammatory activity [8]. One recently published study reported the effectiveness of PDRN in the treatment of chronic rotator cuff disease [9].

The aim of our study was to evaluate the efficacy of UCB-MSCs and/or PDRN injections in regenerating RCT in a rabbit model. This is the first report to compare the regenerative effects of stem cell and PDRN in a model of RCTT.

2. Material and Methods

2.1. Animal Model. Twelve-week-old, male, New Zealand white rabbits ($n = 32$) were housed in separate metal cages at a temperature of $23 \pm 2^{\circ}$C and a relative humidity of $45 \pm 10\%$. They had free access to tap water and were fed a commercial rabbit diet. None of the rabbits received additional exercise, and all were allowed to do normal activities in a $65 \times 45 \times 30$ cm cage. Animal experiments were performed in accordance with internationally accredited guidelines and approved by the University of School of Medicine Animal Care and Use Committee.

Anesthesia was induced using isoflurane (JW Pharmaceutical, Goyang, South Korea) vaporized in oxygen and delivered using a large animal cycling system. Under general anesthesia, 5 mm diameter full-thickness RCTTs (FTRCTTs) were created just proximal to the insertion site on the left subscapularis tendon by punch biopsy excision using a Biopsy Punch 5 mm LZ (SFM, Wächtersbach, Germany). Each excision wound was immediately covered with a resorbable round silicone Penrose drainage tube (Sewoon Medical Co. Ltd., Cheonan, South Korea) to induce a chronic rotator cuff tear. The incision was closed using subcutaneous and skin sutures [10].

2.2. Mesenchymal Stem Cells. UCB was collected from the umbilical veins of pregnant women after neonatal delivery with informed consent. MSCs were isolated from the UCB and cultivated [11, 12]. The cells expressed cluster of differentiation 105 (CD105, 96.93%), CD90 (98.96%), CD29 (98.26%), CD166 (81.29%), CD73 (83.49%), CD45 (0.26%), CD14 (1.0%), and human leukocyte antigen D related (HLA-DR, 0.18%). They also expressed pluripotent markers including octamer-binding transcription factor 4 (30.5%) and stage-specific embryonic antigen 4 (67.7%). UCB-MSCs can differentiate into cell types including respiratory epithelium, osteoblasts, chondrocytes, and adipocytes with specific in vitro induction stimuli [13–15]. We confirmed the differentiation potential and karyotypic stability of the UCB-MSCs up to passage 11. UCB-MSCs were mixed with viscous hyaluronic acid.

2.3. Animal Grouping and Injection. Six weeks after the excisions, the inserted tubes were removed to induce chronic FTRCTT. The site of each full-thickness subscapularis tendon tear was confirmed, and the incision was using subcutaneous and skin sutures. Rabbits were randomly allocated into four treatment groups ($n = 8$ per group) 6 weeks after excision. Group 1 (G1-SAL) was injected with 0.2 mL of normal saline, group 2 (G2-PDRN) with 0.2 mL commercially obtained PDRN (Hidr, BMI Korea, Seoul, Korea; Figure 1(a)), group 3 (G3-MSC) with 0.2 mL (1×106 cells) UCB-MSCs (Figures 1(b)–1(d)), and group 4 (G4-MSC + PDRN) with 0.2 mL UCB-MSCs and 0.2 mL PDRN. All rabbits were euthanized 4 weeks postinjection (Figure 2). All injections were performed under ultrasound (US) guidance using an US system with an 18~5 MHz multifrequency linear transducer (EPIQ 5; Philips Healthcare, Andover, MA, USA). No medication was administered, and all rabbits were immobilized in the equinus position using an elastic bandage for 2 days after the injection.

2.4. Gross Morphology Examination. Gross morphologic examinations were conducted after each rabbit was euthanized. Each tendon tear was classified as partial or full thickness. Gross morphologic tendon tears were photographed to the subscapularis tendon tear using a clear plastic ruler near the center of the tear site to permit calculation of size using ImageJ software (National Institute of Health, Bethesda, MD) by tracing the outlined tear edge preinjection and at 4 weeks postinjection.

2.5. Histological Examination Tissue Preparation. The rabbits were sacrificed under general anesthesia after all intramuscular injections. The tear area of the subscapularis tendon was segmented and fixed with neutral-buffered formalin for 24 hours. Each specimen was embedded in paraffin (Paraplast; Oxford, St. Louis, MO, USA) and sliced sagittally into 5 μm thick serial sections. The specimens were stained with hematoxylin-eosin (H-E) and Masson's Trichrome (MT) stains and examined by light microscopy.

2.6. Immunohistochemistry. Immunohistochemical staining of tendon sections was done for collagen fibers using mouse anti-collagen 1 monoclonal antibody (COL-1, Abcam, Cambridge, UK) and for the marker of proliferating cells using 5-bromo-2′-deoxyuridine (BrdU; Cayman Chemical, Ann Arbor, MI, USA). To accomplish BrdU staining, rabbits were postoperatively given 25 mg/kg BrdU intraperitoneally. Twenty-four hours later, each rabbit was sacrificed and paraffin-embedded sections were prepared. The sections were incubated in 0.1% trypsin for 10 minutes at 37°C and 1 N HCl for 30 minutes at 56°C to denature the DNA. Endogenous peroxidases were inhibited by preincubation in 0.3% hydrogen peroxide (H_2O_2) in phosphate-buffered saline (PBS) for 30 minutes, and nonspecific protein binding was blocked in PBS containing 10% normal horse serum (Vector Laboratories, Burlingame, CA, USA) for 30 minutes. The sections were incubated in monoclonal anti-BrdU (1 : 100,

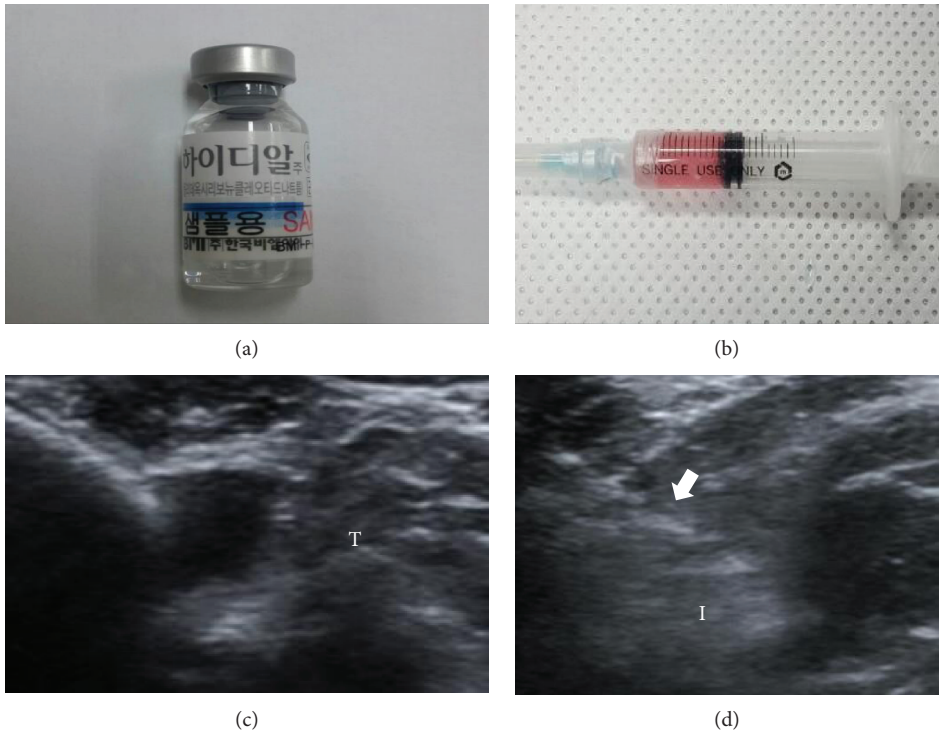

Figure 1: Human umbilical cord blood-derived mesenchymal stem cells (MSCs), polydeoxyribonucleotide (PDRN), and ultrasound images. (a) PDRN. (b) MSCs. (c) Injection was made in the left shoulder subscapularis full-thickness tears under ultrasound guidance. (d) Longitudinal ultrasound image shows the needle (arrow) in the left shoulder subscapularis of the rabbit. T: tendon; I: injectant.

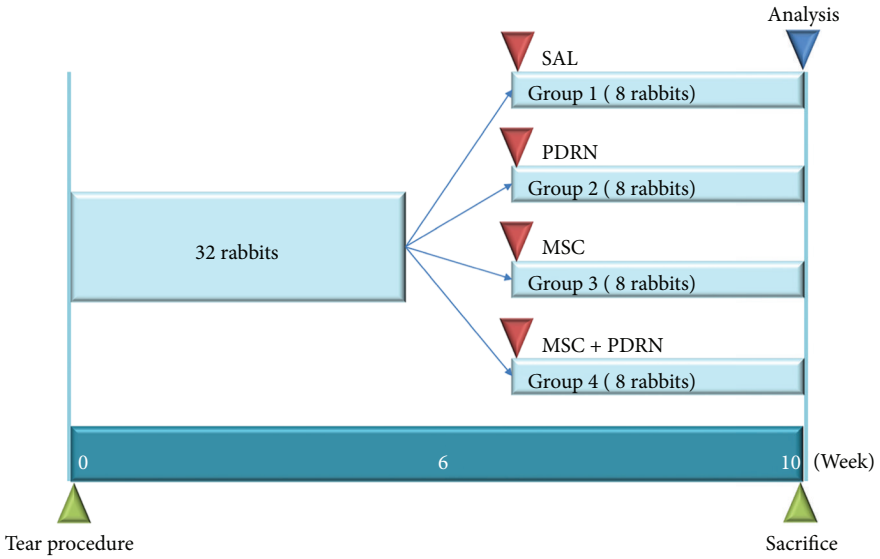

Figure 2: Timeline of saline, PDRN, MSC, and PDRN with MSC injection. Normal saline (0.2 mL; group 1: SAL), PDRN (0.2 mL; group 2: PDRN), MSC (0.2 mL; group 3: MSC), and MSCs with PDRN (both 0.2 mL; group 4: MSC + PDRN) were injected under ultrasound guidance into the left shoulder subscapularis full-thickness tears 6 weeks after the tears were created. The analysis including gross morphology of tear site, histologic examination, and motion analysis was performed 4 weeks after injection of four different solutions. All rabbits were euthanized by carbon monoxide inhalation 4 weeks after injection of the different solutions. PDRN: polydeoxyribonucleotide; MSC: human umbilical cord blood-derived mesenchymal stem cell.

Sigma-Aldrich, St. Louis, MO, USA) for 2 hours at room temperature and washed three times with PBS. The secondary antibody (1 : 100), biotinylated anti-mouse IgG (Vector Laboratories), was placed on the sections for 1 hour at room temperature, followed by three washes with PBS. Avidin-biotin-peroxidase complex (ABC, Vector Laboratories) was placed on the sections for 1 hour, followed by three PBS washes, and further followed by a peroxidase reaction using

0.05 M Tris-HCl (pH 7.6) containing 0.01% H_2O_2 and 0.05% 3,3′-diaminobenzidine (Sigma-Aldrich). The sections were counterstained with hematoxylin and then mounted. The slides were examined with Axiophot Photomicroscope (Carl Zeiss, Germany) and AxioCam MRc5 (Carl Zeiss, Germany). The number of immunopositive cells or nuclei was counted.

The tendon sections were stained for the marker of proliferating cells using mouse anti-proliferating cell nuclear antigen monoclonal antibody (PCNA, PC10, Santa Cruz Biotechnology, Santa Cruz, CA, USA), angiogenic markers using anti-vascular endothelial cell growth factor polyclonal antibody (VEGF, A-20, Santa Cruz Biotechnology), and anti-platelet endothelial cell adhesion molecule-1 polyclonal antibody (PECAM-1, M-20, Santa Cruz Biotechnology). Sections were immunostained for the marker of type I and type III collagen fibers using either mouse COL-I or mouse COL III. The paraffin-embedded sections were cleared, dehydrated, and washed with PBS. Antigen retrieval was performed using ethylenediaminetetraacetic acid (EDTA) buffer (1 mM EDTA, pH 8.0) for 30 minutes at 95°C followed by cooling. Endogenous peroxidases were inhibited by preincubation in 0.3% H_2O_2 in PBS for 30 minutes, and nonspecific protein binding was blocked in PBS containing 10% normal horse serum for 30 minutes. The sections were incubated in primary antibodies (1 : 100 ~ 1 : 200) for 2 hours at room temperature and washed three times with PBS. The secondary antibody (1 : 100), biotinylated anti-mouse IgG or biotinylated anti-rabbit IgG or biotinylated anti-goat IgG (Vector Laboratories), was placed on the sections for 1 hour at room temperature and washed three times with PBS. Sections were exposed to ABC for 1 hour, washed three times with PBS, and subjected to a peroxidase reaction using 0.05 M Tris-HCl (pH 7.6) containing 0.01% H_2O_2 and 0.05% 3,3′-diaminobenzidine (DAB, Sigma-Aldrich). The sections were counterstained with hematoxylin and then mounted. The slides were examined using an Axiophot Photomicroscope equipped with an AxioCam MRc5. Each slide was evaluated according to the intensity of positive immunostaining.

Thirty randomly selected fields from each group were photographed using the AxioCam MRc5 interfaced with the Axiophot Photomicroscope. The AxioVision SE64 (Carl Zeiss, Germany) program was used for analysis. A semiquantitative scoring system for the nuclear BrdU, PCNA, and cytoplasmic markers (VEGF, and PECAM-1) was used considering the staining intensity and extent of the area; this approach is widely accepted and has been used in previous studies [16, 17]. Briefly, the proportion of positive stained cells was scored as 0 (no cells stained positive), 1 (1%–10% stain-positive cells), 2 (11%–33% stain-positive cells), 3 (34%–66% stain-positive cells), and 4 (67%–100% stain-positive cells). The intensity of COL I or COL III positive immunostaining was graded as −, +, ++, and +++ (negative, slight positive, moderate positive, and strong positive staining, resp.).

2.7. Motion Analysis. The motion analysis of the rabbits was conducted at preinjection and 4 weeks postinjection. Rabbits were habituated for 30 minutes to the open field before motion analysis was performed [18]. They were placed on a 3×3 M arena and allowed to freely explore the field for 5 minutes. Their movements were individually assessed using a video-tracking system equipped with a camera (Smart; Panlab, Barcelona, Spain) that recorded the rabbit's horizontal activity. Five-minute walking distance, fast walking time, and mean walking speed were measured.

2.8. Statistical Analysis. Statistical analyses were performed with the SPSS program for Windows program, version 19.0 (SPSS Inc., Chicago, IL, USA). In addition to standard descriptive statistical calculations (means and standard errors), ANOVA was used to determine statistical differences among intragroup and intergroup. When ANOVA yielded significant results indicating that the group was significantly different from the others, Tukey's test was also performed. The mean values were followed by 95% confidence intervals, and all the data are expressed as the means ± standard error. The statistically significant levels were predetermined at $P < 0.05$ and $P < 0.001$.

3. Results

At 4 weeks postinjection, RCTT was observed in all eight rabbits in G1-SAL. In G2-PDRN, a partial-thickness subscapularis tendon tear was observed in three rabbits (37.5%) and full-thickness tendon tear in five rabbits (62.5%). In G3-MSC, a partial-thickness subscapularis tendon tear was observed in three rabbits (37.5%), full-thickness tendon tear in two rabbits (25%), and nearly complete healing in three rabbits (37.5%). In G4-MSC + PDRN, a partial-thickness subscapularis tendon tear was observed in five rabbits (62.5%), full-thickness tendon tear in one rabbit (12.5%), and nearly complete healing in two rabbits (25%) (Figures 3 and 4). There were significant differences in gross morphologic changes between preinjection and four weeks postinjection in G3-MSC and G4-MSC + PDRN.

The gross morphologic mean tendon tear size of each group at 4 weeks postinjection was 13.08 mm^2 (G1-SAL), 13.27 mm^2 (G2-PDRN), 3.36 mm^2 (G3-MSC), and 3.35 mm^2 (G4-MSC + PDRN). The size of the tear in G3-MSC and G4-MSC + PDRN was significantly smaller than that in G1-SAL and G2-PDRN ($P < 0.05$). There were no significant differences in gross morphologic changes and tendon tear size between G3-MSC and G4-MSC + PDRN (Figures 3 and 5).

On H-E staining, a parallel arrangement of hypercellular fibroblastic bundles was observed in G1-SAL, G2-PDRN, and G3-MSC. This arrangement was hardly observed in G1-SAL. On MT staining, regenerated collagen fibers were observed and were stained with COL-1 in G2-PDRN, G3-MSC, and G4-MSC + PDRN, but staining was rare in G1-SAL (Figure 6A1–B4). Numerous PCNA and BrdU-stained cells were also observed in regenerated collagen fibers in G2-PDRN, G3-MSC, and G4-MSC + PDRN, but only rarely in G1-SAL (Figure 6C1–D4). Immunohistochemistry staining revealed numerous VEGF-positive cells, and PECAM-1 positive microvascular densities were observed in G2-PDRN, G3-MSC, and G4-MSC + PDRN (Figure 6E1–F4). In G4-

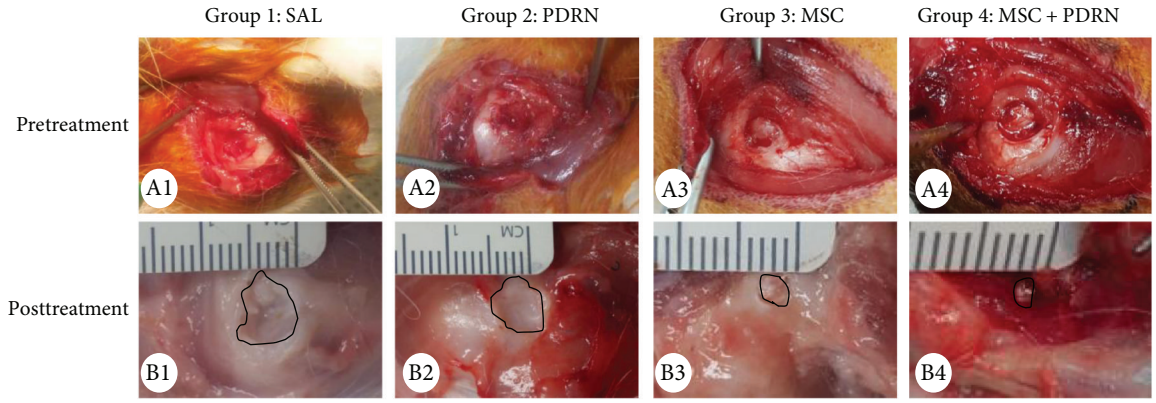

Figure 3: Gross morphological (A1–B4) findings of the subscapularis tendons in groups 1, 2, 3, and 4. (A1–A4) Pretreatment images. FTT is observed in all four groups. (B1–B4) Posttreatment images. FTT is shown and no gross morphologic changes between pretreatment and four weeks posttreatment in G1-SAL and G2-PDRN. There are significant differences in gross morphologic changes between pretreatment and four weeks posttreatment in G3-MSC and G4-MSC + PDRN. Normal saline (0.2 mL; group 1: SAL), PDRN (0.2 mL; group 2: PDRN), MSC (0.2 mL; group 3: MSC), and MSCs with PDRN (both 0.2 mL; group 4: MSC + PDRN). MSC: human umbilical cord blood-derived mesenchymal stem cell; PDRN: polydeoxyribonucleotide; FTT: full-thickness tendon tear.

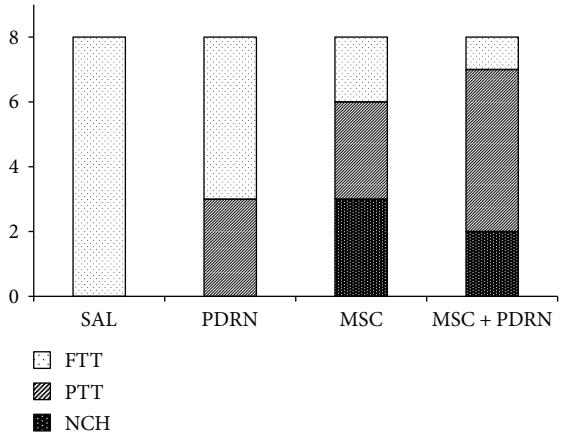

Figure 4: Gross morphology of tear site at 4 weeks postinjection. FTT was observed in all eight rabbits in G1-SAL. In G2-PDRN, a PTT was observed in three rabbits and FTT in five rabbits. In G3-MSC, a PTT was observed in three rabbits, FTT in two rabbits, and CH in three rabbits. In G4-MSC + PDRN, a PTT was observed in five rabbits, FTT in one rabbit, and CH in two rabbits. SAL (normal saline 0.2 mL); PDRN (PDRN 0.2 mL); MSC (MSC 0.2 mL); and MSC + PDRN (MSC 0.2 mL with PDRN 0.2 mL). PDRN: polydeoxyribonucleotide; MSC: human umbilical cord blood-derived mesenchymal stem cell; FTT: full-thickness tendon tear; PTT: partial-thickness tendon tear; CH: nearly complete healing.

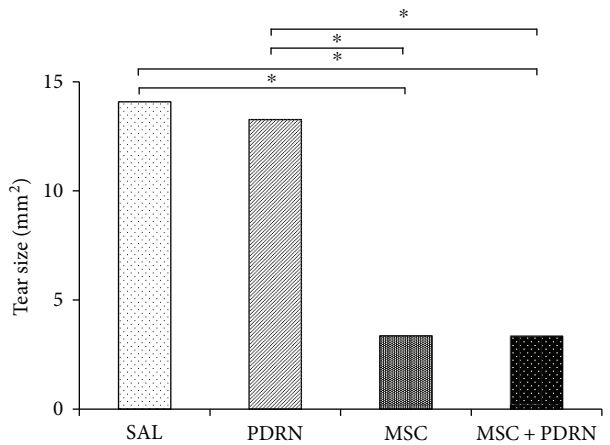

Figure 5: Subscapularis tendon tear size at 4 weeks postinjection. $^*P < 0.05$, one-way ANOVA, Tukey's post hoc test between two groups. SAL (group 1, normal saline 0.2 mL); PDRN (group 2, PDRN 0.2 mL); MSC (group 3, MSC 0.2 mL); and MSC + PDRN (group 4, MSC 0.2 mL with PDRN 0.2 mL). PDRN: polydeoxyribonucleotide; MSC: human umbilical cord blood-derived mesenchymal stem cell.

MSC + PDRN, newly regenerated collagen type 1 fibers, cell proliferation, angiogenesis, walking distance, fast walking time, and mean walking speed were greater than those in the other three groups on histological examination and motion analysis (Figures 7 and 8, Table 1).

4. Discussion

The major finding of this study is the superior therapeutic effect of coinjection with UCB-MSCs together with PDRN, compared with UCB-MSCs alone when evaluated functionally and histologically. PDRN has regenerative properties and stimulates wound healing by enhancing angiogenesis and production of VEGF through the adenosine A_2 receptor stimulation [19]. To our knowledge, this is the first study to analyze the difference between stem cells and PDRN or combination therapies for the regeneration of the rotator cuff tear. UCB-MSCs and PDRN can be produced in large quantities while maintaining the same quality. It would be ideal if the combination of PDRN and UCB-MSCs was synergistic in terms of their effects or if PDRN was effective enough in the regeneration of RCTTs to replace expensive stem cell-based therapy.

PDRN has been shown to improve the skin repair process and enhance wound breaking strength in diabetic animals. These effects were associated with a marked increase in

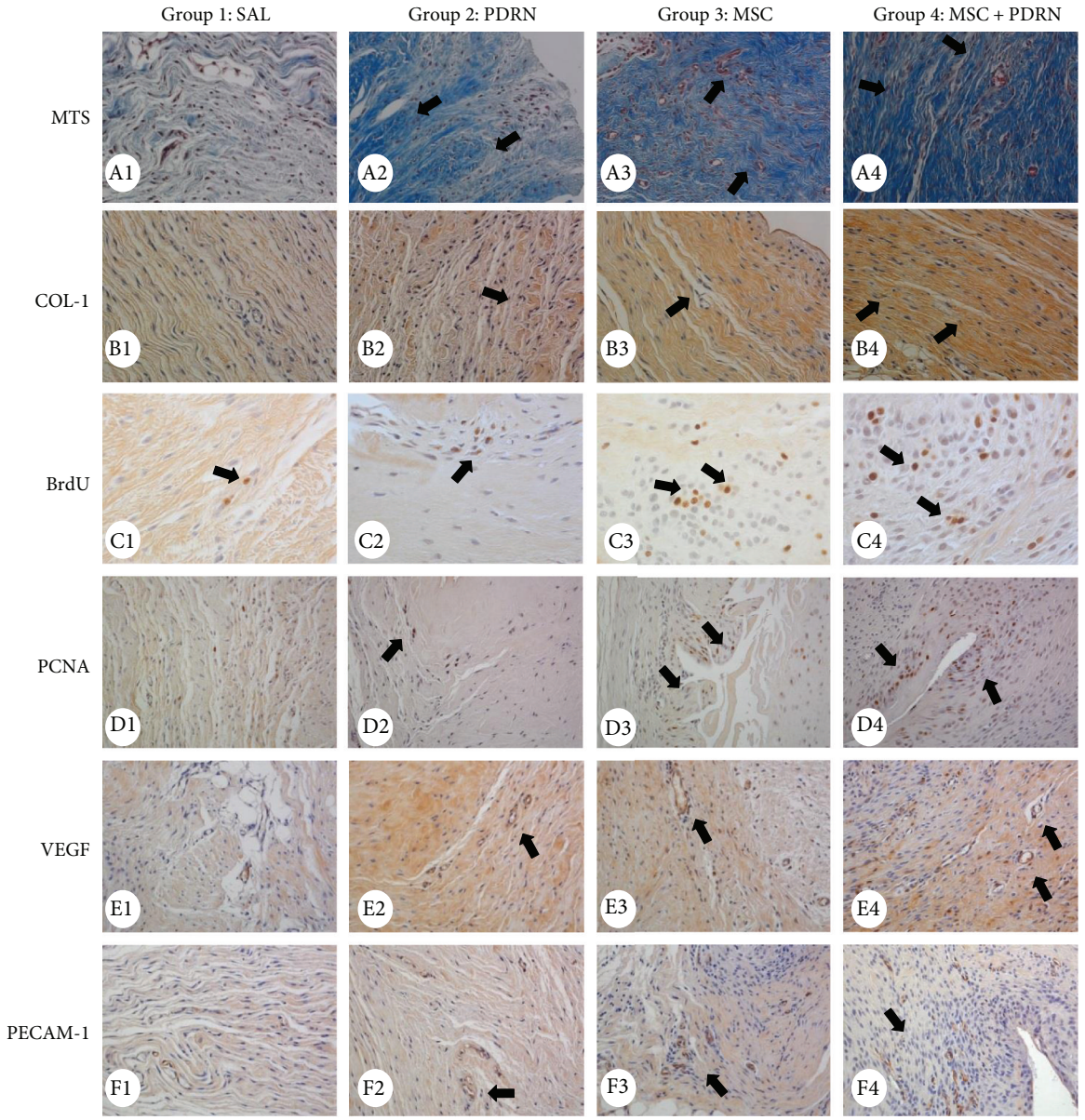

Figure 6: Histological findings of the subscapularis tendons in group 1 (SAL), group 2 (PDRN), group 3 (MSC), and group 4 (MSC + PDRN). (A1–A4) Newly regenerated tendons are shown in the blue-stained fibers (black arrow; Masson's trichrome stain; X200) in groups 2, 3, and 4. Few regenerative collagen fibers were seen in group 1. (B1–B4) Regenerated tendon fibers (black arrow; X200) were stained with anti-type 1 collagen antibody in groups 2, 3, and 4. Few regenerated tendon fibers were seen in group 1. (C1–D4) Numerous BrdU- and PCNA-stained cells (black arrow, X400, X200) were observed in regenerated tendon fibers in groups 2, 3, and 4. Few BrdU- and PCNA-stained cells were observed in group 1. (E1-F4) Numerous VEGF-positive cells and PECAM-1 positive microvascular densities (black arrows, X200) were observed in groups 2, 3, and 4. Few VEGF-positive cells and PECAM-1-positive microvascular densities were observed in group 1. MTS: Masson's trichrome stain; COL-1: collagen type 1; BrdU: 5-bromo-2′-deoxyuridine; PCNA: proliferating cell nuclear antigen; MSC: human umbilical cord blood-derived mesenchymal stem cell; PDRN: polydeoxyribonucleotide; VEGF: vascular endothelial growth factor; PECAM: platelet endothelial cell adhesion molecule.

the expression of VEGF, a master regulator of angiogenesis that is impaired in diabetes-related wound disorders [7]. We postulate that VEGF is a major growth factor that accelerates the healing process by stimulating new vessel formation in regions of poor circulation including full-thickness tendon tear.

UCB-MSCs are an attractive stem cell source. Advantages include noninvasive collection, superior tropism, and differentiation potential [20]. In addition, UCB-MSCs are less immunogenic; a recent study that used UCB-MSCs in anterior cruciate ligament reconstruction in a rabbit model showed no evidence of immune rejection [21]. The present findings are consistent with this benign immune behavior.

PDRN contains a mixture of deoxyribonucleotide polymers with chain lengths ranging from 50 to 2000 bp and is a source of purine and pyrimidine deoxynucleosides/

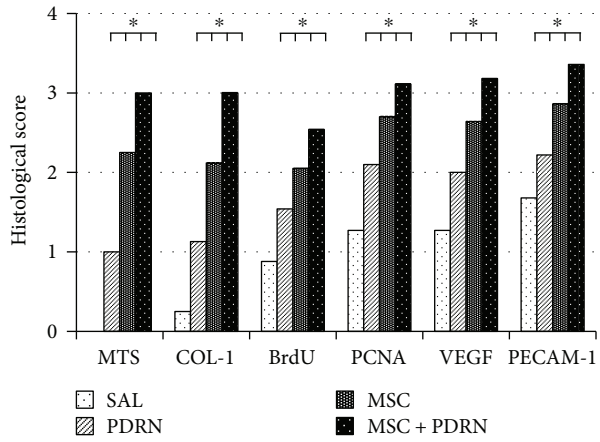

Figure 7: Semiquantitative score of histological findings and immunoreactivity of stain. The immunoreactivity of MTS and anti-type 1 collagen antibody stain and proportion of BrdU-, PCNA-, VEGF-, and PECAM-1-positive cells were scored as detailed in Materials and Methods. $^{*}P < 0.05$ one-way ANOVA, Tukey's post hoc test among groups. SAL (group 1, normal saline 0.2 mL); PDRN (group 2, PDRN 0.2 mL); MSC (group 3, MSC 0.2 mL); and MSC+PDRN (group 4, MSC 0.2 mL with PDRN 0.2 mL). MSC: human umbilical cord blood-derived mesenchymal stem cell; PDRN: polydeoxyribonucleotide; VEGF: vascular endothelial growth factor; PECAM: platelet endothelial cell adhesion molecule.

deoxyribonucleotides and bases [22]. PDRN has regenerative properties and stimulates wound healing by enhancing angiogenesis and production of VEGF through the adenosine A_2 receptor stimulation [19]. PDRN has no antigenic properties since it consists of low-molecular weight DNA fractions that can be defined as deoxyribonucleotide linear polymers [23]. Animal studies have demonstrated that PDRN is not lethal and is nontoxic to the liver, lungs, brain, skeletal muscle, and heart [24].

Another potential advantage of the combination of PDRN and UCB-MSCs is that the effect of exogenous MSCs is not dose-dependent. If the effect of exogenous MSCs is not proportional to dose, it is better to combine PDRN than to administer large amounts of MSCs to regenerate RCTT. A recent study in a porcine model of chronic myocardial infarction found that cardiosphere-derived cells at escalating doses led to equally enhanced preservation of cardiac function and tissue remodeling without a dose-efficacy relationship [25]. Our previous (unpublished) findings agree with this finding. We previously demonstrated that the injection of UCB-MSCs under US guidance has a regenerative effect for chronic full-thickness RCTTs. However, there were no differences in these regenerative effects between the high and the low doses of the UCB-MSCs, which mean that the benefits of UCB-MSCs were not dose-dependent in our rabbit model. Although further studies are needed, the fact that the effect of UCB-MSCs is not dose-dependent makes the rational combination with PDRN more compelling.

In addition to comparing the effect of UCB-MSC and PDRN on FTRCTT, the current study has important features in the method. The first feature is the use of musculoskeletal US for US-guided injection and evaluation of RCTT size after injection. We tried to validate the effect of only UCB-MSCs or PDRN injection, not an adjuvant therapy for surgical treatment in the FTRCTT model. The effect of MSCs combined with surgical repair has been reported in RCTT. However, combined with surgical repair, MSCs are an adjuvant therapy, and the effect of surgical repair overshadows their exact role in regenerating torn tendons [26]. In this context, musculoskeletal US can become a critical interventional tool for regenerative injection therapies because US-guided injections allow the stem cells to be selectively administered to the target area [18, 27]. Musculoskeletal US can also allow the relatively accurate assessment of the extent of the tear during the follow-up period before sacrificing the rabbit. We confirmed full-thickness tendon tear by US 6 weeks after establishing the rotator cuff tear. The four different injectants were separately introduced into the tear area under US guidance. The size of the tendon tear was measured by US at preinjection and 4 weeks postinjection. The motion analysis of the rabbits was also done to evaluate the improvement in functional ability rather than the mechanical properties of a regenerated tendon [18]. Motion analysis including walking distance, fast walking time, and mean walking speed for 5 minutes was conducted at preinjection and 4 weeks postinjection. This analysis is not yet proven to be superior to the mechanical testing that is frequently used in animal models of the rotator cuff tear [28–30]. However, motion analysis is a potentially important tool to assess the therapeutic effect of the rotator cuff tear, since functional tests have been demonstrated to be an important tool to assess the effectiveness of treatments for FTRCTT in human studies [31].

Chronic RCTTs adversely affect and hamper the surgical repair of lesions [32]. In particular, massive FTRCTTs are usually associated with myotendinous retraction, atrophy, and fatty infiltration of the muscles, which are bad prognostic factors for surgical outcomes. Thus, a "chronic" FTRCTT model is needed to accurately assess the clinical utility of MSCs in humans. For this study, we used a rabbit model of a chronic traumatic RCTT after 6 weeks of trauma. Studies in the rabbit supraspinatus muscle have shown fatty degeneration beginning as early as 4 weeks, with a peak at 6 weeks and slow reversal by 12 weeks [33]. FTRCTT becomes irreparable after approximately 6 weeks as the result of excessive tendon retraction and muscle atrophy and stiffening [34]. Accordingly, we selected 6 weeks for the chronic injury although we did not confirm whether the "chronic" findings were present in the tendon injuries [33–35].

There were significant differences in gross morphologic changes between preinjection and 4 weeks postinjection in groups 3 and 4, but not in G1-SAL and G2-PDRN. The difference between the pairs of groups concerns the presence or not of UCB-MSCs. G2-PDRN rabbits treated with PDRN did not show the regeneration effect. This proves that the therapeutic effect does not result from PDRN alone. Although the initial focus of MSC treatment of musculoskeletal injuries was based on their ability to differentiate into several cell types, recent studies suggest that the beneficial effect of stem cell-based therapy depends mainly on a paracrine effect [25, 36]. Paracrine signaling from MSCs modulates many cellular responses including survival,

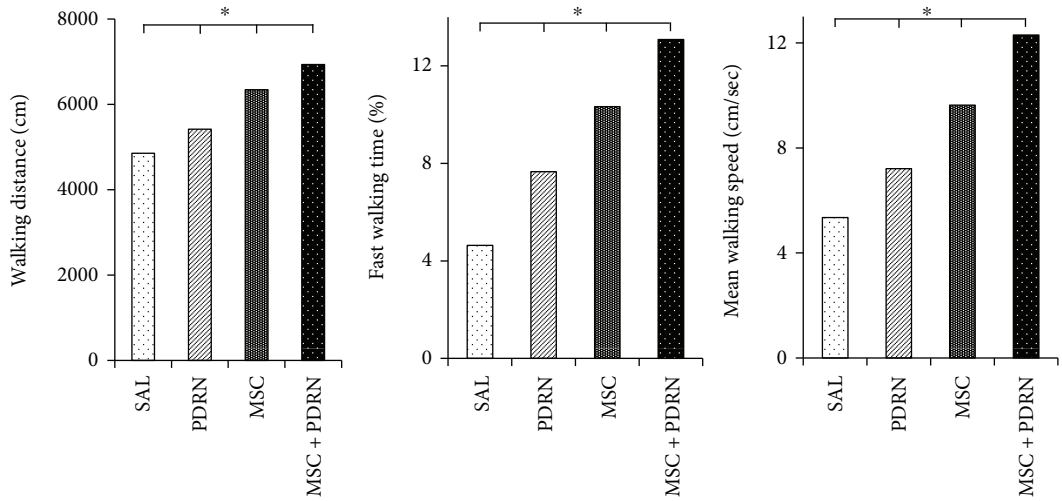

Figure 8: Motion analysis of the rabbits at 4 weeks postinjection. In G4-MSC + PDRN, walking distance, fast walking time, and mean walking speed are greater than those in the other three groups on motion analysis. $^*P < 0.05$ one-way ANOVA, Tukey's post hoc test among groups. Group 1 (normal saline 0.2 mL). Group 2 (PDRN 0.2 mL). Group 3 (MSC 0.2 mL). Group 4 (MSC 0.2 mL with PDRN 0.2 mL). MSC: human umbilical cord blood-derived mesenchymal stem cell; PDRN: polydeoxyribonucleotide.

Table 1: Semiquantitative score of histological findings, immunoreactivity of stain, and motion analysis according to treatment groups at 4 weeks after injection.

	Groups (injection regimens)			
	0.2 mL NS (G1-SAL)	0.2 mL PDRN (G2-PDRN)	0.2 mL MSC (G3-MSC)	0.2 mL MSC + 0.2 mL PDRN (G4-MSC + PDRN)
Histological score				
MTS	0.0 ± 0.0*	0.9 ± 0.56*	2.2 ± 0.42*	3.0 ± 0.0*
Anti-type collagen 1	0.2 ± 0.42*	1.1 ± 0.31*	2.1 ± 0.31*	3.0 ± 0.0*
BrdU	0.88 ± 0.84*	1.54 ± 1.13*	2.05 ± 1.16*	2.54 ± 1.11*
PCNA	1.27 ± 0.91*	2.10 ± 1.07*	2.70 ± 1.08*	3.11 ± 1.00*
VEGF	1.27 ± 0.94*	2.00 ± 1.07*	2.64 ± 0.92*	3.18 ± 0.79*
PECAM-1	1.68 ± 0.93*	2.22 ± 0.92*	2.86 ± 0.98*	3.36 ± 0.75*
Motion analysis				
Walking distance (cm)	4728.37 ± 137.27*	5416.62 ± 323.27*	6343.62 ± 213.57*	6932.37 ± 107.74*
Fast walking time (%)	5.62 ± 1.42*	8.32 ± 0.34*	10.33 ± 2.48*	12.07 ± 1.77*
Mean walking speed (cm/sec)	6.3 ± 0.57*	8.36 ± 0.39*	9.62 ± 1.78*	12.3 ± 1.13*

Values are the mean ± SD. The immunoreactivity of MTS and anti-type 1 collagen antibody stain and proportion of BrdU-, PCNA-, VEGF-, and PECAM-1-positive cells were scored as detailed in Materials and Methods. NS: normal saline; MSC: human umbilical cord blood-derived mesenchymal stem cell; PDRN: polydeoxyribonucleotide; G1-SAL: 0.2 mL normal saline group; G2-PDRN: 0.2 mL PDRN; G3-MSC: 0.2 mL UCB-MSCs; G4-MSC + PDRN: 0.2 mL UCB-MSCs with 0.2 ml PDRN; MTS: Masson's trichrome stain; BrdU: bromodeoxyuridine; PCNA: proliferating cell nuclear antigen; VEGF: vascular endothelial growth factor; PECAM-1: platelet endothelial cell adhesion molecule. $P < 0.05$ one-way ANOVA, Tukey's post hoc test among groups.

proliferation, migration, and gene expression [37, 38]. We observed hypercellular fibroblastic bundles composed of type I collagens in the regenerated tendon 4 weeks after the injection of UCB-MSCs. The main cause of unsuccessful tendon tear surgery is the formation of a fibrovascular scar enriched in type III collagens, which are mechanically weaker than type I, the main component of the extracellular matrices in tendons [39, 40]. The observation supports the idea that the injection of USB-MSCs promotes the normal tendon healing process in the repair of chronic RCTTs, even though USB-MSCs did not presently differentiate into the target cell type.

The gross morphologic mean tendon tear size of each group at 4 weeks postinjection were 13.08 mm^2 (G1-SAL), 13.27 mm^2 (G2-PDRN), 3.36 mm^2 (G3-MSC), and 3.35 mm^2 (G4-MSC + PDRN). Since there were no significant differences in gross morphologic changes and tendon tear size between G3-MSC and G4-MSC + PDRN, we were unable to demonstrate whether the combined therapy with PDRN and USB-MSCs was more effective than USB-MSCs alone. However, in G4-MSC + PDRN, newly regenerated collagen type 1 fibers, cell proliferation, angiogenesis, walking distance, fast walking time, and mean walking speed were

greater than those in the other three groups based on the histological and motion analyses.

Therefore, when combined with USB-MSCs, PDRN might have a synergic or additive effect in the treatment of RCTTs.

The exact mechanism of treatment for both USB-MSCs and PDRN remains unknown. Paradoxically, the value of the combined effect of PDRN and MSCs is due to the limitations of the MSC regenerative effect. Accumulating evidence suggests that the regenerative properties of exogenous MSCs are mainly due to the paracrine mechanism because the engrafted MSCs have poor differentiation and survival rates [41–43]. This paracrine action may be accounted for, at least in part, by microvesicles (MVs) released from MSCs, which deliver proteins, bioactive lipids, and nucleic acids to injured cells [44]. Although exogenous MSCs can be considered a potential therapeutic tool and can contribute to tissue repair, the extent of improvement of injured tissues has not been correlated with cellular engraftment and differentiation of MSCs to tissue cells. It is necessary to develop strategies to obtain sufficient amounts of MVs. Since the paracrine effect of MSCs may not be proportional to the amount of MSCs administered, other additional sources are needed to fully provide the necessary protein (or its precursors), bioactive factors, and nucleic acids [19, 22, 23]. It is assumed that the PDRN can fulfill this role.

In the current study, 0.2 mL of PDRN with or without UCB-MSCs was injected into the right FTSSCT under US guidance. This dose volume of PDRN was the same dose as the stem cells. The optimal dose or route of administration of PDRN required for regenerating the rotator cuff was not established. We estimated and used 0.2 mL of PDRN because rabbits weigh about 5% of the weight of a typical adult. One study used 3 mL in patients with chronic rotator cuff tendinopathy [9]. However, in studies on human subjects, PDRN was injected directly into lesions to demonstrate therapeutic efficacy. A half vial of PDRN (1.5 mL) was injected each week for 3 weeks for the treatment of plantar fasciitis [8], and 5.625 mg in 3 mL of PDRN was injected at weekly intervals for 3 weeks to treat chronic rotator cuff tendinopathy [9]. To confirm the regenerative effect of the rotator cuff tear of the PDRN, it is necessary to clarify the optimal dose and route of administration of PDRN.

There are some limitations in our study. First, we created 5 mm diameter FTRCTTs near the insertion site on the left subscapularis tendon by punch biopsy excision. After each excision was made, each wound was immediately covered with a round silicone tube to induce the chronic rotator cuff tear model. Each wound was closed using subcutaneous and skin sutures. However, these tears were in the tendon body, not exactly at the insertion site, which is not reestablished following surgical repair. This outcome is associated with high recurrence rates [45]. Second, complete regeneration did not occur. Current strategies for using stem cells to regenerate FTRCTTs can be combined with mechanical stimulation, the topography of the extracellular matrix, growth and differentiation factors, gene transfection, and coculture with tendon tissues or cells. Future studies are needed that use UCB-MSCs and/or PDRN with these factors [46]. Third, the optimal dose of UCB-MSCs was determined based on previous studies. However, as mentioned above, the dose of PDRN was determined to be the same as UCB-MSCs for comparison. However, this dose may not be the proper dose of PDRN. Fourth, we did not perform the biomechanical test of the regenerative tendon. Last, there would also have been more "complete" rotator cuff healing if outcomes were measured at 8 weeks or more instead of at 4 weeks.

5. Conclusion

There was no significant difference in gross morphologic change of the tendon tear between UCB-MSCs only and the combination with PDRN injection in a rabbit model of chronic traumatic FTRCTT. However, coinjection of UCB-MSCs and PDRN was more effective than the injection of UCB-MSCs alone in histological and motion analyses. These results of this study regarding the combination of UCB-MSCs and PDRN warrant more investigations.

Disclosure

This research will be presented at the 20th International Conference on Biomaterials Science and Technology (May 3, 2018).

Conflicts of Interest

The authors declare that there is no conflict of interest regarding the publication of this article.

Authors' Contributions

Dong Rak Kwon, Gi-Young Park, and Sang Chul Lee are responsible for the concept and design and the manuscript writing. Dong Rak Kwon provided the study materials. Dong Rak Kwon and Sang Chul Lee are responsible for the data analysis and interpretation. All authors approved the final manuscript.

Acknowledgments

This research was supported by Basic Science Research Program through the National Research Foundation of Korea (NRF) funded by the Ministry of Education (NRF-2016R1D1A1B01014260). The authors deeply appreciate the contribution of professor and anatomist Yong-Suk Moon, Ph.D., to the collection and analysis of histological data presented in this article.

References

[1] K. Yamaguchi, K. Ditsios, W. D. Middleton, C. F. Hildebolt, L. M. Galatz, and S. A. Teefey, "The demographic and morphological features of rotator cuff disease: a comparison of asymptomatic and symptomatic shoulders," *The Journal of Bone & Joint Surgery*, vol. 88, no. 8, pp. 1699–1704, 2006.

[2] R. Castricini, U. G. Longo, M. de Benedetto et al., "Platelet-rich plasma augmentation for arthroscopic rotator cuff repair: a

randomized controlled trial," *The American Journal of Sports Medicine*, vol. 39, no. 2, pp. 258–265, 2011.

[3] M. Young, "Stem cell applications in tendon disorders: a clinical perspective," *Stem Cells International*, vol. 2012, Article ID 637836, 10 pages, 2012.

[4] A. I. Caplan, "Mesenchymal stem cells," *Journal of Orthopaedic Research*, vol. 9, no. 5, pp. 641–650, 1991.

[5] L. Bai, D. Li, J. Li et al., "Bioactive molecules derived from umbilical cord mesenchymal stem cells," *Acta Histochemica*, vol. 118, no. 8, pp. 761–769, 2016.

[6] G. Kasper, L. Mao, S. Geissler et al., "Insights into mesenchymal stem cell aging: involvement of antioxidant defense and actin cytoskeleton," *Stem Cells*, vol. 27, no. 6, pp. 1288–1297, 2009.

[7] M. Galeano, A. Bitto, D. Altavilla et al., "Polydeoxyribonucleotide stimulates angiogenesis and wound healing in the genetically diabetic mouse," *Wound Repair and Regeneration*, vol. 16, no. 2, pp. 208–217, 2008.

[8] J. K. Kim and J. Y. Chung, "Effectiveness of polydeoxyribonucleotide injection versus normal saline injection for treatment of chronic plantar fasciitis: a prospective randomised clinical trial," *International Orthopaedics*, vol. 39, no. 7, pp. 1329–1334, 2015.

[9] Y. C. Yoon, D. H. Lee, M. Y. Lee, and S. H. Yoon, "Polydeoxyribonucleotide injection in the treatment of chronic supraspinatus tendinopathy: a case-controlled, retrospective, comparative study with 6-month follow-up," *Archives of Physical Medicine and Rehabilitation*, vol. 98, no. 5, pp. 874–880, 2017.

[10] S. H. Coleman, S. Fealy, J. R. Ehteshami et al., "Chronic rotator cuff injury and repair model in sheep," *The Journal of Bone & Joint Surgery*, vol. 85, no. 12, pp. 2391–2402, 2003.

[11] M. Baydar, E. Akalin, O. El et al., "The efficacy of conservative treatment in patients with full-thickness rotator cuff tears," *Rheumatology International*, vol. 29, no. 6, pp. 623–628, 2009.

[12] C. Isaac, B. Gharaibeh, M. Witt, V. J. Wright, and J. Huard, "Biologic approaches to enhance rotator cuff healing after injury," *Journal of Shoulder and Elbow Surgery*, vol. 21, no. 2, pp. 181–190, 2012.

[13] C. Gerber, B. Fuchs, and J. Hodler, "The results of repair of massive tears of the rotator cuff," *The Journal of Bone & Joint Surgery*, vol. 82, no. 4, pp. 505–515, 2000.

[14] R. C. Grumet, S. Hadley, M. V. Diltz, T. Q. Lee, and R. Gupta, "Development of a new model for rotator cuff pathology: the rabbit subscapularis muscle," *Acta Orthopaedica*, vol. 80, no. 1, pp. 97–103, 2009.

[15] L. Lafosse, R. Brzoska, B. Toussaint, and R. Gobezie, "The outcome and structural integrity of arthroscopic rotator cuff repair with use of the double-row suture anchor technique," *The Journal of Bone & Joint Surgery*, vol. 90, pp. 275–286, 2008.

[16] C. P. Han, L. F. Kok, P. H. Wang et al., "Scoring of $p16^{INK4a}$ immunohistochemistry based on independent nuclear staining alone can sufficiently distinguish between endocervical and endometrial adenocarcinomas in a tissue microarray study," *Modern Pathology*, vol. 22, no. 6, pp. 797–806, 2009.

[17] K. L. Henriksen, B. B. Rasmussen, A. E. Lykkesfeldt, S. Møller, B. Ejlertsen, and H. T. Mouridsen, "Semi-quantitative scoring of potentially predictive markers for endocrine treatment of breast cancer: a comparison between whole sections and tissue microarrays," *Journal of Clinical Pathology*, vol. 60, no. 4, pp. 397–404, 2007.

[18] G. Y. Park, D. R. Kwon, and S. C. Lee, "Regeneration of full-thickness rotator cuff tendon tear after ultrasound-guided injection with umbilical cord blood-derived mesenchymal stem cells in a rabbit model," *Stem Cells Translational Medicine*, vol. 4, no. 11, pp. 1344–1351, 2015.

[19] F. Squadrito, A. Bitto, D. Altavilla et al., "The effect of PDRN, an adenosine receptor A_{2A} agonist, on the healing of chronic diabetic foot ulcers: results of a clinical trial," *The Journal of Clinical Endocrinology & Metabolism*, vol. 99, no. 5, pp. E746–E753, 2014.

[20] M. Wang, Y. Yang, D. Yang et al., "The immunomodulatory activity of human umbilical cord blood-derived mesenchymal stem cells in vitro," *Immunology*, vol. 126, no. 2, pp. 220–232, 2009.

[21] K. M. Jang, H. C. Lim, W. Y. Jung, S. W. Moon, and J. H. Wang, "Efficacy and safety of human umbilical cord blood–derived mesenchymal stem cells in anterior cruciate ligament reconstruction of a rabbit model: new strategy to enhance tendon graft healing," *Arthroscopy*, vol. 31, no. 8, pp. 1530–1539, 2015.

[22] M. Yu and J. Y. Lee, "Polydeoxyribonucleotide improves wound healing of fractional laser resurfacing in rat model," *Journal of Cosmetic and Laser Therapy*, vol. 19, no. 1, pp. 43–48, 2017.

[23] A. Bitto, F. Polito, D. Altavilla, L. Minutoli, A. Migliorato, and F. Squadrito, "Polydeoxyribonucleotide (PDRN) restores blood flow in an experimental model of peripheral artery occlusive disease," *Journal of Vascular Surgery*, vol. 48, no. 5, pp. 1292–1300, 2008.

[24] F. Polito, A. Bitto, M. Galeano et al., "Polydeoxyribonucleotide restores blood flow in an experimental model of ischemic skin flaps," *Journal of Vascular Surgery*, vol. 55, no. 2, pp. 479–488, 2012.

[25] X. L. Tang, G. Rokosh, S. K. Sanganalmath et al., "Effects of intracoronary infusion of escalating doses of cardiac stem cells in rats with acute myocardial infarction," *Circulation: Heart Failure*, vol. 8, no. 4, pp. 757–765, 2015.

[26] P. Hernigou, C. H. Flouzat Lachaniette, J. Delambre et al., "Biologic augmentation of rotator cuff repair with mesenchymal stem cells during arthroscopy improves healing and prevents further tears: a case-controlled study," *International Orthopaedics*, vol. 38, no. 9, pp. 1811–1818, 2014.

[27] M. N. Brown, B. J. Shiple, and M. Scarpone, "Regenerative approaches to tendon and ligament conditions," *Physical Medicine and Rehabilitation Clinics of North America*, vol. 27, no. 4, pp. 941–984, 2016.

[28] J. Pan, G. M. Liu, L. J. Ning et al., "Rotator cuff repair using a decellularized tendon slices graft: an in vivo study in a rabbit model," *Knee Surgery, Sports Traumatology, Arthroscopy*, vol. 23, no. 5, pp. 1524–1535, 2015.

[29] N. A. Friel, V. M. Wang, M. A. Slabaugh, F. Wang, S. Chubinskaya, and B. J. Cole, "Rotator cuff healing after continuous subacromial bupivacaine infusion: an in vivo rabbit study," *Journal of Shoulder and Elbow Surgery*, vol. 22, no. 4, pp. 489–499, 2013.

[30] J. H. Oh, S. W. Chung, S. H. Kim, J. Y. Chung, and J. Y. Kim, "2013 Neer Award: effect of the adipose-derived stem cell for the improvement of fatty degeneration and rotator cuff healing in rabbit model," *Journal of Shoulder and Elbow Surgery*, vol. 23, no. 4, pp. 445–455, 2014.

[31] J. D. Keener, L. M. Galatz, G. Stobbs-Cucchi, R. Patton, and K. Yamaguchi, "Rehabilitation following arthroscopic rotator cuff repair: a prospective randomized trial of immobilization compared with early motion," *The Journal of Bone & Joint Surgery*, vol. 96, no. 1, pp. 11–19, 2014.

[32] D. Goutallier, J. M. Postel, P. Gleyze, P. Leguilloux, and S. Van Driessche, "Influence of cuff muscle fatty degeneration on anatomic and functional outcomes after simple suture of full-thickness tears," *Journal of Shoulder and Elbow Surgery*, vol. 12, no. 6, pp. 550–554, 2003.

[33] K. Rowshan, S. Hadley, K. Pham, V. Caiozzo, T. Q. Lee, and R. Gupta, "Development of fatty atrophy after neurologic and rotator cuff injuries in an animal model of rotator cuff pathology," *The Journal of Bone and Joint Surgery*, vol. 92, no. 13, pp. 2270–2278, 2010.

[34] K. A. Derwin, A. R. Baker, J. P. Iannotti, and J. A. McCarron, "Preclinical models for translating regenerative medicine therapies for rotator cuff repair," *Tissue Engineering Part B: Reviews*, vol. 16, no. 1, pp. 21–30, 2010.

[35] R. J. Quigley, A. Gupta, J. H. Oh et al., "Biomechanical comparison of single-row, double-row, and transosseous-equivalent repair techniques after healing in an animal rotator cuff tear model," *Journal of Orthopaedic Research*, vol. 31, no. 8, pp. 1254–1260, 2013.

[36] H. R. Hofer and R. S. Tuan, "Secreted trophic factors of mesenchymal stem cells support neurovascular and musculoskeletal therapies," *Stem Cell Research & Therapy*, vol. 7, no. 1, p. 131, 2016.

[37] Y. Chen, J. Z. Shao, L. X. Xiang, X. J. Dong, and G. R. Zhang, "Mesenchymal stem cells: a promising candidate in regenerative medicine," *International Journal of Biochemistry & Cell Biology*, vol. 40, no. 5, pp. 815–820, 2008.

[38] A. M. Hocking and N. S. Gibran, "Mesenchymal stem cells: paracrine signaling and differentiation during cutaneous wound repair," *Experimental Cell Research*, vol. 316, no. 14, pp. 2213–2219, 2010.

[39] M. F. Pittenger, A. M. Mackay, S. C. Beck et al., "Multilineage potential of adult human mesenchymal stem cells," *Science*, vol. 284, no. 5411, pp. 143–147, 1999.

[40] V. Rocha, J. E. Wagner Jr., K. A. Sobocinski et al., "Graft-versus-host disease in children who have received a cord-blood or bone marrow transplant from an HLA-identical sibling," *The New England Journal of Medicine*, vol. 342, no. 25, pp. 1846–1854, 2000.

[41] N. Kotobuki, Y. Katsube, Y. Katou, M. Tadokoro, M. Hirose, and H. Ohgushi, "In vivo survival and osteogenic differentiation of allogeneic rat bone marrow mesenchymal stem cells (MSCs)," *Cell Transplantation*, vol. 17, no. 6, pp. 705–712, 2008.

[42] C. E. Zimmermann, M. Gierloff, J. Hedderich, Y. Açil, J. Wiltfang, and H. Terheyden, "Survival of transplanted rat bone marrow-derived osteogenic stem cells in vivo," *Tissue Engineering Part A*, vol. 17, no. 7-8, pp. 1147–1156, 2011.

[43] Y. Ando, K. Matsubara, J. Ishikawa et al., "Stem cell-conditioned medium accelerates distraction osteogenesis through multiple regenerative mechanisms," *Bone*, vol. 61, pp. 82–90, 2014.

[44] S. Bruno and G. Camussi, "Role of mesenchymal stem cell-derived microvesicles in tissue repair," *Pediatric Nephrology*, vol. 28, no. 12, pp. 2249–2254, 2013.

[45] H. H. Lu and S. Thomopoulos, "Functional attachment of soft tissues to bone: development, healing, and tissue engineering," *Annual Review of Biomedical Engineering*, vol. 15, no. 1, pp. 201–226, 2013.

[46] J. L. Chen, W. Zhang, Z. Y. Liu, B. C. Heng, H. W. Ouyang, and X. S. Dai, "Physical regulation of stem cells differentiation into teno-lineage: current strategies and future direction," *Cell and Tissue Research*, vol. 360, no. 2, pp. 195–207, 2015.

Hindawi
Stem Cells International
Volume 2018, Article ID 9283432, 13 pages
https://doi.org/10.1155/2018/9283432

Research Article

Mathematical Modeling Reveals the Role of Hypoxia in the Promotion of Human Mesenchymal Stem Cell Long-Term Expansion

Shuhua Gao,[1] **Cheng Xiang**,[1] **Kairong Qin**,[2,3] **and Changkai Sun**[3,4,5,6]

[1]*Department of Electrical and Computer Engineering, National University of Singapore, Singapore*
[2]*School of Optoelectronic Engineering and Instrumentation Science, Dalian University of Technology, Dalian, China*
[3]*Research Center for the Control Engineering of Translational Precision Medicine, Dalian University of Technology, Dalian, China*
[4]*School of Biomedical Engineering, Faculty of Electronic Information and Electrical Engineering, Dalian University of Technology, Dalian, China*
[5]*State Key Laboratory of Fine Chemicals, Dalian R&D Center for Stem Cell and Tissue Engineering, Dalian University of Technology, Dalian, China*
[6]*Liaoning Provincial Key Laboratory of Cerebral Diseases, Institute for Brain Disorders, Dalian Medical University, Dalian, China*

Correspondence should be addressed to Changkai Sun; sunck2@dlut.edu.cn

Received 17 January 2018; Revised 18 April 2018; Accepted 29 April 2018; Published 14 May 2018

Academic Editor: Stefania Cantore

Copyright © 2018 Shuhua Gao et al. This is an open access article distributed under the Creative Commons Attribution License, which permits unrestricted use, distribution, and reproduction in any medium, provided the original work is properly cited.

Many experimental studies have found that human mesenchymal stem cells (MSCs) in long-term culture exhibited enhanced cell proliferation and prolonged lifespan under hypoxia (around 1%–7% oxygen) against the normoxic condition (about 21% oxygen). Inspired by the experimental findings, we aimed to investigate the hypoxic effects on MSC expansion quantitatively through mathematical modeling to elucidate the corresponding biological mechanism. A two-compartment model based on ordinary differential equations (ODEs), which incorporate cellular division and senescence via state transition, was developed to describe the MSC expansion process. Parameters of this model were fitted to experimental data and used to interpret the different proliferative capacities of MSCs under hypoxia and normoxia along with model sensitivity analysis. The proposed model was tested on data from two separate experimental studies, and it could reproduce the observed growth characteristics in both conditions. Overall, this compartmental model with a logistic state transition rate was sufficient to explain the experimental findings and highlighted the promotive role of hypoxia in MSC proliferation. This in silico study suggests that hypoxia can enhance MSC long-term expansion mainly by delaying replicative senescence, which is indicated by the slowdown of the state transition rate in our model. Therefore, this explanatory model may provide theoretical proof for the experimentally observed MSC growth superiority under hypoxia and has the potential to further optimize MSC culture protocols for regenerative medicine applications.

1. Introduction

Human mesenchymal stem cells (MSCs) are multipotent stromal cells that are capable of self-renewal and differentiation into various lineages mainly including osteoblasts, chondrocytes, and adipocytes. Their major source *in vivo* is the bone marrow, and they have also been found in many other adult tissues such as the adipose tissue, dental pulp, and umbilical cord [1, 2]. In recent years, MSCs have drawn a lot of biomedical research interest for their great potential in regenerative medicine due to their high proliferative ability and lineage plasticity [3]. Many studies have highlighted the promise of somatic MSCs as putative therapeutics for a number of disorders such as osteoarthritis, osteogenesis imperfecta, and even type II diabetes [1, 4, 5]. Compared with embryonic stem cells, since MSCs can be directly obtained from adult individuals, the ethical controversies associated with stem cell therapies are largely eliminated.

For a comprehensive review of MSC-based clinical trials conducted worldwide, one may refer to the recent survey [4]. As a side note, in literature, the term MSCs may also refer to mesenchymal stromal cells instead of mesenchymal stem cells [3, 6]. The main reason for this debate on MSC definitions is that the isolation of MSCs according to the current ISCT criteria has produced heterogeneous, nonclonal cultures of stromal cells, including stem cells with different multipotent properties [3, 4]. Since the technical discrimination of mesenchymal stem cells and stromal cells is out of the scope of this paper, we simply use the term MSC to specifically describe a cell with documented self-renewal and differentiation characteristics [3], which is also consistent with the terminology used in the two experimental studies from which we obtain the long-term MSC proliferation data [7, 8].

However, although MSCs may be isolated from a variety of tissue sources, their concentration is still very low. Consequently, it is impossible to collect the large number of MSCs required for clinical trials purely from a single donor, which is one of the major limitations in the medical use of MSCs [9, 10]. Therefore, ex vivo expansion is a necessary step for the acquisition of sufficient MSCs [2, 4], and many research efforts have been devoted to the optimization of MSCs culture protocols, including the composition of the basal culture medium, the addition of specific growth factors, the seeding density, and the biophysical environment [11]. In this study, we focus on the effects of oxygen tension on MSC expansion, which has been investigated by plentiful experimental studies [2, 7, 8, 12–15]. While the typical *in vivo* niche of MSCs, the bone marrow, is characterized by a low oxygen concentration (1% to 7%, *hypoxia*), currently, MSCs are often expanded under the atmospheric oxygen concentration around 21% (*normoxia*) [13]. However, lots of studies have reached a general agreement that hypoxia can extend MSC lifespan and thereby enhance their proliferative efficiency greatly in long-term culture [8, 14, 16–19]. The intracellular molecular mechanism of such effects is still unclear, which may involve oxidative stress [18], gene instability [16], and the regulation of p53 and p16 [18, 20, 21], but many experimental studies imply that in principle, hypoxia promotes MSC long-term expansion by slowing down *replicative senescence*, that is, the inherent division limitation of cultured cells even in an ideal environment [11, 12, 16, 22]. Here, we should remark that, in literature, a sharp definition of senescent cells is still lacking since deep understanding of mechanisms that induce cellular senescence is still missing. In particular, regarding the biological features in senescence of MSCs, Capasso et al. have investigated MSC senescence induced by oxidative stress, doxorubicin treatment, X-ray irradiation, and replicative exhaustion, to determine a specific signature for acute and replicative senescent MSCs with changes in autophagy, proteasome activity, and metabolism [6]. In this study, by cellular senescence, we generally refer to replicative senescence, that is, a limitation in the number of times that normal cells can divide, which is induced by prolonged periods of cellular stress, such as continuous proliferation [23]. Despite the experimental observations about replicative senescence, we may also suspect that such promotion is caused by a higher death rate, a lower division rate, or a faster senescence pace under normoxic conditions. Therefore, to verify this hypothesis and to interpret the experimental findings about hypoxic influence on MSC expansion from a theoretical perspective, we seek to assess the interplay between replicative senescence and hypoxia using mathematical modeling and quantitative analysis.

Mathematical studies of stem cell systems and their population dynamics, such as the computational modeling of Nanog dynamics in mouse embryonic stem cells [24], the stress distribution throughout engineered heart muscles [25], the lineage specification of hematopoietic stem cells [26], and tumor growth [27], have succeeded in providing valuable insights and quantitative description of the underlying biological processes. However, regarding MSC expansion, despite the aforementioned numerous experimental studies, as far as we know, there are only two quantitative modeling studies in literature closely related with the impact of oxygen tension on MSC expansion. Lemon et al. proposed an ordinary differential equation- (ODE-) based model to describe the proliferation and differentiation of human MSCs grown inside artificial porous scaffolds under different oxygen concentrations [28]. However, their study was conducted in the context of 3D culture of MSCs inside scaffolds, and their model was formulated around the limited porous volume and the oxygen-dependent secretion of extracellular matrix (ECM). Obviously, such context differs significantly from the common 2D expansion in labs since cells are usually subcultured before confluence, making space not a limitation. In the other study performed by Krinner et al. [29], an individual cell-based stochastic model was constructed for pellet cultures of MSCs to describe their expansion and chondrogenic differentiation, assuming that the oxygen-dependent cell state fluctuations are reversible. Their model is mainly concerned with MSC lineage commitment and the consequent cell population structure. In short, neither of the two studies focuses on the relation between oxygen tension and replicative senescence explicitly. Hence, a concise and easy-to-understand mathematical model is of great need to help elucidate the underlying mechanism of oxygen influence on MSC expansion *in vitro*.

To this end, the purpose of our study is to develop a powerful, yet highly interpretable mathematical model to describe the long-term population dynamics of MSCs commonly cultured in 2D environment, like Petri dishes, and to evaluate the potential influence of hypoxia on replicative senescence quantitatively. As we shall see, starting from some simple assumptions rooted in experimental observations, our model is sufficient to accurately reproduce the MSC proliferation behavior in long-term culture and to clearly explain the remarkable difference of MSC expansion capacity under hypoxic and normoxic conditions.

2. Methods

Ordinary differential equation (ODE) is the most orthodox method to model system dynamics, for example, the classic model for tumor growth predication [27], the computational modeling of megakaryocytic differentiation [30], and

mathematical models to study stem cell population dynamics and stem cell niche regulation [31]. In this section, we will first determine the variables in the ODE system depicting MSC expansion according to existing experimental evidence, then build a two-compartment model composed of two cellular states, and conduct subsequent parameter identification, whose details are described in the following subsections.

2.1. Model Assumption and Experimental Evidence. Motivated by the fact that MSCs have only a limited lifespan in long-term culture, the main assumption of our model is that oxygen tension can influence the progression of replicative senescence during MSC aging. For example, it was observed that most of the MSCs cultured under normoxic conditions were in senescence after 100 days, while fewer senescent cells were identified for those in hypoxic culture, leading to an additional 8–20 population doublings under hypoxia. Such possible inhibiting effect of hypoxia on replicative senescence has been reported in many experimental investigations, though various reasons were speculated to explain this phenomenon [12, 16]. For instance, Estrada and his colleagues attributed this extended lifespan of MSCs at lower oxygen tensions to the reduced oxidative stress and thereby lessened DNA damage [16]. Other researchers concluded that the change of MSC self-renewal competence was caused by the downregulation of p16 and p21 under hypoxia or the upregulation of p53 under normoxia, supported by observations in both short-term and long-term cultures [17, 18, 21]. In this present work, unlike common experimental studies which try to identify the specific molecules dominating cellular response to hypoxia, we placed our research at the cell population level and designed a mathematical model by taking mainly three factors which may possibly affect cell expansion efficiency into consideration, including the cell division rate, the cell death (apoptosis) rate, and the replicative senescence rate. Then, we attempted to substantiate the statement that the growth advantage of MSCs in long-term expansion under hypoxia is mainly attributed to the delayed replicative senescence by quantitative analysis of experimental data using our mathematical model.

2.2. Two-Compartment ODE-Based Model. By its formal definition, a multicompartment model is a mathematical model used to depict the material or energy transmission among the compartments of a system, where each compartment is considered as a homogeneous entity [32]. Based on the experimental observations, there are at least two kinds of MSCs, that is, two homogeneous entities, to be considered in this MSC expansion model: the proliferating and senescent ones. Thus, we developed a two-compartment ODE-based model to incorporate the two cell states and to depict the possible transitions between them. Typically, only few MSCs may differentiate spontaneously in ex vivo expansion unless induced with lineage-specific mediums on purpose [33, 34]. Therefore, cells that cease growth during expansion are mainly senescent ones rather than committed ones. Nonetheless, for comprehensiveness, our model defines two more general cell states, termed *dividing* and *nondividing* cells, of which the latter is mainly composed of senescent cells. Additionally, because replicative senescence is an irreversible permanent cell cycle arrest [22], only cellular state transition from the dividing compartment to the nondividing compartment is allowed in this model. Besides, cells may undergo apoptosis to death in both states. Overall, the concept schematic of our model is illustrated in Figure 1, and the associated governing equations are as follows:

$$\begin{aligned} \dot{x}_1(t) &= r_{11}x_1(t) - r_{10}x_1(t) - r_{12}(t)x_1(t), \\ \dot{x}_2(t) &= r_{12}(t)x_1(t) - r_{20}x_2(t), \end{aligned} \tag{1}$$

where $x_1(t)$ and $x_2(t)$ represent the dividing and nondividing subpopulations, respectively, whose time derivatives are denoted by $\dot{x}_1(t)$ and $\dot{x}_2(t)$ correspondingly. In addition, the division rate r_{11} of dividing cells and the death rate of the two subpopulations, r_{10} and r_{20}, are all assumed to be time independent, that is, constants. This is a widely adopted hypothesis in cell-modeling studies [30, 35–37], since these parameters usually do not change significantly with time, whereas using constant parameters can greatly simplify the mathematics and hence highlight the most important part of the model.

The most interesting and crucial component of our model is the state transition rate $r_{12}(t)$, which is a time-varying function to embody our key assumption about the influence of oxygen tension on replicative senescence. It should be emphasized that, at the population level, senescence is a continuous process instead of a simple off/on binary switch due to the heterogeneity of cells [37–39]. Furthermore, taking the essential features of senescence into account [22, 38], we require the function $r_{12}(t)$ to possess another two properties: (i) it should be low at the early stage and increases monotonically as cells age and (ii) it must have a limited upper bound for biological feasibility. Thus, the well-known logistic function came to our mind as a qualified candidate for state transition rate $r_{12}(t)$, whose general form is as follows:

$$r_{12}(t) = \frac{L}{1 + e^{-k(t-T)}}, \tag{2}$$

where L denotes the upper bound, k depicts the steepness, and T is the midpoint of the sigmoid curve. Visually, $r_{12}(t)$ is shaped by these three parameters, as depicted in Figure 2 using fictitious parameter values as an example.

In experiments of MSC expansion *in vitro*, usually only the total number of cells can be counted directly instead of the two separate subpopulations. Let $y(t)$ be the total cell number, which is the sum of $x_1(t)$ and $x_2(t)$. To facilitate the subsequent parameter identification, the two constants, r_{11} and r_{10}, in (1) are combined into a single quantity, $r_1 \triangleq r_{11} - r_{10}$, denoting the *net division rate*. Then, the overall MSC proliferation model in (1) can be rewritten into a concise state-space form by the following:

$$\begin{aligned} \begin{bmatrix} \dot{x}_1(t) \\ \dot{x}_2(t) \end{bmatrix} &= \begin{bmatrix} r_1 - r_{12}(t) & 0 \\ r_{12}(t) & -r_{20} \end{bmatrix} \begin{bmatrix} x_1(t) \\ x_2(t) \end{bmatrix}, \\ y(t) &= x_1(t) + x_2(t), \end{aligned} \tag{3}$$

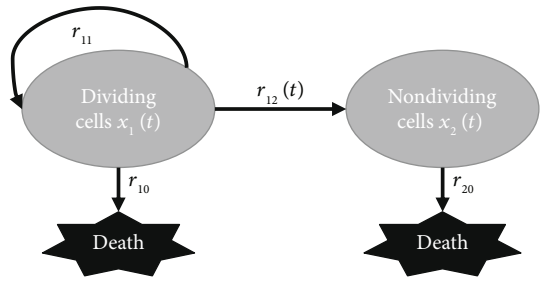

Figure 1: Schematic representation of the two-compartment model. This model conceptualizes the transition of MSCs from the originally dividing state x_1 to the ultimately nondividing state x_2. Cells in both states may die due to internal or external stimuli. r_{11} is the division rate, while r_{10} and r_{20} are the death rate of cells in the two states, respectively, all treated as constants. $r_{12}(t)$ is the time-varying state transition rate.

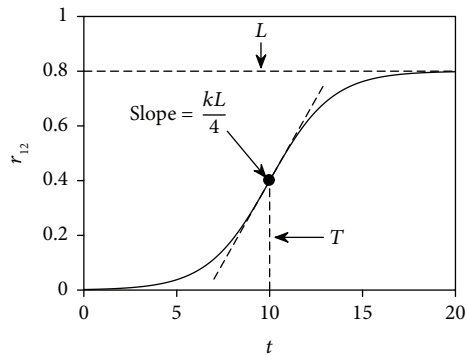

Figure 2: Illustration of the logistic function. It is the form of the state transition rate $r_{12}(t)$ in the two-compartment model, where T is the midpoint and L specifies the upper bound, while k can be used to tune the steepness of the sigmoid curve. The slope of the tangent, that is, the derivative of $r_{12}(t)$ at $t = T$, is also shown by the dashed line.

which is essentially a time-variant second-order linear system due to the time-varying nature of $r_{12}(t)$. Generally, we cannot find a closed-loop solution for $y(t)$ in such systems. Instead, it can be solved by numerical methods [40].

2.3. Model Parameter Fitting. There are five parameters to be determined in the model (3). We thereby gather them into a parameter vector, $\boldsymbol{\theta} = [r_1, \ r_{20}, \ L, \ k, \ T]$, and then identify their values by fitting to the experimental data $D = \{y^m(t_i), \ i = 1, 2, \ldots, N\}$, where $y^m(t_i)$ is the total cell number measured at t_i. The parameters are estimated in the common least-squares sense, that is, to minimize the following cost function:

$$J(\boldsymbol{\theta}) = \sum_{i=1}^{N} (y(t_i) - y^m(t_i))^2, \tag{4}$$

which is the sum of squared residuals. Moreover, we must enforce the biological feasibility of these parameters by imposing proper constraints. Obviously, the three rate parameters r_1, r_{20}, and L should all be positive but cannot be too large for a practical biological system. Besides, a too large steepness k will make the logistic function $r_{12}(t)$ behave more like a step function (Figure 2), which is undesirable because as aforementioned, senescence is a continuous process instead of an abrupt change.

To summarize, after imposing constraints on the parameters, the model parameter fitting is formulated as a constrained optimization problem denoted by the following:

$$\begin{aligned} \min \quad & J(\boldsymbol{\theta}) = \sum_{i=1}^{N} (y(t_i) - y^m(t_i))^2, \\ \text{Subject to} \quad & \begin{cases} 0 < r_1 < 1, \\ 0 < r_{20} < 1, \\ r_1 < L < 1, \\ 0 < k < 1, \\ 0 < T < t_s, \end{cases} \end{aligned} \tag{5}$$

where r_1, r_{20}, L, and k are all assigned a very loose upper bound and t_s is the time when most cells are observed to cease proliferation experimentally. The additional relation $r_1 < L$ stems from the stability requirement of the system (3), that is, we require $r_1 - r_{12}(t) < 0$ for certain $t > t_c$ such that the cell population is prohibited from explosion to infinity [41].

By definition, the optimization in (5) is a nonlinear regression problem, which is generally solved through successive iterations [42]. First, given initial conditions, the numerical solution of $y(t)$ in the model (3) for each time point t_i can be obtained by numerical ODE solvers like the *Runge-Kutta* method. Then, after we get $y(t_i)$, we can tackle the optimization problem (5) with some iterative nonlinear optimization algorithms such as the *Nelder-Mead* simplex search approach. The general workflow of parameter fitting through nonlinear optimization in this study is shown in Figure 3. For practical implementations, we may resort to MATLAB (The MathWorks Inc.) and use its built-in functions such as *ode45*, *fminsearch*, and *fmincon* [27, 28, 43]. More details will be covered in the following parts with respect to specific datasets.

3. Results

In this section, we first investigated our model with two experimental datasets collected from MSC long-term proliferation *in vitro* to examine whether this model could reproduce the observed growth curves and explain the disparity of growth capacity under hypoxia and normoxia. After that, a sensitivity analysis study was performed to reveal which of these parameters have the most significant influence on the population dynamics.

3.1. Collection of Experimental Data. We considered two experiments in literate regarding long-term expansion and differentiation of human MSCs, termed *experiment A* and *experiment B* hereafter. In experiment A, Fehrer and her colleagues cultured MSCs up to about 120 days at 3% oxygen

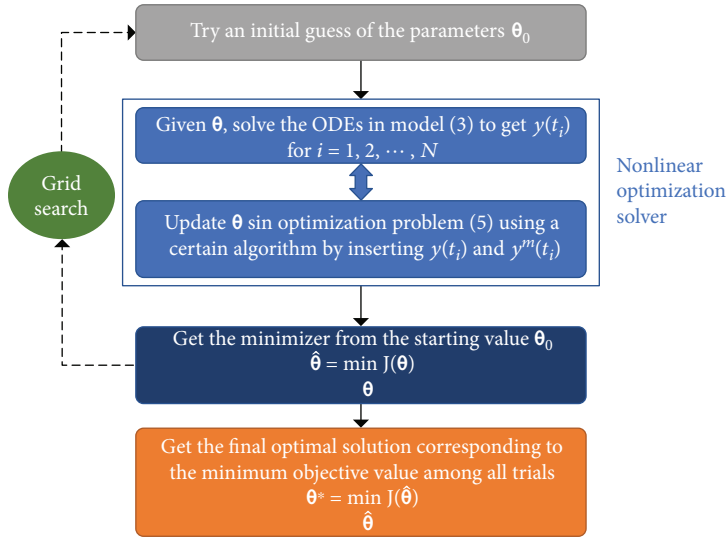

Figure 3: Workflow of parameter fitting via nonlinear regression. First, given initial conditions, we can solve the time-variant ODEs in our model (3) by numerical ODE solvers to get the model predications $y(t_i)$ for N time points in interest. Then, the constrained optimization problem (5) for parameter fitting can be tackled with iterative nonlinear optimization algorithms, for instance, the Nelder-Mead simplex search approach (like the *fminsearch*, *fmincon*, or *lsqcurvefit* functions in MATLAB). Here, it should be noted that to avoid the possible bad local minima associated with nonlinear, nonconvex optimization problems, we may need to try multiple initial guesses of the parameter vector θ_0. We use a systematic approach based on grid search to coordinate multiple initial value trials [44], thanks to the low dimension and small dataset size in this study. This approach can increase the probability that we find the global minimum or at least a good local minimum close to the global one. A detailed description of the fitting procedures is provided in Supplementary Materials (available here).

(hypoxia) and 20% oxygen (normoxia), respectively [7]. In experiment B, to develop a superior protocol for MSC expansion by combining low-density and hypoxic culture, Tsai et al. studied MSCs from 3 donors under normoxic (21% oxygen) and hypoxic (1% oxygen) conditions for about 90 days [8]. Since we focus on MSC expansion in this study, only the proliferation data from the two studies without differentiation induction were adopted. To automatically and accurately extract the experimental data published as figures in these two articles [7, 8], the online tool *WebPlotDigitizer* v3.12 (https://automeris.io/WebPlotDigitizer/) was utilized.

3.2. Experiment A. The experimental data was extracted from Figure 3(a) in the paper [7] including two growth curves of bone marrow-derived MSCs, one from a female donor of age 56 and the other from a 78-year-old male donor, expanded in both oxygen conditions. Since the two datasets are quite similar, here we only show the model fitting and analysis results for the first growth curve (from the female donor of age 56), which includes six measurements for each oxygen condition (Figure 4), and put the other in the Supplementary Materials (Figures S1–S3, Table S1). In consistency with the original paper [7], in this study, the cell number is evaluated by cumulative population doublings (PD), an analogy to the logarithmic scale, defined as follows:

$$y_{\mathrm{PD}}(t) = \log_2 \frac{y(t)}{y(0)}, \tag{6}$$

where $y(0)$ is the initial cell number, $y(t)$ the cell number, and $y_{\mathrm{PD}}(t)$ the corresponding PD at time t.

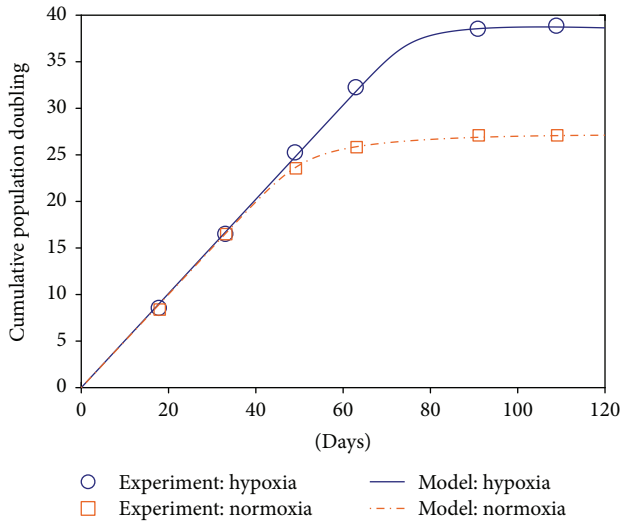

Figure 4: Experimental measurements and model-fitted population dynamics of MSCs under hypoxia and normoxia in experiment A. The cultured MSCs under study were originally obtained from a female donor of age 56. PD: cumulative population doublings.

Now with the six measurements $y^m_{\mathrm{PD}}(t_i)$ at hand, $i = 1, 2, \ldots, 6$, to conduct model parameter fitting, we additionally need the initial cell numbers of the two subpopulations, $x_1(0)$ and $x_2(0)$, to solve the ODE model (3). However, typically in practice, the precise value of $x_1(0)$ and $x_2(0)$ cannot be measured directly. Fortunately, at the beginning, senescent cells only took up a very small portion, observed by checking their morphological appearance, which was further confirmed

through assessment of specific senescence markers [7]. Therefore, we simply assumed that all cells were dividing initially, that is, $x_1(0) = y(0)$ and $x_2(0) = 0$. Then, we can fit the five parameters in our model (3) by minimizing the constrained cost function in (5) with nonlinear least-squares optimization algorithm such as *fmincon* or *fminsearch* in MATLAB. The fitted parameters for the two conditions are listed in Table 1. By inserting these fitted parameter values, we simulated the MSC proliferation process numerically using the model (3). Figure 4 shows the comparison between model-predicted and experimentally measured MSC expansion dynamics under hypoxia and normoxia.

Notably in Figure 4, our model can fit the experimental data in both two conditions nearly perfectly. This impressive fitting performance implies that the logistic function is a good candidate to model the oxygen tension-dependent and time-variant replicative senescence progression process. With this key component, our two-compartment model can well describe the MSC proliferation dynamics in both oxygen conditions with enough explanatory power. Although other functions like the generalized logistic model and the Gompertz model can also display a sigmoid curve, we choose the simple logistic function in our model according to the Occam's razor principle. It is also noted that more complex functions usually have more parameters, which may compromise the interpretability of the theoretical model since it is hard to endow all the parameters with proper biological meanings.

To further verify this argument, we examined the proportion of the dividing and nondividing cells in the whole culture process with data simulated by our model (3), presented in Figure 5. Apparently, almost all MSCs are dividing at the early stage, while the nondividing fraction keeps increasing until most of the cells cease division at the end. Therefore, in agreement with the qualitative experimental findings [7], at population level cells gradually lose their proliferative capability along with their aging. Furthermore, Figure 5 shows that cells under normoxia cease growth much earlier than hypoxic cells. After approximately 50 days, only half of the cells keep dividing under normoxia (Figure 5(b)), while such decline does not happen until about 75 days in hypoxic culture (Figure 5(a)). There is no doubt that such delay of replicative senescence about 25 days will contribute to significantly more population doublings in MSC expansion. This fact further confirms that replicative senescence is indeed slowed down under hypoxia in consistency with multiple experimental observations that considerably more senescent cells are detected in normoxic culture [7, 8, 20, 33].

To acquire a deeper insight of the above observed phenomena, we continued to probe the time evolution of the state transition rate $r_{12}(t)$, defined in (2), under the two oxygen conditions. Figure 6 shows the comparison of the state transition rate $r_{12}(t)$ simulated numerically using the two sets of parameters in Table 1 for hypoxic and normoxic conditions, respectively. To assess the pace of replicative senescence quantitatively, the midpoint time T may act as a good indicator of the senescence pace or roughly the *onset* of massive senescence at population level, since replicative senescence is a continuous process. We notice $T_n = 47.35$ and $T_h = 72.37$ for normoxia and hypoxia, respectively, which clearly exposes the delay of replicative senescence under hypoxia. Here, though the steepness k is close, one may be still wondering the role of L since it looks somewhat different in the two conditions as well (Figure 6). To further check its effect, we deliberately set $T_h = T_n$ in the two conditions and ran simulations again. Results show that, unlike Figure 4, the model predications under hypoxia with such parameters deviate far away from the experimental data (Figure S4). Thus, this inconformity proves the dominant role of T in causing MSC expansion disparity in the two conditions. In fact, it is easy to see from Figure 2 that a larger L value can only tend to speed up senescence and thereby inhibit MSC expansion instead of promotion.

Table 1: Model parameter values for normoxic and hypoxic conditions fitted from MSC expansion data collected in experiment A. r_1: net expansion rate; r_{20}: death rate of nondividing cells; L, k, and T are the upper bound, the steepness, and the midpoint time of the logistic state transition rate $r_{12}(t)$, respectively.

Parameter	Normoxia	Hypoxia
r_1 (day^{-1})	0.3472	0.3505
r_{20} (day^{-1})	0.0133	0.0183
L (day^{-1})	0.3588	0.3967
k	0.3169	0.3944
T (day)	47.3494	72.3664

As a concluding remark of experiment A, our model tells that the distinct MSC proliferation efficiency mainly results from the different senescence pace, indicated by the large difference of T, in the two conditions. Besides, although we simply assume all cells are dividing initially in the present results, the fitted parameter values will remain almost unchanged and therefore our reasoning still applies, even if the initial fraction of nondividing cells is not zero, say, 10%, as shown in Table S2. Next, we will further highlight the competence of our model with another dataset collected from long-term MSC expansion, whose data is not as complete as this one.

3.3. Experiment B. Generally, only after a long time of expansion, roughly more than 100 days or 15 passages [7, 16], will MSCs expanded *in vitro* completely stop proliferation. Consequently, quite few experimental data are available in literature for such a long time. The data of experiment B were extracted from Figure 1(a) in the paper [8] with a culture period of only 84 days. For consistency, the cell number is also measured using PD instead of the original fold increase [8], which can be obtained with the following formula:

$$y_{PD}(t_k) = \log_2 \frac{y(0)\Pi_{i=1}^{k} f(t_i)}{y(0)} = \sum_{i=1}^{k} \log_2 f(t_i), \quad k = 1, 2, \ldots, 7, \tag{7}$$

where $f(t_k)$ is the fold increase of cell number at time t_k. After such data preprocessing, the experimental data of experiment B including seven measurements are shown in Figure 7. We notice that in neither of the two conditions have

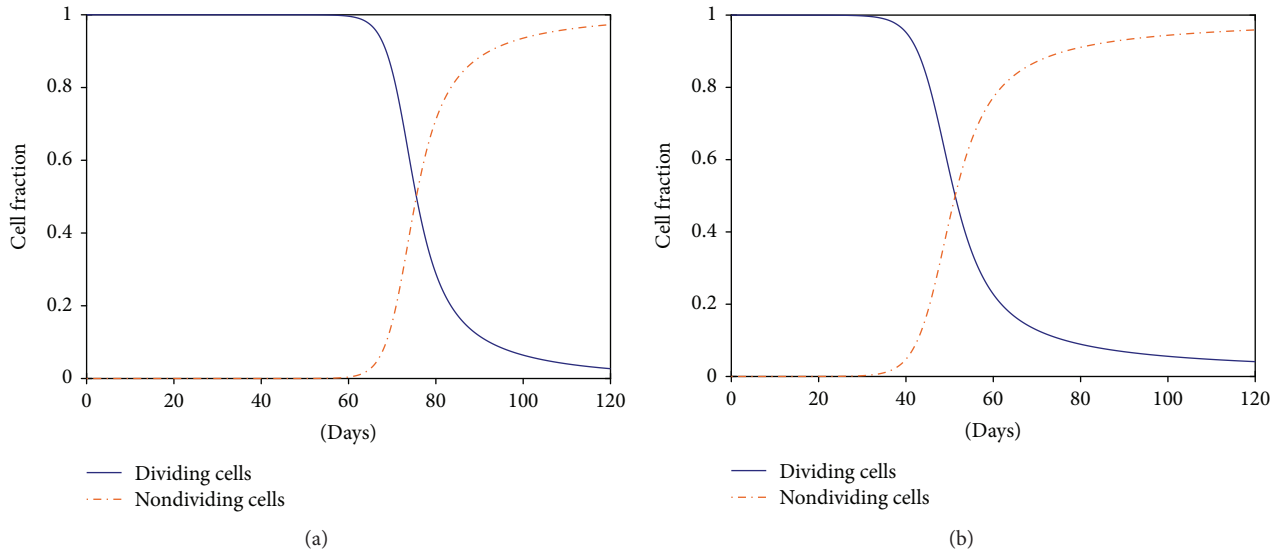

FIGURE 5: Simulation of the dividing and nondividing cell fractions in the two oxygen environments of experiment A. (a) Hypoxia. (b) Normoxia. Initially (at day 0), it is assumed that all cells are dividing in both two conditions.

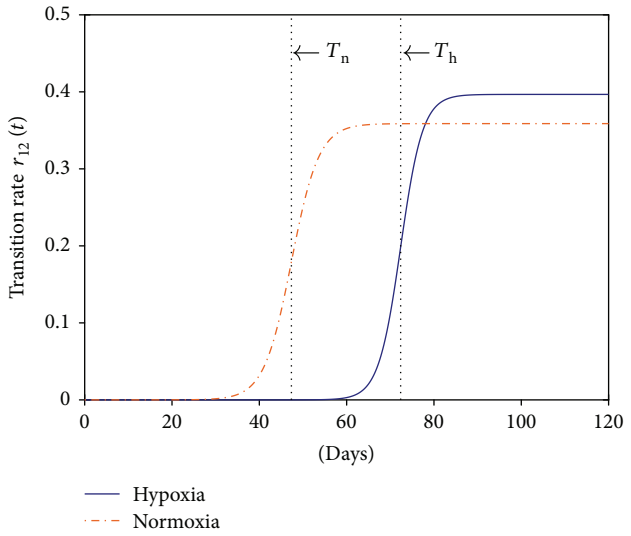

FIGURE 6: Comparison of the time-variant state transition rate $r_{12}(t)$ for MSCs cultured under hypoxia and normoxia in experiment A. The three parameters used to simulate the logistic function $r_{12}(t)$ defined in (2) can be found in Table 1, of which the midpoint time T is annotated in the figure as T_n and T_h for normoxia and hypoxia, respectively.

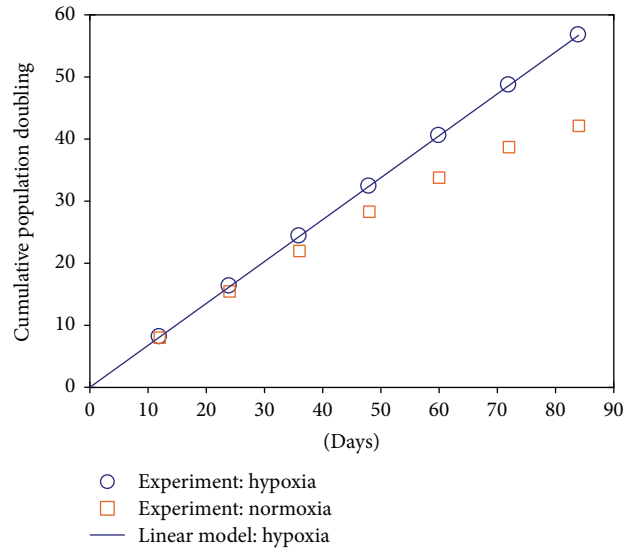

FIGURE 7: Experimental measurements of cell numbers under hypoxia and normoxia and the fitting of the hypoxic data with a linear model in experiment B. The R^2 (coefficient of determination) of this simple linear regression is very close to 1, indicating that the hypoxic data can be well replicated with the linear model.

the expanded MSCs reached the stationary growth phase, that is, they are still proliferating even at the end, which will inevitably cause difficulty in model parameter fitting, especially for the hypoxic case. To examine the universality of the model structure and model characteristics we found in experiment A, we tried to combine the hypoxic and normoxic data together to identify the model parameters.

Now recall our findings in experiment A (Figure 4). If most of the cells are actively dividing, particularly under hypoxia, the cell population will exhibit an exponential growth law, which appears as a straight line when cell numbers are represented by PD, justified by the following:

$$y_{\mathrm{PD}}(t) = \log_2 \frac{y(t)}{y(0)} \approx \log_2 \frac{y(0)e^{r_1 t}}{y(0)} = (r_1 \log_2 e)t, \qquad (8)$$

where $y(0)$ is the initial cell number and r_1 is the net expansion rate of dividing cells. In (8), we simply assume that all cells are dividing such that there exists $\dot{y}(t) = \dot{x}_1(t) = r_1$. Unsurprisingly, we notice that the hypoxic data points in

Figure 7 indeed seem to lie on a straight line. Therefore, it is natural to perform linear regression on the hypoxic data to fit the straight line's slope $s = r_1 \log_2 e$ (Figure 7).

In experiment A, the parameter r_1 we have fitted in the two conditions are approximately equal (Table 1). Thus, it is reasonable to assign $r_1 = s/\log_2 e$ obtained under hypoxia to its normoxic counterpart. With r_1 fixed, it is feasible to fit the remaining four parameters with the normoxic data. Nevertheless, for hypoxia, because all experimental data belong to the exponential growth phase, it is still impossible to determine a *unique* optimal set of parameters by fitting the hypoxic data. To resolve this difficulty, we chose r_{20}, L under hypoxia identical to the ones we have fitted for normoxia based on our experience in experiment A (Table 1) and tuned the parameter k manually to match the exponential grow curve. The parameter fitting results for experiment B are reported in Table 2.

With the parameter values listed in Table 2, we can simulate our model to get the proliferation trajectory for MSCs under normoxia, shown in Figure 8. Once again, the theoretical predications generated by our model, even fitted with incomplete data (i.e., cells are still proliferating at the end), show good agreement with the experimental measurements. Since the parameter T remains unknown for hypoxia (Table 2) due to the fact that all MSCs under hypoxia are still in the exponential growth phase, we tested different values of T to highlight its impact on population dynamics (Figure 8). Apparently, models with $T = 100$, 110,or 120 can match the experimental data equally well. More interestingly, this cluster of growth curves, varied by only one parameter T, exactly demonstrates the paramount influence of T on MSC proliferative capacity: a delay of T by 10 days can bring about roughly an additional 7 PD under hypoxia. This is consistent with our key findings in experiment A, that is, the distinguished MSC expansion ability in long-term culture under hypoxia and normoxia is mainly reflected by the different values of parameter T in our model under these two conditions.

To summarize our work in experiment B, we have first successfully fitted our model with only experimental data before the stationary stage. It is a critical capability of our model to accomplish not only interpolations but also extrapolations with even poor availability of experimental data. This fact reflects that our model has grasped the dominating cellular mechanism responsible for the experimental observations. On the other hand, we must admit that it is unattainable to determine a unique set of model parameters if too little diversity is present in the data because many sets of parameters can work equally well. For example, with only exponential-phase cell proliferation data under hypoxia in this experiment, multiple possible values of T lead to the same fitting performance (Figure 8). Even so, by examining various parameter values tentatively, our model still reveals the pivotal impact of oxygen tension on MSCs expanded *in vitro*: hypoxia can delay the onset of MSC senescence and thus promote their proliferation, implied by the great influence of T. Finally, as a side note, one may notice that the parameter values for Experiments A and B are different. This discrepancy stems from many other variables between the two experiments (from two independent studies [7, 8]), for example, the specific culture condition, the growth media, and the age/sex of the cell donors. It is reasonable to obtain different parameter values since all these variables may influence MSC expansion efficiency. However, in each experiment (A or B), the only control variable between the two conditions (hypoxia and normoxia) is the oxygen tension, and after fitting our model to the data, the value of the parameter T under hypoxia is consistently much larger than the one under normoxia for both experiments.

Table 2: Model parameter values for normoxic and hypoxic conditions fitted from data in experiment B. r_1: net expansion rate; r_{20}: death rate of nondividing cells; L, k, and T are the upper bound, the steepness, and the midpoint time of the logistic state transition rate $r_{12}(t)$, respectively.

Parameter	Normoxia	Hypoxia
r_1 (day^{-1})	0.4679[†]	0.4679[†]
r_{20} (day^{-1})	0.0286	0.0286[‡]
L (day^{-1})	0.5864	0.5864[‡]
k	0.0404	0.15[§]
T (day)	79.0046	?[¶]

[†]Fitted from hypoxic data using linear regression and set r_1 under normoxia equal to the one for hypoxia. [‡]Set equal to their counterparts under normoxia. [§]Tuned manually to fit the hypoxic data. [¶]To be determined.

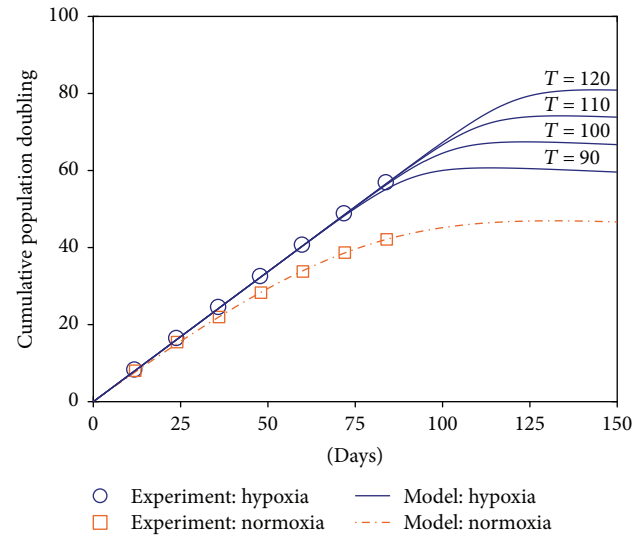

Figure 8: Experimental measurements and model-predicted population dynamics of MSCs under hypoxia and normoxia in experiment B. For the series of growth curves under hypoxia, the first four parameters are fixed (see Table 2), while the last parameter T varies from 90 to 120 equidistantly to demonstrate its significant effect on cell proliferation. PD: cumulative population doublings.

3.4. Sensitivity Analysis. In above experiments, our two-compartment model can effectively describe MSC expansion by approximating replicative senescence with a logistic transition function. To further assess the impact of parameters on model outputs, that is, to evaluate which parameters are the

most influential on the system output when the inputs (the initial condition) are fixed, we investigated their individual sensitivity using one of the most widely used evaluation methods, called *one-at-a-time* [45]. In this strategy, only one parameter is varied at a time while all others are fixed at their nominal (fitted) values; then, the corresponding change of model output is recorded [37, 45]. To quantify the parameter sensitivity, each of the five parameters is perturbed in turn by a random degree ϵ, where ϵ is uniformly distributed between −10% and 10%, and the other parameters are fixed at their nominal (fitted) values. Repeat the parameter perturbation and subsequent model simulation for $K = 1000$ times. Then, the sensitivity s_i of the ith parameter is scored by the standard deviation of the model output y_{sp} (population doublings at the stationary phase) in the total K runs, given as follows:

$$s_i = \sqrt{\frac{1}{K-1}\sum_{j=1}^{K}\left(y_{sp,j} - \mu\right)^2}, \tag{9}$$

where $y_{sp,j}$ is the model output of the jth run and $\mu = 1/K \sum_{j=1}^{K} y_{sp,j}$ is the mean of y_{sp} in the K runs.

In experiment A, we have enough experimental data and have fitted all the parameters for datasets of two donors, that is, one female donor of age 56 (Table 1) and another male donor of age 78 (Table S1). Thus, the sensitivity analysis was conducted using the model obtained in experiment A. The outcome is summarized in Figure 9. Despite the various parameter values in the four cases, their sensitivity distribution shares a notably common pattern, demonstrating the inherent consistency of the parameter sensitivity ranking of our model, even though the absolute values of these parameters are different. This fact indicates that the interpretation of our model is reasonable even in different experimental settings. Regarding the individual sensitivity, as expected, the fundamental driving force of MSC proliferation is the net expansion rate of dividing cells, r_1, highlighted as the most influential parameter, which dominates the exponential growth phase, as demonstrated in (8). Apart from r_1, the second predominant parameter is T, which largely determines the MSC state transition rate from the dividing state to the nondividing state $r_{12}(t)$. On the contrary, the death rate r_{20} and the steepness parameter k only exhibit negligible sensitivity (Figure 9).

In brief, though the two parameters r_1 and L also possess noteworthy influence on model outputs (Figure 9), it is only the parameter T that can explain the impressive difference of the model output, that is, cell number, under hypoxic and normoxic conditions (Figure 4, Figure S1) since r_1 and L have close and comparable values in the two conditions (Table 1, Table S1). However, one may also notice that the value of r_1 is slightly higher under the hypoxic condition (Table 1) and may suspect its role in promotion of MSC expansion. To clarify this point, we made another simulation study by exchanging the r_1 values of the two conditions while leaving the other parameters unchanged. The result is shown in Figure S5. By comparing Figure S5 with Figure 4 in the main text, we can see that the fitting results change quite little, while there is still a large gap between the final population size under the two conditions. Thus, we can conclude that the minute difference of the fitted r_1 values plays just a negligible role and cannot explain the significant difference of MSC expansion under the two oxygen conditions. Essentially, the largest sensitivity of r_1 is attributed to the exponential growth law in the early stage, see (8). However, the r_1 values under the two conditions are so close that they cannot explain the considerable difference in MSC proliferation. As for the parameter L which also has a large sensitivity, it is easy to see from Table 1 and Figure 6 that the larger L value under hypoxia can only speed up the cellular senescence process and thereby impede MSC expansion. Thus, this parameter is definitely not the factor that contributes to MSC proliferation boosting. By eliminating these possibilities, we can be certain that it is only the parameter T (increased around 50% from normoxia to hypoxia) that can explain the impressive difference of the cell number under hypoxic and normoxic conditions.

In summary, with the above analysis of the two parameter sets fitted by MSC expansion data under hypoxia and normoxia, respectively (Table 1, Table 2, and Table S1), we can conclude that it is the parameter T, a qualified indicator of replicative senescence pace, that is responsible for the distinct MSC expansion productivity under different oxygen conditions. Thus, combining the parameter magnitude comparison and the sensitivity analysis has further strengthened our main argument and verified the fundamental hypothesis of our model, that is, hypoxia can promote MSC expansion through slowdown of replicative senescence, from another perspective, indicated by the impressive sensitivity of T as well as the considerable difference of its value under two oxygen conditions.

4. Discussion

Mesenchymal stem cells are considered valuable and easily accessible cell sources for regenerative medicine due to their high proliferation capacity, their potential for multiple differentiation pathways, their active paracrine effects, and their immunomodulatory features for suppression of excessive immunoreactivity [4, 46–48]. Generally, cell-based therapies and tissue engineering require a sufficiently large number of high-quality cells. Accordingly, the efficient ex vivo expansion of MSCs is of critical importance and has drawn a lot of research interest. In literature, the influence of oxygen tension on MSC expansion and differentiation has been investigated extensively by many experimental studies (see review [12, 49]). Despite the abundance of experimental studies, to the best of our knowledge, our work in this study is the first attempt to analyze the effects of hypoxia on MSC expansion in long-term 2D culture through mathematical modeling in a purely data-driven way. Mathematical reasoning and simulation results have demonstrated that hypoxia can postpone replicative senescence and consequently extend the lifespan of MSCs to produce more cells.

There are multiple suspicious factors which might account for the MSC growth disadvantage when subject to

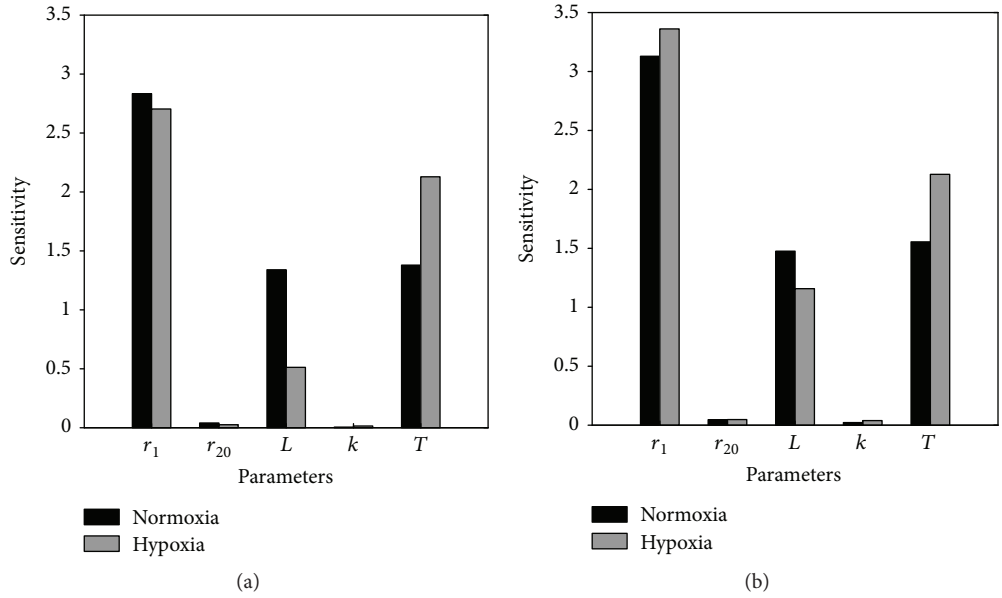

Figure 9: Parameter sensitivity analysis of the two-compartment model. To evaluate the sensitivity, the parameters are perturbed around their nominal values fitted in experiment A with cell data collected from two donors in two conditions: (a) MSCs obtained from a female donor of age 56 and (b) MSCs isolated from a 78-year-old male donor. The exhibited sensitivity is measured by the standard deviation of model outputs in 1000 simulations with randomly perturbed (between ±10%) parameter values using the *one-at-a-time* approach.

a high oxygen tension. For example, we may speculate about a higher death rate or a lower cell division rate under normoxia, considering the typical *in vivo* low-oxygen environment in the bone marrow. To determine the contribution of such factors, we have encoded these hypotheses as parameters in the two-compartment model and then identified parameter values by fitting to the experimental data. Results show that the net expansion rate r_1 and the death rate r_{20} have similar values in both oxygen conditions, implying that the negligible changes of cellular net division rate and death are unlikely to be the main cause of MSC expansion variations. This finding is in agreement with experimental observations: though cell viability might be slightly higher under hypoxia, no obvious differences regarding necrosis or apoptosis were detected experimentally [7, 50]. Besides, MSCs expanded *in vitro* can typically maintain a stable undifferentiated phenotype over time without tumorigenesis [33, 48]. Therefore, the plausible variations in the proportion of committed cells arising from different oxygen tensions cannot explain the dramatically reduced MSC expansion under normoxia, either. By contrast, numerous studies have reported that exposure of MSCs to normoxia can contribute decisively to replicative senescence. They observed a clearly greater number of enlarged and flattened cells, the typical morphology of senescent cells, a higher expression level of senescence markers like SA-β-gal, as well as a shorter telomere length under normoxia than hypoxia, while such phenomena would not appear until many more days later under hypoxia [7, 8, 20, 21]. In our model, because the upper bound L of the state transition rate $r_{12}(t)$ in (2) are similar in the two oxygen conditions (Table 1 and Table 2), it is reasonable to consider the midpoint time parameter T as a representative measurement of the replicative senescence pace. Next, the fitting results and sensitivity analysis tell that the parameter T varies most between hypoxia and normoxia and possesses very high sensitivity, indicating that the most important variable leading to MSC expansion difference in low and high oxygen tensions resides in the replicative senescence progression. In summary, all the above experimental evidence justifies the findings of our two-compartment model, which state that hypoxia can greatly enhance MSC proliferation and prolong their lifespan mainly through inhibition of replicative senescence in long-term culture.

In retrospect, we notice that MSC proliferation displays the typical *S*-shaped growth curve, which may also be represented by others like the exponential-linear or Gompertz model [27]. However, we must emphasize that such models were originally designed to describe the overall population behavior with no discrimination of various cell states. As a result, though such models with only a single-cell state may also fit the data satisfactorily, they cannot reveal the inherent reason which leads to the experimental observations. For example, the cause of the remarkably different MSC expansion capacity under hypoxia and normoxia would still be obscure in a single-compartment model. Thus, the primary merit of our model does not lie in its good fitting of numerical values, though it has demonstrated excellent fitting performance, but rather in its capacity to interpret the qualitative characteristics, to reveal the biological mechanism and to advance our understanding of the experimental data. Intuitively, we use the logistic function to approximate the replicative senescence progression process during cell aging. Thanks to its high interpretability, the profound impact of

hypoxia on replicative senescence has been uncovered and confirmed convincingly.

Technically speaking, the model we have developed in (1) is more of an explanatory model than a predicative one. Explanatory modeling refers to the application of models to data for testing causal hypothesis about theoretical constructs [51]. The top priority of explanatory models is their explanatory power, while predicative modeling focuses on predicative power or *generalization* [51]. Thus, in this study on explanatory modeling, it is the construction and structure of the model based on biological hypothesis that matters most, because the acquired model must be highly interpretable and the parameters should be endowed with biological meanings. This also constitutes our main contribution: we discovered that hypoxia can promote MSC expansion by delaying MSC replicative senescence merely through quantitative analysis of proliferation data with a properly designed two-compartment model, with no need of extra measurements using devoted biological assays, like the detection of cell viability and senescence markers, which may be expensive and time-consuming. Thus, this model is valuable in providing theoretical support for experimentalists' observations. In short, though predictive modeling is forward-looking, explanatory modeling is retrospective [51]. Since our model is not developed for predication purpose, an independent validation experiment is not necessary to test its generalization performance. However, the explanatory power of our model has been validated on multiple experimental datasets, which all lead to the same conclusion: hypoxia causes MSC expansion boosting by inhibiting cellular senescence. With an explanatory model, our study mainly focuses on the comparison of model parameter values fitted under hypoxia and normoxia to explain the underlying mechanism. Thus, it is the relative magnitude of parameters instead of their absolute value that matters.

To enhance MSC expansion to get enough cells for clinical applications, it is of great interest to determine the optimal oxygen concentration so as to maximize the cell yield. However, due to lack of experimental data, the oxygen tension only appears in our model implicitly in the form of hypoxia and normoxia instead of continuous values. Besides, we want to point out that hypoxia and normoxia refer to two coarse ranges of oxygen tension instead of precise concentration values: the former depicts the *in vivo* environment and the latter represents the atmospheric environment. Consequently, we can only demonstrate the superiority of hypoxia against normoxia for MSC long-term expansion, while with the currently available data it is impossible to obtain an accurate predication relationship associating the oxygen tension with the number of MSCs at a given time point. Nevertheless, once we acquire more MSC expansion data systematically at a sequence of oxygen concentrations from dedicated experiments, our model can be extended readily to describe the numerical relationship between oxygen tension and MSC proliferation explicitly. That is, the proposed two-compartment model can serve as a good prototype to be extended into a truly predicative model. Afterwards, the extended model can be used to optimize the oxygen environment and even to build a closed-loop control system for more efficient large-scale cell production by tuning the oxygen tension precisely in real time [52].

Though our model successfully demonstrates that the promoted expansion and the prolonged lifespan of MSCs are mainly attributed to the slowdown of replicative senescence at a reduced oxygen tension, we must admit that it is still a coarse-grained model at the population level and cannot establish the intracellular molecular mechanism for the relevant regulation. In fact, the involved signaling pathways are still controversial and remain to be elucidated, though many speculate that the key response to hypoxia is mediated by the hypoxia-inducible factor- (HIF-) 1 and involves the interaction between p21, p16, and reactive oxygen species (ROS) [8, 12–14, 17, 20]. Thus, a multiscale model integrating the population dynamics and the intracellular biochemical reactions is highly desired to completely dissect the influence of hypoxia on MSC proliferation and differentiation. Further theoretical work on involved signal transduction pathways and gene regulatory networks are planned in our future studies. Lastly, we want to point out that in literature, the effects of hypoxia on short-term MSC proliferation may vary in different studies, which depend on the concrete oxygen tension, the culture conditions, and the cell sources. However, the benefits hypoxia can bring to long-term expansion of MSCs are consistent among various studies even with different culture media and MSC sources [14, 16–19, 49]. As we have addressed since the beginning, our two-compartment model applies specially to the MSC long-term expansion, where the interplay between hypoxia and replicative senescence plays the most important role in determining cell yield.

5. Conclusion

This study underlines the influence of oxygen tension on MSC long-term expansion, and we have presented here, for the first time, a comprehensive two-compartment ODE-based model to characterize the MSC population dynamics under hypoxia and normoxia. A unique aspect of the current study is the adoption of the logistic function to depict the time-variant state transition rate between the two compartments, which is a natural analogy to the continuous senescence progression along with cell aging. Though simplistic in nature, our model has captured the key characteristics of the MSC expansion process and provides a computational basis for deep understanding of the oxygen impacts on MSC proliferation. In accordance with experimental evidence, this theoretical model supports the idea that hypoxia can greatly enhance the proliferation of MSCs and prolong their lifespan in long-term culture through inhibition of replicative senescence. Over the course of this study, we have demonstrated mathematical modeling and analysis as a useful tool for quantitatively interpreting and mining the information hidden in raw experimental data. Since our model is designed and fitted with MSC expansion data in 2D culture (Petri dishes), where oxygen is distributed uniformly in the culture media, it deserves efforts to further explore whether this model can be generalized to the 3D culture scenario such as scaffolds.

Data Availability

The data used to support the findings of this study are available from the corresponding author upon request.

Conflicts of Interest

The authors declare that there is no conflict of interests regarding the publication of this paper.

Acknowledgments

This work was supported by Chinese National Science and Technology Major Special Project on Major New Drug Innovation (no. 2012ZX09503-001-003) and Fundamental Research Funds for the Central Universities (nos. DUT16 ZD227, DUT17ZD222, and DUT18ZD301).

Supplementary Materials

The analysis results for the other dataset (with MSCs from a 78-year-old male donor) are presented in Table S1 and Figures S1–S3, corresponding to Table 1 and Figures 4–6 in the main text. Table S2: model parameter values for normoxic and hypoxic conditions fitted from data in experiment A but with 10% nondividing cells at the beginning. Figure S4: model fitting results by setting $T_h = T_n$ in experiment A as a comparison to Figure 4 in the main text. Figure S5: model fitting results by exchanging the net expansion rate r_1 in Table 1 as a contrast of Figure 4 in the main text. The detailed fitting procedures are also presented. *(Supplementary Materials)*

References

[1] I. Ullah, R. B. Subbarao, and G. J. Rho, "Human mesenchymal stem cells - current trends and future prospective," *Bioscience Reports*, vol. 35, no. 2, article e00191, 2015.

[2] A. Pezzi, B. Amorin, Á. Laureano et al., "Effects of hypoxia in long-term in vitro expansion of human bone marrow derived mesenchymal stem cells," *Journal of Cellular Biochemistry*, vol. 118, no. 10, pp. 3072–3079, 2017.

[3] A. Keating, "Mesenchymal stromal cells: new directions," *Cell Stem Cell*, vol. 10, no. 6, pp. 709–716, 2012.

[4] T. Squillaro, G. Peluso, and U. Galderisi, "Clinical trials with mesenchymal stem cells: an update," *Cell Transplantation*, vol. 25, no. 5, pp. 829–848, 2016.

[5] J. Ankrum and J. M. Karp, "Mesenchymal stem cell therapy: two steps forward, one step back," *Trends in Molecular Medicine*, vol. 16, no. 5, pp. 203–209, 2010.

[6] S. Capasso, N. Alessio, T. Squillaro et al., "Changes in autophagy, proteasome activity and metabolism to determine a specific signature for acute and chronic senescent mesenchymal stromal cells," *Oncotarget*, vol. 6, no. 37, pp. 39457–39468, 2015.

[7] C. Fehrer, R. Brunauer, G. Laschober et al., "Reduced oxygen tension attenuates differentiation capacity of human mesenchymal stem cells and prolongs their lifespan," *Aging Cell*, vol. 6, no. 6, pp. 745–757, 2007.

[8] C.-C. Tsai, Y.-J. Chen, T.-L. Yew et al., "Hypoxia inhibits senescence and maintains mesenchymal stem cell properties through down-regulation of E2A–p21 by HIF–TWIST," *Blood*, vol. 117, no. 2, pp. 459–469, 2011.

[9] L. Aust, B. Devlin, S. J. Foster et al., "Yield of human adipose-derived adult stem cells from liposuction aspirates," *Cytotherapy*, vol. 6, no. 1, pp. 7–14, 2004.

[10] D. S. Kim, Y. J. Ko, M. W. Lee et al., "Effect of low oxygen tension on the biological characteristics of human bone marrow mesenchymal stem cells," *Cell Stress and Chaperones*, vol. 21, no. 6, pp. 1089–1099, 2016.

[11] D. Baksh, L. Song, and R. S. Tuan, "Adult mesenchymal stem cells: characterization, differentiation, and application in cell and gene therapy," *Journal of Cellular and Molecular Medicine*, vol. 8, no. 3, pp. 301–316, 2004.

[12] L. B. Buravkova, E. R. Andreeva, V. Gogvadze, and B. Zhivotovsky, "Mesenchymal stem cells and hypoxia: where are we?," *Mitochondrion*, vol. 19, pp. 105–112, 2014.

[13] M. G. Valorani, E. Montelatici, A. Germani et al., "Pre-culturing human adipose tissue mesenchymal stem cells under hypoxia increases their adipogenic and osteogenic differentiation potentials," *Cell Proliferation*, vol. 45, no. 3, pp. 225–238, 2012.

[14] S.-P. Hung, J. H. Ho, Y.-R. V. Shih, T. Lo, and O. K. Lee, "Hypoxia promotes proliferation and osteogenic differentiation potentials of human mesenchymal stem cells," *Journal of Orthopaedic Research*, vol. 30, no. 2, pp. 260–266, 2012.

[15] S. M. Prasad, M. Czepiel, C. Cetinkaya et al., "Continuous hypoxic culturing maintains activation of Notch and allows long-term propagation of human embryonic stem cells without spontaneous differentiation," *Cell Proliferation*, vol. 42, no. 1, pp. 63–74, 2009.

[16] J. C. Estrada, C. Albo, A. Benguría et al., "Culture of human mesenchymal stem cells at low oxygen tension improves growth and genetic stability by activating glycolysis," *Cell Death & Differentiation*, vol. 19, no. 5, pp. 743–755, 2012.

[17] B. Lv, F. Li, J. Fang et al., "Hypoxia inducible factor 1α promotes survival of mesenchymal stem cells under hypoxia," *American Journal of Translational Research*, vol. 9, no. 3, pp. 1521–1529, 2017.

[18] S. V. Boregowda, V. Krishnappa, J. W. Chambers et al., "Atmospheric oxygen inhibits growth and differentiation of marrow-derived mouse mesenchymal stem cells via a p53 dependent mechanism: implications for long-term culture expansion," *Stem Cells*, vol. 30, no. 5, pp. 975–987, 2012.

[19] F. Dos Santos, P. Z. Andrade, J. S. Boura, M. M. Abecasis, C. L. Da Silva, and J. Cabral, "Ex vivo expansion of human mesenchymal stem cells: a more effective cell proliferation kinetics and metabolism under hypoxia," *Journal of Cellular Physiology*, vol. 223, no. 1, pp. 27–35, 2010.

[20] Y. Jin, T. Kato, M. Furu et al., "Mesenchymal stem cells cultured under hypoxia escape from senescence via down-regulation of p16 and extracellular signal regulated kinase," *Biochemical and Biophysical Research Communications*, vol. 391, no. 3, pp. 1471–1476, 2010.

[21] A. Ito, T. Aoyama, M. Yoshizawa et al., "The effects of short-term hypoxia on human mesenchymal stem cell proliferation, viability and $p16^{INK4A}$ mRNA expression: investigation using a simple hypoxic culture system with a deoxidizing agent," *Journal of Stem Cells & Regenerative Medicine*, vol. 11, no. 1, pp. 25–31, 2015.

[22] J. Campisi and F. d'Adda di Fagagna, "Cellular senescence: when bad things happen to good cells," *Nature Reviews Molecular Cell Biology*, vol. 8, no. 9, pp. 729–740, 2007.

[23] J. M. Van Deursen, "The role of senescent cells in ageing," *Nature*, vol. 509, no. 7501, pp. 439–446, 2014.

[24] L. Marucci, "Nanog dynamics in mouse embryonic stem cells: results from systems biology approaches," *Stem Cells International*, vol. 2017, Article ID 7160419, 14 pages, 2017.

[25] O. J. Abilez, E. Tzatzalos, H. Yang et al., "Passive stretch induces structural and functional maturation of engineered heart muscle as predicted by computational modeling," *Stem Cells*, vol. 36, no. 2, pp. 265–277, 2018.

[26] I. Glauche, M. Cross, M. Loeffler, and I. Roeder, "Lineage specification of hematopoietic stem cells: mathematical modeling and biological implications," *Stem Cells*, vol. 25, no. 7, pp. 1791–1799, 2007.

[27] S. Benzekry, C. Lamont, A. Beheshti et al., "Classical mathematical models for description and prediction of experimental tumor growth," *PLoS Computational Biology*, vol. 10, no. 8, article e1003800, 2014.

[28] G. Lemon, S. L. Waters, F. R. A. J. Rose, and J. R. King, "Mathematical modelling of human mesenchymal stem cell proliferation and differentiation inside artificial porous scaffolds," *Journal of Theoretical Biology*, vol. 249, no. 3, pp. 543–553, 2007.

[29] A. Krinner, M. Zscharnack, A. Bader, D. Drasdo, and J. Galle, "Impact of oxygen environment on mesenchymal stem cell expansion and chondrogenic differentiation," *Cell Proliferation*, vol. 42, no. 4, pp. 471–484, 2009.

[30] J. Hatami, F. C. Ferreira, C. L. da Silva, J. Tiago, and A. Sequeira, "Computational modeling of megakaryocytic differentiation of umbilical cord blood-derived stem/progenitor cells," *Computers & Chemical Engineering*, vol. 94, pp. 117–127, 2016.

[31] K. S. Tieu, R. S. Tieu, J. A. Martinez-Agosto, and M. E. Sehl, "Stem cell niche dynamics: from homeostasis to carcinogenesis," *Stem Cells International*, vol. 2012, Article ID 367567, 9 pages, 2012.

[32] K. Godfrey, *Compartmental Models and Their Application*, Academic Press, New York, NY, USA, 1983.

[33] L. Basciano, C. Nemos, B. Foliguet et al., "Long term culture of mesenchymal stem cells in hypoxia promotes a genetic program maintaining their undifferentiated and multipotent status," *BMC Cell Biology*, vol. 12, no. 1, p. 12, 2011.

[34] M. F. Pittenger, A. M. Mackay, S. C. Beck et al., "Multilineage potential of adult human mesenchymal stem cells," *Science*, vol. 284, no. 5411, pp. 143–147, 1999.

[35] L. G. Marcu, D. Marcu, and S. M. Filip, "*In silico* study of the impact of cancer stem cell dynamics and radiobiological hypoxia on tumour response to hyperfractionated radiotherapy," *Cell Proliferation*, vol. 49, no. 3, pp. 304–314, 2016.

[36] M. D. Cooper, M. L. Tanaka, and I. K. Puri, "Coupled mathematical model of tumorigenesis and angiogenesis in vascular tumours," *Cell Proliferation*, vol. 43, no. 6, pp. 542–552, 2010.

[37] S. Schauble, K. Klement, S. Marthandan et al., "Quantitative model of cell cycle arrest and cellular senescence in primary human fibroblasts," *PLoS One*, vol. 7, no. 8, article e42150, 2012.

[38] W. Wagner, P. Horn, M. Castoldi et al., "Replicative senescence of mesenchymal stem cells: a continuous and organized process," *PLoS ONE*, vol. 3, no. 5, article e2213, 2008.

[39] N. Bhatia-Dey, R. R. Kanherkar, S. E. Stair, E. O. Makarev, and A. B. Csoka, "Cellular senescence as the causal nexus of aging," *Frontiers in Genetics*, vol. 7, 2016.

[40] J. C. Butcher, *The Numerical Analysis of Ordinary Differential Equations: Runge-Kutta and General Linear Methods*, Wiley-Interscience, New York, NY, USA, 1987.

[41] W. J. Rugh and W. J. Rugh, *Linear System Theory*, Prentice-Hall, Inc., Upper Saddle River, NJ, USA, 1996.

[42] H. Motulsky and A. Christopoulos, *Fitting Models to Biological Data Using Linear and Nonlinear Regression: A Practical Guide to Curve Fitting*, Oxford University Press, New York, NY, USA, 2004.

[43] K.-R. Qin and C. Xiang, "Hysteresis modeling for calcium-mediated ciliary beat frequency in airway epithelial cells," *Mathematical Biosciences*, vol. 229, no. 1, pp. 101–108, 2011.

[44] F. Schleer, "Finding starting-values for the estimation of vector STAR models," *Econometrics*, vol. 3, no. 1, pp. 65–90, 2015.

[45] F. Pianosi, K. Beven, J. Freer et al., "Sensitivity analysis of environmental models: a systematic review with practical workflow," *Environmental Modelling & Software*, vol. 79, pp. 214–232, 2016.

[46] S. Aggarwal and M. F. Pittenger, "Human mesenchymal stem cells modulate allogeneic immune cell responses," *Blood*, vol. 105, no. 4, pp. 1815–1822, 2005.

[47] A. C. Yorukoglu, A. E. Kiter, S. Akkaya, N. L. Satiroglu-Tufan, and A. C. Tufan, "A concise review on the use of mesenchymal stem cells in cell sheet-based tissue engineering with special emphasis on bone tissue regeneration," *Stem Cells International*, vol. 2017, Article ID 2374161, 13 pages, 2017.

[48] R. S. Tuan, G. Boland, and R. Tuli, "Adult mesenchymal stem cells and cell-based tissue engineering," *Arthritis Research & Therapy*, vol. 5, no. 1, pp. 32–45, 2002.

[49] C.-C. Tsai, T.-L. Yew, D.-C. Yang, W.-H. Huang, and S.-C. Hung, "Benefits of hypoxic culture on bone marrow multipotent stromal cells," *American Journal of Blood Research*, vol. 2, no. 3, pp. 148–159, 2012.

[50] L. B. Boyette, O. A. Creasey, L. Guzik, T. Lozito, and R. S. Tuan, "Human bone marrow-derived mesenchymal stem cells display enhanced clonogenicity but impaired differentiation with hypoxic preconditioning," *Stem Cells Translational Medicine*, vol. 3, no. 2, pp. 241–254, 2014.

[51] G. Shmueli, "To explain or to predict?," *Statistical Science*, vol. 25, no. 3, pp. 289–310, 2010.

[52] F. Menolascina, G. Fiore, E. Orabona et al., "*In-vivo* real-time control of protein expression from endogenous and synthetic gene networks," *PLoS Computational Biology*, vol. 10, no. 5, article e1003625, 2014.

Hindawi
Stem Cells International
Volume 2018, Article ID 1658195, 10 pages
https://doi.org/10.1155/2018/1658195

Research Article

Human Placenta-Derived Mesenchymal Stem Cells Reduce Mortality and Hematoma Size in a Rat Intracerebral Hemorrhage Model in an Acute Phase

Bo Young Choi,[1] Ok Joon Kim,[2] Sae-Hong Min,[3] Jeong Hyun Jeong,[1] Sang Won Suh,[1] and Tae Nyoung Chung[3]

[1]*Department of Physiology, College of Medicine, Hallym University, Hallymdaehak-gil, Chuncheon 24252, Republic of Korea*
[2]*Department of Neurology, CHA University School of Medicine, 59 Yatap-Ro, Bundang-Gu, Seongnam 13496, Republic of Korea*
[3]*Department of Emergency Medicine, CHA University School of Medicine, 59 Yatap-Ro, Bundang-Gu, Seongnam 13496, Republic of Korea*

Correspondence should be addressed to Sang Won Suh; swsuh@hallym.ac.kr and Tae Nyoung Chung; hendrix74@gmail.com

Received 4 December 2017; Revised 5 April 2018; Accepted 8 April 2018; Published 2 May 2018

Academic Editor: Marco Tatullo

Copyright © 2018 Bo Young Choi et al. This is an open access article distributed under the Creative Commons Attribution License, which permits unrestricted use, distribution, and reproduction in any medium, provided the original work is properly cited.

Intracerebral hemorrhage (ICH) is a critical disease, highly associated with mortality and morbidity. Several studies have demonstrated the beneficial effect of mesenchymal stem cells (MSCs) on ICH, mostly focused on their mid-to-long-term effect. Acute hematoma expansion is one of the most important prognostic factors of ICH. We hypothesized that MSCs would decrease mortality and hematoma size in acute ICH, based on the findings of a few recent researches reporting their effect on blood-brain barrier and endothelial integrity. Rat ICH models were made using bacterial collagenase. One hour after ICH induction, the rats were randomly divided into MSC-treated and control groups. Mortality, hematoma volume, ventricular enlargement, brain edema, and degenerating neuron count were compared at 24 hours after ICH induction. Expression of tight junction proteins (ZO-1, occludin) and coagulation factor VII mRNA was also compared. Mortality rate (50% versus 8.3%), hematoma size, ventricular size, hemispheric enlargement, and degenerating neuron count were significantly lower in the MSC-treated group ($p = 0.034$, 0.038, 0.001, 0.022, and <0.001, resp.), while the expression of ZO-1 and occludin was higher ($p = 0.007$ and 0.012). Administration of MSCs may prevent hematoma expansion in the hyperacute stage of ICH and decrease acute mortality by enhancing the endothelial integrity of cerebral vasculature.

1. Introduction

Nontraumatic intracerebral hemorrhage (ICH) is highly associated with mortality and morbidity, with a substantially worse prognosis than ischemic stroke [1, 2]. Moreover, it is highly associated with acute mortality; nearly 50% of patients die before 30 days after the onset of ICH, and half of them die within 48 hours [3–5]. Though various therapeutic approaches to overcome the extremely poor prognosis of ICH have been studied, including the administration of neuroprotective agents and exogenous coagulation factors, only symptomatic treatments are currently considered effective therapeutic options for ICH [2, 6, 7]. Stem cell therapy is currently regarded as one of the most promising strategies for the treatment of many incurable diseases and has shown neuroprotective effects on various neuronal injury and degenerative disease models. Various preclinical studies have also shown the beneficial neuroprotective effects of stem cell therapy for ICH via secretion of neurotrophic factors [8, 9].

In addition to loss of brain parenchymal tissue, early hematoma expansion is known to be an important prognostic factor of ICH that can predict mortality and poor functional outcome [1, 10, 11]. Various medical therapies to overcome poor prognosis due to hematoma expansion, including the administration of corticosteroids, glycerol, and mannitol, have been studied, but none of these have shown beneficial effects in clinical trials [12–14]. Recently, recombinant coagulation factor VII administration, an

approach to improve the prognosis of acute ICH by limiting early hematoma growth via the factor's acute hemostatic effect, showed potential benefits in an early-phase clinical trial but failed to show a significant effect in a phase III clinical trial [15, 16]. Most studies of stem cell therapy for ICH have focused on neuronal death, functional outcome, and hematoma size in subacute-to-chronic stages of the disease but not on the prognosis of the acute-stage or early hematoma expansion [8, 9]. Results of recent studies showing that the administration of mesenchymal stem cells (MSCs) prevents blood-brain barrier (BBB) disruption and endothelial damage suggest that MSCs may improve the prognosis of ICH through the prevention of ongoing bleeding in the acute stage by intensification of the cerebral vasculature [17, 18].

We aimed to assess the effect of MSCs on ICH, specifically focusing on prognosis and hematoma size in the acute stage, and to suggest a possible mechanism. We hypothesized that the administration of MSCs would decrease mortality and hematoma size in the acute stage of ICH through a mechanism associated with the enhancement of cerebrovascular integrity.

2. Methods

2.1. Experimental Animals. Animal care protocol and experimental procedures were approved by the Institutional Animal Care and Use Committee of Hallym University (Protocol number Hallym 2013-126). All experiments were performed in accordance with relevant guidelines and regulations. Adult male Sprague-Dawley rats (250–350 g) were used in this study. Rats were housed in a regulated environment ($22 \pm 2^{\circ}$C, $55 \pm 5\%$ humidity, and 12 : 12-hour light : dark cycle with lights on at 8:00 am) and received a standard diet (Purina, Gyeonggi, Korea). Food and water were accessible ad libitum.

2.2. Intracerebral Hemorrhage (ICH) Model. To reproduce ICH with ongoing bleeding, we injected bacterial collagenase intrastriatally, as previously described [19]. Rats were deeply anesthetized with isoflurane (3% for induction, 1-2% for maintenance) in a 70 : 30 mixture of nitrous oxide and oxygen using an isoflurane vaporizer (VetEquip Inc., Livermore, CA) and were placed in a stereotaxic frame (Kopf Instruments, Tujunga, CA). A burr hole was made, and a 30-gauge needle was inserted through the burr hole into the striatum (coordinates: 0.2 mm posterior, 5.0 mm ventral, and 3.0 mm lateral to the bregma). We then injected collagenase type IV (0.1 U, 1 μL) for 5 min (Figure 1(a)). After placement for another 4 min, the needle was removed slowly. The burr hole was sealed with bone wax. Following suture of the skin incision, anesthetics were discontinued. When rats showed spontaneous respiration, they were returned to a recovery room maintained at 37°C. Core temperature was kept at 36.5–37.5°C with a homoeothermic blanket control (Harvard Apparatus, Holliston, MA). Sham-operated rats received the same neck skin incision under isoflurane anesthesia, but they were administered 1 μL sterile saline into the right striatum.

2.3. MSC Preparation and Experimental Procedures. Human placenta-derived mesenchymal stem cells (PD-MSCs) were isolated and characterized as previously described [20]. Placenta tissue was obtained with informed consent from healthy mother donors, under the approval of the institutional review board of CHA Bundang Medical Center. The chorioamniotic membrane was separated from the placenta, and the amnion and innermost membrane from the chorion and decidua were removed. The cells of the chorionic plate side were removed from the membrane, the remainder of which was dissected and minced. The minced tissue was enzymatically digested by a mixture of trypsin, DNase I, and collagenase IV at 37°C for 30 min under shaking conditions. The harvested cells were cultured in T25 flasks in MEM-α GlutaMAX supplemented with 10% fetal bovine serum, 25 ng/mL FGF4 (R&D System, Minneapolis, MN), and 1 μg/mL heparin at 37°C in an atmosphere of 5% CO_2 and 3% O_2. Fluorescence-activated cell sorting analysis was used to identify the phenotype of the cells. The expression of CD44, CD73, CD90, CD105, and human leukocyte antigen- (HLA-) ABC and the lack of CD45, CD34, CD31, and HLA-DR were assessed to confirm the MSC identity of the cells.

One hour after ICH induction, the animals were randomly assigned to two groups: the MSC-treated group, composed of those receiving a 500 μL suspension of PD-MSCs (1×10^6 cells) slowly for 5 min via the tail vein, and the vehicle-treated group, composed of those receiving the same volume of saline. The experimental procedures are summarized in Figure 1. Mortality rates at 24 hours after ICH induction were calculated, and surviving animals were sacrificed to acquire brain samples for analyses at the same time point. The same procedures were repeated to add more animals, as the sample size was insufficient for statistical analyses of histological evaluation in any of the groups because of mortalities.

2.4. Tissue Preparation. For the histological evaluation, rats were anesthetized by intraperitoneal injection of 1.5 g/kg urethane in sterile 0.9% NaCl at a volume of 0.01 mL/g body weight. A toe pinch was used to evaluate the effectiveness of anesthesia. Animals were transcardially perfused with 0.9% saline followed by 4% paraformaldehyde (PFA) in PBS. The brains were postfixed with 4% PFA in PBS for 1 hour and then immersed in 30% sucrose for cryoprotection. Thereafter, the entire brain was frozen and coronally sectioned with a cryostat microtome at 30 μm thickness.

For the analysis of Western blot and real-time polymerase chain reaction (PCR), rats were anesthetized and perfused with cold PBS. The brains were immediately harvested.

2.5. Measurement of the Hematoma Volume. For the measurement of hematoma volume at 24 hours after ICH, rats were divided into two groups. These groups were composed of a vehicle-treated ICH group ($n = 7$) and MSC-treated ICH group ($n = 8$). The hematoma volume was quantified using coronal sections at 28 rostral-caudal levels that were spaced every 270 μm from +2.04 mm to −5.52 mm relative to the bregma. The volume measurement was computed by summation of the areas multiplied by the interslice distance (270 μm). Digital photographs of the serial slices were taken, and the

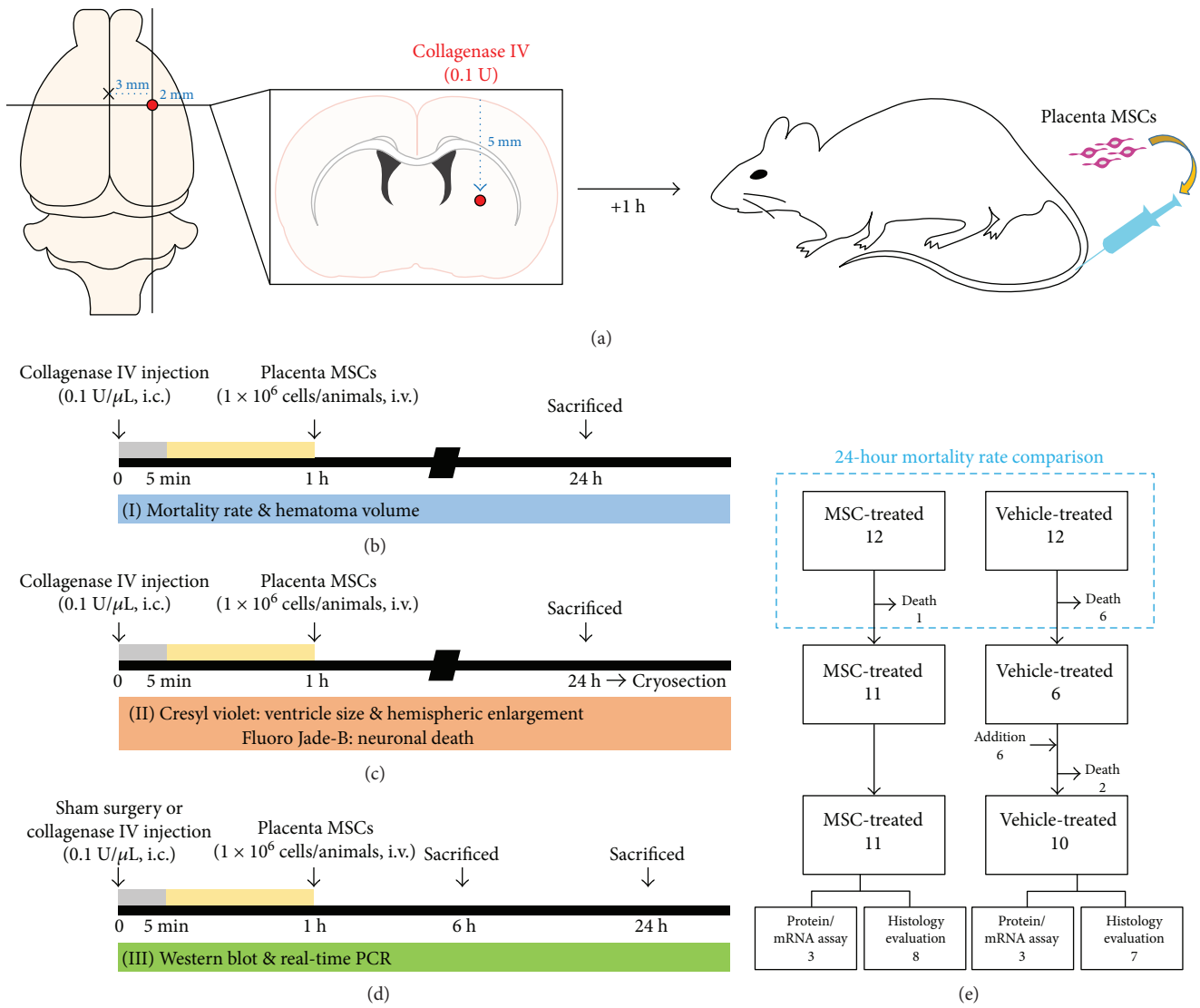

Figure 1: Conceptual illustrations of the experimental protocol. (a) Schematic diagrams of a rat intracranial hemorrhage (ICH) model with the administration of human placenta-derived mesenchymal stem cells (PD-MSCs). ICH was induced by the infusion of bacterial collagenase type IV (0.1 U, 1 μL) into the striatum. PD-MSCs (1×10^6 cells) were injected slowly via the tail vein at 1 hour after ICH. (b–d) Brief timeline of the experimental procedures which represent all the animal cohorts used and analyses performed: (b) mortality rate and hematoma volume; (c) ventricle size, hemispheric enlargement, and neuronal death; and (d) Western blot and real-time PCR. (e) Flow diagram which described how rats were used in a stepwise fashion.

percentage of hematoma volume [(hematoma volume/hemispheric brain volume) × 100] was measured using ImageJ (NIH, Bethesda, MA) [21]. This analysis was performed by an investigator blinded to the experimental cohort.

2.6. Ventricle Size and Hemispheric Enlargement Analysis. For the investigation of ventricle size and hemispheric enlargement at 24 hours after ICH, rats were divided into two groups. These groups were composed of a vehicle-treated ICH group ($n = 7$) and MSC-treated ICH group ($n = 8$). Brains were cut coronally with a cryostat microtome at 30 μm thickness. Sections were stained with cresyl violet and visualized under a light microscope (Olympus upright microscope IX70, Olympus, Tokyo, Japan). The whole brain area and the area of the ventricle were measured using ImageJ, with the area of the ventricle expressed as a percentage of the total brain area [22–24]. As a previously described method [25], brain edema was measured using ImageJ software as the percentage of hemispheric enlargement, which was calculated by the following formula: [(ipsilateral hemisphere volume − contralateral hemisphere volume)/contralateral hemisphere volume] × 100 [25–27]. These analyses were performed by an observer blinded to the experimental cohort.

2.7. Detection of Neuronal Death. Neuronal death was evaluated by Fluoro-Jade B (FJB, Histo-Chem, Jefferson, AR) staining 24 hours after ICH [28]. The sections were rinsed in PBS and mounted onto gelatin-coated slides and then dried on a slide warmer. The slides were immersed in 100% ethanol for 3 min, followed by 70% ethanol for 1 min and distilled water

(DW) for 1 min. The slides were then transferred to 0.06% potassium permanganate for 15 min and gently agitated. After rinsing in DW for 1 min, the slides were incubated for 30 min in 0.001% FJB, freshly prepared by adding 20 mL of a 0.01% FJB solution to 180 mL of 0.1% acetic acid, with gentle shaking in the dark. After rinsing for 1 min in each of three changes of DW, the slides were dried, dehydrated in xylene, and coverslipped with DPX (Sigma-Aldrich Co., St. Louis, MO). To quantify neuronal death in the perihematomal region after ICH, rats were divided into two groups. These groups were composed of a vehicle-treated ICH group ($n = 7$) and MSC-treated ICH group ($n = 8$). Sections were collected at +1.2 mm to −1.2 mm from the bregma according to the coordinates of Slotnick and Leonard [29], and seven coronal sections were analyzed from each animal using a microscope with a 20x objective. An observer masked to the treatment condition counted the number of FJB-positive (+) neurons by sampling an area of $4.72 \times 4.72\,\text{mm}^2$ immediately adjacent to the hematoma in 3 regions of interest (ROIs) from the ipsilateral hemisphere after ICH. The number of FJB-positive cells from 21 randomly selected locations per mouse (3 fields per section × 7 sections per mouse) in the perihematomal region was averaged and expressed as FJB-positive cells per square millimeter.

2.8. Western Blot. Rats were perfused with cold PBS at 6 or 24 hours after ICH or sham operation for the analysis of the expression of tight junction proteins using Western blot. A 2 mm coronal section (+0.8 mm to −1.2 mm relative to the bregma) from the ipsilateral hemisphere was homogenized in ice-cold RIPA buffer (Thermo Fisher Scientific, Waltham, MA). Total protein concentration was measured by the BCA Protein Assay Kit (Thermo Fisher Scientific, Waltham, MA). Then, 40 μg of protein from each sample was subjected to SDS-PAGE and transferred to a PVDF membrane (GE Healthcare Bio-Sciences, Pittsburgh, PA). Membranes were probed with the following primary antibodies: rabbit anti-occludin (Thermo Fisher Scientific, Waltham, MA), rabbit anti-zonula occludens-1 (ZO-1) (Abcam, Cambridge, MA), and mouse anti-β-actin (Santa Cruz Biotechnology Inc., Dallas, TX). β-Actin was used as an internal loading control. The secondary antibodies were all from GeneTex. Western blot was performed with an ECL Detection Kit (Bio-Rad, Hercules, CA). The relative band density of each sample was analyzed using ImageJ. These analyses were performed by an observer blinded to the experimental cohort.

2.9. Real-Time PCR. For the analysis of the expression of coagulation factor VII (F7) mRNA at 6 or 24 hours after ICH or sham operation, we performed real-time polymerase chain reaction (PCR). Total RNA was isolated from ipsilateral regional brain tissue using NucleoZOL (Macherey-Nagel, Düren, Germany) following the manufacturer's instruction. cDNA was synthesized using the PrimeScript™ 1st-strand cDNA Synthesis Kit (Takara Bio, Shiga, Japan). mRNA was quantified using iQ™ SYBR® Green Supermix (Bio-Rad) with the CFX Connect™ Real-Time PCR Detection System (Bio-Rad). Thermal cycling parameters were determined from the manufacturer's instruction (2 min at 95°C and 40 cycles of 95°C for 10 s, 60°C for 10 s, and 72°C for 30 s). The following primers were used: rat F7-specific primers (forward, GCT TCT GCC CCC TAG ACT TT; reverse, CCG CAT GGG TAC TCA ACT TT) and rat GAPDH-specific primers (forward, ACC ACA GTC CAT GCC ATC AC; reverse, TCC ACC ACC CTG TTG CTG TA). The relative band density of each sample was analyzed using ImageJ. These analyses were performed by an observer blinded to the experimental cohort.

2.10. Statistical Analysis. Comparisons between the MSC-treated and vehicle-treated groups were conducted using the t-test, except for the comparison of mortalities, which used Fisher's exact test. Data are presented as the mean ± standard error of the mean (SEM), and differences were considered significant at $p < 0.05$. IBM SPSS statistics 24.0 (IBM, Armonk, NY) was used for statistical calculation. A sample size of 20 was calculated to detect a significant difference in the proportion of deaths at 24 hours after ICH induction between the MSC-treated and vehicle-treated groups (power = 0.8), using G ∗ Power 3.1 (Heinrich-Heine Universität, Düsseldorf, Germany) [30].

3. Results

First, 24 rats were assigned to two groups (12 each). Six rats in the vehicle-treated group died before 24 hours had passed, while one rat in the MSC-treated group died before 24 hours. Six more rats were enrolled and assigned to the vehicle-treated group, and among them, two rats died within 24 hours. Finally, seven rats in the vehicle-treated group and eight rats in the MSC-treated group were included in the histologic analyses, and three rats in each group were enrolled for Western blot and real-time PCR (Figure 1(e)).

3.1. PD-MSCs Decreased Mortality Rate and Hematoma Volume in an Acute Stage of ICH. Administration of PD-MSCs significantly reduced the mortality rate from 50% (6 of 12 rats) in the vehicle-treated group to 8.3% (1 of 12 rats) in the MSC-treated group ($p = 0.034$, Figure 2(a)). The most important predictor of early death is the size of the hematoma after brain injury, followed by ICH. To assess whether the reduction in mortality rate in the MSC-treated group correlated with reduced hematoma size, we examined the hematoma size at 24 hours following ICH. Hematoma size was significantly smaller in the MSC-treated group (13.98 ± 2.59%) than in the vehicle-treated group (23.73 ± 2.81%, $p = 0.038$; Figures 2(b) and 2(c)). These results suggest that administration of PD-MSCs decreases the mortality rate and the hematoma size in the acute stage of ICH.

3.2. PD-MSCs Reduced Ventricular Enlargement and Brain Edema after ICH. To determine whether administration of PD-MSCs decreased ventricular enlargement and brain edema after ICH, we measured changes in the lateral ventricle and hemispheric enlargement, respectively. The ventricular size and hemispheric volume were unchanged at the designated time point in animals that underwent sham surgery (data not shown). At 24 hours after ICH, the vehicle-treated rats exhibited larger ventricle size than the sham-

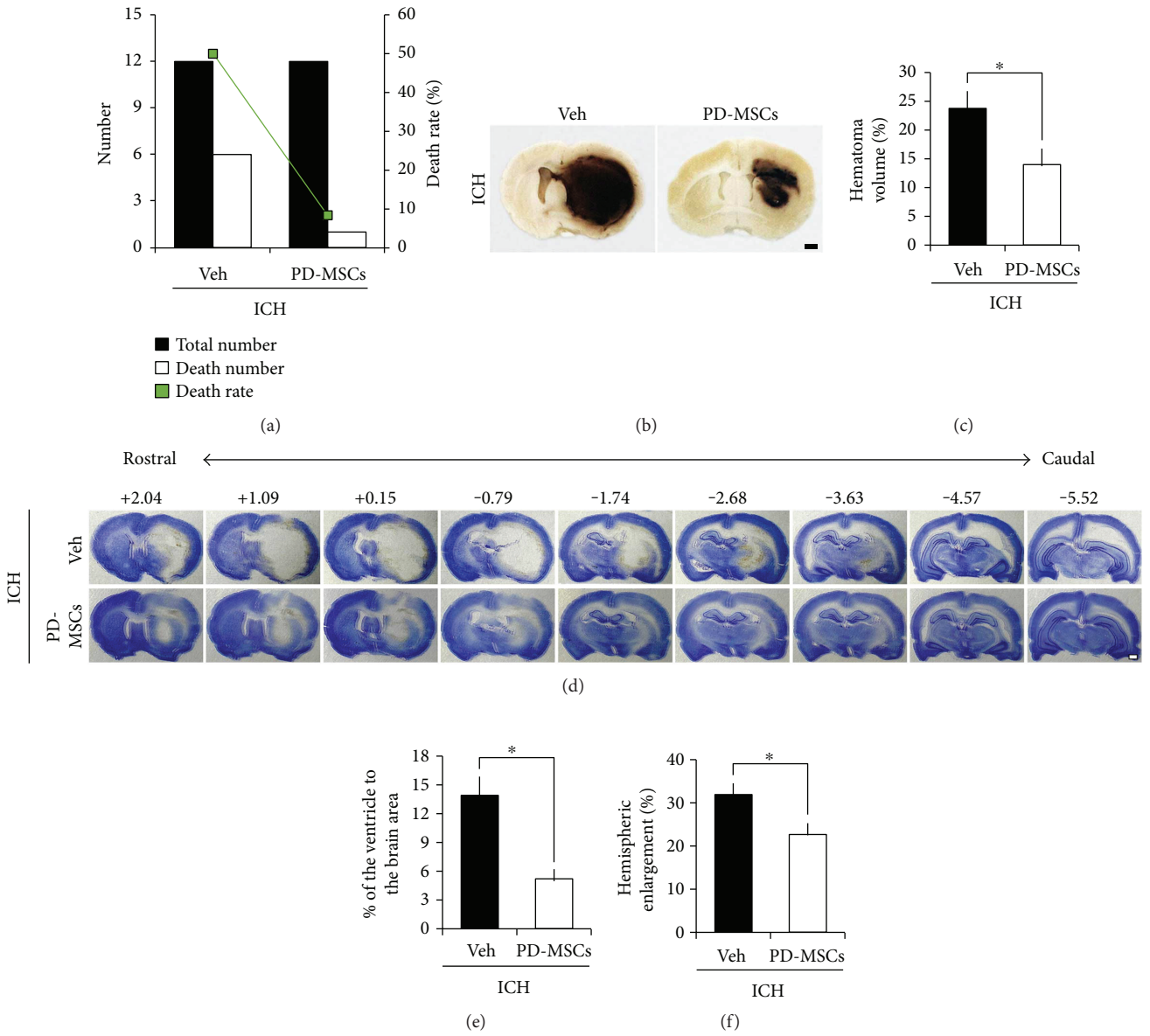

Figure 2: Effect of human placenta-derived mesenchymal stem cell (PD-MSC) administration on mortality, hematoma volume, ventricular enlargement, and brain edema of the rats at 24 hours after the induction of intracranial hemorrhage (ICH). (a) Mortalities in each group at 24 hours after ICH ($n = 12$ from each group). (b) Digital photographs showing location of a core hemorrhagic region at 0.2 mm from the bregma. Scale bar = 1 mm. (c) The bar graphs represent the hematoma volume of the vehicle-treated and the PD-MSC-treated groups at 24 hours after ICH induction. The volume of hematoma is expressed as the proportion in the total brain area (%). Data are mean + SEM; $n = 7$-8 from each group (ICH-Veh, $n = 7$; ICH-MSC, $n = 8$), $^*p < 0.05$. (d) Representative images of cresyl violet staining depicting a coronal whole-brain section at rostral-caudal levels from +2.04 to −5.52 from the bregma. Scale bar = 1 mm. (e) The bar graphs represent the ventricular size of the vehicle-treated and the PD-MSC-treated groups at 24 hours after ICH induction. The size of the lateral ventricle is expressed as the proportion in the total brain area (%). Data are mean + SEM; $n = 7$-8 from each group (ICH-Veh, $n = 7$; ICH-MSC, $n = 8$), $^*p < 0.05$. (f) The bar graphs represent the degree of the hemispheric enlargement of the vehicle-treated and the PD-MSC-treated groups at 24 hours after ICH induction. The hemispheric enlargement is expressed as the percentage of increase in hemispheric size compared with that of the contralateral hemisphere. Data are mean + SEM; $n = 7$-8 from each group (ICH-Veh, $n = 7$; ICH-MSC, $n = 8$), $^*p < 0.05$.

operated group, and the ventricle size was reduced in the MSC-treated group compared to the vehicle-treated group ($13.89 \pm 1.87\%$ versus $5.2 \pm 0.91\%$, $p = 0.001$; Figures 2(d) and 2(e)). In addition, hemispheric enlargement was significantly smaller in the MSC-treated group ($22.64 \pm 2.55\%$) than in the vehicle-treated group ($31.90 \pm 2.44\%$, $p = 0.022$; Figures 2(d) and 2(f)). These results indicate that PD-MSC treatment attenuates ICH-induced brain edema formation and hydrocephalus.

3.3. PD-MSCs Reduced Neuronal Death after ICH. To determine the neuroprotective effect of PD-MSCs on collagenase-

induced ICH, we performed FJB staining to detect degenerating neurons. The MSC-treated group had significantly fewer FJB-positive cells in the perihematomal region 24 hours after ICH than the vehicle-treated group (433.22 ± 34.17 versus 120.36 ± 15.22 cells/field, $p < 0.001$; Figures 3(a)–3(c)). Moreover, contrary to the vehicle-treated group, no FJB-positive cells were observed in the ipsilateral hippocampus of the MSC-treated group at 24 hours after ICH (Figures 3(d) and 3(e)). FJB-positive cells were not observed in the contralateral hemisphere. These data suggest that administration of PD-MSCs effectively reduces neuronal death after collagenase-induced ICH injury.

3.4. PD-MSCs Increased the Expression of the Tight Junction Proteins after ICH. We investigated the expression of tight junction proteins at 6 and 24 hours after ICH to assess changes in microvascular integrity using Western blot. The level of expression of ZO-1 and occludin was significantly higher in the MSC-treated group than in the vehicle-treated group at 24 hours after ICH induction ($p = 0.007$ and 0.012), but not at 6 hours after ICH induction ($p = 0.744$ and 0.558, Figures 4(a)–4(c)). These results suggest that PD-MSCs block the leakage of blood components from ruptured vessels to brain parenchyma after ICH, indicating an enhancement of tight junction barrier function.

3.5. PD-MSCs Did Not Affect the Level of F7 mRNA Expression. We investigated the expression of F7 mRNA at 6 and 24 hours after ICH or sham operation. The level of F7 mRNA expression was significantly higher in the vehicle-treated group than in the MSC-treated group at 24 hours after ICH induction ($p = 0.003$) but not at 6 hours after ICH induction ($p = 0.861$, Figure 4(d)). However, there was no significant difference in the level of F7 mRNA expression between the vehicle-treated and MSC-treated groups at 24 hours after sham operation ($p = 0.963$, Figure 4(d)).

4. Discussion

In this study, we found that PD-MSC administration decreased the mortality of ICH in the acute stage by suppressing hematoma expansion and by various neuroprotective effects, including the amelioration of hydrocephalus, perihematomal neuronal death, and brain edema. The present study also showed that administration of PD-MSCs increased the expression of tight junction proteins associated with the enhancement of cerebrovascular integrity. These results suggest that PD-MSCs may have a high therapeutic potential for treating acute-phase ICH.

Here, we showed that the systemic administration of PD-MSCs decreased mortality, hematoma size, and brain edema/hydrocephalus at 24 hours after ICH induction. This suggests that stem cell therapy may be useful not only as a treatment option for functional recovery after ICH because of its mid-to-long-term neuroprotective, neurotrophic, and regenerative effects but also as a treatment option for decreasing acute-stage mortality and severe complications of ICH. Recently, many trials have examined the use of MSCs in the field of acute/intensive care medicine because of their effects of reducing inflammation and preventing systemic ischemia/reperfusion injury [31]. Therefore, the results of our study also suggest that administration of MSCs may be used as a complementary therapeutic option to the conventional therapy for acute-stage ICH including surgical intervention, which may significantly improve prognosis.

The hematoma area reduction effect of stem cell therapy for ICH is well known from the results of various preclinical studies [32–36]. Most of these studies focused on the mid-to-long-term replacement of lost brain tissue through the neurotrophic and neuronal regeneration effects of administered stem cells. In contrast, our study showed that the administration of PD-MSCs had a strong effect of hematoma size reduction even in the acute stage of ICH. This suggests that administered stem cells may also directly affect suppression of hematoma expansion, considering that there was not enough time for regeneration and replacement of lost tissue. The results of the Western blot, which showed significantly higher expression of tight junction proteins in the MSC-treated group at 24 hours after ICH induction, suggest that suppression of acute hematoma expansion may be due to PD-MSC-mediated enhancement of the endovascular integrity of brain microvasculature in a relatively short time. This finding is consistent with that of previous research, which shows that MSC administration decreases blood-brain barrier permeability and endothelial damage and increases the expression of tight junction proteins after ICH [17, 18, 37]. In most cases of ICH, hematoma expansion occurs within 24 hours after the onset regardless of its extent, implying that there may be an active bleeding process in the hyperacute phase of ICH [1, 38]. Thus, our results showing a significant decrease in hematoma size and increase in vascular integrity at the time point of 24 hours after ICH induction suggest that MSC administration in the early stage of ICH may effectively attenuate this active bleeding process.

Because hydrocephalus and cerebral edema, which reflect and also cause an increase in intracranial pressure (ICP), are the major complications of ICH, most therapeutic strategies for the acute stage of ICH focus on preventing and treating these complications [2, 6]. We showed a significant decrease in ventricular size and hemispheric enlargement in the MSC-treated group compared with the vehicle-treated group, suggesting that the amelioration of these serious complications of ICH may be an important mechanism underlying the effects of PD-MSCs on acute mortality from ICH. In addition, the significant decrease in neuronal death in the MSC-treated group, observed by FJB immunostaining, suggests that direct neuroprotective effects of PD-MSCs may also contribute to improved prognosis. In particular, the absence of degenerating neurons in the hippocampus of the MSC-treated group, compared to the presence of degenerating neurons in the vehicle-treated group, implies that MSCs may also ameliorate global ischemic injury caused by increased ICP. However, further study may be necessary to elucidate whether this result is a mere consequence of the decrease in hematoma expansion and ICP or due to the direct neuroprotective effects of MSCs.

A few recent studies reported that MSCs have procoagulant features [39, 40]. Notably, one study showed that MSCs

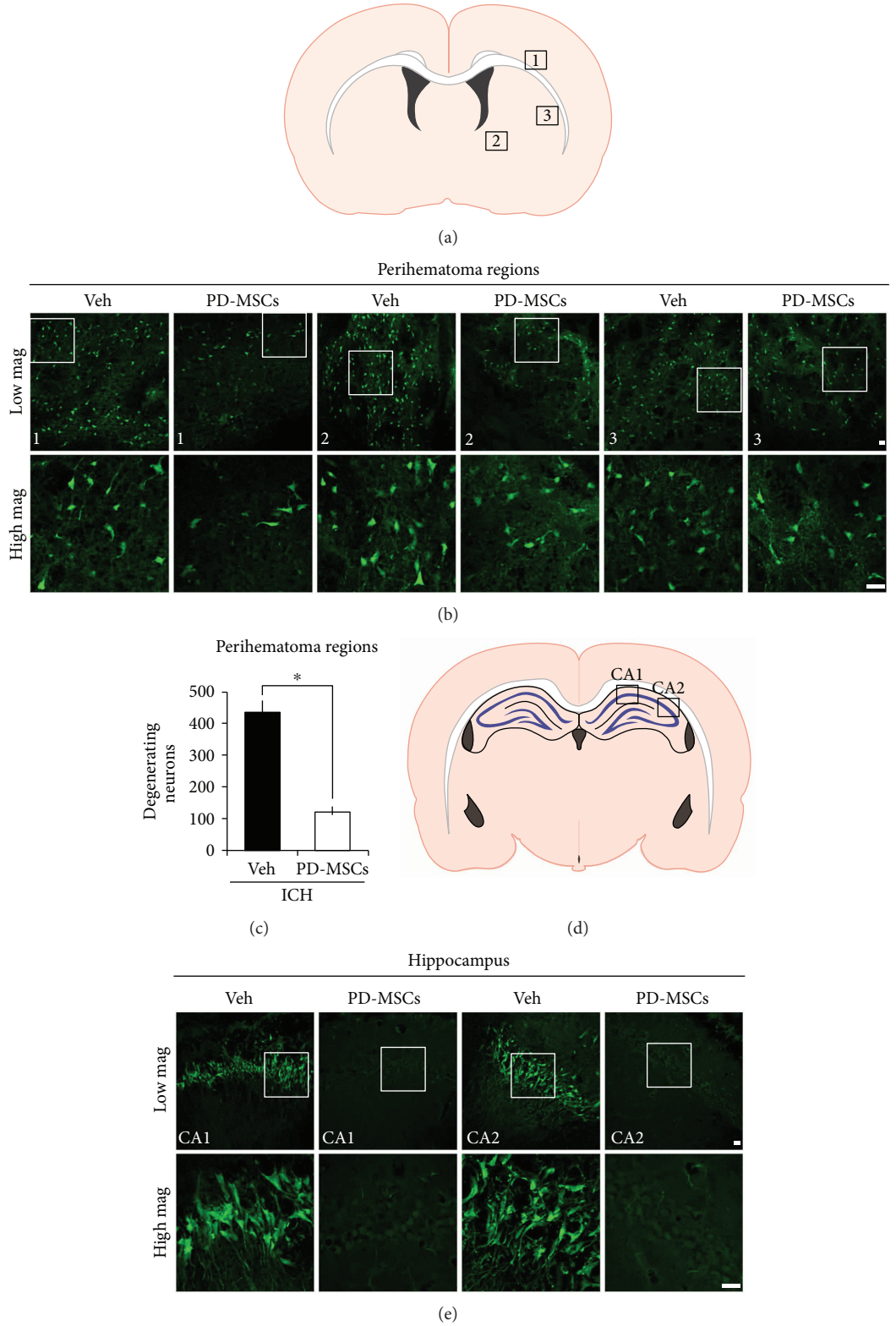

Figure 3: Human placenta-derived mesenchymal stem cells (PD-MSCs) reduced neuronal death in the brains of rats subjected to intracranial hemorrhage (ICH). (a) The location of core hemorrhagic regions at 0.2 mm from the bregma. (b) Fluorescence images reveal the degenerating neurons in the perihematomal region at 24 hours after ICH. Degenerating neurons are detected by Fluoro-Jade B (FJB) staining (green). Scale bar = 20 μm. (c) The bar graphs represent the count of FJB-positive neurons in the perihematomal region from the vehicle-treated and the PD-MSC-treated groups at 24 hours after ICH induction. Data are mean + SEM; $n = 7 - 8$ from each group (ICH-Veh, $n = 7$; ICH-MSC, $n = 8$), $^*p < 0.05$. (d) The location of hippocampal regions at −3.6 mm from the bregma. (e) Fluorescence images reveal the degenerating neurons only in the hippocampal CA1 and CA2 region of the vehicle-treated group at 24 hours after ICH. Scale bar = 20 μm.

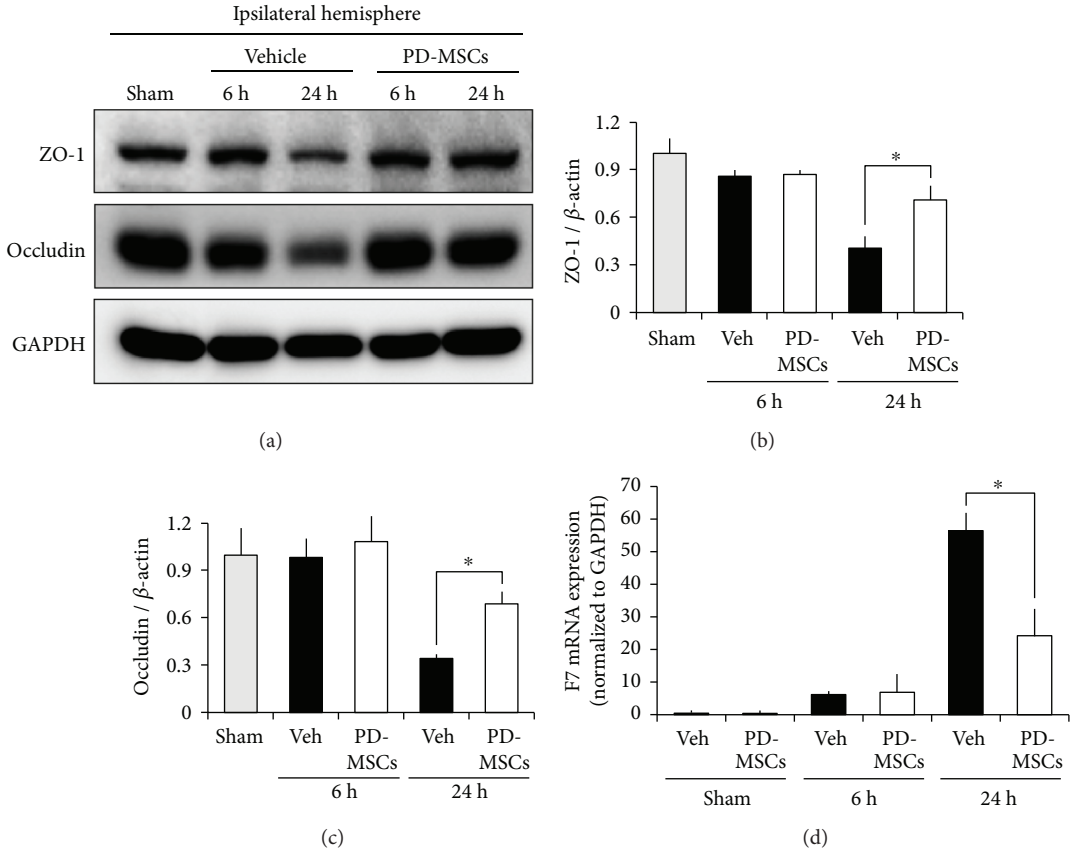

Figure 4: Human placenta-derived mesenchymal stem cells (PD-MSCs) enhanced the expression of tight junction proteins at 24 hours after ICH induction but did not affect the expression of coagulation factor VII mRNA. (a) Results of Western blot of ZO-1 and occludin at 6 and 24 hours after ICH induction. Bar graphs indicate the level of ZO-1 (b) and occludin (c) expression measured by the densitometric analysis of the bands. β-Actin was used as a loading control. Data are mean + SEM; $n = 3$ from each group, $^*p < 0.05$. (d) Real-time PCR analysis of coagulation factor VII (F7) at 6 and 24 hours after ICH induction, and that at 24 hours after sham operation. The level of F7 mRNA was normalized to that of GAPDH mRNA. Data are mean + SEM; $n = 3$ from each group, $^*p < 0.05$.

contribute to the production of endogenous coagulation factor VIII [41]. Thus, we aimed to determine whether MSCs would increase the production of F7, which has been used as an acute hemostatic therapy for ICH. However, we found no significant difference in the expression of F7 mRNA between the MSC-treated and the vehicle-treated sham-operated animals, indicating that PD-MSCs do not cause an increase in endogenous F7 in the ICH model. Rather, we showed a significantly higher level of F7 mRNA expression in the vehicle-treated group than in the MSC-treated group at 24 hours after ICH induction. This increase in mRNA expression may be a response to the increased consumption of coagulation factor due to ongoing bleeding, which was more pronounced in the vehicle-treated group. Additional studies are needed to determine whether the effect of MSCs on acute hematoma expansion is related to their procoagulant properties or to other factors in the coagulation system.

Our study has a few limitations. First, we used a collagenase injection model to reproduce ICH with acute hematoma expansion, producing a pathophysiology quite different from the real disease, which is usually caused by mechanical tension due to hypertension or aneurysm. However, the pronounced effects shown in this model, which involve a strong trend of ongoing bleeding and hematoma expansion due to the continuous action of injected collagenase, suggest that MSCs may demonstrate therapeutic efficacy in a real clinical setting. Moreover, this model is known to generate consistent and predictable ICH and provides the best imitation of the bleeding-rebleeding phenomenon of the real human condition [42]. Second, we did not assess the multiorgan effect of systemically administered MSCs. Considering the systemic effects of MSCs on inflammation and ischemia/reperfusion injury, the effects on other vital organs might also contribute to the decreased acute mortality in our results. Third, our quantification methods for measuring hemispheric and ventricular enlargement cannot exclusively reflect overall brain edema. Hence, the effect of MSCs on ICH-induced brain edema formation and hydrocephalus might be a consequence of smaller hemorrhage volume. Further study may be necessary to examine this possibility in depth.

5. Conclusions

The administration of MSCs may prevent hematoma expansion in the hyperacute stage of ICH and decrease acute mortality by enhancing the endothelial integrity of cerebral

vasculature, in addition to exerting their neuroprotective and neurotrophic effects as shown in previous studies.

Disclosure

Bo Young Choi and Ok Joon Kim equally contributed as the first authors.

Conflicts of Interest

The authors declare no competing financial interests.

Authors' Contributions

Tae Nyoung Chung and Sang Won Suh designed the study and wrote the manuscript. Bo Young Choi and Ok Joon Kim helped to design the study and wrote the manuscript. Bo Young Choi, Sae-Hong Min, and Jeong Hyun Jeong conducted the experimental procedures. Sae-Hong Min and Jeong Hyun Jeong helped to write the document. Bo Young Choi and Tae Nyoung Chung prepared Figure 1 and 2, and Sae-Hong Min and Tae Nyoung Chung prepared Figure 3. All authors read and approved the finally drafted manuscript.

Acknowledgments

This research was supported by a grant from the Korea Health Technology R&D Project through the Korea Health Industry Development Institute (KHIDI), funded by the Ministry of Health and Welfare (Grant no. HI16C1559) to Ok Joon Kim. This work was also supported by the Basic Science Research Program through the National Research Foundation of Korea (NRF) funded by the Ministry of Education (2016R1D1A1B03934928) to Tae Nyoung Chung.

References

[1] S. M. Davis, J. Broderick, M. Hennerici et al., "Hematoma growth is a determinant of mortality and poor outcome after intracerebral hemorrhage," *Neurology*, vol. 66, no. 8, pp. 1175–1181, 2006.

[2] A. I. Qureshi, A. D. Mendelow, and D. F. Hanley, "Intracerebral haemorrhage," *The Lancet*, vol. 373, no. 9675, pp. 1632–1644, 2009.

[3] J. Broderick, S. Connolly, E. Feldmann et al., "Guidelines for the management of spontaneous intracerebral hemorrhage in adults: 2007 update: a guideline from the American Heart Association/American Stroke Association Stroke Council, High Blood Pressure Research Council, and the Quality of Care and Outcomes in Research Interdisciplinary Working Group," *Circulation*, vol. 116, no. 16, pp. e391–e413, 2007.

[4] Y. Hua, R. F. Keep, J. T. Hoff, and G. Xi, "Brain injury after intracerebral hemorrhage: the role of thrombin and iron," *Stroke*, vol. 38, no. 2, pp. 759–762, 2007.

[5] E. Zia, G. Engström, P. J. Svensson, B. Norrving, and H. Pessah-Rasmussen, "Three-year survival and stroke recurrence rates in patients with primary intracerebral hemorrhage," *Stroke*, vol. 40, no. 11, pp. 3567–3573, 2009.

[6] J. S. Balami and A. M. Buchan, "Complications of intracerebral haemorrhage," *The Lancet Neurology*, vol. 11, no. 1, pp. 101–118, 2012.

[7] J. C. Hemphill 3rd, S. M. Greenberg, C. S. Anderson et al., "Guidelines for the management of spontaneous intracerebral hemorrhage: a guideline for healthcare professionals from the American Heart Association/American Stroke Association," *Stroke*, vol. 46, no. 7, pp. 2032–2060, 2015.

[8] M. F. Cordeiro and A. P. Horn, "Stem cell therapy in intracerebral hemorrhage rat model," *World Journal of Stem Cells*, vol. 7, no. 3, pp. 618–629, 2015.

[9] Y. Hu, N. Liu, P. Zhang et al., "Preclinical studies of stem cell transplantation in intracerebral hemorrhage: a systemic review and meta-analysis," *Molecular Neurobiology*, vol. 53, no. 8, pp. 5269–5277, 2016.

[10] C. Delcourt, Y. Huang, H. Arima et al., "Hematoma growth and outcomes in intracerebral hemorrhage: the INTERACT1 study," *Neurology*, vol. 79, no. 4, pp. 314–319, 2012.

[11] Y. Fujii, S. Takeuchi, O. Sasaki, T. Minakawa, and R. Tanaka, "Multivariate analysis of predictors of hematoma enlargement in spontaneous intracerebral hemorrhage," *Stroke*, vol. 29, no. 6, pp. 1160–1166, 1998.

[12] N. Poungvarin, W. Bhoopat, A. Viriyavejakul et al., "Effects of dexamethasone in primary supratentorial intracerebral hemorrhage," *New England Journal of Medicine*, vol. 316, no. 20, pp. 1229–1233, 1987.

[13] S. Santambrogio, R. Martinotti, F. Sardella, F. Porro, and A. Randazzo, "Is there a real treatment for stroke? Clinical and statistical comparison of different treatments in 300 patients," *Stroke*, vol. 9, no. 2, pp. 130–132, 1978.

[14] Y. L. Yu, C. R. Kumana, I. J. Lauder et al., "Treatment of acute cerebral hemorrhage with intravenous glycerol. A double-blind, placebo-controlled, randomized trial," *Stroke*, vol. 23, no. 7, pp. 967–971, 1992.

[15] S. A. Mayer, N. C. Brun, K. Begtrup et al., "Efficacy and safety of recombinant activated factor VII for acute intracerebral hemorrhage," *New England Journal of Medicine*, vol. 358, no. 20, pp. 2127–2137, 2008.

[16] S. A. Mayer, N. C. Brun, K. Begtrup et al., "Recombinant activated factor VII for acute intracerebral hemorrhage," *New England Journal of Medicine*, vol. 352, no. 8, pp. 777–785, 2005.

[17] T. N. Chung, J. H. Kim, B. Y. Choi, S. P. Chung, S. W. Kwon, and S. W. Suh, "Adipose-derived mesenchymal stem cells reduce neuronal death after transient global cerebral ischemia through prevention of blood-brain barrier disruption and endothelial damage," *Stem Cells Translational Medicine*, vol. 4, no. 2, pp. 178–185, 2015.

[18] T. N. Chung, J. H. Kim, B. Y. Choi et al., "Effect of adipose-derived mesenchymal stem cell administration and mild hypothermia induction on delayed neuronal death after transient global cerebral ischemia," *Critical Care Medicine*, vol. 45, no. 5, pp. e508–e515, 2017.

[19] M. R. D. Bigio, H.-J. Yan, R. Buist, J. Peeling, and G. J. del Zoppo, "Experimental intracerebral hemorrhage in rats. Magnetic resonance imaging and histopathological correlates," *Stroke*, vol. 27, no. 12, pp. 2312–2320, 1996.

[20] M. J. Jang, H. S. Kim, H. G. Lee et al., "Placenta-derived mesenchymal stem cells have an immunomodulatory effect that can control acute graft-versus-host disease in mice," *Acta Haematologica*, vol. 129, no. 4, pp. 197–206, 2013.

[21] C. A. Schneider, W. S. Rasband, and K. W. Eliceiri, "NIH image to ImageJ: 25 years of image analysis," *Nature Methods*, vol. 9, no. 7, pp. 671–675, 2012.

[22] M. Okauchi, Y. Hua, R. F. Keep, L. B. Morgenstern, and G. Xi, "Effects of deferoxamine on intracerebral hemorrhage-induced brain injury in aged rats," *Stroke*, vol. 40, no. 5, pp. 1858–1863, 2009.

[23] E. B. Yan, S. C. Hellewell, B. M. Bellander, D. A. Agyapomaa, and M. C. Morganti-Kossmann, "Post-traumatic hypoxia exacerbates neurological deficit, neuroinflammation and cerebral metabolism in rats with diffuse traumatic brain injury," *Journal of Neuroinflammation*, vol. 8, no. 1, p. 147, 2011.

[24] W. Zhu, Y. Gao, C. F. Chang, J. R. Wan, S. S. Zhu, and J. Wang, "Mouse models of intracerebral hemorrhage in ventricle, cortex, and hippocampus by injections of autologous blood or collagenase," *PLoS One*, vol. 9, no. 5, article e97423, 2014.

[25] J. Wang and S. Dore, "Heme oxygenase 2 deficiency increases brain swelling and inflammation after intracerebral hemorrhage," *Neuroscience*, vol. 155, no. 4, pp. 1133–1141, 2008.

[26] T. Kondo, A. G. Reaume, T. T. Huang et al., "Reduction of CuZn-superoxide dismutase activity exacerbates neuronal cell injury and edema formation after transient focal cerebral ischemia," *The Journal of Neuroscience*, vol. 17, no. 11, pp. 4180–4189, 1997.

[27] G. T. Manley, M. Fujimura, T. Ma et al., "Aquaporin-4 deletion in mice reduces brain edema after acute water intoxication and ischemic stroke," *Nature Medicine*, vol. 6, no. 2, pp. 159–163, 2000.

[28] L. C. Schmued and K. J. Hopkins, "Fluoro-Jade B: a high affinity fluorescent marker for the localization of neuronal degeneration," *Brain Research*, vol. 874, no. 2, pp. 123–130, 2000.

[29] B. M. Slotnick and C. M. Leonard, *A Stereotaxic Atlas of the Albino Mouse Forebrain*, U.S. Dept. of Health, Education, and Welfare, Public Health Service, Alcohol, Drug Abuse, and Mental Health Administration, Rockville, MD, USA, 1975.

[30] F. Faul, E. Erdfelder, A. G. Lang, and A. Buchner, "G*Power 3: a flexible statistical power analysis program for the social, behavioral, and biomedical sciences," *Behavior Research Methods*, vol. 39, no. 2, pp. 175–191, 2007.

[31] A. Monsel, Y. G. Zhu, S. Gennai, Q. Hao, J. Liu, and J. W. Lee, "Cell-based therapy for acute organ injury: preclinical evidence and ongoing clinical trials using mesenchymal stem cells," *Anesthesiology*, vol. 121, no. 5, pp. 1099–1121, 2014.

[32] W. Liao, J. Zhong, J. Yu et al., "Therapeutic benefit of human umbilical cord derived mesenchymal stromal cells in intracerebral hemorrhage rat: implications of anti-inflammation and angiogenesis," *Cellular Physiology and Biochemistry*, vol. 24, no. 3-4, pp. 307–316, 2009.

[33] L. Otero, M. Zurita, C. Bonilla et al., "Late transplantation of allogeneic bone marrow stromal cells improves neurologic deficits subsequent to intracerebral hemorrhage," *Cytotherapy*, vol. 13, no. 5, pp. 562–571, 2011.

[34] S.-P. Wang, Z.-H. Wang, D.-Y. Peng, S.-M. Li, H. Wang, and X.-H. Wang, "Therapeutic effect of mesenchymal stem cells in rats with intracerebral hemorrhage: reduced apoptosis and enhanced neuroprotection," *Molecular Medicine Reports*, vol. 6, no. 4, pp. 848–854, 2012.

[35] C. Yang, L. Zhou, X. Gao et al., "Neuroprotective effects of bone marrow stem cells overexpressing glial cell line-derived neurotrophic factor on rats with intracerebral hemorrhage and neurons exposed to hypoxia/reoxygenation," *Neurosurgery*, vol. 68, no. 3, pp. 691–704, 2011.

[36] M. Seghatoleslam, M. Jalali, M. R. Nikravesh, D. Hamidi Alamdari, M. Hosseini, and A. Fazel, "Intravenous administration of human umbilical cord blood-mononuclear cells dose-dependently relieve neurologic deficits in rat intracerebral hemorrhage model," *Annals of Anatomy - Anatomischer Anzeiger*, vol. 195, no. 1, pp. 39–49, 2013.

[37] M. Chen, X. Li, X. Zhang et al., "The inhibitory effect of mesenchymal stem cell on blood-brain barrier disruption following intracerebral hemorrhage in rats: contribution of TSG-6," *Journal of Neuroinflammation*, vol. 12, no. 1, p. 61, 2015.

[38] S. A. Mayer, "Ultra-early hemostatic therapy for intracerebral hemorrhage," *Stroke*, vol. 34, no. 1, pp. 224–229, 2003.

[39] B. A. Christy, M. C. Herzig, R. K. Montgomery et al., "Procoagulant activity of human mesenchymal stem cells," *Journal of Trauma and Acute Care Surgery*, vol. 83, 1 Supplement 1, pp. S164–S169, 2017.

[40] B. M. Gleeson, K. Martin, M. T. Ali et al., "Bone marrow-derived mesenchymal stem cells have innate procoagulant activity and cause microvascular obstruction following intracoronary delivery: amelioration by antithrombin therapy," *Stem Cells*, vol. 33, no. 9, pp. 2726–2737, 2015.

[41] C. Sanada, C. J. Kuo, E. J. Colletti et al., "Mesenchymal stem cells contribute to endogenous FVIII:c production," *Journal of Cellular Physiology*, vol. 228, no. 5, pp. 1010–1016, 2013.

[42] M. L. James, D. S. Warner, and D. T. Laskowitz, "Preclinical models of intracerebral hemorrhage: a translational perspective," *Neurocritical Care*, vol. 9, no. 1, pp. 139–152, 2008.

Hindawi
Stem Cells International
Volume 2018, Article ID 9594235, 10 pages
https://doi.org/10.1155/2018/9594235

Review Article

Adjunctive Platelet-Rich Plasma (PRP) in Infrabony Regenerative Treatment: A Systematic Review and RCT's Meta-Analysis

Mubashir Saleem,[1] Flavio Pisani,[1] Faisal Maqbool Zahid,[2] Ioannis Georgakopoulos,[3] Teuta Pustina-Krasniqi,[4] Edit Xhajanka,[5] and Maher Almasri[1]

[1]*Faculty of Dentistry, School of Health, MClinDent in Periodontology, BPP University Birmingham, Birmingham, UK*
[2]*Department of Statistics, Ludwig-Maximilians-University Munich, Munich, Germany*
[3]*World Academy of Growth Factors and Stem Cells in Dentistry, Athens, Greece*
[4]*Universiteti I Prishtines "Hasan Prishtina", Prishtine, Kosovo*
[5]*Universiteti I Mjekesise Dentare, Tirane, Albania*

Correspondence should be addressed to Flavio Pisani; flaviopisani@bpp.com

Received 25 November 2017; Accepted 11 January 2018; Published 19 March 2018

Academic Editor: Marc L. Turner

Copyright © 2018 Mubashir Saleem et al. This is an open access article distributed under the Creative Commons Attribution License, which permits unrestricted use, distribution, and reproduction in any medium, provided the original work is properly cited.

Background and Objective. The purpose of this study was to highlight the clinical performance of platelet-rich plasma (PRP) used as an adjunctive tool for regeneration in infrabony periodontal defects using different biomaterials or performing different surgical flap approaches. Comparative evaluation of main clinical outcomes as probing pocket depth reduction, clinical attachment gain, and recession reduction with and without the use of PRP has been analysed. *Materials and Methods.* According to the focused question, an electronic and hand searching has been performed up to December 2016. From a batch of 73 articles, the selection strategy and Jadad quality assessment led us to include 15 studies for the meta-analysis. *Results.* Despite the high heterogeneity found and the lack of complete data regarding the selected clinical outcomes, a comparative analysis has been possible by the categorization of used biomaterials and surgical flap approaches. This method led us to observe the best performance of grafts with the use of adjunctive PRP in CAL gain and PPD reduction. No difference has been outlined with a specific surgical flap. *Conclusions.* Although PRP is considered a cheap and patient's derived growth factor, the not conclusive data reported would suggest that its use in addition to bone substitutes could be of some clinical benefit in the regenerative treatment of infrabony defects. *Clinical Relevance.* This systematic review was intended to sort out the huge controversial debate in the field about the possible use of PRP in regenerative surgery in infrabony defect. The clinical relevance of using blood-borne growth factors to conventional procedures is effective as these could determine a better performance and outcomes despite the surgical approach adopted and limit the use of additional biomaterials for the blood clot stabilization.

1. Introduction

The ultimate goal of periodontal therapy in the case of infrabony defects is regeneration. Regeneration means "reproduction or reconstitution of a lost or injured part. It takes into account all the procedures attempting to regenerate lost periodontal structures through differential tissue responses and by different biomaterials such as grafts, membranes or Biomodulators as Enamel Matrix Proteins" (*Glossary of Periodontal Terms*, AAP, 2001). These procedures would temporarily delay the apical migration of the gingival epithelium allowing the granulation tissue derived from the periodontal ligament and osseous tissue to repopulate the space adjacent to the denuded root surface [1].

Several materials are available in daily practice, but none can be considered as an ideal one. In order to achieve a successful regeneration, biomaterials should fulfil four main characteristics: (1) structural integrity, (2) to work as a scaffold for tissue ingrowth, (3) favoured by stem cells that can potentially differentiate and support

the regeneration, and (4) contain factors for regeneration and/or repair.

Growth factors (GFs) are expressed during different phases of healing, and they are key elements in promoting regeneration of tissues; these are considered the most relevant factors in osseoregenerative process.

Platelet-rich plasma (PRP) is considered a cheap way to obtain many growth factors (GFs) in physiological proportion, and it has already been largely applied as a GF's carrier in different tissues due to its properties of inducing healing response even in cases with low potential [2].

Substantially, PRP is a blood derivate growth factor with a higher platelet concentration up to 338% that can release all polypeptide GFs from alpha granules: platelet-derived growth factor (PDGF), transforming growth factor-β1 and transforming growth factor-β2 (TGF-β1 and TGF-β2), and insulin-like growth factors 1 and 2 (IGF-1,2) [3].

In clinical dental practice, the effective use of PRP has been described in sinus grafting procedures [4], alveolar socket preservation techniques [5], and also as an adjunctive procedure to support the regenerative process in periodontal infrabony and furcation defects [6].

Although its clinical benefits have been demonstrated several times, the adjunctive use of autologous PRP in regenerative procedures has produced controversial outcomes ranging from significant to null effects, as demonstrated from different published systematic reviews [3, 7].

This review investigates and updates the clinical efficacy of PRP when added to grafting materials and/or to membranes or biomodulators in cases of periodontal infrabony defects in patients with advanced chronic periodontitis. In particular, it was aimed to highlight the most relevant clinical outcome changes (vertical pocket probing depth, vertical clinical attachment level, and the recession) in GTR coupled with PRP compared to the same procedure without it. In order to get stronger evidence, a SR on published RCTs was chosen.

2. Materials and Methods

2.1. Focused Question. The focused question that this systematic review is intending to answer is

"What are the Vertical Probing Pocket Depth Reductions, the Vertical Clinical Attachment Level Gains and the Recession Reduction at infra-bony defects at least 6 months after Regenerative Surgery with the adjunctive use of PRP as documented in Randomized Clinical Trials, compared to the same clinical procedures and biomaterials performed without the use of PRP?"

2.2. Eligibility Criteria for Studies to be Included in This Review. According to the P.I.C.O system [8], inclusion criteria were outlined as follows:

2.2.1. Study Population. Studies were limited to human subjects older than 18 years and in good general health, with a diagnosis of chronic periodontitis and with at least one pair of specular infrabony defects. Studies considering individuals with a history of aggressive periodontitis or conducted on animal models were excluded from our consideration.

2.2.2. Type of Interventions. GTR surgical procedures with and without PRP will be the interventions considered for the comparative evaluation. The specific regenerative techniques and biomaterials investigated in this study were

(1) autologous bone grafts,

(2) bone substitutes (allogenic, xenogenic, and synthetic grafts),

(3) barrier membranes (resorbable and not resorbable),

(4) enamel matrix proteins (EMD).

2.2.3. Type of Comparison. Infrabony defects treated by regenerative surgery with PRP were considered the test group and compared to the same defects treated by the same regenerative therapy without PRP that were considered the control group.

2.2.4. Outcome Measures. Outcome variables considered in this study were

(i) probing pocket depth reduction (PPDRed mm),

(ii) clinical attachment level gain (CALGain mm),

(iii) recession reduction (RECRed).

These were evaluated as the mean difference (mm) from the time of surgery until the end of the evaluation period not before 6 months.

2.2.5. Types of Studies. To be considered for inclusion in this review, studies should be randomized controlled clinical trials (RCTs) only; no cohort studies (CHT) or case-control studies were included. Case series and case reports studies were also not considered as they would provide a low strength of evidence.

2.3. Information Sources. The search has been performed by the use of the following electronic databases: Pubmed, Cochrane Oral Library, Embase, and LILACS.

Trial registers have been searched using Current Controlled Trials (http://www.controlled-trials.com/), ClinicalTrials.gov (http://clinicalTrials.gov/ct2/home) and the World Health Organization International Trials Registry Platform search portal (http://www.who.int/trialsearch/Default.aspx).

Conference abstracts have been searched using the ISI Web of knowledge (http://isiwebofknowledge.com) and the Grey literature using Open Grey (http://www.opengrey.eu).

Hand searching included a complete search of Journal of Periodontology and Journal of Clinical Periodontology up to December 2016 and bibliographies of all relevant papers and review articles. In the case of ambiguous or missing data, experts have been contacted directly.

The search has been performed up to and including December 2016.

3. Search Strategy

The following search strategy has been used as a combination of MeSH terms and free text words:

(i) Intervention and materials: ("PRP" [txt words] OR "Platelet Rich Plasma" [txt words] OR "Platelet" [mesh] OR "guided tissue regeneration" [mesh] OR "periodontal" [all fields] OR "regeneration [mesh] OR "guided-tissue-regeneration" [txt words] OR "GTR" [txt words] OR "periodontal regeneration" [txt words] OR "Bone filler" [txt words] OR "Autologous bone grafts" [txt words] OR "Autogenous bone" [txt words] OR "bone substitutes" [mesh] OR "allogenic grafts" [txt words] OR "Allografts" [txt words] OR "xenogenic grafts" [txt words] OR "xenografts" [mesh] OR "synthetic grafts" [txt words] OR "Barrier membranes" [txt words] OR "membranes" [mesh] OR "resorbable membrane" [txt words] OR "non-resorbable membrane" [txt words] OR "guided bone regeneration" [txt words] OR "GBR" [txt words] OR "freeze dried bone allograft" [txt words] OR "demineralized freeze dried bone allograft" [txt words] OR "DFDBA" [txt words] OR "FDBA" [txt words] OR "Bio-Oss" [txt words] OR "Bio-Oss Collagen" [txt words] OR "Alloplast" [txt words] OR "tricalciumphosphate" [txt words] OR "cerasorb" [txt words] OR "Bioglass" [txt words] OR "polymeric" [txt words] OR "collagen sponge" [txt words] OR "Collagen" [txt words] OR "Biogide" [txt words] OR "Ossix" [txt words] OR "Gore tex" [txt words] OR "Enamel Matrix Proteins" [txt words] OR "Emdogain" [txt words] OR "EMD" [txt words]);

(ii) Disease: ("periodontal defects" [mesh] OR "periodontal [all fields] OR "infrabony defects" [txt words]);

(iii) Study design: (."randomized clinical trials" [mesh] OR randomized controlled study" [mesh] OR "clinical trial" [mesh] OR "cohort study" [mesh] OR "clinical trial" [mesh] OR "comparative study" [mesh] OR "systematic review" [mesh] OR "case control study" [mesh] OR "longitudinal study" [mesh]).

Adopted filters have been "humans," and articles were published in English language.

3.1. Methods of the Review

3.1.1. Screening and Selection. Initially, titles and abstracts of all reports were screened independently by two reviewers (MS and FP). Subsequently, for studies appearing to meet the inclusion criteria, or for which there were insufficient data in the title and abstract to make a clear decision, the full report was obtained and independently assessed by three reviewers (MS, FP, and MA) to establish whether the study met the inclusion criteria. Any disagreements were resolved by discussion among the reviewers. All studies meeting the inclusion criteria then underwent validity assessment. The reasons for rejecting studies at this or at subsequent stages were recorded.

Special attention was paid not to duplicate publications in order to avoid a likely bigger impact of the same data in the global result.

3.1.2. Quality Assessment/Risk of Bias. The quality assessment of the included studies was undertaken independently by two reviewers based on the content of the articles. The reviewers were blind to the name of the authors, institutions, and journal titles.

A commonly used three-item, five-point quality scale was used to rate the quality of the studies [9]. The minimum score for the inclusion was 2, and the maximum was 5.

Points were awarded according to the following criteria:

(1) Was the study randomized? If yes, +1 point.

Was the randomization procedure appropriate and clearly reported in the study? If yes, +1 point. If no, all points deleted.

(2) Was the study double-blinded? If yes, +1 point.

Was the double-blinding method appropriate and clearly reported in the study? If yes, +1 point. If no, all points deleted.

(3) Were the reasons for patient withdrawals and dropouts described, for each treatment group? If yes, +1 point.

A separate scoring for quality assessment was obtained and independently assessed by two reviewers (MS, FP) to establish whether the study met the quality criteria in order to reduce the risk of bias. The level of agreement between the two reviewers was calculated using kappa statistics.

3.1.3. Data Extraction. Two reviewers (MS and FP) independently using specially designed data extraction forms extracted the necessary data. Any disagreement was discussed, and a third reviewer (MA) was consulted when necessary.

Authors of studies were contacted for clarification or missing information. Data was excluded until further clarification could be available or if an agreement could not be reached. When the results of a study were published more than once or results were detailed in a number of publications, the most complete data set was sought from all sources and included only once.

Using a standard protocol, the following data were collected from the studies:

(i) name of the authors, date of publication, name of the journal, and setting;

(ii) details on the study design;

(iii) sample size (number/gender);

(iv) follow-up (months);

(v) treated infrabony defects (number), position of the defects (maxillary/mandibular);

(vi) intervention/barrier-augmentation material, soft tissue closure, eventual antibiotic intake, reassessment;

(vii) control group: intervention/barrier-augmentation material;

(viii) clinical attachment level gain (CALgain);

(ix) pocket probing depth reduction (PPDRed);

(x) recession reduction (RECRed).

3.1.4. Heterogeneity Assessment. The statistical heterogeneity among studies has been assessed in two different ways: Cochran's Q statistical test [10] and I^2 test [11] were applied to the selected studies. A fixed-effects model was adopted due to the hypothesis of a population of studies with similar characteristics.

In the case of high heterogeneity values, subgroups, and sensitivity, analysis was performed based on

(i) study site (maxillary/mandibular);

(ii) regenerative material/s used (bone graft and/or resorbable/not resorbable barrier);

(iii) surgical technique used.

3.1.5. Data Synthesis. To summarize and compare studies, data were displayed as a weighted mean difference (WMD) in primary and secondary outcomes. Using this index, data from articles was directly pooled together (means and 95% CI).

(i) For dichotomous outcomes, the estimates were expressed as relative risk ratio (RR) together with 95% CI.

(ii) For continuous outcomes, standardized mean differences and 95% confidence intervals were used to summarize the data for each study.

The study-specific estimates were pooled using the fixed-effects model (Woolf's method). If a significant heterogeneity was found, the random effect model result was presented.

Forest plots were created to illustrate the effects of the different studies and the global estimation.

SPSS Statistics™ software was used to perform all analyses. Statistical significance has been defined as a p value <0.05.

3.1.6. Sensitivity Analysis and Bias Detection. Sensitivity analysis was performed excluding each of the studies step by step from the meta-analysis and evaluating the changes in the global estimation.

Publication biases were evaluated using a funnel plot and Egger's linear regression method.

3.1.7. Final Recommendation. A final recommendation will be extracted from the results of this meta-analysis, considering their clinical significance.

4. Results

4.1. Study Selection. The search identified 39 articles on a record of 73 further filtered for "Humans," "Clinical Trial," and "English Language." The independent screening of the titles and abstracts led to the rejection of 18 papers. The full text of the remaining 21 papers was then searched. For 1 study, the full text was not obtained [12], so the final pool was 20 studies. Out of these, 3 papers were further rejected for the following reasons: two studies did not provide a control group [13, 14] and one was not a fully RCT [15]. Two articles were rejected because they did not provide comprehensive data and/or standard deviations to be analysed [16, 17].

On the first screening, agreement between the reviewers was met for all the articles except one [18], because of the lab method for PRP gel preparation. The 3rd reviewer solved the debate by accepting it.

The final number of included studies was 15, and their characteristics are reported in Table 1. Not all the considered studies reported the mean change and the SD value for each outcome; in these cases, the studies were excluded from meta-analysis regarding the missing data (Figure 1).

4.1.1. Classification of Studies according to Treatments. The included studies were grouped according to provided treatment. This action allowed us to analyse better the performance of PRP adding in the following test groups:

Group 1: biomodulators versus biomodulators and PRP (2 articles),

Group 2: grafts versus grafts and PRP (6 articles),

Group 3: none versus PRP alone (1 article),

Group 4: grafts and membranes versus grafts, membranes, and PRP (6 articles).

4.2. Methodological Quality of Included Studies. The quality of the included studies was assessed according to Jadad scoring [9].

Scoring was independently assessed by the reviewers, and all the studies reported a minimum of 2 points or above, allowing them to be included.

To test the extent of interagreement between the two reviewers, Cohen's Kappa Statistics was used.

Its value lies between −1 and 1, where 1 is the perfect agreement, 0 is exactly what would be expected by chance, and negative values indicate agreement less than chance, that is, potential systematic disagreement.

The calculated point estimate of Cohen's kappa statistic κ was 0.74, which according to the commonly cited scale for interpretation of kappa statistic (Landis and Koch [33]) indicates a substantial agreement between the two reviewers. The Z score = 5.77 with p value <.0001 showed that κ is different from zero. The 95% confidence limits for κ were (0.52, 0.97).

4.3. Heterogeneity Assessment. In order to evaluate if a within-study or between-study variability occurred, heterogeneity was assessed. Cochran's Q test was calculated although the small number of included studies led to the consideration of I^2 statistics in a fixed-effects model. The I^2 statistics showed a substantial heterogeneity for VCAL and

Table 1: Included studies.

Study	Design	Study location	Population mean age	M/F ratio	Intervention	Outcomes	Follow-up	Flap placement
[19]	RCT BA	Department of Periodontology, Semmelweis University, Budapest	32–56 years	13 M/11 F	EMD + NBM + PRP versus EMD + NBM	Regenerative surgery of deep infrabony defects	12 months, 5 years	Coronal advancement
[18]	RCT SM	University of Dammam, College of Dentistry, Kingdom of Saudi Arabia	41.4 ± 2.61 years	7 M/5 F	PRP + torus mandibularis chips versus torus mandibularis chips	Treatment for periodontal infrabony defects	6 months	Original
[20]	RCT	Department of Periodontics, Government Dental College and Research Institute, Bangalore, India	36.8 years	NA	PRP versus OFD	Treatment for periodontal infrabony defects	9 months	Coronal advancement
[21]	RCT	Department of Periodontology, Faculty of Dentistry, Gazi University, Ankara, Turkey	48.96 ± 6.6 years	9 M/5 F	B-TCP + PRP versus B-TCP	Therapeutic efficacy of platelet-rich plasma in infrabony defects	6 months	Original
[22]	RCT SM	Department of Periodontia, Saveetha Dental College and Hospitals Chennai	20 and 50 years	NA	PRP + HA + B-TCP versus HA + TCP	Clinical effectiveness of regenerative techniques	6 months	Original
[23]	RCT BA	Department of Periodontology, Semmelweis University, Budapest, Hungary	28 to 65 years	9 M/21 F	PRP + ABBM versus ABBM	Modality to enhance the outcome of regenerative surgery	12 months	Coronal advancement
[24]	RCT SM	School of Dentistry, University of Belgrade, Republic of Serbia	47 ± 10 years	9 M/14 F	BPBM + GTR + PRP versus BPBM + GTR	Additional benefits provided by the incorporation of platelet-rich plasma (PRP) into a regenerative protocol	6 months	Original
[25]	RCT	Division of Periodontology, Polytechnic University of Marche, Ancona Torrette, Italy	47 to 72 years	31 M/29 F	DFDBA + PRP versus DFDBA	Compare PRP combined with DFDBA to DFDBA in the treatment of human intrabony defects	12 months	Coronal advancement
[26]	RCT BA	Department of Periodontology, Semmelweis University, Budapest, Hungary	28 to 58 years	12 M/16 F	PRP + B-TCP + GTR versus B-TCP + GTR	To enhance the outcome of regenerative surgery	12 months	Coronal advancement
[27]	RCT	Department of Periodontology, Semmelweis University, Budapest, Hungary	32–56 years	12 M/14 F	EMD + NBM + PRP versus EMD + NBM	To enhance the outcomes of regenerative surgery significantly	12 months	Coronal advancement
[28]	RCT BA	Department of Periodontology, Semmelweis University, Budapest, Hungary	26 to 55 years	10 M/14 F	PRP + ABBM + GTR or ABBM + GTR	To clinically evaluate the effect of PRP on the healing of deep intrabony defects	12 months	Coronal advancement
[29]	RCT	Division of Periodontology, Niigata University Graduate School of Medical and Dental Sciences, Niigata, Japan	55.5 ± 8.2 years	21 M/49 F	PRP + HA versus HA + saline	To compare platelet-rich plasma (PRP) combined with a biodegradable ceramic in the treatment of human intrabony defects	12 months	Original
[30]	RCT SM	School of Dentistry, University of California, Los Angeles	41 ± 13 years	16 M/12 F	BPBM + GTR + PRP versus OFD	Clinical effectiveness of a combination therapy in the regeneration of periodontal intrabony defects in humans	6 months	Original
[31]	RCT SM	Private practice, Houston and Department of Periodontics, The University of Texas Health Science Center at Houston, TX	37 to 74 years	5 M/8 F	PRP + BDX versus BDX	The combination of PRP and BDX to those obtained from the use of the bone replacement graft alone	6 months	Coronal advancement
[32]	RCT SM	Clinical Specialties, Section of Periodontics, UCLA School of Dentistry, Los Angeles, CA, USA	39 ± 9 years	8 M/10 F	PRP + BPBM + GTR versus GTR	Combination therapy in promoting clinical signs of periodontal regeneration in intrabony defects	6 months	Original

EMD: enamel matrix derivative; NBM: natural bone mineral; PRP: platelet-rich plasma; OFD: open flap debridement; B-TCP: beta-tricalcium phosphate; ABBM: anorganic bovine bone mineral; BPBM: bovine porous bone mineral; GTR: guided tissue regeneration; DFDBA: demineralized freeze-dried bone allograft; BDX: bovine-derived xenograft.

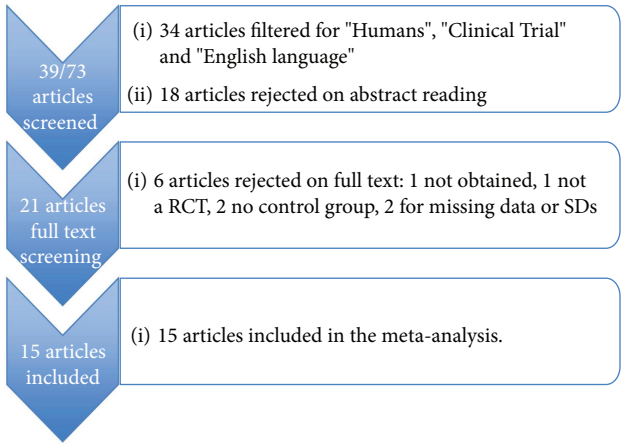

Figure 1: Flow chart of the screening process.

VPD outcomes, while no heterogeneity was found according to REC.

4.4. Change in Vertical Clinical Attachment Level (VCAL) (Closed Assessment). To test the effectiveness of using PRP in addition to the adopted treatment, 95% confidence intervals were constructed for difference between the means of test and control groups. The graphical presentation is reported in Figure 2. Out of nine articles, results of five articles led us to accept the hypothesis of no difference between the test and control groups, whereas four articles (Hanna et al. [31], Okuda et al. [29], Piemontese et al. [25], and Kaushick et al. [22]) suggested results in favour of the test group as the SDs showed a mean CAL gain of 2 mm compared to the control group.

4.5. Change in Vertical Probing Depth (VPD). Twelve articles were able to provide data regarding vertical probing depth (VPD).

Four out of these 12 [23, 26–28] studies showed no difference between the test and control groups, whereas the remaining 8 favoured the addition of PRP showing a VPDRed of about 1.5 mm (see Figure 3).

4.6. Change in Recession. Out of 8 articles providing useful data for analysis, only one [20] seemed to show the effectiveness of the test group versus the control group in recession reduction of about 0.5 mm after treatment. The other seven studies did not provide any evaluable difference between groups (see Figure 4).

4.7. Change in Clinical Outcomes Regarding Treatment Groups. According to the categorization of treatments into 4 groups, only 2 of them provided evaluable data regarding the adopted clinical outcomes: grafts + PRP and grafts + PRP + membranes.

Biomodulators and PRP alone included one single evaluable observation as the other selected articles did not provide any mean baseline-final VCAL, VPD, and REC change or the SD.

When comparing VPD in grafts + PRP and grafts + PRP + membrane, five articles' sample data were available for each of $\bar{X}$ grafts + PRP and $\bar{X}$ grafts + PRP + membrane. The t statistic value $t = 4.60$ with p value <0.0001 suggested that we may reject null hypothesis in favour of μgrafts + PRP at $\alpha = 5\%$.

When comparing VCAL in "grafts + PRP" and "grafts + PRP + membrane," two articles' sample data were available for $\bar{X}$ grafts + PRP and five articles' data for $\bar{X}$ grafts + PRP + membrane. The t statistic value $t = 2.86$ with p value = 0.0045 suggested that we may reject null hypothesis in favour of μgrafts + PRP at $\alpha = 5\%$.

When comparing REC in "grafts + PRP" and "Grafts + PRP + membrane," two articles' data were available for computing $\bar{X}$ grafts + PRP whereas four available articles provided values for $\bar{X}$ grafts + PRP + membrane. The t statistic value $t = 8.68$ with p value <0.0001 again suggested to reject null hypothesis in favour of μgrafts + PRP at $\alpha = 5\%$.

4.8. Comparison of Clinical Outcomes Regarding the Adopted Surgical Technique. For VCAL, the mean of the test group, that is, "coronally placed" (based on test group of seven articles) was compared with the mean of control group, that is, "original position" (based on test group of two articles).

For VPD, the mean of the test group, that is, "coronally placed" (based on test group of seven articles) is compared with the mean of control group, that is, "original position" (based on test group of five articles).

For VCAL, to test the hypothesis H0, μcoronally placed = μoriginal position, $\bar{X}$ coronally is computed on the basis of seven observations/articles and $\bar{X}$ original is the mean of two observations/articles. The value of t statistic is calculated as $t = 0.16$ with p value = 0.3777. So we may accept the null hypothesis of equality of two means at 0.05 level of significance.

For VPD, to test the hypothesis H0, μcoronally placed = μoriginal position, $\bar{X}$ coronally is computed on the basis of seven observations/articles and $\bar{X}$ original is the mean of five observations/articles. The value of t statistic $t = -1.26$ with p value = 0.2071 again leads to accept the equality of two means at 0.05 level of significance.

5. Discussion

The present systematic review was intended to investigate the controversial results raised from similar papers already published and to update those. The objective was to provide a possible evidence for a better performance of regenerative surgery in infrabony defects with the adjunctive use of autologous blood-derived growth factors as PRP or focusing on the different surgical techniques adopted and subsequently to address future research on the topic.

According to the CONSORT guidelines, our consideration aimed to include only RCTs with a quality assessment equal or more than 2 according to Jadad classification. This allowed us to include only 15 articles from a starting batch of 73.

Although we followed a strict selection and the quality testing of the included studies, a significant heterogeneity was found, leading us to implement other strategies for categorizations of studies in order to assess and solve it. The

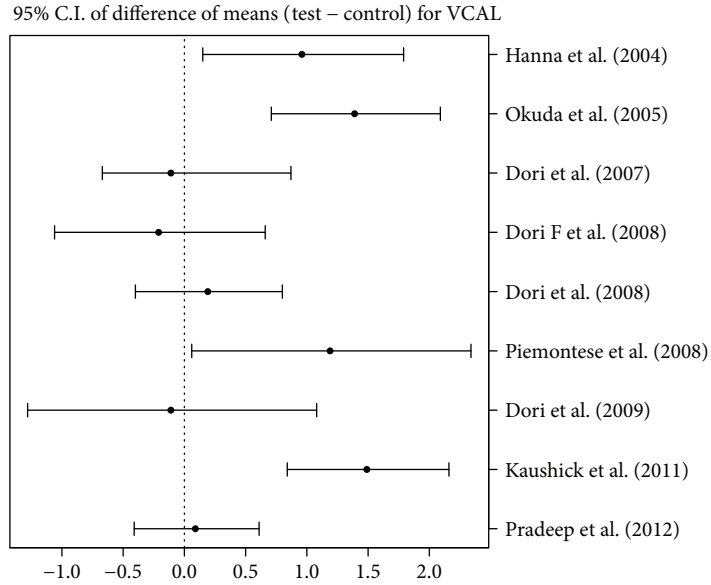

Figure 2: 95% confidence interval presentation for difference between means of test group and control group for VCAL, that is, mean (test) – mean (control).

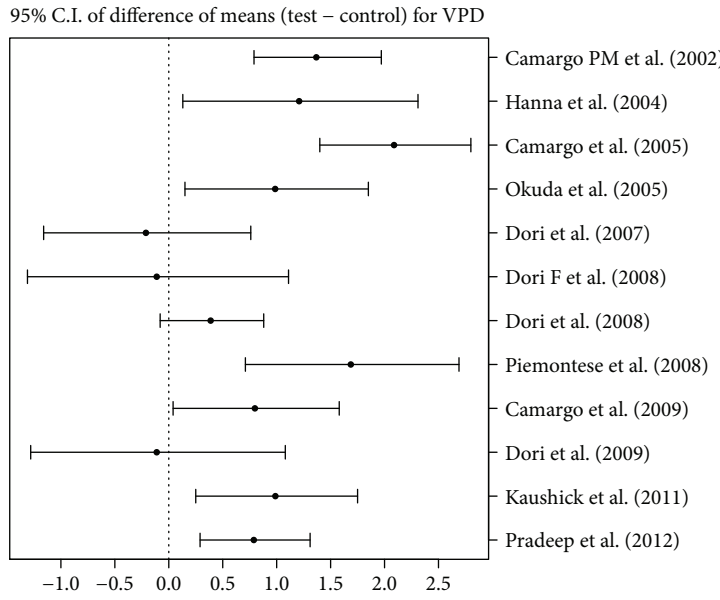

Figure 3: 95% confidence interval presentation for difference between means of test group and control group for VPD, that is, mean (test) – mean (control).

adopted solutions categorized the studies according to the treatment in 4 classes (biomodulators, grafts, grafts + resorbable membranes, and treatment without materials). It also categorized it according to the surgical flap approach (coronally placed or replaced).

Another problem was the high number of the studies that did not provide standard deviations about the provided outcome values. This matter did not allow us to consider them in the meta-analysis due to the need of data regarding the sample variations and of the mean change of the outcomes from baseline examination to the reassessment after the follow-up.

5.1. Overall Intergroup Analysis. The overall meta-analysis performed on the main clinical outcomes (VPD, VCAL, and REC) led us to explore the behaviour of the test group (PRP added) in favouring a better healing in infrabony defect.

The reported 95% confidence intervals of 4 main studies [22, 25, 29, 31] were presenting favourable results for VPD or VCAL, while not the same for REC. This aspect would suggest an efficient clinical attachment gain inside the infrabony defect due to the adjunctive use of PRP as an appropriate regenerative method. Nevertheless, no radiographic comparison of the alveolar bone levels

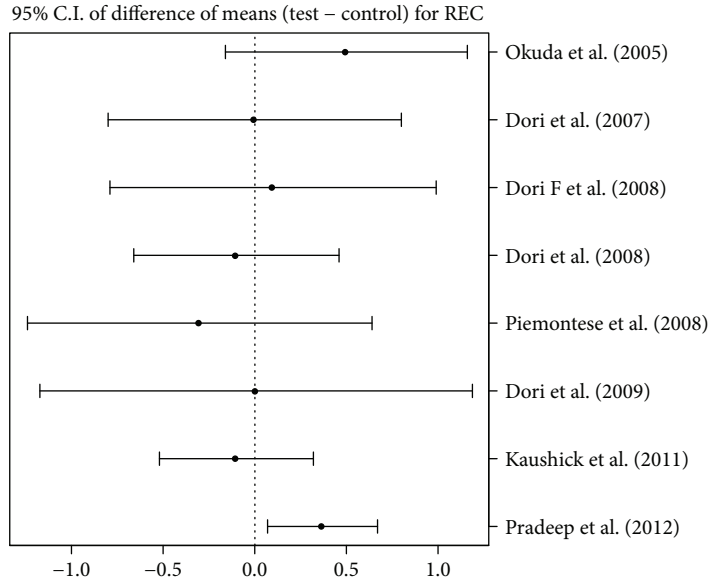

Figure 4: 95% confidence interval presentation for difference between means of test group and control group for REC, that is, mean (test) – mean (control).

before and after treatment has been reported or systematically assessed, so we cannot provide a precise interpretation about the healing process.

In all the considered studies, the main treatment performed was the combination of a bone graft (HA, DFDBA, and TCP) with PRP without the use of any barrier or a membrane. The performed surgical procedure was flap repositioning without any coronal advancement.

5.2. Intragroup Analysis. When comparing the efficacy of different regenerative materials or techniques among them, the analysis was possible only when considering 2 out of 4 classes of categorization due to missing data.

The combination of bone grafts with PRP was always producing better clinical results in terms of CALgain and pocket reduction than the adjunctive use of membranes after short- and longer term reassessment.

This finding is in line with another systematic review on the same topic [7], which suggested that maybe PRP itself can act as a barrier due to the dense fibrin network produced after platelet activation. The adjunctive use of a membrane either resorbable or not could not allow any interaction between the chemokines and GFs released in the wound area and the overlying connective tissue.

When we looked if the grafting material showed any possible effect, no differences have been identified favouring a specific category. It is therefore suggested that the grafting material is acting as a scaffold leaving the PRP to execute the inductive phase of the healing process.

5.3. Adopted Surgical Technique. According to the evidence of a better performance in CALgain of coronally placed flaps in the regenerative approach to infrabony defects [34], our investigation moved to analyse if the adopted surgical technique or the use of adjunctive PRP could justify the observed better results in the test groups of selected studies. The considered surgical approaches were the replacement and the coronal placement. Due to the assessed high heterogeneity, a categorization according to the technique was performed using the test groups (PRP added) of the included studies. In comparison, the test group was the coronally advanced flap and the control was the replaced flap.

Although not the same number of articles were reporting the use of each one, a "*t* test" was possible considering only 2 main clinical outcomes: VPD and VCAL.

In all cases, no differences in terms of CAL gain or PPD reduction between the two adopted techniques have been highlighted. The blood clot stability was achieved in both conditions, and the healing process could reasonably happen due to the presence of the growth factors. Even the recession reduction could be outlined with the replaced flap as the evidence in the overall analysis regarding REC outcomes has been suggested [20].

6. Conclusions

We conclude from the data in this systematic review that the adjunctive use of PRP in the regenerative treatment of infrabony defects can be considered as an affordable technique to get a better CAL gain and PPD reduction in the surgical treatment of periodontal infrabony defects. Anyway, the limitations of the provided studies are the lack of baseline data regarding the defect size and their morphology, the absence of reports of other relevant clinical outcomes, as the bone fill, and the heterogeneity between studies.

On the basis of this systematic review, the regeneration/repair of infrabony defects would favour the use of adding PRP to a simple surgical repositioned flap technique, like in the open flap debridement (OFD), with the use of bone grafts (xenografts, HA, or TCP). No better results would be achievable using combinations with biomodulators (Emdogain) or membranes, the PRP just would act as a biomodulator itself.

In a biological sense, this observation would state for the biomolecular signalling action between PRP and the surrounding cellular environment that any membrane could interrupt or modify. The use of bone grafts would state as a blood clot stabilizer enhancing the osteoinductive properties of the PRP itself.

7. Future Research/Observations

According to the main reported pitfalls, future studies should be aimed first, designed according to RCT schemes in order to provide clinical evidences.

A comparison between a surgical flap approach alone and the adjunctive use of PRP would be needful in order to explore the role of growth factors alone in periodontal regeneration and the healing process, as well as the radiographic bone level assessment before and after treatment, as they represent a critical parameter in success assessment.

In order to explore which growth factor would be better suited in periodontal procedures, a multiple-arm RCT would be needful comparing PRP with other blood-derived agents available as well as with the different techniques adopted to deliver it.

Ethical Approval

This article does not contain any studies with human participants or animals performed by any of the authors.

Conflicts of Interest

Mubashir Saleem declares that he has no conflict of interest. Flavio Pisani declares that he has no conflict of interest. Faisal Maqbool Zahid declares that he has no conflict of interest. Ioannis Georgakopoulos declares that he has no conflict of interest. Teuta Pustina-Krasniqi declares that she has no conflict of interest. Edit Xhajanka declares that she has no conflict of interest. Maher Almasri declares that he has no conflict of interest.

Authors' Contributions

Mubashir Saleem and Flavio Pisani contributed equally to this paper.

References

[1] G. Polimeni, A. V. Xiropaidis, and U. M. E. Wikesjo, "Biology and principles of periodontal wound healing/regeneration," *Periodontology 2000*, vol. 41, no. 1, pp. 30–47, 2006.

[2] B. L. Eppley, W. S. Pietrzak, and M. Blanton, "Platelet-rich plasma: a review of biology and applications in plastic surgery," *Plastic and Reconstructive Surgery*, vol. 118, no. 6, pp. 147e–159e, 2006.

[3] S. Kotsovilis, N. Markou, E. Pepelassi, and D. Nikolidakis, "The adjunctive use of platelet-rich plasma in the therapy of periodontal intraosseous defects: a systematic review," *Journal of Periodontal Research*, vol. 45, no. 3, pp. 428–443, 2010.

[4] N. S. Arora, T. Ramanayake, Y. F. Ren, and G. E. Romanos, "Platelet-rich plasma in sinus augmentation procedures: a systematic literature review: Part II," *Implant Dentistry*, vol. 19, no. 2, pp. 145–157, 2010.

[5] D. Simon, S. Manuel, V. Geetha, and B. R. Naik, "Potential for osseous regeneration of platelet-rich plasma–a comparative study in mandibular third molar sockets," *Indian Journal of Dental Research*, vol. 15, no. 4, pp. 133–136, 2004.

[6] A. R. Pradeep, S. K. Shetty, G. Garg, and S. Pai, "Clinical effectiveness of autologous platelet-rich plasma and peptide-enhanced bone graft in the treatment of intrabony defects," *Journal of Periodontology*, vol. 80, no. 1, pp. 62–71, 2009.

[7] M. Del Fabbro, M. Bortolin, S. Taschieri, and R. Weinstein, "Is platelet concentrate advantageous for the surgical treatment of periodontal diseases? A systematic review and meta-analysis," *Journal of Periodontology*, vol. 82, no. 8, pp. 1100–1111, 2011.

[8] CEBM, "Centre for Evidence-Based Medicine," http://www.cebm.net/.

[9] A. R. Jadad, R. A. Moore, and D. Carroll, "Assessing the quality of reports of randomized clinical trials: is blinding necessary?," *Controlled Clinical Trials*, vol. 17, no. 1, pp. 1–12, 1996.

[10] W. G. Cochran, "The combination of estimates from different experiments," *Biometrics*, vol. 10, no. 1, pp. 101–129, 1954.

[11] J. P. T. Higgins and S. G. Thompson, "Quantifying heterogeneity in a meta-analysis," *Statistics in Medicine*, vol. 21, no. 11, pp. 1539–1558, 2002.

[12] X. Y. Ouyang and J. Qiao, "Effect of platelet-rich plasma in the treatment of periodontal infra-bony defects in humans," *Chinese Medical Journal*, vol. 119, no. 18, pp. 1511–1521, 2006.

[13] D. Moder, F. Taubenhansl, K. A. Hiller, G. Schmalz, and M. Christgau, "Influence of autogenous platelet concentrate on combined GTR/graft therapy in intrabony defects: a 7-year follow-up of a randomized prospective clinical split-mouth study," *Journal of Clinical Periodontology*, vol. 39, no. 5, pp. 457–465, 2012.

[14] A. R. Pradeep, S. Pai, G. Garg, P. Devi, and S. K. Shetty, "A randomized clinical trial of autologous platelet-rich plasma in the treatment of mandibular degree II furcation defects," *Journal of Clinical Periodontology*, vol. 36, no. 7, pp. 581–588, 2009.

[15] J. Czuryszkiewicz-Cyrana and J. Banach, "Autogenous bone and platelet-rich plasma (PRP) in the treatment of intrabony defects," *Advances in Medical Sciences*, vol. 51, Supplement 1, pp. 26–30, 2006.

[16] L. Harnack, R. H. Boedeker, I. Kurtulus, S. Boehm, J. Gonzales, and J. Meyle, "Use of platelet-rich plasma in periodontal surgery–a prospective randomised double blind clinical trial," *Clinical Oral Investigations*, vol. 13, no. 2, pp. 179–187, 2009.

[17] Z. Yassibag-Berkman, O. Tuncer, T. Subasioglu, and A. Kantarci, "Combined use of platelet-rich plasma and bone grafting with or without guided tissue regeneration in the treatment of anterior interproximal defects," *Journal of Periodontology*, vol. 78, no. 5, pp. 801–809, 2007.

[18] K. S. Hassan, A. S. Alagl, and A. Abdel-Hady, "Torus mandibularis bone chips combined with platelet rich plasma gel for treatment of intrabony osseous defects: clinical and radiographic evaluation," *International Journal of Oral & Maxillofacial Surgery*, vol. 41, no. 12, pp. 1519–1526, 2012.

[19] F. Döri, N. Arweiler, T. Húszár, I. Gera, R. J. Miron, and A. Sculean, "Five-year results evaluating the effects of platelet-rich plasma on the healing of intrabony defects treated with enamel matrix derivative and natural bone mineral," *Journal of Periodontology*, vol. 84, no. 11, pp. 1546–1555, 2013.

[20] A. R. Pradeep, N. S. Rao, E. Agarwal, P. Bajaj, M. Kumari, and S. B. Naik, "Comparative evaluation of autologous platelet-rich fibrin and platelet-rich plasma in the treatment of 3-wall intrabony defects in chronic periodontitis: a randomized controlled clinical trial," *Journal of Periodontology*, vol. 83, no. 12, pp. 1499–1507, 2012.

[21] B. Ozdemir and E. Okte, "Treatment of intrabony defects with beta-tricalciumphosphate alone and in combination with platelet-rich plasma," *Journal of Biomedical Materials Research Part B:Applied Biomaterials*, vol. 100B, no. 4, pp. 976–983, 2012.

[22] B. T. Kaushick, N. D. Jayakumar, O. Padmalatha, and S. Varghese, "Treatment of human periodontal infrabony defects with hydroxyapatite+ β tricalcium phosphate bone graft alone and in combination with platelet rich plasma: a randomized clinical trial," *Indian Journal of Dental Research*, vol. 22, no. 4, pp. 505–510, 2011.

[23] F. Döri, V. Kovács, N. B. Arweiler et al., "Effect of platelet-rich plasma on the healing of intrabony defects treated with an anorganic bovine bone mineral: a pilot study," *Journal of Periodontology*, vol. 80, no. 10, pp. 1599–1605, 2009.

[24] P. M. Camargo, V. Lekovic, M. Weinlaender, T. Divnic-Resnik, M. Pavlovic, and E. B. Kenney, "A surgical reentry study on the influence of platelet-rich plasma in enhancing the regenerative effects of bovine porous bone mineral and guided tissue regeneration in the treatment of intrabony defects in humans," *Journal of Periodontology*, vol. 80, no. 6, pp. 915–923, 2009.

[25] M. Piemontese, S. D. Aspriello, C. Rubini, L. Ferrante, and M. Procaccini, "Treatment of periodontal intrabony defects with demineralized freeze-dried bone allograft in combination with platelet-rich plasma: a comparative clinical trial," *Journal of Periodontology*, vol. 79, no. 5, pp. 802–810, 2008.

[26] F. Döri, T. Huszár, D. Nikolidakis et al., "Effect of platelet-rich plasma on the healing of intrabony defects treated with Beta tricalcium phosphate and expanded polytetrafluoroethylene membranes," *Journal of Periodontology*, vol. 79, no. 4, pp. 660–669, 2008.

[27] F. Döri, D. Nikolidakis, T. Húszár, N. B. Arweiler, I. Gera, and A. Sculean, "Effect of platelet-rich plasma on the healing of intrabony defects treated with an enamel matrix protein derivative and a natural bone mineral," *Journal of Clinical Periodontology*, vol. 35, no. 1, pp. 44–50, 2008.

[28] F. Döri, T. Huszár, D. Nikolidakis, N. B. Arweiler, I. Gera, and A. Sculean, "Effect of platelet-rich plasma on the healing of intrabony defects treated with an anorganic bovine bone mineral and expanded polytetrafluoroethylene membranes," *Journal of Periodontology*, vol. 78, no. 6, pp. 983–990, 2007.

[29] K. Okuda, H. Tai, K. Tanabe et al., "Platelet-rich plasma combined with a porous hydroxyapatite graft for the treatment of intrabony periodontal defects in humans: a comparative controlled clinical study," *Journal of Periodontology*, vol. 76, no. 6, pp. 890–898, 2005.

[30] P. M. Camargo, V. Lekovic, M. Weinlaender, N. Vasilic, M. Madzarevic, and E. B. Kenney, "A reentry study on the use of bovine porous bone mineral, GTR, and platelet-rich plasma in the regenerative treatment of intrabony defects in humans," *International Journal of Periodontics & Restorative Dentistry*, vol. 25, no. 1, pp. 49–59, 2005.

[31] R. Hanna, P. M. Trejo, and R. L. Weltman, "Treatment of intrabony defects with bovine-derived xenograft alone and in combination with platelet-rich plasma: a randomized clinical trial," *Journal of Periodontology*, vol. 75, no. 12, pp. 1668–1677, 2004.

[32] P. M. Camargo, V. Lekovic, M. Weinlaender, N. Vasilic, M. Madzarevic, and E. B. Kenney, "Platelet-rich plasma and bovine porous bone mineral combined with guided tissue regeneration in the treatment of intrabony defects in humans," *Journal of Periodontal Research*, vol. 37, no. 4, pp. 300–306, 2002.

[33] J. R. Landis and G. G. Koch, "The measurement of observer agreement for categorical data," *Biometrics*, vol. 33, no. 1, pp. 159–174, 1977.

[34] G. Zucchelli and M. De Sanctis, "A novel approach to minimizing gingival recession in the treatment of vertical bony defects," *Journal of Periodontology*, vol. 79, no. 3, pp. 567–574, 2008.

Hindawi
Stem Cells International
Volume 2018, Article ID 6958713, 9 pages
https://doi.org/10.1155/2018/6958713

Research Article

Vitamin D Promotes MSC Osteogenic Differentiation Stimulating Cell Adhesion and $\alpha V\beta 3$ Expression

Francesca Posa,[1,2] **Adriana Di Benedetto**,[1] **Elisabetta A. Cavalcanti-Adam**,[2] **Graziana Colaianni**,[3] **Chiara Porro**,[1] **Teresa Trotta**,[1] **Giacomina Brunetti**,[4] **Lorenzo Lo Muzio**,[1] **Maria Grano**,[3] **and Giorgio Mori**[1]

[1]*Department of Clinical and Experimental Medicine, Medical School, University of Foggia, Foggia, Italy*
[2]*Institute of Physical Chemistry, Department of Biophysical Chemistry, University of Heidelberg and Max Planck Institute for Intelligent Systems, Stuttgart, Germany*
[3]*Department of Emergency and Organ Transplantation, University of Bari, Bari, Italy*
[4]*Department of Basic and Medical Sciences, Neurosciences and Sense Organs, University of Bari, Bari, Italy*

Correspondence should be addressed to Giorgio Mori; giorgio.mori@unifg.it

Received 5 October 2017; Accepted 15 January 2018; Published 28 February 2018

Academic Editor: Dario Coletti

Copyright © 2018 Francesca Posa et al. This is an open access article distributed under the Creative Commons Attribution License, which permits unrestricted use, distribution, and reproduction in any medium, provided the original work is properly cited.

Vitamin D (Vit D) by means of its biological active form, 1α,25-dihydroxyvitamin D_3 (1,25$(OH)_2D_3$), has a protective effect on the skeleton by acting on calcium homeostasis and bone formation. Furthermore, Vit D has a direct effect on mesenchymal stem cells (MSCs) in stimulating their osteogenic differentiation. In this work, we present for the first time the effect of 1,25$(OH)_2D_3$ on MSC adhesion. Considering that cell adhesion to the substrate is fundamental for cell commitment and differentiation, we focused on the expression of $\alpha_V\beta_3$ integrin, which has a key role in the commitment of MSCs to the osteoblastic lineage. Our data indicate that Vit D increases $\alpha_V\beta_3$ integrin expression inducing the formation of focal adhesions (FAs). Moreover, we assayed MSC commitment in the presence of the extracellular matrix (ECM) glycoprotein fibronectin (FN), which is able to favor cell adhesion on surfaces and also to induce osteopontin (OPN) expression: this suggests that Vit D and FN synergize in supporting cell adhesion. Taken together, our findings provide evidence that Vit D can promote osteogenic differentiation of MSCs through the modulation of $\alpha_V\beta_3$ integrin expression and its subcellular organization, thus favoring binding with the matrix protein (FN).

1. Introduction

Vitamin D (Vit D) is well known to be important for bone health, although its mechanism of action, direct or indirect, is still a matter of debate; its effects on bone tissue and bone cells have not yet been completely clarified.

Several studies speculated on the role of Vit D in the differentiation of osteoblasts and, more recently, on mesenchymal stem cells (MSCs), which are known for their abilities in promoting bone repair and regeneration in cell reconstructive therapies [1–3].

1,25$(OH)_2D_3$, the most active form of Vit D [4], has been identified as osteoinductive, being able to promote *in vitro* the differentiation of human MSCs into osteoblasts [5, 6].

Although MSCs from bone marrow represent an ideal source of stem cells for bone regenerative therapies, their harvesting is comprehensibly complicated for patients; that is why in recent years numerous less invasive alternatives of MSCs have been proposed. Among them, multipotent stem cells from dental tissues (DSCs) have been tested as reliable candidates in tissue repair, primarily because they can be obtained from unnecessary organs such as the third molars [7–9].

Our cell model is represented by dental bud stem cells (DBSCs): postnatal MSCs isolated from the immature form

of the wisdom tooth, the dental bud (DB), in children (8–12 years old). DBSCs meet all the standards to be considered MSCs, expressing more than 95% of mesenchymal stem cell markers; they can differentiate into osteoblast-like cells if cultured in an osteogenic medium (OM) [10], and this process is favored by the downregulation of the nuclear receptor NURR1 [11]; furthermore, these cells show a pattern of adhesion molecules comparable to the one described for MSCs [12]. Thus, DBSCs represent an optimal model of MSCs useful to study bone formation processes.

We have recently demonstrated that the active metabolite of Vit D, $1,25(OH)_2D_3$, is able to stimulate the osteoblastic differentiation of DBSCs by inducing the expression of the typical osteoblastic markers and determining a higher mineralization rate *in vitro*. Moreover, the action of this molecule was particularly evident in the early stages of differentiation, decreasing over time. We concluded that Vit D acts on MSCs, driving the early phases of cell commitment toward the osteoblastic lineage [13].

Cell adhesion to the substrate is of fundamental importance for proliferation, commitment, and differentiation of MSCs [14]; no data are available at present in the literature concerning the effect of Vit D on cell adhesion molecules in MSCs, but there are evidences that the use of titanium substrates and Vit D has an additive effect in regulating the integrin expression of human osteoblast-like cells [15]; moreover, a crosstalk between the two signals, the integrin one and that induced by Vit D in promoting osteoblastic differentiation, has been hypothesized [16].

In light of this, we hypothesized that Vit D drives MSC commitment by affecting cell adhesion.

Integrins, heterodimeric transmembrane adhesion receptors, are fundamental for the extracellular matrix (ECM) assembly and, interacting with numerous extracellular and intracellular ligands, are crucial for cell fate control. As a matter of fact, as shown in different studies, the ECM contains molecules able to provide signals which on the one hand guide cell adhesion, growth, proliferation, and migration and on the other hand can define cell differentiation through the activation of integrin subunits [17–20].

Integrins, by using signaling proteins, are able to modulate both focal adhesion dynamics and cellular functions [21].

Although the specific contribution of these receptors during MSC commitment is still unclear, integrins $\alpha_v\beta_3$ and $\alpha_5\beta_1$ have been proven to possess key functions for bone biology: β_1 integrin subfamily is predominant in osteoprogenitor cells and osteoblasts [22]; the activation of these integrins is at the basis of many processes needed for bone development on substrates, such as the formation of focal adhesions [23–25], force sensing, and mechanotransduction [26], and osteogenesis [27, 28].

$\alpha_v\beta_3$ integrin adhesion and the signals triggered by this receptor might be necessary for osteoblastic differentiation process, as proposed by Schneider et al. [20]. The expression levels of both α_v and β_3 subunits, as well as their assembling to form the functional receptor, are enhanced during DBSC osteogenic differentiation [12].

It has been shown that $\alpha_5\beta_1$ integrin and its interaction with fibronectin (FN), an adhesive ECM glycoprotein, are necessary for preosteoblast adhesion to the ECM and their subsequent differentiation into mature osteoblasts [29].

Hamidouche et al. [19] showed that the expression of α_5 integrin is upregulated in MSCs under osteogenic conditions and that activation of this subunit is sufficient to induce osteoblastic differentiation. These observations also implicate $\alpha_5\beta_1$ integrin in the control of osteoblastogenesis.

Although there are many findings supporting an involvement of these adhesion molecules in osteoblastic differentiation process, the topic is still under debate [17].

In this study, we investigated whether Vit D can influence the expression and subcellular localization of integrins in MSCs, so defining the cell fate and consequently the acquisition of osteoblastic features.

We focused on the specific expression of $\alpha_v\beta_3$ integrin in DBSCs cultured on fibronectin (FN) in presence of Vit D treatment.

1.1. Patients, Materials, and Methods

1.1.1. Materials. 1α,25-Dihydroxyvitamin D_3, ascorbic acid, dexamethasone, poly-L-lysine (PLL), and fibronectin (FN) were from Sigma Aldrich, St. Louis, MO, USA.

Antibody anti-$\alpha_V\beta_3$ clone LM609 was from Millipore; antibodies anti-integrin αV and β3 were from BD Bioscience; anti-RUNX2 antibody was from Abnova.

The following primer pairs were used for the RT-PCR amplification: sense *Coll I* (*COL1A1*) 5′-CGTGGCAGTGA TGGAAGTG-3′; antisense *Coll I* 5′-AGCAGGACCAGCGT TACC-3′; sense *RUNX2* 5′-GGAATGCCTCTGCTGT TATG-3′; antisense *RUNX2* 5′-TTCTGTCTGTGCCTTC TGG-3′; sense *OPN* (*SPP1*) 5′-CTGATGAATCTGATGA ACTGGTC-3′; antisense *OPN* 5′-GTGATGTCCTCGTCTG TAGC-3′; sense *β-actin* (*ACTB*) 5′-AATCGTGCGTGACA TTAAG-3′; antisense *β-actin* 5′-GAAGGAAGGCTGGA AGAG-3′; sense β_2 *microglobulin* (*B2M*) 5′-ATGAGTATG CCTGCCGTGTGA-3′; antisense β_2 *microglobulin* 5′-GGCA TCTTCAAACCTCCATG-3′.

1.2. Patients and Cell Cultures. The dental buds (DBs) were collected from the third molars of 10 healthy pediatric patients aged between 8 and 12 years.

The study was approved by the Institutional Review Board of the Department of Clinical and Experimental Medicine, University of Foggia, and patients' parents gave written informed consent.

The central part of DB was cut into small pieces in a culture dish under laminar flow hood by using a sterile scalpel. Subsequently, enzymatic digestion was performed under stirring, for 1 hour at 37°C, using a 3 mg/ml solution of type I collagenase plus 4 mg/ml of dispase (Gibco Ltd., Uxbridge, UK). Single cell suspension, obtained by filtering the cells through a 70 μm BD Falcon filter (Falcon) (Becton Dickinson, Sunnyvale, CA), was centrifuged at 1300 rpm for 5 min.

The resulting pellet was resuspended in a mesenchymal stem cell culture medium supplemented with 5% fetal bovine serum (FBS), 100 U/ml penicillin-G, 100 μg/ml streptomycin

(Gibco Limited, Uxbridge, UK). Cells seeded at a density of 5×10^3 cells/cm^2 were cultured at 37°C and 5% CO_2, renewing the medium every 3 days.

To examine Vit D effect on cell adhesion during the osteoblastic differentiation process, 3000 cells/cm^2 were seeded and cultured in an osteogenic medium made up of α-MEM supplemented with 2% FBS, 10^{-8} M dexamethasone and 50 μg/ml ascorbic acid (Sigma Aldrich, St. Louis, MO, USA).

1,25$(OH)_2D_3$ (Sigma Aldrich, St. Louis, MO, USA) was reconstituted at 10^{-4} M in 95% ethanol and stored at −20°C.

The cells were grown in replicate using 1,25$(OH)_2D_3$ as treatment and an equivalent concentration of 95% ethanol as vehicle (VHC).

1.3. ECM Glycoproteins and Coating Procedure. Tissue culture-treated polystyrene surfaces were coated with fibronectin (FN, human plasma, 5 μg/cm^2, Sigma) diluted in 1 × phosphate buffered saline (PBS, pH 7.2, PAA, Cölbe, Germany) according to the manufacturers' suggestions. Poly-L-lysine (PLL, 2 μg/cm^2, Sigma) was used as control (CTR).

These amounts ensure the complete coating of the surface with the ECM protein (FN). The surfaces were incubated with FN solution for 30 minutes at 37°C then washed twice with PBS and blocked with bovine serum albumin (BSA, Sigma) at 1% in PBS for 10 minutes at RT. Then surfaces were sterilized in UV light for 30 minutes. The protein content of the coating solution was measured by micro-BCA assay, to ensure the correct coating adsorption and to quantify the residual protein content in the solution.

In addition, coatings were confirmed by fluorescence microscopy using labeled proteins (data not shown).

1.4. Immunofluorescence. A defined amount of cells was seeded and cultured on glass coverslips with the osteogenic differentiation medium, and then the cell fixation in 4% (PFA)/PBS is followed. Subsequently, the cells so treated were washed with PBS and blocked in a solution of 1% BSA and 5% normal goat serum in PBS for 20 minutes. The samples were incubated with the $\alpha_V\beta_3$ antibody (clone LM609 antibody) and washed; the bound antibody was detected using 2 μg/ml of fluorescently labeled goat anti-mouse secondary antibody (Alexa Fluor 488, Invitrogen); cytoskeleton was counterstained with phalloidin (Invitrogen). A multispectrum confocal microscope Leica TCS SP5 was used to visualize and photograph the cells.

1.5. Real-Time PCR. The extraction of total RNA was carried out utilizing spin columns (RNeasy, Qiagen, Hilden, Germany) and then in the amount of 2 μg was reverse transcribed (RT) by using SuperScript First-Strand Synthesis System kit (Invitrogen Life Technologies, Carlsbad, CA, USA). An amount of 20 ng of the synthesized cDNA was subjected to quantitative PCR. Real-time PCR analysis was performed using a BioRad CFX96 Real-Time System with the SYBR Green PCR method as described by the manufacturer's protocol (BioRad iScript Reverse Transcription Supermix cat. 170-8841). The mean cycle threshold value (Ct) from triplicate samples was used to calculate gene expression, and cDNA was normalized to the average of β-actin and β_2 microglobulin (B2M) levels for each reaction.

1.6. Western Blot. Revelation of α_V and β_3 integrin subunits and osteoblastic markers as protein levels was performed using SDS-PAGE gel electrophoresis and Western blot analysis. Cells were lysed after 12 days of osteogenic differentiation, the lysates were centrifuged at 13000 rpm for 15 minutes at 4°C, and then a protein assay (BIORAD) was used to determine the total protein concentration of the supernatant. Proteins were separated by SDS-PAGE and then transferred to nitrocellulose membranes (Invitrogen, Carlsbad, CA). After incubation with primary and secondary antibodies, the Odyssey Infrared Imaging System of LI-COR (LI-COR Biotechnology Lincoln, Nebraska, USA) was used for immunodetection.

1.7. Statistical Analyses. Statistical analyses were performed by Student's *t*-test with the Statistical Package for the Social Sciences (spssx/pc) software (SPSS, Chicago, IL, USA). The results were considered statistically significant for $p < 0.05$.

2. Results

2.1. Vitamin D Treatment Induces Focal Adhesion via $\alpha_V\beta_3$ Subcellular Distribution. To investigate how Vit D can influence the early stages of cell adhesion to the substrate defining, as a result, the cell fate, and consequently the acquisition of osteoblastic features, DBSCs were cultured on coated surfaces in osteogenic conditions and treated with 1,25$(OH)_2D_3$. Cells were analyzed by immunofluorescence for the subcellular distribution of $\alpha_V\beta_3$ integrins.

Since DBSCs reach confluency after few days in culture-forming multilayers, the $\alpha_V\beta_3$ subcellular organization was monitored after the first steps of osteogenic differentiation (3–7 days).

Vit D treatment induced a different integrin organization that appeared to be more clustered and localized in the basal part of the cell if compared to its distribution in the untreated cells (Vehicle, VHC). This effect was evident after 3 and 7 days of differentiation (Figure 1).

$\alpha_V\beta_3$ integrin was distributed throughout the cell in undifferentiated cells cultured for 3 days without Vit D; after 7 days of differentiation, it seemed to have a mild presence in focal adhesion sites (Figure 1(c)), although to a lesser extent compared to treatment with Vit D. In cells with Vit D, the integrin was clearly present and organized in FAs both at day 3 and 7 (Figures 1(b)–1(d)), with the formation of elongated clusters after one week of differentiation (Figure 1(d)).

2.2. Vitamin D Treatment Increases $\alpha_V\beta_3$-Mediated Focal Adhesions on Fibronectin-Coated Surfaces. In order to mimic the interaction of integrins with their ECM partners, as it occurs in the bone microenvironment, we seeded DBSCs on a coating of the major cell adhesion glycoprotein: fibronectin (FN). Indeed, interaction of integrins with ECM proteins significantly induces DBSC differentiation toward osteoblastic lineage; this differentiation was enhanced when cells were grown on ECM glycoproteins containing the integrin-binding sequence, the so-called "RGD motif" [12].

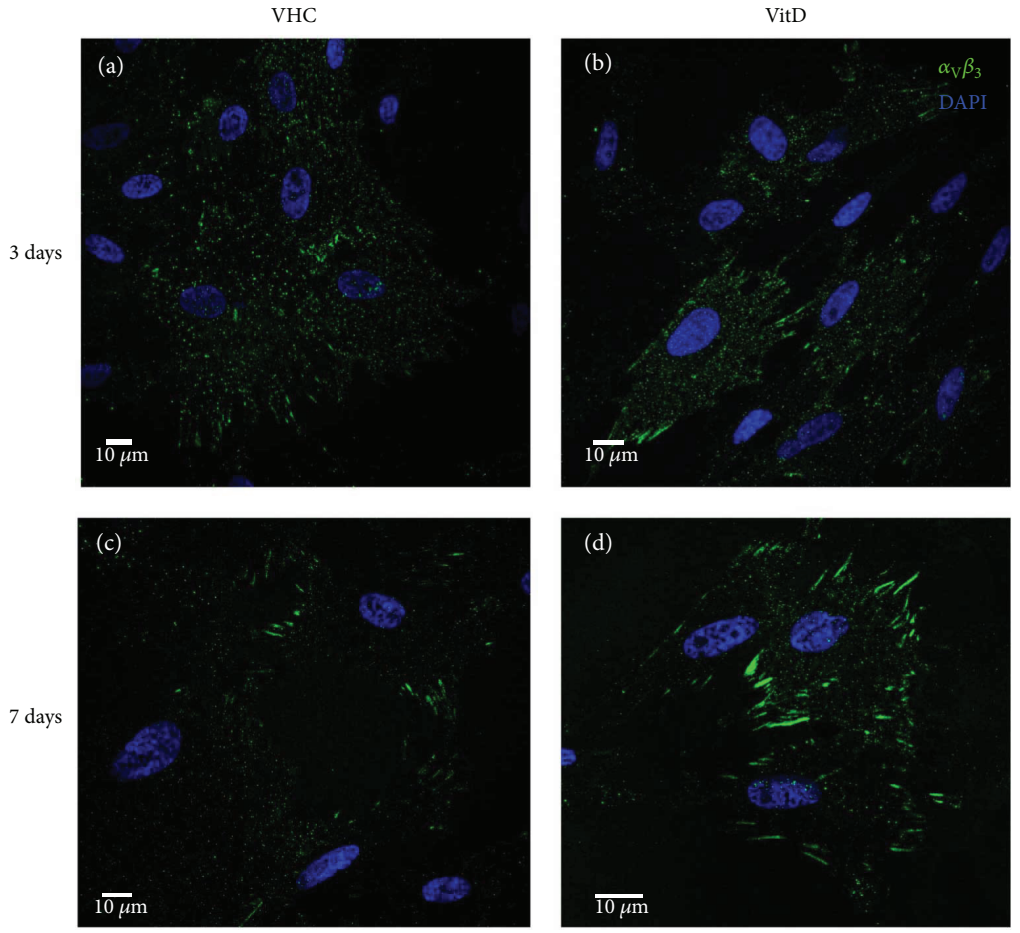

	Number of FAs per cell	Area of FA (square pixels)
VHC 3 days	3.16 ± 1	25.1 ± 6.4
VHC 7 days	5.3 ± 2	52.68 ± 8.3
Vit D 3 days	20.7 ± 3	116.83 ± 18.4
Vit D 7 days	15.67 ± 3	148.53 ± 21.8

Figure 1: Vit D induces a clustered localization of $\alpha_V\beta_3$. Midsection confocal microscopy images show the expression of integrin $\alpha_V\beta_3$ (green) in DBSCs differentiated for 3 and 7 days; (a-b) show that at 3 days, the integrin was distributed in multiple sites in the cells. After 7 days of differentiation, $\alpha_V\beta_3$ is localized on the periphery of the cell where the focal adhesion sites are present (c-d). Vit D treatment seemed to produce a different integrin organization leading to the formation of typical strings particularly evident after 7 days of culture. Blue for nuclei, green for $\alpha_V\beta_3$. The table shows the FA quantification performed with ImageJ software. The data is presented as average ± standard error. Number of FAs per cell = total number of FAs identified in one cell. Area of FA = area of a single FA.

To understand how Vit D treatment could affect cell adhesion in the presence of ECM glycoproteins, we prepared surfaces coated with poly-L-lysine (PLL), as control (CTR) and FN. Cells were seeded and cultured on these surfaces in osteogenic conditions for 7 or 12 days, in the presence or not of Vit D treatment, and then focal adhesion formation was analyzed looking at $\alpha_V\beta_3$ subcellular distribution.

The first observation was that a higher number of cells uniformly colonized the FN-coated surface after 24 hours compared to the CTR (data not shown); furthermore, the cells seeded on FN coating showed a clustered organization of $\alpha_V\beta_3$ into focal adhesions, which was sporadic in the CTR. In addition, we observed that the treatment with Vit D was able to assist the effect of the FN coating in the formation of focal adhesions. Indeed, as shown in Figure 2, the cells treated with Vit D displayed highly visible elongated clusters (typical pattern of $\alpha_V\beta_3$ in FAs) if compared with untreated cells.

Furthermore, we evaluated the expression trend of α_v and β_3 single subunits at protein level by Western blot analysis. As shown in Figure 3, Vit D treatment highly induced the protein expression of α_v, which appears to be almost doubled compared to the VHC; the same is observed with respect to β_3, although with a lower effect. It is clear that FN did not affect the protein expression amount while the treatment with Vit D determines a strong increase in protein expression.

2.3. Vitamin D Treatment Increases Osteoblast Markers Expression on Fibronectin-Coated Surfaces. In previous work [13], we demonstrated that Vit D induced the osteoblastic

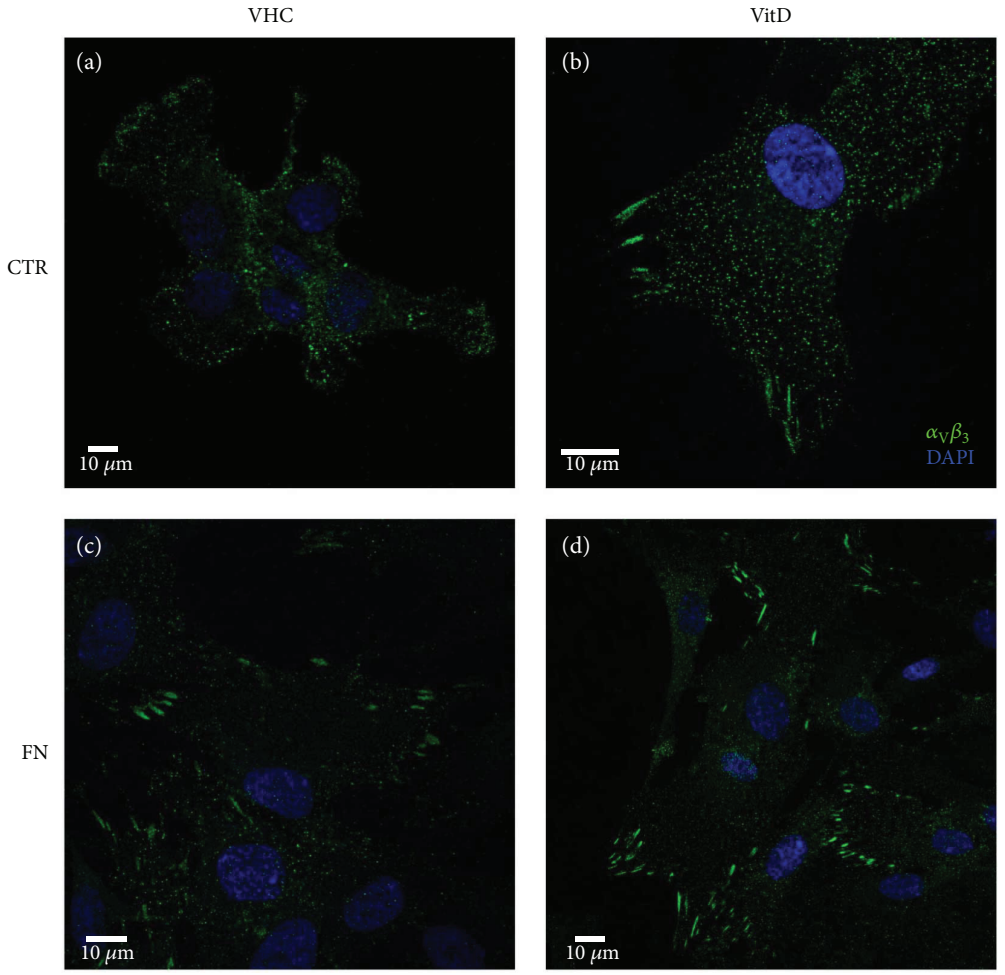

	Number of FAs per cell	Area of FA (square pixels)
VHC CTR	6.5 ± 2	88.53 ± 11.5
VHC FN	16.4 ± 3	134.65 ± 18.7
Vit D CTR	16 ± 3	109.18 ± 23.1
Vit D FN	21 ± 3	152.25 ± 19.5

Figure 2: Vit D effect on $\alpha_V\beta_3$ clustering is enhanced on FN-coated surfaces. Confocal images showing the expression of integrin $\alpha_V\beta_3$ (green) after 7 days of osteogenic differentiation. (a-b) show the integrin distribution in cells cultured on PLL coating (CTR); in the case of untreated cells (vehicle (VHC)), $\alpha_V\beta_3$ appeared to be present homogeneously in the whole cell, while Vit D treatment induced an accumulation of the receptor in the focal contacts (b–d). $\alpha_V\beta_3$ clustering was increased on FN coating (c-d), more evident in Vit D treatment (d) compared to the VHC (c). Blue for nuclei and green for $\alpha_V\beta_3$. The table shows the FA quantification performed with ImageJ software.

differentiation of DBSCs by increasing the expression of the typical osteoblastic markers. To determine if FN could influence DBSC osteoblastic features, we differentiated the cell cultures in the opportune conditions and performed a RT-PCR to evaluate the main osteoblastic markers mRNA expression.

Cells were seeded and cultured on the above-mentioned surfaces in osteogenic conditions for 12 days, in the presence or not of Vit D treatment.

Figure 4 shows that Coll I and RUNX2 mRNA levels greatly increased in the cells treated with Vit D, on control surfaces as well as on FN coating, corroborating that Vit D is able to determine the acquisition of the typical osteoblastic features in DBSCs cultured in osteogenic medium.

The effect of FN emerged by looking at the untreated samples; indeed, a significant induction of Coll I and RUNX2 mRNA expression was also observed on FN coating, when compared to CTR.

Obviously, due to the prominent effect of Vit D, the inductive influence of FN, emerged in the untreated samples, was quenched when the cells were treated with Vit D, resulting in no significant differences.

A similar trend to the one described for RUNX2 mRNA was observed at the protein level. Western blot analysis, performed after 12 days of culture, showed an increase in RUNX2 expression due to the action of Vit D, but no appreciable variation in response to FN substrate (Figure 3).

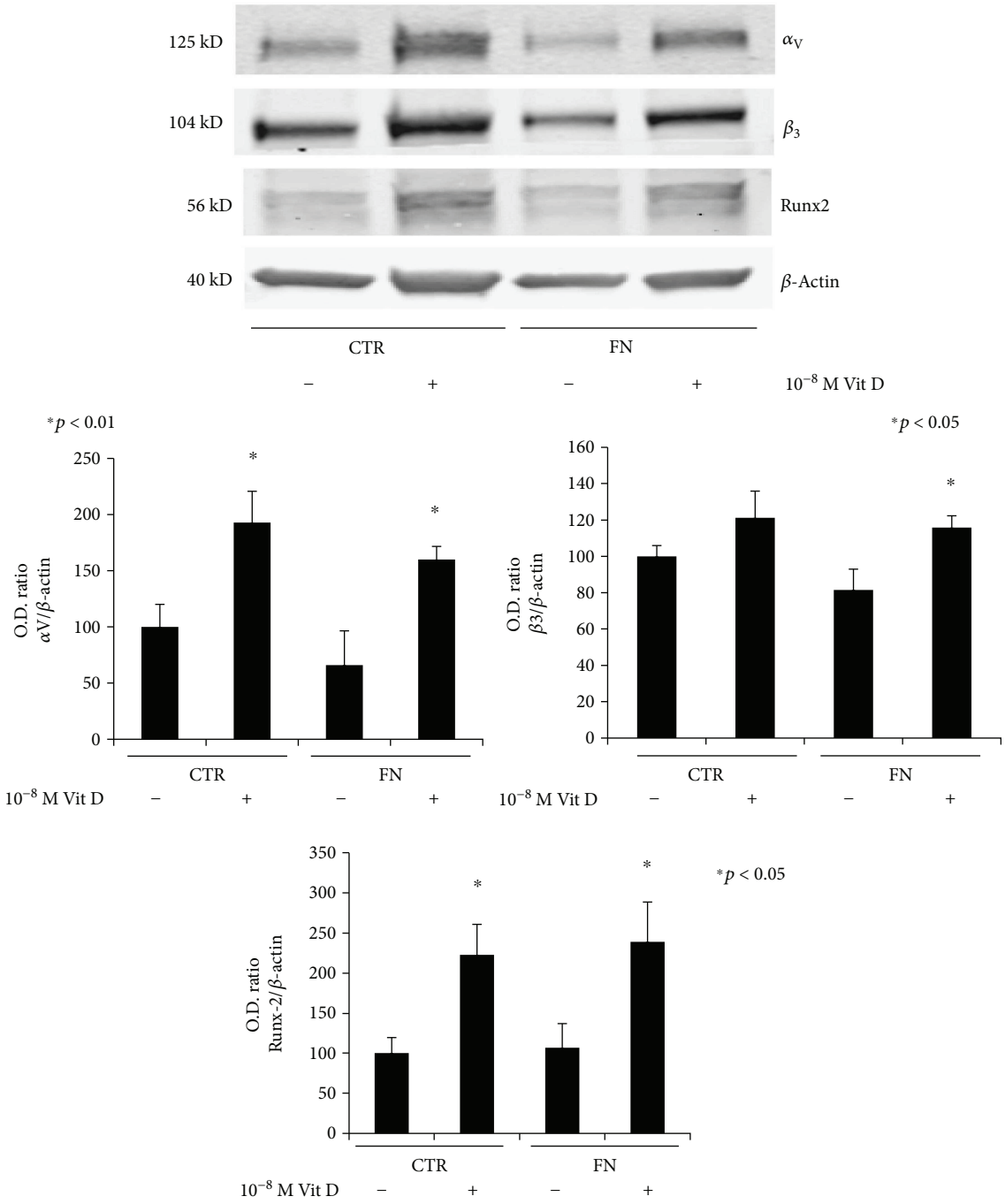

FIGURE 3: Protein expression of osteogenic markers. Immunoblots showing the expression profile of α_V, β_3, RUNX2, and Coll I in DBSCs cultured for 12 days in osteogenic medium with vehicle (–) and $1,25(OH)_2D_3$ (+), on PLL-coated surfaces (CTR) or FN-coated surfaces (FN). Each graph represents means ± SEM of 3 independent experiments.

Contrary to what was observed for Coll I and RUNX2, the increase in protein expression levels of osteopontin (OPN) can be attributed to the coating with FN and only to a lesser extent to the Vit D treatment. OPN expression in untreated cells on FN showed a 4-fold increase relative to CTR and upregulation, even more in presence of Vit D, showing more than 5-fold increase compared to CTR (Figure 3). These results are in line with those obtained in our previous report [13], according to which no particular effect on OPN expression may be attributed to the vitamin.

3. Discussion

There are not many data in the literature about the influence of Vit D in cell adhesion, but it is well known that interactions between cells and surfaces are involved in the activation

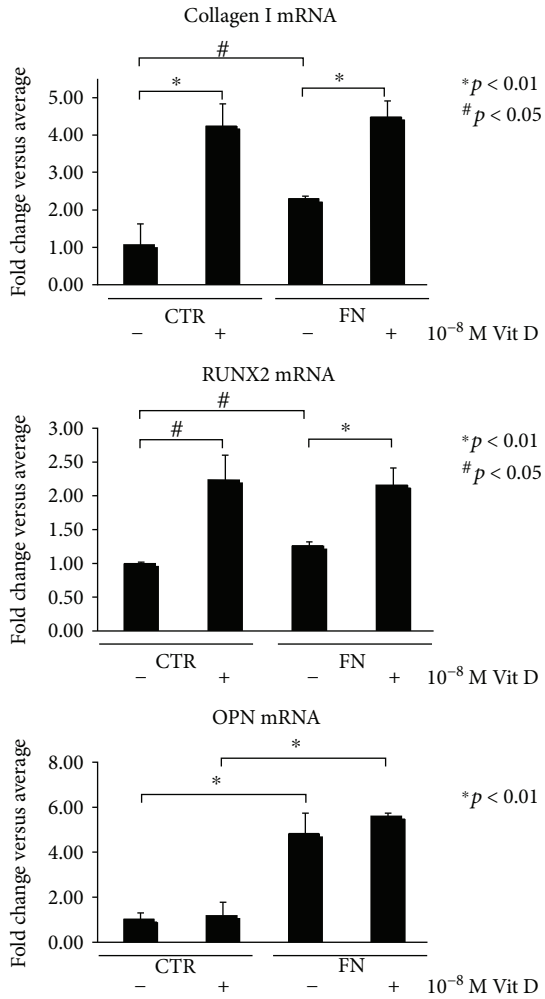

FIGURE 4: mRNA expression of osteogenic markers. qPCR analysis of Coll I, RUNX2, and OPN performed on DBSCs after 12 days of osteogenic differentiation using a medium with vehicle (–) and $1,25(OH)_2D_3$ (+), on PLL-coated surfaces (CTR) or FN-coated surfaces (FN). Expression was normalized to the average of β-actin and β_2 microglobulin (B2M) levels for each reaction. $^*p < 0.01$ and $^\#p < 0.05$.

of a series of signals that in turn are responsible for cell commitment and differentiation. Thus, a recent *in vivo* study indicated that Vit D administration decreased the serum levels of the intracellular adhesion molecules L-CAM-1 and V-CAM-1 in hemodialysis patients [30]. Since the few data available are referred only to osteoblast-like cells [15, 16], we tried to determine if Vit D might, or not, have a role also in cell adhesion mechanisms of MSCs.

In this work, we analyzed the effect of Vit D on $\alpha_V\beta_3$ integrin expression and subcellular organization in DBSCs during their osteogenic differentiation. Moreover, the effect of the molecule was evaluated on cells growing on the ECM glycoprotein FN.

We first cultured DBSCs on normal surfaces, under differentiating conditions, in the presence or not of Vit D, with the purpose to investigate whether this factor could have an effect on this integrin that has been already demonstrated to be involved in the osteogenic commitment of MSCs [12].

In this previous work, we determined that the interaction of DBSCs with ECM glycoproteins increased the osteogenic commitment and we showed that $\alpha_V\beta_3$ integrin assumed a key role in this result; in fact, the perturbation of this receptor led to a reduction of both the alkaline phosphatase (ALP) expression and the mineralization process. In the light of this knowledge, we focused our attention on $\alpha_V\beta_3$ distribution in DBSCs cultured in the presence of Vit D.

Our data indicated that $\alpha_v\beta_3$ was expressed in DBSCs cultured under osteogenic conditions, and its localization underwent changes with the advancement of the osteogenic differentiation in untreated cells, but the Vit D treatment, interestingly, enhanced $\alpha_v\beta_3$ accumulation in clusters corresponding to the adhesion sites represented by FAs (Figure 1).

Although there are many different types of integrins with specificity to different ECM proteins, a large number of cellular and biophysical studies have focused on $\alpha_5\beta_1$ and $\alpha_v\beta_3$ integrins and some of them identified in $\alpha_v\beta_3$ a valid substitute to $\alpha_5\beta_1$ for fibronectin binding [31–33]. We cultured our cell model of MSCs on FN-coated surfaces and studied the effects of Vit D on these integrin-glycoprotein interactions during osteogenic differentiation. DBSCs created a uniform monolayer after few days of culture, but we observed that the cells seeded on FN exhibited a more flattened morphology and seemed to be more numerous compared to the CTR (data not shown).

Integrins bind the ECM through their extracellular domains. Subsequently, their cluster and their short cytoplasmic tails interact with intracellular molecules for signal transduction pathway [34], giving rise to focal adhesions (FAs) [35].

Stable FAs were highlighted by immunofluorescence with $\alpha_v\beta_3$ antibody. After 7 days in culture, DBSCs treated with Vit D on FN-coated surfaces showed large and discrete $\alpha_v\beta_3$-positive clusters while a lower number of $\alpha_v\beta_3$-containing complexes could be seen in untreated cells (Figure 2).

Our findings revealed a high adhesive interaction between MSCs and FN, as also observed in other researches, confirming the mesenchymal features of DBSCs [25, 36–39].

Thus, these results are consistent with a recent study in which it has been proven that FN coating can be considered able to induce $\alpha_v\beta_3$ integrin expression in MSCs [40]. Our study goes forward identifying in Vit D a further support to the effect of FN by increasing FA formation. Our data confirmed that FN is capable of organizing $\alpha_v\beta_3$ integrin in FAs and, above all, they indicated that Vit D leads to a significant enhancement in the receptor subunit expression, contributing to its organization in clearly visible strips.

This detail is highly relevant because it is known that effective adhesion is strictly connected with cell differentiation: in particular, osteogenesis needs a large number of FAs, while both adipogenesis and chondrogenesis are promoted when the formation of strong FAs is prevented [41].

It has been previously demonstrated that DBSC osteogenic differentiation is increased by Vit D, [13]: we hypothesized that the effect of Vit D in inducing osteoblastic differentiation in our cell model could have been mediated

by an effect of the vitamin on cell adhesion. Thus, we investigated FA aspect during DBSC osteoblastic differentiation in cultures incubated with Vit D: in particular, we studied its ability to act on the expression of $\alpha_v\beta_3$ integrin which plays a pivotal role during the commitment of MSCs to osteoblast lineage. Vit D prompts the expression of $\alpha_v\beta_3$ integrin in turn favoring the formation of FAs, peculiar for MSC commitment and osteogenic differentiation: this finding is supported by the increased expression of RUNX2 and collagen I, two of the main early osteoblastic markers.

In conclusion, our results identified $\alpha_v\beta_3$ integrin as the possible mediator of Vit D effect on MSC commitment into osteoblast-like cells further demonstrating that Vit D enhanced the interaction of $\alpha_v\beta_3$ with its ECM partner FN.

The nature of FN action towards $\alpha_v\beta_3$ in MSCs is just to promote cell adhesion; in fact, FN induces integrin clustering but has no effect on its expression.

Indeed, Vit D is responsible for the $\alpha_v\beta_3$ integrin protein expression, and this is the point of force of our work: Vit D determines MSC commitment to the osteogenic lineage precisely through a modulation of the integrin receptor expression, resulting in the binding to its corresponding matrix protein.

Conflicts of Interest

The authors declare no conflicting financial or other competing interests.

Authors' Contributions

Francesca Posa and Adriana Di Benedetto contributed equally to this work.

Acknowledgments

This work was partially awarded from Ministero dell'Istruzione, dell'Università e della Ricerca—PRIN 20098KM9RN, PI Giorgio Mori (Progetto di Ricerca d'Interesse Nazionale—Grant 2009). The author Adriana Di Benedetto has received funding from the Fondo di Sviluppo e Coesione 2007-2013, APQ Ricerca Regione Puglia 'Programma regionale a sostegno della specializzazione intelligente e della sostenibilità sociale ed ambientale-Future In Research.' The article has been published with the contribution of 5x1000 IRPEF funds in favor of the University of Foggia, in the memory of Gianluca Montel.

References

[1] S. P. Bruder, D. J. Fink, and A. I. Caplan, "Mesenchymal stem cells in bone development, bone repair, and skeletal regeneration therapy," *Journal of Cellular Biochemistry*, vol. 56, no. 3, pp. 283–294, 1994.

[2] A. I. Caplan, "Mesenchymal stem cells: cell–based reconstructive therapy in orthopedics," *Tissue Engineering*, vol. 11, no. 7-8, pp. 1198–1211, 2005.

[3] J. Shao, W. Zhang, and T. Yang, "Using mesenchymal stem cells as a therapy for bone regeneration and repairing," *Biological Research*, vol. 48, no. 1, p. 62, 2015.

[4] S. Geng, S. Zhou, Z. Bi, and J. Glowacki, "Vitamin D metabolism in human bone marrow stromal (mesenchymal stem) cells," *Metabolism Clinical and Experimental*, vol. 62, no. 6, pp. 768–777, 2013.

[5] P. Liu, B. O. Oyajobi, R. G. Russell, and A. Scutt, "Regulation of osteogenic differentiation of human bone marrow stromal cells: interaction between transforming growth factor-β and 1,25$(OH)_2$ vitamin D_3*in vitro*," *Calcified Tissue International*, vol. 65, no. 2, pp. 173–180, 1999.

[6] M. van Driel, M. Koedam, C. J. Buurman et al., "Evidence that both 1α,25-dihydroxyvitamin D_3 and 24-hydroxylated D_3 enhance human osteoblast differentiation and mineralization," *Journal of Cellular Biochemistry*, vol. 99, no. 3, pp. 922–935, 2006.

[7] E. Giorgini, C. Conti, P. Ferraris et al., "FT-IR microscopic analysis on human dental pulp stem cells," *Vibrational Spectroscopy*, vol. 57, no. 1, pp. 30–34, 2011.

[8] G. Mori, G. Brunetti, A. Oranger et al., "Dental pulp stem cells: osteogenic differentiation and gene expression," *Annals of the New York Academy of Sciences*, vol. 1237, no. 1, pp. 47–52, 2011.

[9] G. Mori, M. Centonze, G. Brunetti et al., "Osteogenic properties of human dental pulp stem cells," *Journal of Biological Regulators and Homeostatic Agents*, vol. 24, no. 2, pp. 167–175, 2010.

[10] G. Mori, A. Ballini, C. Carbone et al., "Osteogenic differentiation of dental follicle stem cells," *International Journal of Medical Sciences*, vol. 9, no. 6, pp. 480–487, 2012.

[11] A. Di Benedetto, F. Posa, C. Carbone et al., "NURR1 downregulation favors osteoblastic differentiation of MSCs," *Stem Cells International*, vol. 2017, 10 pages, 2017.

[12] A. Di Benedetto, G. Brunetti, F. Posa et al., "Osteogenic differentiation of mesenchymal stem cells from dental bud: role of integrins and cadherins," *Stem Cell Research*, vol. 15, no. 3, pp. 618–628, 2015.

[13] F. Posa, A. Di Benedetto, G. Colaianni et al., "Vitamin D effects on osteoblastic differentiation of mesenchymal stem cells from dental tissues," *Stem Cells International*, vol. 2016, Article ID 9150819, 9 pages, 2016.

[14] Y. K. Wang and C. S. Chen, "Cell adhesion and mechanical stimulation in the regulation of mesenchymal stem cell differentiation," *Journal of Cellular and Molecular Medicine*, vol. 17, no. 7, pp. 823–832, 2013.

[15] P. Raz, C. H. Lohmann, J. Turner et al., "1α,25$(OH)_2D_3$ regulation of integrin expression is substrate dependent," *Journal of Biomedical Materials Research Part A*, vol. 71, no. 2, pp. 217–225, 2004.

[16] Z. Schwartz, B. F. Bell, L. Wang, G. Zhao, R. Olivares-Navarrete, and B. D. Boyan, "Beta-1 integrins mediate substrate dependent effects of 1α,25$(OH)_2D_3$ on osteoblasts," *The Journal of Steroid Biochemistry and Molecular Biology*, vol. 103, no. 3-5, pp. 606–609, 2007.

[17] S. L. Cheng, C. F. Lai, S. D. Blystone, and L. V. Avioli, "Bone mineralization and osteoblast differentiation are negatively modulated by integrin $\alpha v\beta 3$," *Journal of Bone and Mineral Research*, vol. 16, no. 2, pp. 277–288, 2001.

[18] S. F. El-Amin, M. Attawia, H. H. Lu et al., "Integrin expression by human osteoblasts cultured on degradable polymeric materials applicable for tissue engineered bone," *Journal of Orthopaedic Research*, vol. 20, no. 1, pp. 20–28, 2002.

[19] Z. Hamidouche, O. Fromigue, J. Ringe et al., "Priming integrin alpha5 promotes human mesenchymal stromal cell osteoblast differentiation and osteogenesis," *Proceedings of the National Academy of Sciences of the United States of America*, vol. 106, no. 44, pp. 18587–18591, 2009.

[20] G. B. Schneider, R. Zaharias, and C. Stanford, "Osteoblast integrin adhesion and signaling regulate mineralization," *Journal of Dental Research*, vol. 80, no. 6, pp. 1540–1544, 2001.

[21] S. H. Kim and S. H. Kim, "Antagonistic effect of EGF on FAK phosphorylation/dephosphorylation in a cell," *Cell Biochemistry & Function*, vol. 26, no. 5, pp. 539–547, 2008.

[22] S. Gronthos, K. Stewart, S. E. Graves, S. Hay, and P. J. Simmons, "Integrin expression and function on human osteoblast-like cells," *Journal of Bone and Mineral Research*, vol. 12, no. 8, pp. 1189–1197, 1997.

[23] B. Geiger, J. P. Spatz, and A. D. Bershadsky, "Environmental sensing through focal adhesions," *Nature Reviews Molecular Cell Biology*, vol. 10, no. 1, pp. 21–33, 2009.

[24] M. R. Morgan, A. Byron, M. J. Humphries, and M. D. Bass, "Giving off mixed signals—distinct functions of $\alpha_5\beta_1$ and $\alpha_v\beta_3$ integrins in regulating cell behaviour," *IUBMB Life*, vol. 61, no. 7, pp. 731–738, 2009.

[25] E. H. Schwab, M. Halbig, K. Glenske, A. S. Wagner, S. Wenisch, and E. A. Cavalcanti-Adam, "Distinct effects of RGD-glycoproteins on integrin-mediated adhesion and osteogenic differentiation of human mesenchymal stem cells," *International Journal of Medical Sciences*, vol. 10, no. 13, pp. 1846–1859, 2013.

[26] P. Roca-Cusachs, N. C. Gauthier, A. del Rio, and M. P. Sheetz, "Clustering of $\alpha_5\beta_1$ integrins determines adhesion strength whereas $\alpha_v\beta_3$ and talin enable mechanotransduction," *Proceedings of the National Academy of Sciences of United States of America*, vol. 106, no. 38, pp. 16245–16250, 2009.

[27] O. Fromigué, J. Brun, C. Marty, S. Da Nascimento, P. Sonnet, and P. J. Marie, "Peptide-based activation of alpha5 integrin for promoting osteogenesis," *Journal of Cellular Biochemistry*, vol. 113, no. 9, pp. 3029–3038, 2012.

[28] C. F. Lai and S. L. Cheng, "Alphavbeta integrins play an essential role in BMP-2 induction of osteoblast differentiation," *Journal of Bone and Mineral Research*, vol. 20, no. 2, pp. 330–340, 2005.

[29] C. Damsky, "Extracellular matrix–integrin interactions in osteoblast function and tissue remodeling," *Bone*, vol. 25, no. 1, pp. 95-96, 1999.

[30] A. E. Naeini, F. Moeinzadeh, S. Vahdat, A. Ahmadi, Z. P. Hedayati, and S. Shahzeidi, "The effect of vitamin D administration on intracellular adhesion molecule-1 and vascular cell adhesion molecule-1 levels in hemodialysis patients: a placebo-controlled, double-blinded clinical trial," *Journal of Research in Pharmacy Practice*, vol. 6, no. 1, pp. 16–20, 2017.

[31] E. H. J. Danen, P. Sonneveld, C. Brakebusch, R. Fässler, and A. Sonnenberg, "The fibronectin-binding integrins $\alpha5\beta1$ and $\alpha v\beta3$ differentially modulate RhoA–GTP loading, organization of cell matrix adhesions, and fibronectin fibrillogenesis," *Journal of Cell Biology*, vol. 159, no. 6, pp. 1071–1086, 2002.

[32] K. Wennerberg, L. Lohikangas, D. Gullberg, M. Pfaff, S. Johansson, and R. Fiissler, "Beta 1 integrin-dependent and -independent polymerization of fibronectin," *Journal of Cell Biology*, vol. 132, no. 1, pp. 227–238, 1996.

[33] J. T. Yang and R. O. Hynes, "Fibronectin receptor functions in embryonic cells deficient in alpha 5 beta 1 integrin can be replaced by alpha V integrins," *Molecular Biology of the Cell*, vol. 7, no. 11, pp. 1737–1748, 1996.

[34] M. A. Schwartz, "Integrin signaling revisited," *Trends in Cell Biology*, vol. 11, no. 12, pp. 466–470, 2001.

[35] A. Shekaran and A. J. Garcia, "Extracellular matrix-mimetic adhesive biomaterials for bone repair," *Journal of Biomedical Materials Research Part A*, vol. 96A, no. 1, pp. 261–272, 2011.

[36] S. Gronthos, P. J. Simmons, S. E. Graves, and P. G. Robey, "Integrin-mediated interactions between human bone marrow stromal precursor cells and the extracellular matrix," *Bone*, vol. 28, no. 2, pp. 174–181, 2001.

[37] R. F. Klees, R. M. Salasznyk, K. Kingsley, W. A. Williams, A. Boskey, and G. E. Plopper, "Laminin-5 induces osteogenic gene expression in human mesenchymal stem cells through an ERK-dependent pathway," *Molecular Biology of the Cell*, vol. 16, no. 2, pp. 881–890, 2005.

[38] S. Lavenus, P. Pilet, J. Guicheux, P. Weiss, G. Louarn, and P. Layrolle, "Behaviour of mesenchymal stem cells, fibroblasts and osteoblasts on smooth surfaces," *Acta Biomaterialia*, vol. 7, no. 4, pp. 1525–1534, 2011.

[39] A. Ode, G. N. Duda, J. D. Glaeser et al., "Toward biomimetic materials in bone regeneration: functional behavior of mesenchymal stem cells on a broad spectrum of extracellular matrix components," *Journal of Biomedical Materials Research Part A*, vol. 95A, no. 4, pp. 1114–1124, 2010.

[40] H.-S. Hung, C.-M. Tang, C.-H. Lin et al., "Biocompatibility and favorable response of mesenchymal stem cells on fibronectin-gold nanocomposites," *PLoS One*, vol. 8, no. 6, article e65738, 2013.

[41] P. S. Mathieu and E. G. Loboa, "Cytoskeletal and focal adhesion influences on mesenchymal stem cell shape, mechanical properties, and differentiation down osteogenic, adipogenic, and chondrogenic pathways," *Tissue Engineering Part B: Reviews*, vol. 18, no. 6, pp. 436–444, 2012.

Hindawi
Stem Cells International
Volume 2018, Article ID 6913594, 14 pages
https://doi.org/10.1155/2018/6913594

Research Article

TGFβ1-Induced Differentiation of Human Bone Marrow-Derived MSCs Is Mediated by Changes to the Actin Cytoskeleton

Mona Elsafadi,[1,2,3] Muthurangan Manikandan,[1] Sami Almalki,[4] Mohammad Mobarak,[5] Muhammad Atteya,[1,6] Zafar Iqbal,[7] Jamil Amjad Hashmi,[8] Sameerah Shaheen,[1] Nehad Alajez,[1] Musaad Alfayez,[1] Moustapha Kassem,[1,2,3] Raed Abu Dawud,[9] and Amer Mahmood[1]

[1]*Stem Cell Unit, Department of Anatomy, College of Medicine, King Saud University, Riyadh, Saudi Arabia*
[2]*KMEB, Department of Endocrinology, University Hospital of Odense, Odense, Denmark*
[3]*KMEB, Department of Endocrinology, University of Southern Denmark, Odense, Denmark*
[4]*College of Agriculture, King Saud University, Riyadh, Saudi Arabia*
[5]*Department of Histopathology, College of Medicine, King Saud University, Riyadh, Saudi Arabia*
[6]*Department of Histology, Faculty of Medicine, Cairo University, Cairo, Egypt*
[7]*Department of Basic Sciences, College of Applied Medical Sciences, King Saud Bin Abdulaziz University for Health Sciences (KSAU-HS), National Guard Health Affairs, Al Ahsa, Saudi Arabia*
[8]*Center for Genetics and Inherited Diseases, Taibah University, Medina, Al Madinah, Saudi Arabia*
[9]*Department of Comparative Medicine, King Faisal Specialist Hospital and Research Centre, Riyadh, Saudi Arabia*

Correspondence should be addressed to Amer Mahmood; ammahmood@ksu.edu.sa

Received 26 September 2017; Accepted 23 November 2017; Published 15 February 2018

Academic Editor: Andrea Ballini

Copyright © 2018 Mona Elsafadi et al. This is an open access article distributed under the Creative Commons Attribution License, which permits unrestricted use, distribution, and reproduction in any medium, provided the original work is properly cited.

TGFβ is a potent regulator of several biological functions in many cell types, but its role in the differentiation of human bone marrow-derived skeletal stem cells (hMSCs) is currently poorly understood. In the present study, we demonstrate that a single dose of TGFβ1 prior to induction of osteogenic or adipogenic differentiation results in increased mineralized matrix or increased numbers of lipid-filled mature adipocytes, respectively. To identify the mechanisms underlying this TGFβ-mediated enhancement of lineage commitment, we compared the gene expression profiles of TGFβ1-treated hMSC cultures using DNA microarrays. In total, 1932 genes were upregulated, and 1298 genes were downregulated. Bioinformatics analysis revealed that TGFβl treatment was associated with an enrichment of genes in the skeletal and extracellular matrix categories and the regulation of the actin cytoskeleton. To investigate further, we examined the actin cytoskeleton following treatment with TGFβ1 and/or cytochalasin D. Interestingly, cytochalasin D treatment of hMSCs enhanced adipogenic differentiation but inhibited osteogenic differentiation. Global gene expression profiling revealed a significant enrichment of pathways related to osteogenesis and adipogenesis and of genes regulated by both TGFβ1 and cytochalasin D. Our study demonstrates that TGFβ1 enhances hMSC commitment to either the osteogenic or adipogenic lineages by reorganizing the actin cytoskeleton.

1. Introduction

Fat and bone tissues both originate from bone marrow progenitor cells called skeletal stem cells, also known as bone marrow-derived multipotent stromal cells or mesenchymal stem cells (MSCs). The formation of these tissues is regulated throughout an organism's lifetime by homeostatic mechanisms within the marrow cavity. It has been suggested that an imbalance between osteogenic and adipogenic lineage commitment and differentiation is

responsible for age-related impairment of bone formation, and a number of therapeutic interventions targeting and activating MSCs, thus enhancing bone mass, have been proposed. Indeed, the identification of novel strategies to steer human skeletal (mesenchymal) stem cell differentiation towards the production of osteoblastic cells, thus increasing bone formation, is very topical in the bone biology field.

The transforming growth factor (TGF) superfamily consists of over 40 members, including activins, inhibins, bone morphogenetic proteins (BMPs), growth and differentiation factors (GDFs), and TGFβs [1]. TGF family members are multifunctional regulators of cell growth and differentiation, playing pivotal roles during embryonic development, organogenesis, and tissue homeostasis [2]. The cytokine TGFβ1 is among the most abundant in bone matrix [3] and is secreted by endothelial cells, epithelial cells, fibroblasts, smooth muscle cells, and most immune cells [4]. TGFβ1 is deposited in bone matrix as an inactive, latent complex with latency-associated protein (LAP), the binding of which masks the receptor domains of active TGFβ1. During bone formation, osteoclast-mediated bone resorption activates TGFβ1 by cleaving LAP and releasing it from bone matrix, thus creating a transient gradient of active TGFβ1 that attracts MSCs to bone remodeling sites, where they undergo osteoblastic differentiation [5]. Furthermore, TGFβ1 is known to regulate the proliferation and differentiation of osteoprogenitor cells [6].

Actin microfilaments are composed of polymers of actin, the most abundant cellular protein which also forms the thinnest part of the cytoskeleton, and are primarily responsible for skeletal structure [7]. Cellular actin exists in two forms, filamentous polymerized actin (F-actin) and globular/monomer depolymerized actin (G-actin), and transitions between these forms during highly dynamic intracellular polymerization and depolymerization processes [8]. In mammals, actin polymerization factors regulate actin polymerization and depolymerization [9]. While the stiffness of actin is lower than that of microtubules, actin molecules form a highly organized structural network, supported by a large number of interacting cross-linking proteins, which together confer a substantial amount of mechanical strength [10]. The cytoskeleton is known to be important for determining cell morphology and for mediating changes in adhesion and differentiation [11]. Indeed, during human MSC (hMSC) lineage commitment, cells undergo significant morphological changes and actin cytoskeletal reorganization which contribute to the determination of cellular fate [7, 12].

In this study, we investigated the effect of TGFβ-induced actin cytoskeleton modifications on the potential of hMSCs to differentiate into osteogenic and adipogenic lineages, as well as the effect of the actin polymerization inhibitor cytochalasin D (CYD). Our data suggest that TGFβ-induced actin cytoskeleton reorganization is a prerequisite for hMSC differentiation into osteocytic or adipocytic lineages.

2. Results

2.1. TGFβ1 Treatment Enhanced the Osteogenic Differentiation of hMSCs. A single treatment with TGFβ1 (10 ng/ml, for 2 days) enhanced hMSC osteogenic differentiation, as shown by the increased mineralized matrix formation made evident by alizarin red S staining (Figures 1(a) and 1(b)). Conversely, when TGFβ1 signaling was blocked with the inhibitor SB-431542 (10 μM), significantly lower mineralized matrix formation was observed (Figures 1(a) and 1(b)). Consistent with this, higher expression of the osteoblastic genes alkaline phosphatase (*ALP*), runt-related transcription factor 2 (*RUNX2*), and osteocalcin (*OCN*) was observed in hMSCs undergoing osteogenic differentiation in the presence of TGFβ1, while treatment with the TGFβ1 inhibitor SB-431542 severely inhibited this expression (Figure 1(c)).

2.2. TGFβ1 Treatment Enhanced the Adipogenic Differentiation of hMSCs. Next, we examined the effect of treating hMSCs with a single dose of TGFβ1 (10 ng/ml, for 2 days) on adipogenic differentiation. We found that adipogenic differentiation was enhanced following TGFβ1 treatment, as shown by an increase in the number of lipid-filled adipocytes (Figures 1(d) and 1(e)). Similarly, the expression of several adipogenic gene markers, including lipoprotein lipase (*LPL*), peroxisome proliferator-activated receptor gamma 2 (*PPARG-2*), adipocyte protein 2 (*aP2*), and *ADIPOQ*, was upregulated following TGFβ1 treatment, while treatment with SB-431542 reversed these effects (Figure 1(f)).

2.3. TGFβ1 Stimulation Has No Effect on hMSC Viability or Proliferation. The effect of TGFβ1 on hMSC cell viability was assessed using alamarBlue assay reagent. No significant effect on viability was observed after 4 days of treatment (Figure 2(a)). To investigate the effect of TGFβ1 on cellular proliferation, we used the xCELLigence RTCA DP® cell proliferation assay system, which allows the continuous monitoring of cell numbers over time. As shown in Figure 2(b), there was no measurable difference in hMSC proliferation in the presence or absence of TGFβ1.

2.4. Molecular Phenotype of TGFβ1-Treated hMSCs. To understand the molecular mechanisms underlying the TGFβl-mediated regulation of hMSC differentiation, we compared global gene expression in TGFβl-treated hMSCs and vehicle-treated control cells using microarray analysis. In total, 1932 gene transcripts were significantly upregulated, and 1298 were significantly downregulated following TGFβl treatment. Significant changes were defined as a fold change ≥ 2, $p < 0.05$ and are listed in Supplementary Tables S1 and S2. Hierarchical clustering of differentially expressed genes revealed a clear distinction between TGFβl-treated and control samples (Figure 3(a)). Next, we used performed gene ontology analysis to identify the biological processes that were favored following TGFβl treatment. We found that the genes that were significantly altered in TGFβl-treated MSCs were enriched within several skeletal and extracellular matrix categories, including extracellular matrix (53 genes), extracellular matrix organization (51 genes), and proteinaceous extracellular matrix (Supplementary Table S3). Furthermore, pathway analysis of significantly changed genes revealed the significant enrichment of several signaling pathways in TGFβl-treated hMSCs. Among these, the most

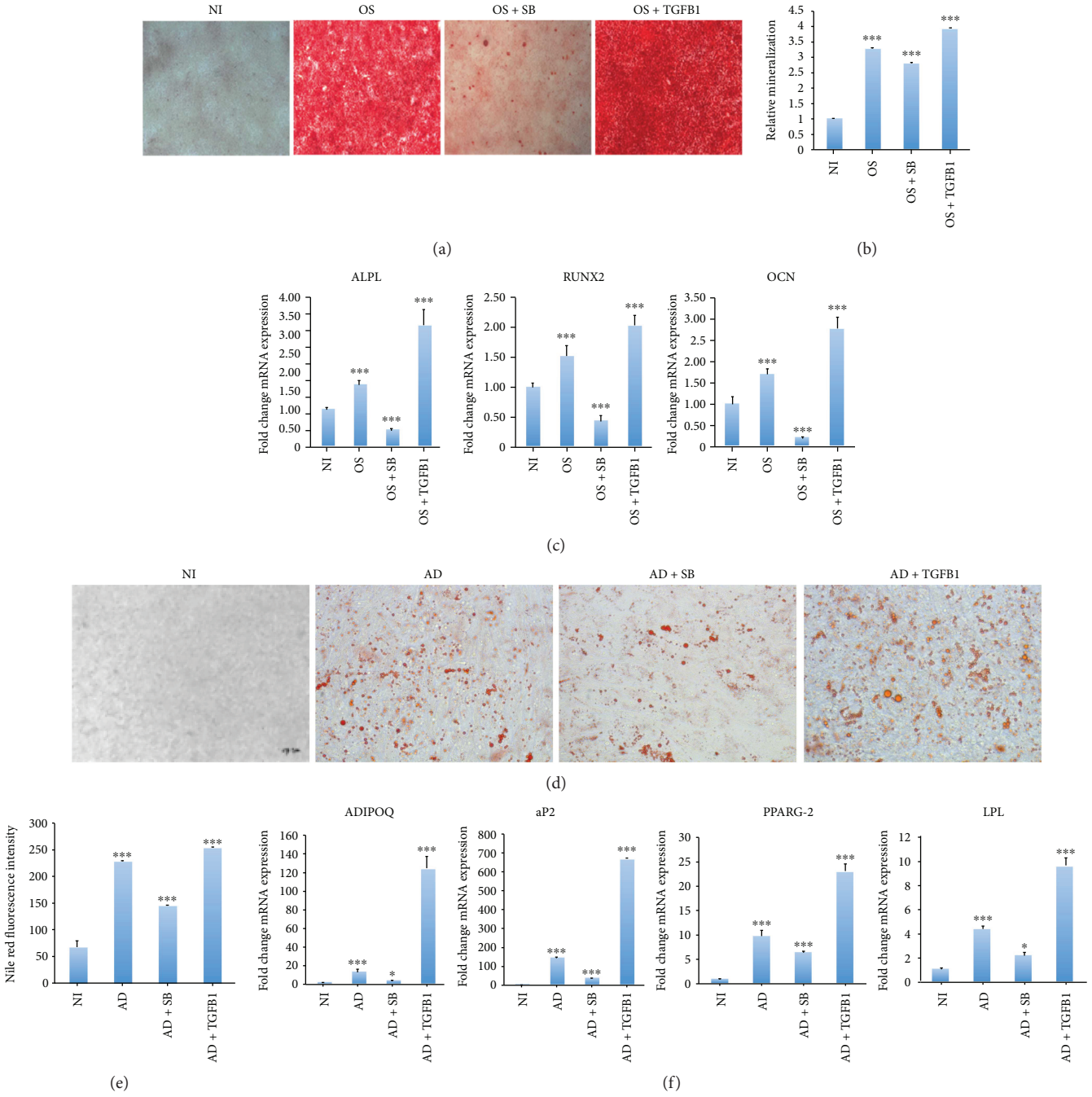

FIGURE 1: TGFβ1 induces osteogenic and adipogenic differentiation. MSCs underwent osteogenic or adipogenic differentiation by culturing cells in the appropriate medium for 7 days. (a) Micrographs showing the degree of mineralized calcium deposition in noninduced cells (NI), osteoinduced cells (OS), osteoinduced cells + SB-431542 (OS + SB), and osteoinduced cells + TGFβ1 (OS + TGFB), as assessed by alizarin red S staining (20x magnification). (b) Quantification of mineralization in the alizarin red S stained groups shown in (a). Data are shown as the mean ± SD of three independent experiments ($^{***}p < 0.005$). (c) mRNA expression of the osteogenic markers *ALPL*, *RUNX2*, and *OCN*, normalized to GAPDH, as determined by RT-PCR. Data are shown as the mean ± SD of three independent experiments ($^{*}p < 0.05$; $^{***}p < 0.0005$). (d) Micrographs showing the accumulation of lipid droplets in noninduced cells (NI), adipoinduced cells (AD), adipoinduced cells + SB-431542 (AD + SB), and adipoinduced cells + TGFβ1 (AD + TGFB), as determined by Oil red O staining (20x magnification). (e) Quantification of mature adipocytes in the NI, AD, AD + SB, and AD + TGFB groups, as determined by Nile red fluorescence intensity. Data are shown as the mean ± SD of three independent experiments ($^{***}p < 0.005$). (f) mRNA expression of the adipogenic markers *LPL*, *aP2*, *PPARG-2*, and *ADIPOQ*, normalized to GAPDH, as determined by RT-PCR. Data are shown as the mean ± SD of three independent experiments ($^{*}p < 0.05$; $^{***}p < 0.0005$).

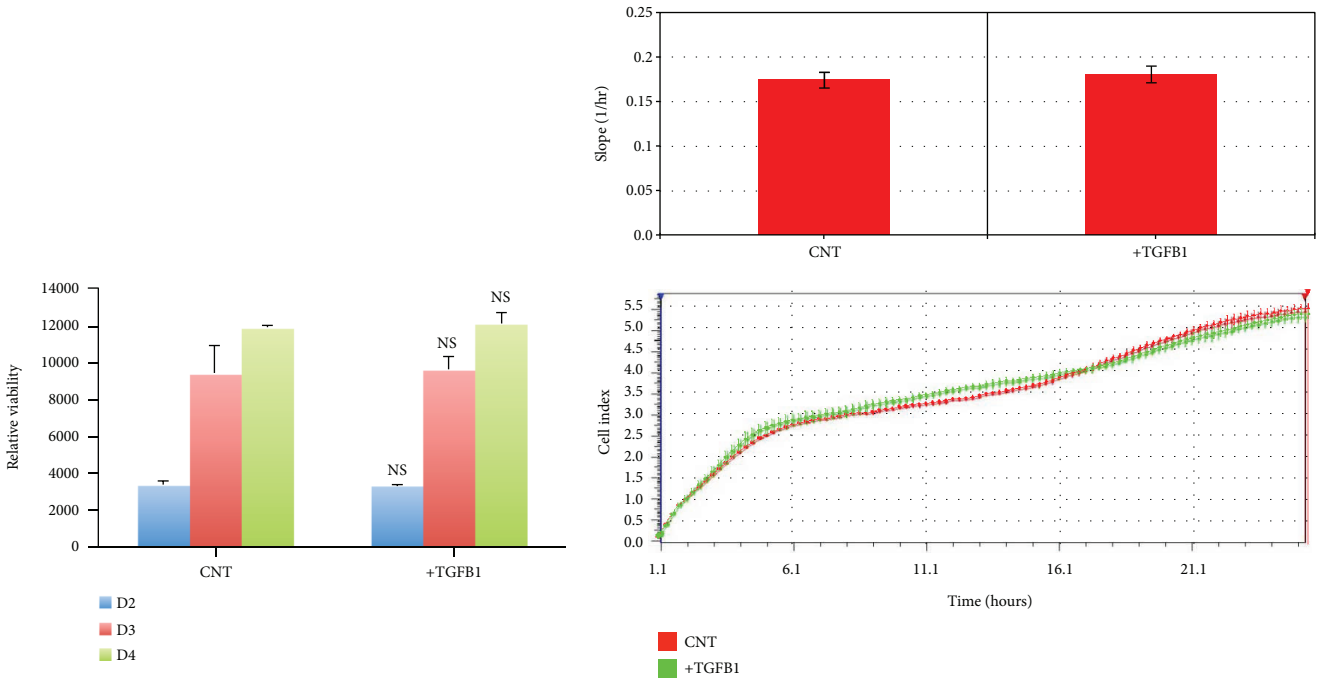

Figure 2: TGFβ1 does not affect hMSC proliferation or viability. (a) Chart showing the relative hMSC viability in the absence (CNT) or presence (TGFB1) of TGFβ1, as determined by alamarBlue assay reagent. Shown are cell viabilities on days 2 (D2), 3 (D3), and 4 (D4) of culture. (b) Real-time proliferation assay data using the xCELLigence RTCA DP system for hMSC cells with and without TGFβ1 treatment. Lower panel: cell proliferation was measured at 15-minute intervals for a total duration of 24 hours. Upper panel: summary data showing cellular proliferation after 24 hours. Data are shown as the mean ± SD of two independent experiments ($n = 6$). NS: not significant.

enriched pathways were "regulation of actin cytoskeleton," "MAPK signaling," "focal adhesion," "TGFβ1 signaling," "adipogenesis," "endochondral ossification," and "osteoblast signaling" (Figure 3(b)). Table 1 lists the genes within osteogenesis- and adipogenesis-related signaling pathways that were upregulated in TGFβ1-treated cells. A selected panel of genes known to be involved in cell differentiation and TGFβ signaling that were significantly changed in the microarray data were examined by qRT-PCR. In general, a good degree of concordance was observed between the microarray and qRT-PCR data (Figure 3(c)).

2.5. Actin Microfilaments in MSCs Are Altered following Treatment with TGFβ1 or the Actin Polymerization Inhibitor CYD. Our molecular phenotyping analysis of TGFβl-treated hMSCs revealed a significant enrichment of genes associated with cytoskeletal changes. Based on this, and on our previous observations that TGFβl treatment triggers significant morphological changes in hMSCs, we examined the effect of TGFβl on the cytoskeleton using transmission electron microscopy (TEM), which has the power to reveal structural changes in actin microfilaments. Actin microfilament polymerization was found to be inhibited in cells treated with either the potent actin polymerization inhibitor CYD or the TGFβ inhibitor SB-431542. In contrast, TGFβ1 treatment was associated with a prominent distribution of actin filaments, organized as bundles/aggregates, in the perinuclear area and at one cell pole (Figure 4). The ultrastructural characteristics of the cells under the various treatment conditions are summarized in Supplementary Table S4.

2.6. CYD Regulates Osteogenic and Adipogenic Differentiation in the Presence of TGFβ1. To confirm that TGFβ1 regulates actin cytoskeletal dynamics, hMSCs undergoing either osteogenic or adipogenic differentiation were treated with TGFβ1 in the absence or presence of the actin polymerization inhibitor CYD. CYD treatment significantly inhibited hMSC osteogenic differentiation in both the presence and absence of TGFβl, as shown by reduced mineralization (Figure 5(a)). Similarly, expression of the osteogenic marker genes *ALPL*, *RUNX2*, and *OCN* was inhibited by CYD treatment, with and without TGFβl (Figure 5(b)). Conversely, CYD treatment enhanced hMSC adipogenic differentiation, as shown by a greatly increased number of lipid-filled mature adipocytes and the increased expression of the adipogenic marker genes *LPL* and *PPARG-2*. These effects were maintained when cells were treated concomitantly with TGFβl (Figures 5(c) and 5(d)).

2.7. Molecular Phenotype of CYD-Treated Cells. The data presented above suggest that CYD and TGFβ1 target similar molecular pathways during hMSC osteogenic and adipogenic differentiation. In order to investigate this further and to elucidate the molecular mechanisms underlying the CYD-

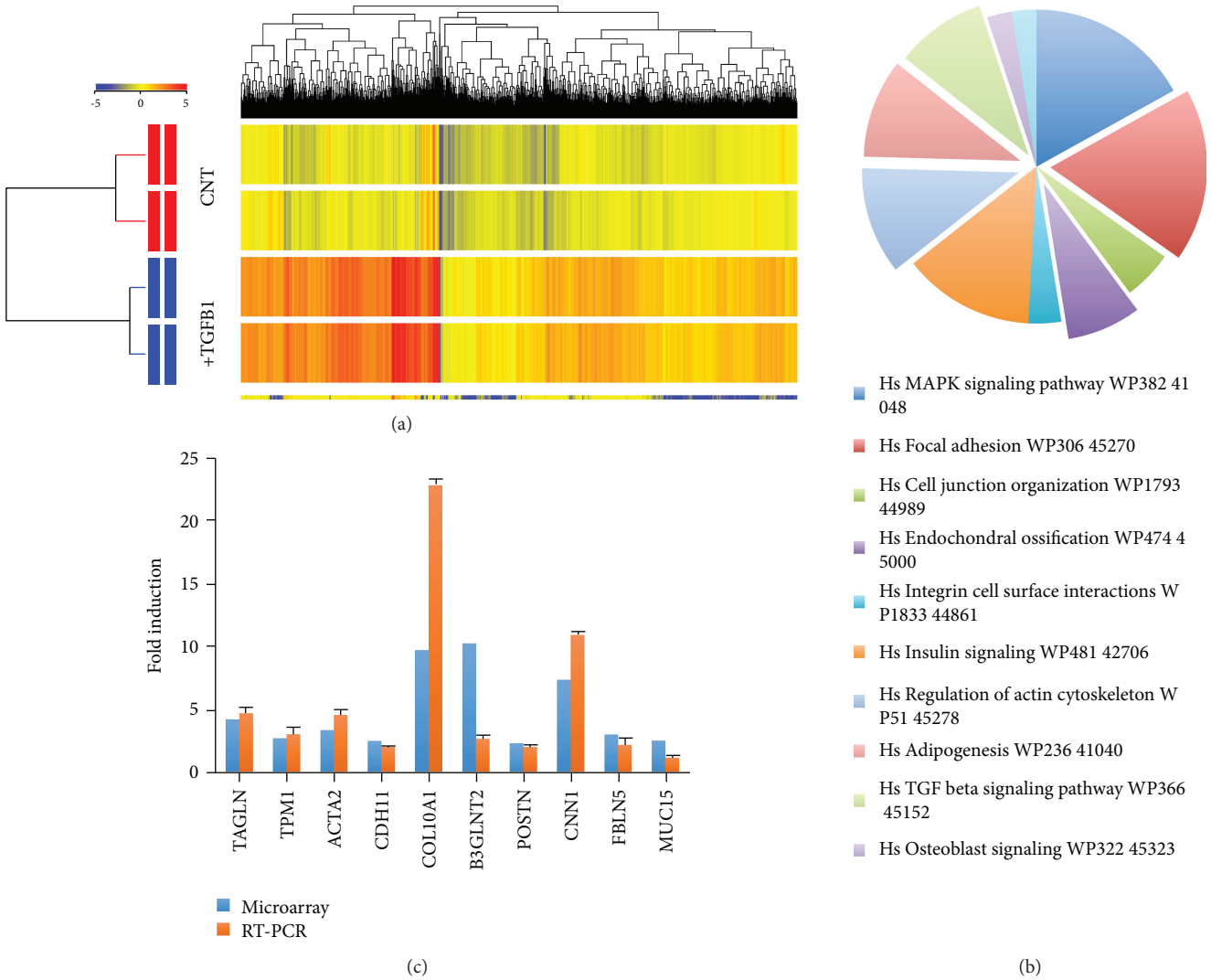

Figure 3: Molecular phenotype of TGFβ1-treated hMSCs. (a) Hierarchical clustering of genes that were differentially expressed in TGFβl-treated and untreated control (CNT) hMSCs. Rows represent individual gene expression for duplicate treated and untreated samples, as indicated. Columns represent individual transcripts. Relative expression levels are presented colorimetrically, according to the scale shown in the color bar. (b) Pie chart showing the pathways with the highest enrichment of genes significantly upregulated in TGFβ1-treated cells. (c) qRT-PCR validation of selected genes that were upregulated in the microarray data ($n = 3$, $^{*}p < 005$; $^{***}p < 0001$). Cells treated with vehicle (DMSO) were used as controls.

mediated effects on hMSC differentiation, microarray analysis was performed to establish global gene expression profiles for CYD-treated and controls cells. In total, 10,855 genes were significantly upregulated, and 2523 genes were significantly downregulated following CYD treatment. Genes were defined as significantly changed if they had a fold change ≥ 2 and $p < 0.05$ and are listed in Supplementary Tables S5 and S6. As was seen with TGFβ1 treatment, hierarchical clustering of the differentially expressed genes revealed a clear distinction between untreated and CYD-treated hMSCs (Figure 6(a)). Pathway analysis of these genes revealed several molecular pathways that were enriched upon CYD treatment (Figure 6(b)). Among the most significant were pathways involved in the regulation of the actin cytoskeleton, focal adhesion signaling, endochondral ossification, TGFβ1 signaling, regulation of the microtubule cytoskeleton, and MAPK signaling (Figure 6(b)). The genes that are associated with these pathways that were upregulated in CYD-treated cells are listed in Table 2. Forty-two genes that are involved in adipogenesis-related pathways were significantly enriched in CYD-treated cells (Table 3). Interestingly, 218 genes were both upregulated in TGFβ1-treated hMSCs and downregulated in CYD-treated hMSCs (Figure 6(c)), showing that the molecular signature on CYD treatment is the inverse of that seen with TGFβ1 treatment and suggesting that these genes may be involved in TGFβ-mediated cytoskeletal reorganization (Table 4).

3. Discussion

TGFβ is a potent regulator of various biological functions in many cell types, but its effects on hMSC differentiation are, to

Table 1: Osteogenesis- and adipogenesis-related genes, from the most enriched pathways, that are upregulated in TGFβ1-treated cells.

Endochondral ossification	Actin cytoskeleton	Focal adhesion	TGFβ signaling	MAPK signaling	Adipogenesis
VEGFA	FGF2	COL11A1	SMURF1	MAPK8	FOXO1A
ADAMTS4	FGFR1	COL3A1	MAPK8	NGFB	TRIB3
PLAT4	TMSB4X	COL4A1	SKP1	PDGFRB	PCK2
COL10A1	GNA13	COL4A2	NEDD9	RASA2	EGR2
TGFB2	PDGFA	COL4A4	ETS1	SOS2	DDIT3
PTHrP	FGF1	COL5A1	KLF11	KRAS	GADD45A
FGF2	ENAH	COL5A2	ATF3	MRAS	GADD45B
C4ST1	MSN	COL1A1	FOSB	NF1	HIF1A
FGFR1	GSN	LAMC2	SKIL	RAP1B	IRS1
PDGFRB	PDGFRB	THBS2	SMURF1	DUSP1	MEF2D
COL1	KRAS	CAV2	ZFYVE16	DDIT3	FAS
	MRAS	ARHGAP5		HSPB1	SPOCK
	SOS2	PTEN		IL1A	
		AKT3		FAS	
		PDGFA		TGFB2	
		PDGFC		MAP313	
		PGF		ZAK	
		ITGA2		AKT3	
		PDGFRB		MAP3K8	
		RAP1B		GADD45A	
		MAPK8			

date, poorly understood. In the present study, we contribute to this understanding and demonstrate that TGFβ can enhance both osteoblastic and adipocytic lineage commitment by modulating changes to the actin cytoskeleton.

TGFβ1 is known to regulate the proliferation and differentiation of osteoprogenitor cells [6, 13–15], and it reportedly stimulates bone matrix apposition and bone cell replication [16]. Several studies have demonstrated that TGFβ1 promotes bone formation *in vitro* by recruiting osteoblast progenitors and inducing bone matrix formation at early stages of differentiation. In addition to this direct regulation of bone formation, TGFβ1, along with BMPs, enhances *RUNX2* expression at early differentiation stages [17]. This is consistent with our finding that TGFβ1 promoted osteogenesis and was associated with the upregulation of the osteogenic genes *ALPL*, *RUNX2*, and *OCN*.

Furthermore, we showed that TGF-β1 treatment enhanced the *in vitro* adipocytic differentiation of hMSCs. This is consistent with several previously reported studies which demonstrate that TGFβ1 has a positive effect on adipogenic differentiation under specific culture conditions [18, 19]; an early study considering rat brown adipocytes showed an upregulation of lipogenic enzymes following TGFβ1 treatment [19].

Our results showed that TGFβ1 treatment did not affect MSC cell growth *in vitro*. Previously, conflicting results have been published; some studies reported that TGFβ1 regulated osteoprogenitor proliferation *in vitro* [13, 20], whereas Yu et al. reported that TGFβ1 treatment strongly inhibited the proliferation of human lung epithelial cells [21]. The mitogenic effects of TGFβ on cells are reportedly variable; while progressive mitogenesis was stimulated in confluent cells following treatment with 0.15–15 ng/ml TGFβ, in sparse cultures 0.15 ng/ml TGFβ exhibited inhibitory effects. However, at all cell densities, 15 ng/ml TGFβ stimulated collagen synthesis, with this effect being most pronounced when DNA synthesis was declining [22]. Most of the published data on TGFβ has shown a mitogenic effect on osteoprogenitors [16, 23–26], but relatively few studies have examined the growth inhibitory effect of this cytokine on osteoblast-like cells [27, 28]. It is likely that these contradictory observations reflect the fact that the effect TGFβ has on cellular proliferation is dependent upon TGFβ concentration, culture conditions including cell density, the cell model system (tumorigenic versus nontumorigenic), the differentiation stage of the target cell population, and/or the presence of other growth factors.

The cytoskeleton is known to be important for cell morphology and for mediating changes in adhesion and differentiation [11]. Furthermore, significant changes in cytoskeletal components reportedly occur during hMSC lineage commitment and differentiation [7, 11]. While changes in cell shape can be influenced by differentiation, several studies have shown that the differentiation of precommitted mesenchymal stem cells is itself influenced by changes in cellular morphology resulting from the altered expression of cadherins, integrins, and cytoskeletal proteins [29]. Recently, the inhibition of actin depolymerization was shown to enhance both hMSC differentiation into osteoblasts and *in vivo* bone formation, with these effects being mediated by several

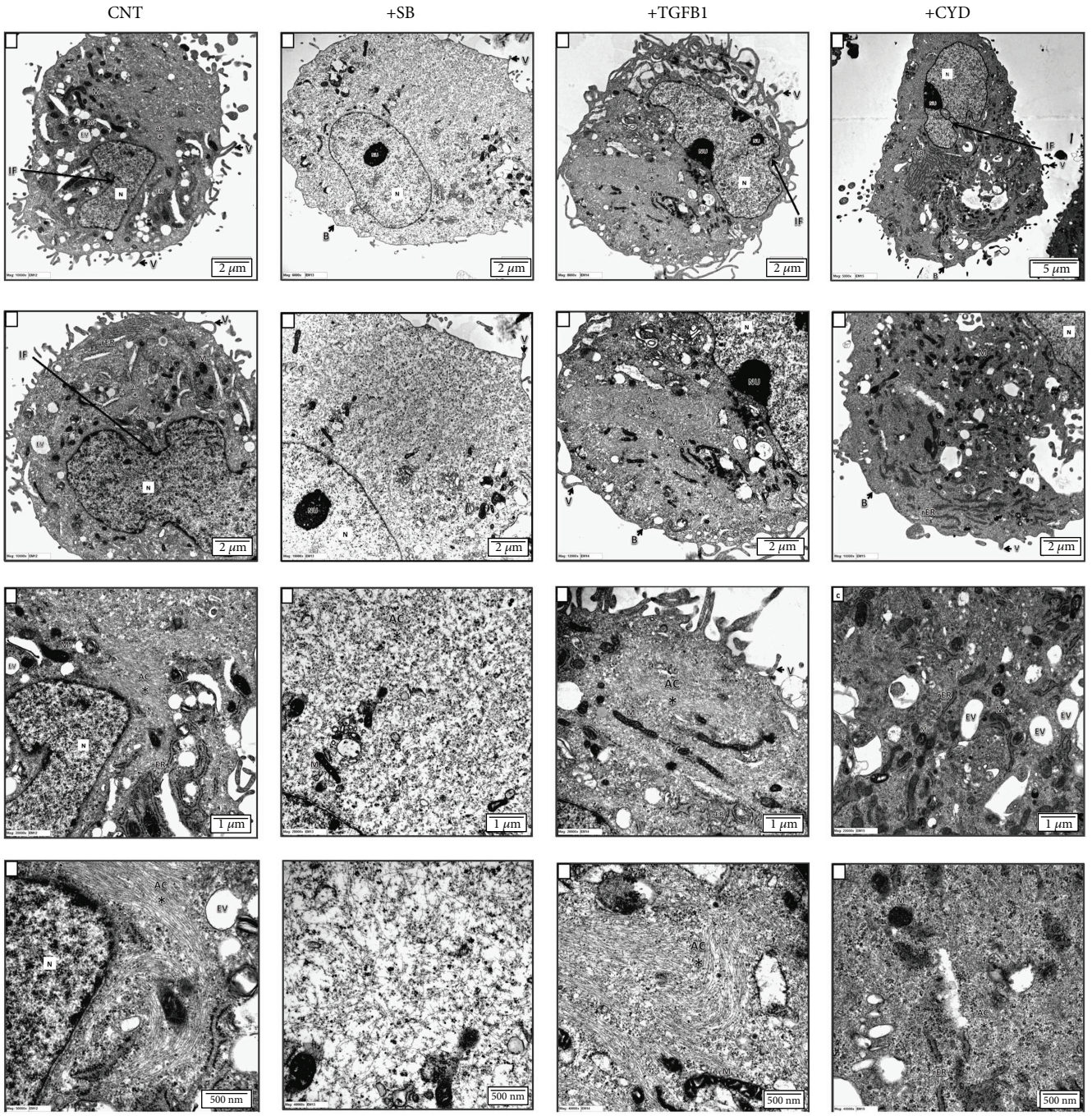

Figure 4: Transmission electron microscopy of MSCs with and without treatment with SB-431542, TGFβ1, or CYD. TEM ultrastructural analysis of MSCs following no treatment (CNT) or treatment with SB-431542 (SB), TGFβ1, or CYD. Increasing levels of magnification are indicated by scale bars. N: nucleus; Nu: nucleolus; AC: actin filaments; V: microvilli; M: mitochondria; PL: primary lysosome; SL: secondary lysosome; rER: rough endoplasmic reticulum; G: Golgi bodies; B: cell blebs; P: cell processes; IF: nuclear membrane infolding; EV: endocytotic vacuole.

signaling pathways and involving focal adhesion kinase (FAK), p38, and JNK activation [7]. Furthermore, a separate study reported that the suppression of actin polymerization, a very early event in hMSC differentiation, following the downregulation of p38 MAPK activity, inhibited osteogenesis [30]. Additionally, α-smooth muscle actin is important for both the identification of osteoprogenitors in hMSCs and their differentiation fate [31], and Rho GTPase-mediated cytoskeletal modification is essential for controlling hMSC differentiation and migration [32].

On the other hand, adipocytic differentiation is associated with the morphological change from fibroblast-like cells to spherical cells filled with fat droplets [33]. These morphological alterations are also associated with cytoskeletal changes and

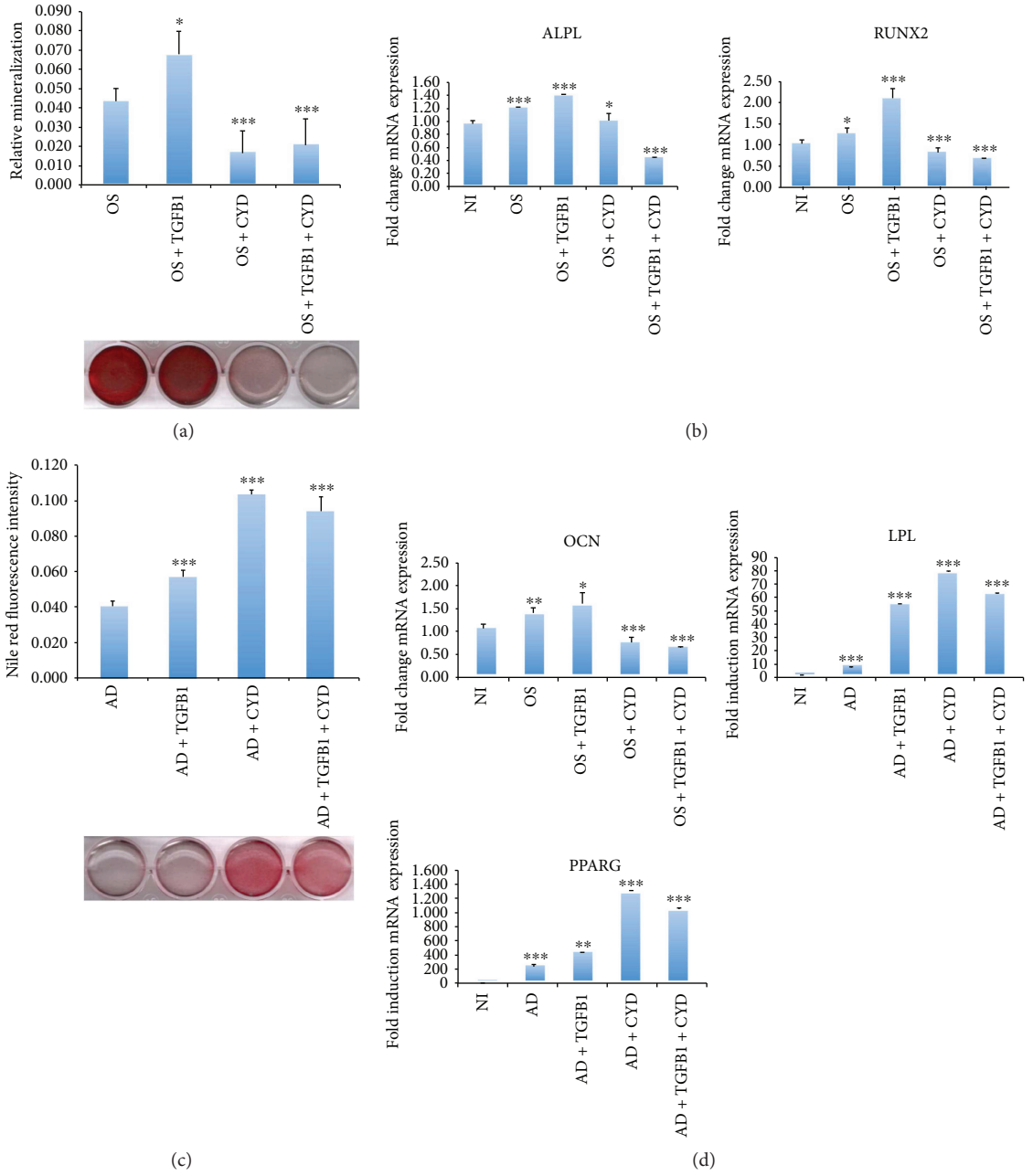

Figure 5: Inhibition of actin polymerization promotes adipogenic differentiation but inhibits osteogenic differentiation in MSCs. MSCs underwent osteogenic or adipogenic differentiation by culturing cells in the appropriate medium for 7 days. Cells also underwent the indicated treatments. (a) Mineralized calcium deposition, as determined by alizarin red S staining in MSCs that were osteoinduced (OS), osteoinduced with TGFβ1 treatment two days prior to induction (OS + TGFβ1), osteoinduced with CYD treatment at the onset of induction (OS + CYD), or osteoinduced with both TGFβ1 and CYD treatment at the time points described above (OS + TGFβ1 + CYD). Lower panel: micrograph of stained wells. Upper panel: quantification of mineralized matrix formation under the indicated treatment conditions. Data are shown as the mean ± SD of three independent experiments ($^{*}p < 0.05$; $^{***}p < 0.005$). (b) Gene expression of the osteogenic markers *ALPL*, *RUNX2*, and *OCN*, normalized to GAPDH, as determined by qRT-PCR. Cells were either not induced (NI) or induced under the conditions described in (a). Data are shown as the mean ± SD of three independent experiments ($^{*}p < 0.05$; $^{**}p < 0.005$, $^{***}p < 0.0005$). (c) Adipogenic differentiation of MSCs that were adipoinduced (AD), adipoinduced with TGFβ1 treatment 2 days prior to induction (AD + TGFβ1), adipoinduced with CYD treatment, initiated at the onset of induction (AD + CYD), or adipoinduced with both TGFβ1 and CYD treatment at the time points described above (AD + TGFβ1 + CYD). Lower panel: Oil red O staining of the indicated cells. Upper panel: Nile red quantification of oil content under the indicated conditions. (d) Gene expression of the adipogenic marker genes *PPARG* and *LPL*, determined by qRT-PCR and normalized to GAPDH, under the indicated treatment regimens. Data are shown as the mean ± SD of three independent experiments ($^{**}p < 0.005$, $^{***}p < 0.0005$). All controls were treated with vehicle only.

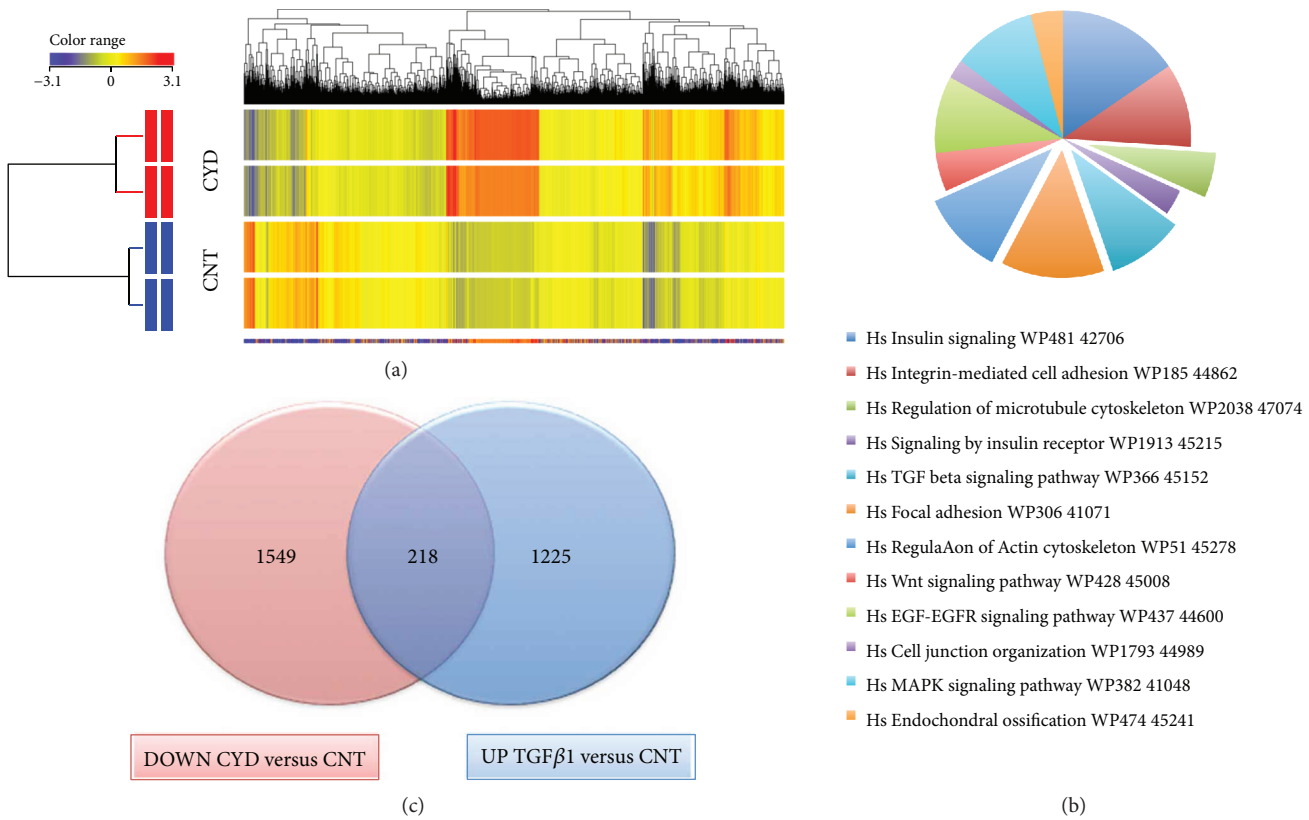

FIGURE 6: Molecular phenotype of CYD-treated hMSCs. (a) Hierarchical clustering of genes that were differentially expressed in CYD-treated and untreated control (CNT) hMSCs. Rows represent individual gene expression for duplicate treated and untreated samples, as indicated. Columns represent individual transcripts. Relative expression levels are presented colorimetrically, according to the scale shown in the color bar. (b) Pie chart showing the pathways with the highest enrichment of genes significantly upregulated in CYD-treated cells. (c) Venn diagram depicting the overlap between the upregulated genes in TGFβ1-treated cells (UP TGFβ1 versus CNT) and the downregulated genes in CYD-treated cells (DOWN CYD versus CNT).

actin reorganization, which takes place in the early lineage commitment stage, prior to the upregulation of many adipocytic-specific gene markers [34]. The differentiation of hMSCs into the adipocytic lineage *in vitro* is known to be influenced by the cytoskeletal tension that results following actin reorganization [32]. Furthermore, TGFβ1 Ca^{2+} signaling is known to regulate osteoblast adhesion through enhanced α5 integrin expression, the formation of focal contacts, and the mediation of cytoskeleton reorganization [35, 36]. Additionally, the TGFβ1-mediated stimulation of DNA synthesis in mouse osteoblastic cells is reportedly associated with morphological changes and is accompanied by the enhanced synthesis and polymerization of cytoskeletal proteins [37]. Consistent with this, our data suggests that TGFβ1 enhances hMSC lineage commitment by regulating the morphology of the actin cytoskeleton, focal adhesion, and endochondral ossification, via the TGFβ1 and MAPK signaling pathways.

Also consistent with our results are reports that CYD-mediated reductions in actin polymerization stimulate adipogenesis, but inhibit osteogenesis [30], suggesting that cytoskeletal modification is a prerequisite for cell fate determination. Our gene expression profiling revealed that the genes *FGF1*, *FGF2*, and *KRAS*, which commonly regulate actin cytoskeleton reorganization, were upregulated and downregulated in TGFβ1- and CYD-treated cells, respectively, suggesting that they are involved in the actin polymerization-mediated differentiation of MSCs.

We showed that during osteogenesis, TGFβ1 treatment reorganized the cytoskeleton, but this reorganization, and thus osteogenesis, could be disturbed by CYD treatment. Conversely, treatment with either TGFβ1 or CYD promoted adipogenesis. This observation can potentially be explained by considering that TGFβ1 and CYD promote the formation of different cytoskeleton patterns, both of which support adipogenesis. Alternatively, it is possible that cytoskeletal reorganization leading to adipogenesis can be promoted by both TGFβ1-dependent and -independent mechanisms, and that CYD-mediated cytoskeletal reorganization cannot override the TGFβ1-independent mechanism.

We propose a model wherein TGFβ1 regulates cytoskeletal organization by modulating actin cytoskeleton-related genes, leading to enhanced hMSC differentiation into both osteoblasts and adipocytes (Figure 7). We propose that CYD enhances adipogenesis and inhibits osteogenesis by regulating the expression of a number of key candidate genes, including *FGF2*, *TGFβ2*, *Plat*, *EGR2*, *MEF2D*, and *IRS1*. These genes were modulated by both TGFβ1 and CYD and

Table 2: Genes involved in osteogenesis-related pathways that are downregulated in CYD-treated hMSCs.

Endochondral ossification	Actin cytoskeleton	Focal adhesion	TGFβ signaling	MAPK signaling
FGF2	FGF1	ITGA6	UCHL5	STMN1
TGFB2	FGF2	STYK1	CDC2	DUSP1
PLAT	FGF5	CAV1	SMURF2	TRAF2
CALM1	FGF22	CAV2	NEDD9	BDNF
ADAMTS1	KRAS	CAV3	STAMBPL1	MAP3K5
OPG	NRAS	LAMC2	CCNB2	ACVR1C
	C11orf13	THBS1	RBL1	KRAS
	F2R	PXN	MAPK8	TGFB2
	CRK	RHOB	PARD6A	NRAS
	PAK1	PDPK1	CAV1	PPP5C
	ARHGEF7	MYLK2	TFDP1	PAK1
	VIL2	PAK1	KLF6	CRK
	PXN	MAPK8	FST	MAPK8
		BCL2	SERPINE1	
		CCND3	THBS1	
		CRK	NOG	
			HRAS	

are thus heavily implicated in the determination of hMSC fate. In summary, our study provides novel molecular insights into the role of the intracellular TGFβ signaling pathway in bone and bone marrow adipose tissue formation. This signaling involves the reorganization of the actin cytoskeleton in order to control the lineage-specific differentiation of hMSCs.

4. Materials and Methods

4.1. Cell Culture. An hMSC-TERT cell line was created previously to serve as a model of human primary MSCs by overexpressing human telomerase reverse transcriptase (hTERT) in normal human bone marrow MSCs [38]. This cell line has been extensively characterized and exhibits a similar cellular and molecular phenotype to primary MSCs [39]. For the current experiments, we used a previously characterized subline derived from hMSC-TERT cells, termed hMSC-TERT-CL1 [40]. For ease, this cell line is referred to as "hMSC" for the remainder of the manuscript. Cells were cultured in Dulbecco's modified Eagle's medium (DMEM) supplemented with 4500 mg/l D-glucose, 4 mM L-glutamine, 110 mg/l sodium pyruvate, 10% fetal bovine serum (FBS), 1× penicillin/streptomycin (pen/strep), and nonessential amino acids. All reagents were purchased from Gibco, USA.

4.2. In Vitro Osteoblastic Differentiation. To induce osteoblastic differentiation, cells were initially grown in standard DMEM growth medium in 6-well plates at a density of 0.3×10^6 cells/ml. Once 70–80% confluence was reached, the medium was replaced with DMEM supplemented with osteoblast induction mixture, containing 10% FBS, 1% pen/strep, 50 μg/ml L-ascorbic acid (Wako Chemicals, Neuss, Germany), 10 mM β-glycerophosphate (Sigma), 10 nM calcitriol (1α,25-dihydroxyvitamin D_3; Sigma), and 10 nM dexamethasone (Sigma). The medium was replaced 3 times per week. Cells were cultured in standard culture medium in parallel as controls.

Table 3: Genes involved in adipogenesis-related pathways that are upregulated in CYD-treated hMSCs.

Gene symbol	Fold change versus control
PPARGC1A	2.4170778
AGT	15.447543
GDF10	9.77814
BMP2	9.539022
UCP1	9.416412
SFRP4	6.513523
IRS4	5.973821
MEF2C	5.1696005
LPL	5.150721
PLIN1	5.144724
LEP	5.1005282
NDN	5.0982733
CNTFR	4.9715867
LIF	3.9070668
PRLR	3.855135
RXRG	3.8392398
EGR2	3.6894956
PCK1	3.6815107
CYP26A1	3.170688
TGFBI	3.1407108
STAT2	3.0656292
BMP3	2.9982927
IGF1	2.9808753
PTGIS	2.8547947
INSR	2.8151898
SLC2A4	2.747039
CEBPB	2.7001002
IRS1	2.5992496
LPIN1	2.579549
AHRR	2.5087466
IL6	2.4654725
IRS2	2.3497624
STAT5A	2.2441745
CEBPA	2.2439373
SCD	2.216643
STAT1	2.205384
SPOCK1	2.201062
SREBF1	2.0996578
EPAS1	2.0842645
MEF2D	2.0606902
BMP1	2.0168457
LPIN3	2.0103807

Table 4: Genes involved in both osteogenesis- and adipogenesis-related pathways that are significantly changed in TGFβ-treated cells and CYD-treated cells.

Endochondral ossification	Actin cytoskeleton	Focal adhesion	TGFB signaling	MAPK signaling	Adipogenesis
TGFB2	FGF1	CAV2	NEDD9	TGFB2	EGR2
FGF2	FGF2	MAPK8	MAPK8	MAPK8	IRS1
PLAT	KRAS	LAMC2		KRAS	MEF2D
				DUSP1	

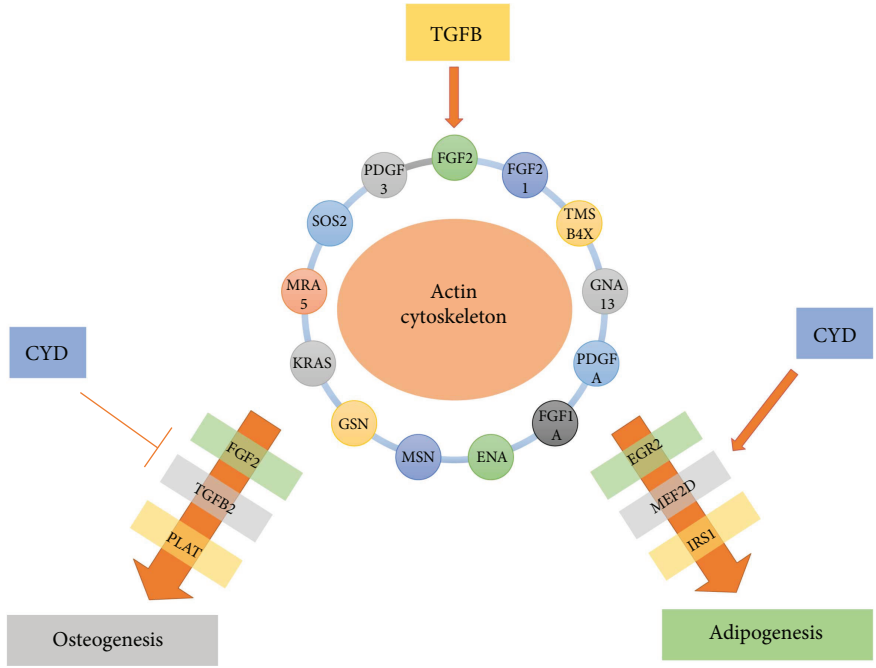

Figure 7: TGFβ1 signaling in hMSC differentiation. Schematic showing how TGFβ and CYD affect hMSC osteogenic and adipogenic differentiation through the modulation of genes associated with the actin cytoskeletal pathway. Suggested downstream targets are also shown.

4.3. In Vitro Adipocytic Differentiation. To induce adipocytic differentiation, cells were initially grown in standard DMEM growth medium in 6-well plates at a density of 0.3×10^6 cells/ml. Once 90–100% confluence was reached, the medium was replaced with DMEM supplemented with adipogenic induction mixture, containing 10% FBS, 10% horse serum (Sigma), 1% pen/strep, 100 nM dexamethasone, 0.45 mM isobutyl methylxanthine [41] (Sigma), 3 μg/ml insulin (Sigma), and 1 μM rosiglitazone [42] (Novo Nordisk, Bagsvaerd, Denmark). The medium was replaced 3 times per week, and cells cultured in parallel in standard culture medium were used as controls.

4.4. Cytochemical Staining

4.4.1. Alizarin Red S Staining for Mineralized Matrix. Once cells had grown sufficiently, the cell monolayer was washed with phosphate-buffered saline (PBS) and then fixed with 4% paraformaldehyde for 15 minutes at room temperature. Cells were then rinsed 3 times in distilled water and stained with 2% alizarin red S Stain (Cat. number 0223; ScienCell, Carlsbad, CA, USA) for 20–30 minutes at room temperature. Cells were washed further 3–5 times with water to remove excess dye and then stored in water to prevent them drying out. Cells were then visualized using an inverted microscope (ZEISS AX10). To quantify alizarin red S staining, and hence mineralization, plates were air dried, and then the alizarin red S dye was eluted by adding 800 μl acetic acid to each well and incubating for 30 minutes at room temperature, as described previously [43]. The stain was then quantified by measuring the absorbance at 405 nm with an Epoch spectrophotometer (BioTek Inc., Winooski, VT, USA).

4.4.2. OsteoImage Mineralization Assay. The formation of mineralized matrix *in vitro* was quantified using an OsteoImage mineralization assay kit according to manufacturer's instructions (Cat. number PA-1503; Lonza, USA). Briefly, culture medium was removed, and cells were washed once with PBS and then fixed with 70% cold ethanol for 20 minutes. Next, diluted staining reagent was added at a level recommended by the manufacturer, and plates were incubated in the dark for 30 minutes at room temperature. The cells were then washed, and staining was quantified using a fluorescence plate reader (Molecular Devices Co., Sunnyvale, CA, USA) with excitation and emission wavelengths of 492 and 520 nm, respectively.

4.4.3. Oil Red O Staining for Lipid Droplets. Cytoplasmic lipid droplets within mature adipocytes were visualized using Oil red O staining. Cells were washed with PBS, fixed in 4% formaldehyde for 10 minutes at room temperature, rinsed once with 3% isopropanol, and then stained for 1 hour at room temperature with filtered Oil red O staining solution (prepared by dissolving 0.5 g Oil red O powder in 60% isopropanol). In order to quantify mature adipocytes, Oil red O stain was eluted from cells by adding 100% isopropanol to each well, and then the absorbance at 510 nm was measured using an Epoch spectrophotometer.

4.4.4. Nile Red Staining for the Quantification of Mature Adipocytes. A 1 mg/ml stock solution of Nile red fluorescent stain was prepared in DMSO and stored in the dark at −20°C. Cultured undifferentiated and differentiated cells were fixed in 4% paraformaldehyde (Sigma) for 15 minutes and then washed once with PBS. PBS was then removed, and cells were stained with 5 μg/ml Nile red stain in PBS for 10 minutes at room temperature. The fluorescence signal was measured using a SpectraMax/M5 fluorescence spectrophotometer (Molecular Devices Co.) in bottom-well scan mode. Nine readings were taken per well using excitation and emission wavelengths of 485 nm and 572 nm, respectively.

4.5. Quantitative Real-Time PCR (qRT-PCR). Total RNA was extracted from cells using a PureLink RNA mini kit (Cat number 12183018A; Ambion, USA) according to manufacturer's recommendations and quantified using a NanoDrop 2000 spectrophotometer (Thermo Scientific, USA). Complementary DNA (cDNA) was synthesized from 1 μg RNA using a high-capacity cDNA reverse transcription kit (Applied Biosystems, USA) and a MultiGene thermal cycler (Labnet) according to manufacturer's instructions. Relative mRNA levels were inferred from the cDNAs using Power SYBR Green master mix (Applied Biosystems, UK) and TaqMan Universal master mix II, no UNG (Applied Biosystems, USA), both according to manufacturer's instructions, and a real-time PCR detection system (Applied Biosystems). Relative mRNA levels were normalized to the reference gene GAPDH, and then gene expression quantification was performed using a comparative Ct method, wherein ΔCT is defined as the difference between the target and reference gene CT values. Primers are listed in Supplementary Tables S7 and S8. These primers were either TaqMan primers (Applied Biosystems) or custom primers whose sequences have been published previously.

4.6. Global Gene Expression Profiling by Microarray. Total RNA was extracted from cells using a PureLink RNA mini kit, according to manufacturer's recommendations. One hundred and fifty nanograms of total RNA was then labeled and hybridized to a SurePrint G3 Human GE 8 × 60 K microarray chip (Agilent Technologies). All microarray experiments were conducted by the Microarray Core Facility (Stem Cell Unit, College of Medicine, King Saud University). Normalization and data analyses were performed using GeneSpring GX software (Agilent Technologies), and pathway analysis was conducted using the Single Experiment Pathway analysis feature of the GeneSpring 12.0 software package (Agilent Technologies) as described previously (66). In addition, we used the web-based software DAVID Bioinformatics Resources 6.8, where all genes that were upregulated by TGfb were uploaded into DAVID and signaling pathways were achieved. Significant changes were defined as a fold change of ≥2 and $p < 0.02$.

4.7. Cell Proliferation Assays

4.7.1. AlamarBlue Cell Viability Assay. Cell viability was measured using alamarBlue assay reagent (AbD Serotec, Raleigh, NC, USA) according to manufacturer's recommendations. Briefly, cells were cultured in 96-well plates in 100 μl of the appropriate medium before 10 μl alamarBlue substrate was added at the indicated time points. Plates were then incubated in the dark at 37°C for 1 hour. AlamarBlue fluorescence was then detected using a Synergy II microplate reader (Bio-Tek Inc.) with excitation and emission wavelengths of 530 nm and 590 nm, respectively.

4.8. RTCA Cell Proliferation Assay. An xCELLigence RTCA (real-time cell analysis) DP system (ACEA Biosciences Inc., San Diego, CA) was used to measure the rate of cellular proliferation according to manufacturer's protocol. Briefly, 100 μl DMEM supplemented with 10% FBS was loaded onto each well of an E-plate 16 chamber slide, which was then placed inside the humidified incubator of the RTCA DP analyzer for 1 hour at 37°C to allow the membrane surface and medium to equilibrate. After 1 hour, background measurements were performed. Next, 5000 cells/100 μl DMEM + 10% FBS were added per well, and measurements were recorded at 15-minute intervals for various total durations, depending on the experimental setup.

4.9. Transmission Electron Microscopy (TEM). For TEM, cells were trypsinized, washed with PBS, pelleted, and then fixed in 2.5% glutaraldehyde (Cat. number 16500; Electron Microscopy Sciences) in 0.1 M phosphate buffer (pH 7.2) at 4°C for 4 hours. Next, the cells were washed in 0.1 M phosphate buffer (pH 7.2) 3 times for 30 minutes each and then treated with 1% osmium tetroxide (OsO_4) in 0.1 M phosphate buffer (pH 7.2) for 2 hours. Cells were then dehydrated in increasing concentrations of ethanol (10%, 30%, 50%, 70%, 90%, and 100%) for 15 minutes each, before being resuspended in acetone and incubated for 15 minutes. The resulting cell suspension was then aliquoted into BEEM® embedding capsules and infiltrated firstly with a 2 : 1 acetone : resin mixture for 1 hour and secondly with a 1 : 2 acetone : resin mixture for 1 hour. Following infiltration, the BEEM capsules were centrifuged at 2500 rpm for 5 minutes and embedded in pure resin for 2 hours. The resin was then polymerized by baking in an oven at 70°C for 12 hours. Semithin sections (0.5 μm thickness) were prepared and stained with 1% toluidine blue. Ultrathin sections (70 nm thickness) were prepared and mounted on copper grids and then stained firstly with uranyl acetate (saturated ethanol solution) for 30 minutes, rinsed with double distilled water and then stained with Reynold's lead citrate solution for 5

minutes before a final rinse with distilled water. The contrasted ultrathin sections were examined and photographed under a JEOL 1010 transmission electron microscope (JEOL, Tokyo, Japan).

4.10. Statistical Analysis. All results are presented as the mean ± SD of at least 3 independent experiments. Differences between groups were assessed using Student's t-test, and p values < 0.05 were considered statistically significant.

Conflicts of Interest

The authors declare that they have no conflicts of interest.

Acknowledgments

The authors would like to extend their sincere appreciation to the Deanship of Scientific Research at King Saud University for its funding of this research through the Research Group Project no. RGP-1438-032.

Supplementary Materials

Supplementary 1. Figure S1: DAVID microarray functional gene analysis. One thousand nine hundred genes were uploaded to DAVID online software. KEGG pathway analysis showed many interested pathways which are upregulated after TGFb-1 treatment of hBMCs. Here, we show the top most upregulated pathways which include key osteoblast differentiation pathways.

Supplementary 2. Table S1: whole genome microarray mRNA data showing gene ENTITIES for TG1 versus CNT DOWN 1298 genes.

Supplementary 3. Table S2: whole genome microarray mRNA data showing gene ENTITIES for TG1 versus CNT UP 1932 genes.

Supplementary 4. Table S3: upregulated biological processes and related genes in TGFB1-treated cells using GO analysis.

Supplementary 5. Table S4: ultrastructural characteristics of CL1 cells under different treatment conditions.

Supplementary 6. Table S5: whole genome microarray mRNA data showing gene entities for CYD versus CNT up to 10,855 genes.

Supplementary 7. Table S6: whole genome microarray mRNA data showing gene entities for CYD versus CNT DOWN 2523 genes.

Supplementary 8. Table S7: real-time PCR human primer sequences used in this study.

Supplementary 9. Table S8: TAQMAN real-time PCR primers.

References

[1] N. Oshimori and E. Fuchs, "The harmonies played by TGF-β in stem cell biology," *Cell Stem Cell*, vol. 11, no. 6, pp. 751–764, 2012.

[2] J. Massagué, J. Seoane, and D. Wotton, "Smad transcription factors," *Genes & Development*, vol. 19, no. 23, pp. 2783–2810, 2005.

[3] J. Pfeilschifter, L. Bonewald, and G. R. Mundy, "Characterization of the latent transforming growth factor ß complex in bone," *Journal of Bone and Mineral Research*, vol. 5, no. 1, pp. 49–58, 1990.

[4] D. Sheppard, "Transforming growth factor β: a central modulator of pulmonary and airway inflammation and fibrosis," *Proceedings of the American Thoracic Society*, vol. 3, no. 5, pp. 413–417, 2006.

[5] Y. Tang, X. Wu, W. Lei et al., "TGF-β1–induced migration of bone mesenchymal stem cells couples bone resorption with formation," *Nature Medicine*, vol. 15, no. 7, pp. 757–765, 2009.

[6] K. Janssens, P. ten Dijke, S. Janssens, and W. Van Hul, "Transforming growth factor-β1 to the bone," *Endocrine Reviews*, vol. 26, no. 6, pp. 743–774, 2005.

[7] L. Chen, K. Shi, C. E. Frary et al., "Inhibiting actin depolymerization enhances osteoblast differentiation and bone formation in human stromal stem cells," *Stem Cell Research*, vol. 15, no. 2, pp. 281–289, 2015.

[8] S. Ono, "Mechanism of depolymerization and severing of actin filaments and its significance in cytoskeletal dynamics," *International Review of Cytology*, vol. 258, pp. 1–82, 2007.

[9] P. Lappalainen and D. G. Drubin, "Cofilin promotes rapid actin filament turnover *in vivo*," *Nature*, vol. 388, no. 6637, pp. 78–82, 1997.

[10] D. A. Fletcher and R. D. Mullins, "Cell mechanics and the cytoskeleton," *Nature*, vol. 463, no. 7280, pp. 485–492, 2010.

[11] G. Yourek, M. A. Hussain, and J. J. Mao, "Cytoskeletal changes of mesenchymal stem cells during differentiation," *ASAIO Journal*, vol. 53, no. 2, pp. 219–228, 2007.

[12] M. Elsafadi, M. Manikandan, R. A. Dawud et al., "Transgelin is a TGFβ-inducible gene that regulates osteoblastic and adipogenic differentiation of human skeletal stem cells through actin cytoskeleton organization," *Cell Death & Disease*, vol. 7, no. 8, article e2321, 2016.

[13] H. Jian, X. Shen, I. Liu, M. Semenov, X. He, and X. F. Wang, "Smad3-dependent nuclear translocation of β-catenin is required for TGF-β1-induced proliferation of bone marrow-derived adult human mesenchymal stem cells," *Genes & Development*, vol. 20, no. 6, pp. 666–674, 2006.

[14] A. Erlebacher, E. H. Filvaroff, J. Q. Ye, and R. Derynck, "Osteoblastic responses to TGF-β during bone remodeling," *Molecular Biology of the Cell*, vol. 9, no. 7, pp. 1903–1918, 1998.

[15] E. Filvaroff, A. Erlebacher, J. Ye et al., "Inhibition of TGF-beta receptor signaling in osteoblasts leads to decreased bone remodeling and increased trabecular bone mass," *Development*, vol. 126, no. 19, pp. 4267–4279, 1999.

[16] J. M. Hock, E. Canalis, and M. Centrella, "Transforming growth factor-β stimulates bone matrix apposition and bone cell replication in cultured fetal rat calvariae," *Endocrinology*, vol. 126, no. 1, pp. 421–426, 1990.

[17] S. Spinella-Jaegle, S. Roman-Roman, C. Faucheu et al., "Opposite effects of bone morphogenetic protein-2 and transforming growth factor-β1 on osteoblast differentiation," *Bone*, vol. 29, no. 4, pp. 323–330, 2001.

[18] R. A. Ignotz and J. Massagué, "Type beta transforming growth factor controls the adipogenic differentiation of 3T3 fibroblasts," *Proceedings of the National Academy of Sciences of*

the United States of America, vol. 82, no. 24, pp. 8530–8534, 1985.

[19] T. Teruel, A. M. Valverde, M. Benito, and M. Lorenzo, "Transforming growth factor β_1 induces differentiation-specific gene expression in fetal rat brown adipocytes," *FEBS Letters*, vol. 364, no. 2, pp. 193–197, 1995.

[20] S. Maeda, M. Hayashi, S. Komiya, T. Imamura, and K. Miyazono, "Endogenous TGF-β signaling suppresses maturation of osteoblastic mesenchymal cells," *The EMBO Journal*, vol. 23, no. 3, pp. 552–563, 2004.

[21] H. Yu, M. Königshoff, A. Jayachandran et al., "Transgelin is a direct target of TGF-β/Smad3-dependent epithelial cell migration in lung fibrosis," *The FASEB Journal*, vol. 22, no. 6, pp. 1778–1789, 2008.

[22] M. Centrella, T. L. McCarthy, and E. Canalis, "Transforming growth factor beta is a bifunctional regulator of replication and collagen synthesis in osteoblast-enriched cell cultures from fetal rat bone," *The Journal of Biological Chemistry*, vol. 262, no. 6, pp. 2869–2874, 1987.

[23] P. G. Robey, M. F. Young, K. C. Flanders et al., "Osteoblasts synthesize and respond to transforming growth factor-type beta (TGF-beta) in vitro," *The Journal of Cell Biology*, vol. 105, no. 1, pp. 457–463, 1987.

[24] T. L. Chen and R. L. Bates, "Recombinant human transforming growth factor β_1 modulates bone remodeling in a mineralizing bone organ culture," *Journal of Bone and Mineral Research*, vol. 8, no. 4, pp. 423–434, 1993.

[25] T. Yamada, N. Kamiya, D. Harada, and M. Takagi, "Effects of transforming growth factor-β1 on the gene expression of decorin, biglycan, and alkaline phosphatase in osteoblast precursor cells and more differentiated osteoblast cells," *The Histochemical Journal*, vol. 31, no. 10, pp. 687–694, 1999.

[26] M. Kassem, M. Kveiborg, and E. F. Eriksen, "Production and action of transforming growth factor-β in human osteoblast cultures: dependence on cell differentiation and modulation by calcitriol," *European Journal of Clinical Investigation*, vol. 30, no. 5, pp. 429–437, 2000.

[27] M. Noda and G. A. Rodan, "Type β transforming growth factor (TGFβ) regulation of alkaline phosphatase expression and other phenotype-related mRNAs in osteoblastic rat osteosarcoma cells," *Journal of Cellular Physiology*, vol. 133, no. 3, pp. 426–437, 1987.

[28] M. E. Antosz, C. G. Bellows, and J. E. Aubin, "Effects of transforming growth factor β and epidermal growth factor on cell proliferation and the formation of bone nodules in isolated fetal rat calvaria cells," *Journal of Cellular Physiology*, vol. 140, no. 2, pp. 386–395, 1989.

[29] B. M. Gumbiner, "Cell adhesion: the molecular basis of tissue architecture and morphogenesis," *Cell*, vol. 84, no. 3, pp. 345–357, 1996.

[30] H. Sonowal, A. Kumar, J. Bhattacharyya, P. K. Gogoi, and B. G. Jaganathan, "Inhibition of actin polymerization decreases osteogeneic differentiation of mesenchymal stem cells through p38 MAPK pathway," *Journal of Biomedical Science*, vol. 20, no. 1, p. 71, 2013.

[31] N. P. Talele, J. Fradette, J. E. Davies, A. Kapus, and B. Hinz, "Expression of α-smooth muscle actin determines the fate of mesenchymal stromal cells," *Stem Cell Reports*, vol. 4, no. 6, pp. 1016–1030, 2015.

[32] R. McBeath, D. M. Pirone, C. M. Nelson, K. Bhadriraju, and C. S. Chen, "Cell shape, cytoskeletal tension, and RhoA regulate stem cell lineage commitment," *Developmental Cell*, vol. 6, no. 4, pp. 483–495, 2004.

[33] J. Y. Fan, J. L. Carpentier, E. van Obberghen, C. Grunfeld, P. Gorden, and L. Orci, "Morphological changes of the 3T3-L1 fibroblast plasma membrane upon differentiation to the adipocyte form," *Journal of Cell Science*, vol. 61, pp. 219–230, 1983.

[34] J. Antras, F. Hilliou, G. Redziniak, and J. Pairault, "Decreased biosynthesis of actin and cellular fibronectin during adipose conversion of 3T3-F442A cells. Reorganization of the cytoarchitecture and extracellular matrix fibronectin," *Biology of the Cell*, vol. 66, no. 3, pp. 247–254, 1989.

[35] L. J. Nesti, E. J. Caterson, M. Wang et al., "TGF-β1-stimulated osteoblasts require intracellular calcium signaling for enhanced α5 integrin expression," *Annals of the New York Academy of Sciences*, vol. 961, no. 1, pp. 178–182, 2002.

[36] L. J. Nesti, E. J. Caterson, M. Wang et al., "TGF-β1 calcium signaling increases α5 integrin expression in osteoblasts," *Journal of Orthopaedic Research*, vol. 20, no. 5, pp. 1042–1049, 2002.

[37] A. Lomri and P. J. Marie, "Effects of transforming growth factor type β on expression of cytoskeletal proteins in endosteal mouse osteoblastic cells," *Bone*, vol. 11, no. 6, pp. 445–451, 1990.

[38] J. L. Simonsen, C. Rosada, N. Serakinci et al., "Telomerase expression extends the proliferative life-span and maintains the osteogenic potential of human bone marrow stromal cells," *Nature Biotechnology*, vol. 20, no. 6, pp. 592–596, 2002.

[39] M. Al-Nbaheen, R. Vishnubalaji, D. Ali et al., "Human stromal (mesenchymal) stem cells from bone marrow, adipose tissue and skin exhibit differences in molecular phenotype and differentiation potential," *Stem Cell Reviews*, vol. 9, no. 1, pp. 32–43, 2013.

[40] M. Elsafadi, M. Manikandan, M. Atteya et al., "Characterization of cellular and molecular heterogeneity of bone marrow stromal cells," *Stem Cells International*, vol. 2016, Article ID 9378081, 18 pages, 2016.

[41] A. Hildebrand, M. Romarís, L. M. Rasmussen et al., "Interaction of the small interstitial proteoglycans biglycan, decorin and fibromodulin with transforming growth factor β," *The Biochemical Journal*, vol. 302, no. 2, pp. 527–534, 1994.

[42] R. Serra and C. Chang, "TGF-β signaling in human skeletal and patterning disorders," *Birth Defects Research Part C: Embryo Today: Reviews*, vol. 69, no. 4, pp. 333–351, 2003.

[43] C. A. Gregory, W. G. Gunn, A. Peister, and D. J. Prockop, "An alizarin red-based assay of mineralization by adherent cells in culture: comparison with cetylpyridinium chloride extraction," *Analytical Biochemistry*, vol. 329, no. 1, pp. 77–84, 2004.